UNIVERSITAT POLITÈCNICA DE VALÈNCIA

Departamento de Máquinas y Motores Térmicos

DOCTORAL THESIS:

Numerical study of EGR mixing and distribution in a piston engine intake line

---

Presented by: D. Guillermo García
Supervised by: Dr. D. Roberto Navarro

in fulfillment of the requirements for the degree of

Doctor of Philosophy

Valencia, November 2021

Doctoral Thesis

Numerical study of EGR mixing and distribution in a piston engine intake line

Presented by: D. Guillermo García
Supervised by: Dr. D. Roberto Navarro

THESIS EXAMINERS

Dr. D. Miguel Ángel Reyes
Dr. D. Oscar García
Dr. D. María Arantzazu Gómez

DEFENSE COMMITTEE

Chairman: Dr. D. José Manuel Luján
Secretary: Dr. D. Octavio Armas:
Member: Dr. D. Miguel Ángel Reyes

Valencia, November 2021

Abstract

Considering the amount of internal combustion engines (ICEs) existing nowadays, and the pollutants that they could potentially emit, it is no surprise that international standards are getting increasingly severe regarding the allowed limits of pollutants that can be released by such engines. For this reason, different techniques have been developed in order to diminish pollutants, as *downsizing* in which the engine size is reduced to decrease the consumption, the hybridation of engines and the exhaust gases recirculation (EGR). This recirculation technique can be addressed by 2 different paths: Low Pressure EGR (LP-EGR) which reintroduce the exhaust gases before the compressor, while High Pressure EGR (HP-EGR) injects exhaust gases after the compressor in the intake manifold. Since both configurations deal with a direct injection of the recirculated flow in the main stream, in the present work a numerical study of the mixing between air and EGR flows is proposed, using a commercial code of computational fluid dynamics (STAR-CCM+).

In LP-EGR configuration has been proposed the study of the influence of a heterogeneous inlet (composed by air and exhaust gases) on the main performance of a centrifugal compressor. To do that, 9 different operating points have been analyzed, trying to cover the whole map of the compressor with a constant injection rate. It has been demonstrated the necessity of a transient scheme for obtaining reliable results in the complete domain of the compressor. On the other hand, it has been proved that, with standard penetration rates of the flow, EGR do not have a remarkable impact in the performance of the compressor, besides the surge zone. In LP-EGR scheme, a numerical design of experiments has been developed with the aim to find correlations between the generated volume condensation (which can appear under some operating points of the engine) and the mixing between air and exhaust gases. It has been proved that the penetration of the EGR in the main stream is a key factor in volume condensation, increasing the amount of mixing between the streams.

In HP-EGR configuration, different studies of numerical configuration have been conducted trying to find the influence of factors like mesh, time-step size, and turbulence models in the final distribution of exhaust gases between the cylinders of the engine. RANS submodels have demonstrated that can predict most of the operating points both average and instantaneous variables

in comparison with experimental measurements. After that, fixing a numerical setup, different mixers in 4 and 6 cylinder manifolds have been calculated, showing the applicability of the developed mixing indexes, and quantifying the influence of the different physical effects that can influence in the mixing and distribution between air and exhaust gases streams.

Keywords: Mixing; LP-EGR; HP-EGR; CFD simulation; STAR-CCM+; Compressor; Condensation; Manifold

Resumen

Teniendo en cuenta la cantidad de motores de combustión interna que se encuentran en activo actualmente, y sus potenciales emisiones de contaminación si se realizaran de forma incontrolada por el parque automovilístico, las normativas internacionales son cada vez más estrictas en cuanto a la cantidad de gases perjudiciales para el medio ambiente que pueden emitir dichos motores de manera unitaria. Debido a ello, se han ido desarrollando e implantando técnicas de reducción de contaminantes como el *downsizing* en el cual se reduce el tamaño del motor para reducir el consumo, la implantación de motores híbridos y la Recirculación de Gases de Escape. Esta técnica de recirculación puede abordarse de dos maneras alternativas: la Recirculación de Gases de Escape de Ruta Larga inyecta dichos gases antes del compresor, mientras que la Recirculación de Gases de Escape de Ruta Corta (o alta presión) los reinyecta después del compresor, en el mismo colector de admisión del motor. Dado que en ambas configuraciones se produce una inyección directa del flujo recirculado en la corriente principal, en el presente trabajo se propone un estudio numérico de la mezcla entre las corrientes de aire y gases recirculados usando un software comercial de mecánica de fluidos computacional (STAR-CCM+).

En la configuración de Ruta Larga se ha propuesto en primer lugar estudiar el efecto en los parámetros globales del compresor de una entrada heterogénea compuesta por aire y gases de escape. Para ello, se han analizado 9 puntos de funcionamiento distintos, tratando de abarcar el mapa completo del compresor centrífugo con una tasa de inyección constante. Se ha demostrado, por un lado, la necesidad de un esquema transitorio de cálculo para la obtención de resultados confiables en todo el dominio del compresor. Por otro lado, se ha demostrado que, con tasas de penetración de flujo estándar, la inyección de gases recirculados no tiene un impacto reseñable en las prestaciones del compresor, con excepción de la zona de bombeo. En segundo lugar, se ha desarrollado un diseño numérico de experimentos en configuración de Ruta Larga con el objetivo de encontrar correlaciones entre la condensación generada en dichas uniones (la cual puede aparecer bajo ciertas condiciones de operación del motor) y la mezcla entre las corrientes de aire y gases de escape. Se ha demostrado que la penetración de los gases en la corriente principal es un factor clave en la condensación generada, aumentando la cantidad de mezcla entre ambas corrientes.

En la configuración de Ruta Corta se han realizado estudios de configuración numérica tratando de estudiar la influencia de factores como malla, tamaño del paso temporal y modelos de turbulencia en la distribución final de los gases de escape entre los diferentes cilindros del motor. Se ha demostrado que los submodelos RANS pueden predecir la mayor parte de puntos de operación tanto en variables medias como instantáneas comparando resultados numéricos con mediciones experimentales. Fijando una configuración numérica, posteriormente se han analizado diferentes mezcladores en colectores de motores de 4 y 6 cilindros, demostrando la aplicabilidad de los índices de mezclado desarrollados y cuantificando la influencia de los diferentes efectos físicos que influyen en la distribución y mezcla de los gases de escape en la corriente principal.

Resum

Tenint en compte la quantitat de motors de combustió interna que es troben en actiu actualment, i les seues potencials emissions de contaminació si es realitzaren de manera incontrolada pel parc automobilístic, les normatives internacionals són cada vegada més estrictes quant a la quantitat de gasos perjudicials per al medi ambient que poden emetre aquests motors de manera unitària. A causa d'això, s'han anat desenvolupant i implantant tècniques de reducció de contaminants com el *downsizing* en el qual es redueix la grandària del motor per a reduir el consum, la implantació de motors híbrids i la Recirculació de Gasos de Fuita. Aquesta tècnica de recirculació pot abordar-se de dues maneres alternatives: la Recirculació de Gasos de Fuita de Ruta Llarga injecta aquests gasos abans del compressor, mentre que la Recirculació de Gasos de Fuita de Ruta Curta (o alta pressió) els reinjecta després del compressor, en el mateix collector d'admissió del motor. Atés que en totes dues configuracions es produeix una injecció directa del flux recirculat en el corrent principal, en el present treball es proposa un estudi numèric de la mescla entre els corrents d'aire i gasos recirculats usant un programari comercial de mecànica de fluids computacional (STAR-CCM+).

En la configuració de Ruta Llarga s'ha proposat en primer lloc estudiar l'efecte en els paràmetres globals del compressor d'una entrada heterogènia composta per aire i gasos de fuita. Per a això, s'han analitzat 9 punts de funcionament diferents, tractant d'abastar el mapa complet del compressor centrífug amb una taxa d'injecció constant. S'ha demostrat, d'una banda, la necessitat d'un esquema transitori de càlcul per a l'obtenció de resultats de confiança en tot el domini del compressor. D'altra banda, s'ha demostrat que, amb taxes de penetració de flux estàndard, la injecció de gasos recirculats no té un impacte ressenyable en les prestacions del compressor, amb excepció de la zona de bombament. En segon lloc, s'ha desenvolupat un disseny numèric d'experiments en configuració de Ruta Llarga amb l'objectiu de trobar correlacions entre la condensació generada en aquestes unions (la qual pot aparéixer sota unes certes condicions d'operació del motor) i la mescla entre els corrents d'aire i gasos de fuita. S'ha demostrat que la penetració dels gasos en el corrent principal és un factor clau en la condensació generada, augmentant la quantitat de mescla entre tots dos corrents.

En la configuració de Ruta Curta s'han realitzat estudis de configuració numèrica tractant d'estudiar la influència de factors com a malla, grandària del pas temporal i models de turbulència en la distribució final dels gasos de fuita entre els diferents cilindres del motor. S'ha demostrat que els submodelos RANS poden predir la major part de punts d'operació tant en variables mitjanes com instantànies comparant resultats numèrics amb mesuraments experimentals. Fixant una configuració numèrica, posteriorment s'han analitzat diferents mescladors en col · lectors de motors de 4 i 6 cilindres, demostrant l'aplicabilitat dels índexs de barrejat desenvolupats i quantificant la influència dels diferents efectes físics que influeixen en la distribució i mescla dels gasos de fuita en el corrent principal.

List of publications

This thesis is based on the work contained in the following papers:

[1] J. Galindo, H. Climent, R. Navarro, G. García-Olivas, S. Guilain, and R. Boubennec. "Effect of Numerical Configuration on Predicted EGR Cylinder-to-Cylinder Dispersion." In: *SAE Technical Paper*. 2020. DOI: 10.4271/2020-01-1113

[2] Galindo, J. and Serrano, J.R. and Navarro, R. and García Olivas, G. "Numerical modeling of centrifugal compressors with heterogeneous incoming flow due to low pressure exhaust gas recirculation." In: *Proceedings of ASME Turbo Expo 2020: Turbomachinery Technical Conference and Exposition*. GT2020-16030. American Society of Mechanical Engineers. 2020. DOI: 10.1115/gt2020-16030

[3] J. Galindo, H. Climent, R. Navarro, and G. García-Olivas. "Assessment of the numerical and experimental methodology to predict EGR cylinder-to-cylinder dispersion and pollutant emissions." *International Journal of Engine Research* 22(10) (2021), pp. 3128–3146. DOI: 10.1177/1468087420972544

[4] J Galindo, A Gil, R Navarro, and G García-Olivas. "Numerical assessment of mixing of humid air streams in three-way junctions and impact on volume condensation." *Applied Thermal Engineering* 201 (2022), p. 14. DOI: https://doi.org/10.1016/j.applthermaleng.2021.117676

Division of work between authors

The work leading up to this thesis was done in collaboration with other researchers. The respondent is the corresponding author of all papers on which this thesis is based (authors signatures are in order of seniority). The respondent produced the set-up, simulation, campaings and postprocessing of all the CFD cases. However, Francisco Moya is acknowledged for the 0D condensation model simulations of chapter 3 and Daniel Tarí is acknowledged for the development of CFD condensation model of chapter 3. Julián Miguel García is acknowledged by the experimental measurements and 1D model calibration of chapter 4 and 5. In any case, the respondant processed the results of such tools (OD and 1D models, together with experimental measurements) included in this Thesis. Methodology and results discussion were performed in collaboration with supervisor Prof. Navarro, Prof. Galindo and rest of co-authors.

Other publications by the respondent

The following is the publication in which the respondent has been involved during his doctorate studies, but are not included in the theis. This contribution are based on the numerical influence of compressor in the conditions of T-junction, so its development has been essential for carry out chapter 3.

[5] J. Galindo, R. Navarro, D. Tarí, and G. García-Olivas. "Centrifugal compressor influence on condensation due to Long Route-Exhaust Gas Recirculation mixing." *Applied Thermal Engineering* 144 (2018), pp. 901 –909. ISSN: 1359-4311. DOI: 10.1016/j.applthermaleng.2018.09.005

Acknowledgments

First of all, I would like to greatly thank Prof. Roberto Navarro for sharing his knowledge and advice throughout the long journey that this thesis has been. And of course, a thousand thanks for his enormous patience with my catastrophic English. I also want to thank CMT-Motores Térmicos and Universitat Politècnica de València for this opportunity that they gave me.

Of course, I would like to thank Prof. Galindo for his guidance in the paths and decisions made throughout the thesis. In the same way, a big thank to Prof. Climent for all the support provided in EGR essays and for that exceptional kindness.

Many thanks to all the people who have helped me in different parts of the thesis allowing it to come to fruition: Daniel Tarí in my beginnings with all the support and teaching about CFD; Julián Miguel García for all his work with the 1D models and experimental results and Francisco Moya with his help with the condensation model and experimental data. Many thanks to the rest of the technicians, administration staff and the rest of the people who make it possible for this research institute to advance properly.

Many thanks to my friends who have always been making me smile in the worst (and best) moments on this long road. Thanks to my friends from CMT Miguel Ángel, Pau, Alberto, Nico, Lucas and Fran (again) for those moments of rest between results and publications. Thanks to my degree mates Mario, Abián, María and Natalia for your support and for those post-meal talks. And special thanks to María Martínez for testing me with your questions, and your encouragement inside and outside the CMT. And thanks to my work colleagues for this support and boost in the final moments of the thesis.

Last but not least, infinite thanks to my family, especially my mother for all your patience and guidance with a disastrous son absent almost 100% of the time. A million thanks to my grandmother, because with her experience and her humor she always makes me smile. And many thanks to my cousins and uncles for supporting me in the worst moments and laughing with me in the good ones.

Valencia, October 2021.

"Do or do not. There is no try."

Master Yoda.

Contents

List of Tables

List of Figures

List of symbols

Latin characters

A	Area	m^2
A_{strm-n}	Area of streamline n	m
a	Speed of sound	$m \cdot s^{-1}$
C	Courant number	$-$
C_p	Specific heat	$J \cdot kg^{-1} \cdot K^{-1}$
dA	Differential area	m^2
D	Duct diameter	m
f_v	Viscous forces	$kg \cdot m \cdot s^{-2}$
I	Turbulent intensity	%
Imb	EGR Mass imbalance	%
J	Branch-to-main momentum ratio	$-$
K	Number of simulations inside the numerical campaign	$-$
L	Latent heat	$J \cdot kg^{-1}$
L_{strm-n}	Length of streamline n	m
$\dot{m}$	Mass flow rate	$kg \cdot s^{-1}$
M_R	Main-to-branch momentum ratio	$-$
N	Compressor rotational speed	rpm
N	Engine speed	rpm
N	Number of elements in a cross section	$-$
N	Number of EGR pulses	$-$
n	Number of runners	$-$
n	Number of cycles	$-$
P	Pressure	bar
p	Pressure	bar
R^2	Correlation coefficient	$-$
S	Source term	
T	Temperature	K
t	Time	s
$\vec{u}$	Velocity	$m \cdot s^{-1}$
$\overrightarrow{\overrightarrow{u(t)}}_{intake-n}$	Mean velocity field of intake n	$m \cdot s^{-1}$
U	Velocity magnitude	$m \cdot s^{-1}$

V	Velocity magnitude	$m \cdot s^{-1}$
W_{strm-n}	Width of streamline n	m
w	Specific humidity	$g_{H_2O} \cdot kg_{air}^{-1}$
w_v	Viscous work	$kg \cdot m^{-1} \cdot s^{-3}$
x	Axial coordinate	m
y	EGR rate	$-$
$y+$	Non-dimensional wall distance	$-$
Y	Mass fraction	
Z	Number of cylinders	

Greek characters

α	Branch insertion angle	$^\circ$
β	Backflows coefficient	%
γ	Ratio of specific heats	$-$
Δt	Time-step size	s
ϵ	Local mixing rate	$-$
ϵ_{COV}	Co-variance error	%
$\epsilon_{outlets}$	error Horiba-outlet	$-$
η	Compressor efficiency	%
κ	Thermal conductivity	$W \cdot m^{-1} \cdot K^{-1}$
λ	Excess of air factor	$-$
μ	Dynamic viscosity	$Pa \cdot s$
Π	Pressure ratio	$-$
ρ	Density	$kg \cdot m^{-3}$
ϕ	Scalar composition	$-$
θ	Azimuthal coordinate	$^\circ$
ω	Rotational speed	$rad \cdot s^{-1}$

Sub- and Superscripts

0	Stagnation variable
ad	Adiabatic
$adim$	Non-dimensional
b	Branch
$cycle$	Engine cycle
i	Certain cell face

i	Runner/Cylinder
in	Inlet
k	Certain simulation inside the numerical campaign
m	Main
$norm$	Normalized
out	Outlet
PM	Perfect Mixing
rad	Radial
ref	Reference value
s	Isentropic
sat	Saturation
$strm$	Streamline
t, t	Total-to-total
tan	Tangential
tot	Total
$w1 - w2 - w3$	Window 1-2-3

Acronyms

0D	Zero dimensional
1D	One dimensional
3D	Three dimensional
BMEP	Brake mean effective pressure
CFD	Computational fluid dynamics
CF	Convexity factor
CI	Compression ignited
COV	Coefficient of variance
CO_2	Carbon dioxide
EGR	Exhaust gas recirculation
FSN	Filter smoke number
HP-EGR	High pressure EGR
ICE	Internal combustion engine
LES	Large eddy simulation
LIC	Line integral convolution
LP-EGR	Low pressure EGR
M	Millions of cells
MP	Mixing plane
MI	Mixing index

OP	Operating point
P2P	Point-to-point
NO_x	Mono-nitrogen oxides
r.p.m	Revolutions per minute
RANS	Reynolds-Averaged Navier-Stokes
RH	Relative humidity
RMSE	Root mean square error
SF	Symmetry factor
SI	Spark ignited
Std	Standard/1 inlet domain
TRI	Transient rate index
URANS	Unsteady RANS
URF	Under-relaxation factor
VR	Velocity ratio

Chapter 1

Introduction

Contents

1.1 Motivation

Despite the fact that a significant number of investigations and innovations are still being developed nowadays regarding internal combustion engines (ICEs), this technology has more than 100 years of life. When in the last decades of XIX century the automobile was invented and developed, the impact in the whole world was perceived gradually. After that, millions of jobs, industries, roads were created because of that innovation, and its impact still being remarkable nowadays, taking into account that an unnumbered quantity of engines have been built around the world. In fact, in 2020 more than 78 millions of vehicles were manufactured around the world, giving a total amount of vehicles in circulation of almost one billion. In addition, internal combustion engines are not only employed by automobiles, its flexibility is exceptional and the scope in which can be used is very big, for example, ships, aircrafts, motorbikes, heavy industry, power suppliers, etc.

The first improvements regarding internal combustion engines were focused in the increment of its power and performance. In the area of power increase, one of the main objectives is introduce a bigger amount of air than the ambient conditions can provide. This is the main objective of the compressors, which can be driven by the engine itself or, thanks to Alfred Büchi, by the exhaust gases, after the invention of the turbocharger. Of course, the implementation was not easy, and took more years to perform an optimal system that works together with the engine. Usually, all the improvements in the engine were tested firstly in competition, because as Ford company used to say, "Win on Sunday, sell on Monday". When the improvement is so important and provide a lot of benefits, its implementation arrives faster to the public, and turbocharger was implemented in passenger cars around 1980.

However, after years and years of using a huge amount of engines with little to no limitations, major concerns were raised about the role of ICEs in the increasing pollution of the environment and the air quality. In the last decades, the climatic change has an important role in the development of new technologies [6, 7]. Thus, internal combustion engines are not outside of this range, and more and more exigent standards in terms of pollutant emissions are applied to these machines, in order to control and reduce the quantity of pollution that the environment suffers due to ICEs after decades of non-control

emissions. One developed technique in order to reduce the amount of pollutants (besides other objectives) is the so-called *downsizing*, that consists in the reduction of cylinder displacement while keeping the developed power (by turbocharging the engine) and the consequent reduction in terms of emissions [8]. Another strong technique that are very used actually is the combination of a combustion engine and electrical engine, what is called an hybrid powertrain [9, 10]. Obviously, if the use of the thermal engine is limited for a specific range, the hybrid powertrain emissions will be lower.

As was explained the reduction of pollutant emissions is still being one of the objectives in the investigation on ICEs, but the type of emissions will depend of the type on combustion engine. Spark ignited engines (SI) uses an electrical igniter to start the combustion reaction. The hydrocarbons and carbon monoxides that SI engines will produce are usually mitigated by catalytic converters [10]. On the other hand the compression ignited engines (CI) uses the high pressure of the combustion chamber to auto-ignite the fuel and start the combustion. In this process, the most common pollutants that are produced is the soot and the nitrogen oxides (NOx). Usually, the way to mitigate the soot that arrives to the atmosphere is using a particulate filter (DPFs). However, the reduction of NOx can be achieved using 2 different paths:

- Active measures. Avoiding the NOx generation during the combustion process of the engine.
- Passive measures. Capture the NOx after their generation with aftertreatment devices.

Focusing in the active measures, one of the most widely techniques used in order to reduce NOx formation is the so-called EGR, which is the acronym of exhaust gas recirculation system [11]. The main purpose of this technique is the reintroduction of some part of the exhaust gases that are produced during the combustion again in the main intake line. With this, the maximum temperature in the combustion chamber is reduced [12, 13] and the NOx formation decrease, with a slightly influence in the particulate emission. In fact, the perspectives indicate that engines will work with higher EGR rates in the engine [14].

Considering this, the union between the fresh air and the recirculated gases that comes of the combustion chamber can be performed by 2 main paths (considering that the engine has a turbocharger configuration). In the high-pressure EGR (HP-EGR) the exhaust gases are reintroduced after the compressor, in the main manifold of the engine. On the other hand, in the low pressure EGR (LP-EGR) the gases are injected before the compressor, and therefore, this path is called too long route EGR.

Although these techniques are different in terms of performance and implementation, Desantes et al. demonstrates that both of them can be applied at the same time [12]. In fact, Park et al. study optimal proportions of HP-EGR and LP-EGR depending of the operating conditions [15]. To summarize, both configurations present some advantages and disadvantages:

- HP-EGR is still the most employed configuration due to its simplicity, a quicker engine response [16] and the reduction in the pumping losses [12]. However, the most important disadvantage of this approach is getting an uniform distribution of EGR between the cylinders of the engine [17, 18] and the feasibility to achieve higher EGR rates. In fact, Maiboom et al. demonstrates that bad distributions of EGR will produce a huge increment in NOx and PM emissions [19]. Thus, the influence of the mixing between air and EGR stream in the good performance of this configuration is clear.
- LP-EGR avoids soot deposition in the EGR line, because the exhaust gases are taken downstream the after-treatment devices. However, some problems may appear in cold operating conditions, because volume condensation can be produced [5, 20, 21] and could be dangerous to the compressor integrity [22]. Considering that condensation conditions can be produced when air and EGR streams encounters one each other, mixing between them will be an important factor in order to study this phenomenon.

Depending on the selected technique, the union of the two streams have to be analyzed under very different conditions. In the low pressure EGR, the mixing will take place practically at ambient pressure, near to steady inlet conditions and very close to the impeller of the compressor. In high pressure EGR the mixing will take place in a compressed manifold, with highly transient

boundary conditions and with different geometrical conditions. Although the mixing between different streams is a widely studied phenomena, the different conditions at the 2 different paths of EGR and the improvement of this technique make very necessary the assessment in a deeper way of this phenomenon.

1.2 Background

After this introduction, it is clear that mixing phenomena will have an important role in the improvement of the high pressure and long pressure EGR configurations, but is not the only application in which mixing is very important. For example, in nuclear engineering the meeting and mixing of two streams is very common and widely studied [23, 24, 25, 26, 27] due to the relevance of the thermal mixing in this field of investigation. In other technological areas like the oil industry [28, 29] the mixing between two streams plays an important role in his good development. However, in this document, the main analysis of the mixing will be focus in the described EGR configurations, taking into account the advantages and disadvantages of every technique that have been described in previous section.

Knowing that mixing presents a strong impact in EGR performance, it is interesting to continue by providing an overview of the relevant works that have been published regarding mixing phenomena in the scope of EGR. For both HP and LP configurations of EGR, the state of the art is reviewed and the in-house background on the topic is discussed.

1.2.1 LP-EGR

Mixing in low pressure EGR configurations can appear in very different conditions, taking into account the operating points of the engine and the compressor that are placed downstream of the union of the two flows (air and EGR). Put aside the condensation effects that can appear as was explained before, the mixing between air and EGR before the compressor have been studied previously in the works of Brune et al. [30, 31]. In these works, different types of inlets have been studied in a numerical and experimental way, focusing in

the pressure losses and the mixing behavior. On the other hand, the effects of flow homogeneity or heterogeneity on the global compressor performance was assessed experimentally and numerically by Reihani et al. [32, 33]. In these works, one of the most important parameters that is considered is the EGR/air momentum ratio (J), which can be defined as:

$$J = \frac{\rho_{EGR} \cdot U_{EGR}^2}{\rho_{air} \cdot U_{air}^2}. \tag{1.1}$$

This parameter is very useful to compute the penetration of the EGR stream inside the main stream of air. In fact, Reihani et al. [32] demonstrates that the velocity ratio (very related with J) is crucial in the mixing before the compressor. In addition, Reihani demonstrates that, in some operating points and conditions, the EGR stream can improve the compressor performance, modifying the inducer velocity triangle.

Obviously, the geometrical design of a LP-EGR junction plays an important role regarding the mixing between air and EGR. Junctions have been widely studied in many fields of investigations as was exposed before, specifically three way junctions have been assessed by many different authors. In fact, Hosseini et al. [34] suggested a classification regarding the penetration of the flow, while Kamide et al. [24] and Kimura et al. [25] fixed the classification in 3 categories: wall-jet, deflecting-jet and impinging-jet. In these categories, the main parameter considered is J so the influence in mixing of this parameter will be remarkable. Apart from the mentioned works of Kamide et al. [24] and Kimura et al. [25], other authors study the mixing in T-junction using the experimental approach, as Wang et al. [35], Li et al. [36] and Chuang et al. [37]. On the other hand, the numerical approach is widely used to compute the mixing in T-junctions. In fact, regarding numerical simulations, turbulence modelling is one of the key features to be considered and can be developed using RANS (reynolds average navier stokes) approach, LES (large eddy simulations) approach and DNS (direct numerical simulations) approach. For example Evrim et al. [38, 39] use LES to study the thermal mixing in this type of junctions, while Gupta et al. [40] employed the RANS approach.

In addition, it is necessary to mention that volume condensation in this type of configurations has been studied too, with most of the works developed

in CMT-Motores Térmicos. Volume condensation appears when dew conditions are reached by some humid stream, and this is a very undesirable phenomenon in internal combustion engines [41] considering that this technique can introduce higher mass flow rates of EGR [42] and can be very harmful to the compressor integrity [22, 41]. Considering that this phenomenon appears more frequently in cold ambient, the applicability of this configuration is more limited [43, 44]. The prediction and effects of this phenomenon in the scope of LP-EGR have been studied in the work of Serrano et al. [21] and Galindo et al. [45, 46].

1.2.2 HP-EGR

As was explained before, mixing in HP-EGR is one of the most critical phenomena regarding the development of this configuration, and there are some relevant works that have been focused in this field of investigation. In fact, the main objective of this configuration is achieving an homogeneous distribution between the cylinders of the exhaust gases [17], considering that very uneven distributions will produce, as a consequence, that the emission of NOx and PM grow up very fast, as was found by Maiboom et al. [19]. CMT-Motores Térmicos has a notable experience regarding HP-EGR studies. For instance, the mixing between air and EGR has been studied in experimental way by Luján et al. [17, 47] and the effects of higher values of EGR dispersion in terms of opacity and NOx emissions have been studied by Macián et al. [48]. In addition, some NOx and PM models have been developed using experimental measuremens as base [49, 50, 48] that could be implemented later in 0D-1D models. However, one of the main drawbacks of the experimental approach is the neccesity of manufacturing real parts and the measurements of the main variables of the flow, which could be very difficult in complex geometries. In addition, the rate of acquisition data could be very limited in the measurement of important variables.

The other way to study the mixing in high pressure EGR configurations is the numerical approach, in which all the flows variables can be studied in all the considered domain, independently of the type of geometry and the time scale of some phenomenon. Some important works using this approach have been developed, for example the studies of Sakowitz et al. [51, 52, 53, 54]. In these works, one of the main focus is the used approach to model

the turbulence, which can be RANS (reynolds average navier stokes), LES (large eddy simulations) and DNS (direct numerical simulations). DNS are very expensive in terms of computational resources and time so it is not used in this field of investigation. However, most of the numerical works have used LES approach (especially the works of Sakowtiz et al.) or RANS approach [17, 55, 56, 57, 58, 59] taking into account that the RANS approach is cheaper in terms of computational resources. However, despite the referred works, most of the investigations using numerical approach are focused in the mixing between the streams near the union of the flows, considering different types of mixers, as T-junctions (as was exposed before) and radial mixers [60, 61], Other works are focused in the active improvement of the geometry, focusing always in better distributions of air and EGR as Minocha et al. [62]. The other point of view is the geometric modifications in order to achieve better volumetric efficiency in the whole manifold, as is demonstrated in the work of De Souza et al. [63].

1.3 Objectives

The main objective of this thesis is to contribute to the understanding of the mixing phenomena in the EGR configurations, both HP-EGR and LP-EGR. Concisely, this objective can be splitted in:

- Assess the influence of the heterogeneity of the mixing between air and EGR on the overall compressor performance in LP-EGR configurations.
- Understand the correlation between mixing and condensation in order to obtain design criteria for reducing volume condensation in LP-EGR configurations.
- Understand the correlation of EGR dispersion and pollutant emissions using 3D-CFD simulations in HP-EGR configurations.
- Assess the influence of geometrical modifications in the final EGR dispersion and the role of the mixing between air and EGR in HP-EGR configurations.

1.4 Approach and methodological objectives

In this section the main methods that are used in this document are presented. Some of the next tools have not been directly configurated by the author (see the division of work on page ix), but it has been used in the calculations and postprocessing data.

1.4.1 3D-CFD simulations

Considering the objectives that have been described in section 1.3, 3-dimensional CFD simulations will be used throughout this document as the main tool, to get the main performance and local features of the flow that are important in terms of mixing between air and EGR in both LP and HP EGR configurations. The simulations will be carried out in the commercial code Star-CCM+, which is based on finite-volume approach from version 12.06 [64] to version 14.02 [65].

1.4.2 Turbocompressor measurements

In chapter 2, the influence of the heterogeneity in the global compressor performance is assessed numerically. However, EGR-less compressor was measured experimentally as a reference. The experimental installation to measure compressor data is the same that the used in the works of Galindo et al. [66]. In addition, the features to postprocess the experimental data are provided by the works of Galindo et al. [67] and Serrano et al. [68].

1.4.3 0D condensation model

In chapter 3, junction 0D model is used in order to get the maximum volume condensation, using different thermodynamical and psychrometric conditions in air and EGR inlets. This model was developed by Serrano et al. [41] and assuming mixing air-EGR streams at the outlet of the domain. More details of this model are exposed in chapter 3.

1.4.4 1D engine model

In chapter 4, and chapter 5 different operating points and engines have been considered with the aim of performing different CFD calculations of intake manifolds with HP-EGR. In order to achieve reliable data of different engine variables in a wide range of operation, a 1D model is necessary to be developed, in order to impose the transient boundary conditions of the 3D CFD cases that have been performed. The used 1D model follows the same structure that the used in the work of Macian et al. [48] and different engines and operating points have been simulated as will be described in chapter 4 and 5. It must be taken into account, that the calibration of the 1D model in chapter 4 is developed in the mentioned work of Macián et al. [48].

1.4.5 Engine experimental measurements

All the numerical approaches that have been used in this document, both 1D and 3D-CFD simulations need a reliabe source of data in order to improve the numerical models and validate them after the simulations. Therefore, results from different experimental campaigns back up the numerical predictions of this Thesis. Regarding LP-EGR, a set of experimental measurements conducted aside from this Thesis validate the employed condensation submodel, as will be explained in chapter 3. This Thesis does feature EGR dispersion and CO_2 transient data measured at the intake manifold for two engines with HP-EGR, as will be showed in chapter 4. Furthermore, the performance of the HP-EGR system of these 4-cylinder and a 6-cylinder engines has been measured using different air-EGR mixers, as discussed in chapter 5. The used experimental facility follows the same structure, probes and methods that the presented by Luján et al. [69, 47].

1.5 Methodological objectives

Considering that CFD is the selected approach in order to achieve the presented objectives of section 1.3 some issues needs to be solved in order to advance the investigation. As a summary the main methodological objectives are:

- Despite that the introduction of EGR in LP-EGR configurations before the compressor has been analyzed numerically by Reihani et al. [32] using 3D-CFD simulations, it is necessary to evaluate the best numerical setup in order to perform different operating points with heterogeneous inlet.
- Considering that mixing is one of the basis of this document, it is necessary to compute the amount of mixing in different conditions, that is in LP-EGR and HP-EGR, even with transient phenomena. Thus, different index needs to be defined for a better understanding of the mixing process.
- It is necessary to find the best numerical configuration in HP-EGR domains in order to model in a correct way the mixing between air and EGR under transient conditions, different operating points and geometries, trying to apply the indexes that have been commented before.

1.6 Thesis outline

The rest of this document is structured as follows:

1. Chapter 2 deals with the influence of a heterogeneous flow at the inlet of a radial compressor, in low pressure EGR configuration. Different operating points will be calculated, and the main features of the numerical setup will be assessed.
2. In chapter 3 a whole numerical design of experiments is performed in a T-junction domain. With this, condensation in different LP-EGR conditions is assessed and correlated with different non-dimensional indicators, as jet penetration factor (J) and mixing indicators, which are developed too.
3. Chapter 4 is devoted to find the optimal numerical setup on different engine manifolds in HP-EGR configurations. Different operating points will be analyzed, and a pollutant emission model will be developed to correlate EGR dispersion with NOx and PM variations.
4. In chapter 5, different geometrical modifications are analyzed in the manifolds that are used in chapter 4. In this chapter, the mixing between

air and EGR are assessed, including transient evolutions of the main variables in the key points of the considered domains.

5. Finally, in chapter 6 the thesis findings and main contributions are depicted, including some recommendations of possible future works that could be developed as a continuation of this Thesis.

Chapter 1 Bibliography

[5] J. Galindo, R. Navarro, D. Tarí, and G. García-Olivas. "Centrifugal compressor influence on condensation due to Long Route-Exhaust Gas Recirculation mixing." *Applied Thermal Engineering* 144 (2018), pp. 901 –909. ISSN: 1359-4311. DOI: 10.1016/j.applthermaleng.2018.09.005 (cit. on pp. x, 4, 22, 24, 25, 27, 28, 41, 42, 53, 54, 58, 61, 73, 124).

[6] J. S. Gaffney and N. A. Marley. "The impacts of combustion emissions on air quality and climate - From coal to biofuels and beyond." *Atmospheric Environment* 43(1) (2009). Atmospheric Environment - Fifty Years of Endeavour, pp. 23 –36. ISSN: 1352-2310. DOI: 10.1016/j.atmosenv.2008.09.016 (cit. on p. 2).

[7] J. Janaun and N. Ellis. "Perspectives on biodiesel as a sustainable fuel." *Renewable and Sustainable Energy Reviews* 14(4) (2010), pp. 1312–1320. DOI: 10.1016/j.rser.2009.12.011 (cit. on p. 2).

[8] M.-B. Ricardo, P. Apostolos, and M. Yang. "Overview of boosting options for future downsized engines." *Science China Technological Sciences* 54(2) (2011), pp. 318–331. DOI: 10.1007/s11431-010-4272-1 (cit. on p. 3).

[9] A. García, J. Monsalve-Serrano, S. Martínez-Boggio, and K. Wittek. "Potential of hybrid powertrains in a variable compression ratio downsized turbocharged VVA Spark Ignition engine." *Energy* 195 (2020), p. 117039. DOI: 10.1016/j.energy.2020.117039 (cit. on p. 3).

[10] A. G. Des Buttes, B. Jeanneret, A. Kéromnès, L. Le Moyne, and S. Pélissier. "Energy management strategy to reduce pollutant emissions during the catalyst light-off of parallel hybrid vehicles." *Applied Energy* 266 (2020), p. 114866. DOI: 10.1016/j.apenergy.2020.114866 (cit. on p. 3).

[11] N. Ladommatos, S. Abdelhalim, and H. Zhao. "The effects of exhaust gas recirculation on diesel combustion and emissions." *International Journal of Engine Research* 1(1) (2000), pp. 107–126. DOI: 10.1243/1468087001545290 (cit. on pp. 3, 99).

[12] J. M. Desantes, J. M. Luján, B. Pla, and J. A. Soler. "On the combination of high-pressure and low-pressure exhaust gas recirculation loops for improved fuel economy and reduced emissions in high-speed direct-injection engines." *International Journal of Engine Research* 14(1) (2013), pp. 3–11. DOI: 10.1177/1468087412437623 (cit. on pp. 3, 4, 22, 54, 99, 102).

[13] M. Lapuerta, A. Ramos, D. Fernandez-Rodriguez, and I. Gonzalez-Garcia. "High-pressure versus low-pressure exhaust gas recirculation in a Euro 6 diesel engine with lean-NOx trap: Effectiveness to reduce NOx emission." *International Journal of Engine Research* - (Nov. 14, 2018), pp. 0–9. DOI: 10.1177/1468087418817447 (cit. on p. 3).

[14] R. D. Reitz, H. Ogawa, R. Payri, T. Fansler, and S. Kokjohn. "IJER editorial: The future of the internal combustion engine." *International Journal of engine Research* 21 (1 2020), pp. 0–8. DOI: 10.1177/1468087419877990 (cit. on pp. 3, 100).

[15] Y. Park and C. Bae. "Experimental study on the effects of high/low pressure EGR proportion in a passenger car diesel engine." *Applied energy* 133 (2014), pp. 308–316. DOI: 10.1016/j.apenergy.2014.08.003 (cit. on pp. 4, 54).

[16] F. Millo, P. F. Giacominetto, and M. G. Bernardi. "Analysis of different exhaust gas recirculation architectures for passenger car diesel engines." *Applied energy* 98 (2012), pp. 79–91. DOI: 10.1016/j.apenergy.2012.02.081 (cit. on pp. 4, 99).

[17] J. M. Luján, J. Galindo, J. R. Serrano, and B. Pla. "A methodology to identify the intake charge cylinder-to-cylinder distribution in turbocharged direct injection Diesel engines." *Measurement Science and Technology* 19(6) (2008), p. 065401. DOI: 10.1088/0957-0233/19/6/065401 (cit. on pp. 4, 7, 8, 99, 100, 108, 116).

[18] C. Guardiola, B. Pla, P. Bares, and A. Stefanopoulou. "Cylinder charge composition observation based on in-cylinder pressure measurement." *Measurement* 131 (2019), pp. 559–568. DOI: 10.1016/j.measurement.2018.08.024 (cit. on p. 4).

[19] A. Maiboom, X. Tauzia, and J.-F. Hétet. "Influence of EGR unequal distribution from cylinder to cylinder on NOx-PM trade-off of a HSDI automotive Diesel engine." *Applied Thermal Engineering* 29(10) (2009), pp. 2043 –2050. ISSN: 1359-4311. DOI: 10.1016/j.applthermaleng.2008.10.017 (cit. on pp. 4, 7, 99).

[20] J. Galindo, P. Piqueras, R. Navarro, D. Tarí, and C. Meano. "Validation and sensitivity analysis of an in-flow water condensation model for 3D-CFD simulations of humid air streams mixing." *International Journal of Thermal Sciences* 136 (2019), pp. 410 –419. ISSN: 1290-0729. DOI: 10.1016/j.ijthermalsci.2018.10.043 (cit. on pp. 4, 22, 28, 54, 58, 59, 61–63, 73).

[21] J. Serrano, P. Piqueras, R. Navarro, D. Tarí, and C. Meano. "Development and verification of an in-flow water condensation model for 3D-CFD simulations of humid air streams mixing." *Computers & Fluids* 167 (2018), pp. 158 –165. ISSN: 0045-7930. DOI: 10.1016/j.compfluid.2018.02.032 (cit. on pp. 4, 7, 54, 61, 62, 73).

[22] S Karstadt, J Werner, S Münz, and R Aymanns. "Effect of water droplets caused by low pressure EGR on spinning compressor wheels." In: *Aufladetechnische Konferenz, Dresden*. 2014 (cit. on pp. 4, 7, 22, 54).

[23] J. Kickhofel, V. Valori, and H.-M. Prasser. "Turbulent penetration in T-junction branch lines with leakage flow." *Nuclear Engineering and Design* 276 (2014), pp. 43–53. DOI: 10.1016/j.nucengdes.2014.05.002 (cit. on pp. 5, 53).

[24] H Kamide, M Igarashi, S Kawashima, N Kimura, and K Hayashi. "Study on mixing behavior in a tee piping and numerical analyses for evaluation of thermal striping." *Nuclear Engineering and Design* 239(1) (2009), pp. 58–67. DOI: 10.1016/j.nucengdes.2008.09.005 (cit. on pp. 5, 6, 53, 64, 77, 78).

[25] N. Kimura, H. Ogawa, and H. Kamide. "Experimental study on fluid mixing phenomena in T-pipe junction with upstream elbow." *Nuclear Engineering and Design* 240(10) (2010), pp. 3055–3066. DOI: 10.1016/j.nucengdes.2010.05.019 (cit. on pp. 5, 6, 53, 64, 77, 159).

[26] T. Lu, D. Attinger, and S. M. Liu. "Large-eddy simulations of velocity and temperature fluctuations in hot and cold fluids mixing in a tee junction with an upstream straicht or elbow main pipe." *Nu-*

clear Engineering and Design 263 (Apr. 2, 2013), pp. 32–41. DOI: 10.1016/j.nucengdes.2013.04.002 (cit. on pp. 5, 53).

[27] R. Tunstall, D. Laurence, R. Prosser, and A. Skillen. "Large eddy simulation of a T-Junction with upstream elbow: The role of Dean vortices in thermal fatigue." *Applied Thermal Engineering* 107 (Aug. 25, 2017), pp. 672–680. DOI: 10.1016/j.applthermaleng.2016.07.011 (cit. on p. 5).

[28] J.-l. Chen, L.-m. He, X.-m. Luo, H.-t. Bai, and Y.-h. Wei. "Simulation of oil-water two phase flow and separation behaviors in combined T junctions." *Journal of Hydrodynamics* 24(6) (2012), pp. 848–857. DOI: 10.1016/s1001-6058(11)60312-0 (cit. on p. 5).

[29] L. Yang, J. Wang, Y. Jiang, and L. Zou. "Oil-water flow splitting in eccentric annular T-junction tubes. Experimental and CFD analysis." *Chemical Engineering Science* 228 (2020), p. 116000. DOI: 10.1016/j.ces.2020.116000 (cit. on pp. 5, 53).

[30] K.-H. Brune, B. Stoffel, B. Matyschok, et al. "CFD-Analysis of the Flow Consisting of Two Mass Flows With Different Temperatures and/or Two Phases in a Turbocompressor." In: *ASME 2006 2nd Joint US-European Fluids Engineering Summer Meeting Collocated With the 14th International Conference on Nuclear Engineering*. American Society of Mechanical Engineers Digital Collection. 2006, pp. 701–711 (cit. on pp. 5, 22, 24, 27, 28, 36, 67, 68).

[31] K.-H. Brune, H.-P. Schiffer, R Christmann, and M Gnewikow. "Experimental investigations of the disturbed inlet-flow structure caused by mixing geometries and its influence on the performance of a turbocharger centrifugal compressor." In: *ASME Turbo Expo 2009: Power for Land, Sea, and Air*. American Society of Mechanical Engineers Digital Collection. 2009, pp. 1295–1304 (cit. on pp. 5, 22, 24, 41).

[32] A. Reihani, J. Hoard, S. Klinkert, C.-K. Kuan, and D. Styles. "Numerical Evaluation of the Effects of Low Pressure EGR Mixer Configuration on Turbocharger Compressor Performance." In: *ASME 2018 Internal Combustion Engine Division Fall Technical Conference*. American Society of Mechanical Engineers Digital Collection. 2018 (cit. on pp. 6, 11, 23, 34, 36, 47, 198).

[33] A. Reihani, J. Hoard, S. Klinkert, C.-K. Kuan, D. Styles, and G. McConville. "Experimental response surface study of the effects of low-pressure exhaust gas recirculation mixing on turbocharger compressor performance." *Applied Energy* 261 (2020), p. 114349. DOI: 10.1016/j.apenergy.2019.114349 (cit. on pp. 6, 58, 77).

[34] S. M. Hosseini, K. Yuki, and H. Hashizume. "Classification of turbulent jets in a T-junction area with a 90-deg bend upstream." *International Journal of heat and mass transfer* 51(9-10) (2008), pp. 2444–2454. DOI: 10.1016/j.ijheatmasstransfer.2007.08.024 (cit. on pp. 6, 53).

[35] Y. Wang, P. Wang, and T. Lu. "Experimental investigation of the thermal fluctuations in hot and cold fluids mixing in a T-junction filled with spherical particles." *Applied thermal engineering* 71(1) (2014), pp. 310–316. DOI: 10.1016/j.applthermaleng.2014.06.010 (cit. on p. 6).

[36] W.-f. Li, Y. Wei, G.-y. Tu, Z.-h. Shi, H.-f. Liu, and F.-c. Wang. "Experimental study about mixing characteristic and enhancement of T-jet reactor." *Chemical Engineering Science* 144 (2016), pp. 116–125. DOI: 10.1016/j.ces.2016.01.024 (cit. on p. 6).

[37] G. Chuang and Y. Ferng. "Experimentally investigating the thermal mixing and thermal stripping characteristics in a T-junction." *Applied Thermal Engineering* 113 (2017), pp. 1585–1595 (cit. on p. 6).

[38] C. Evrim, X. Chu, and E. Laurien. "Analysis of thermal mixing characteristics in different t-junction configurations." *International Journal of Heat and Mass Transfer* 158 (2020), p. 120019. DOI: 10.1016/j.ijheatmasstransfer.2020.120019 (cit. on pp. 6, 53).

[39] C. Evrim and E. Laurien. "Numerical study of thermal mixing mechanisms in t-junctions." *Applied Thermal Engineering* 183 (2021), p. 116155. DOI: 10.1016/j.applthermaleng.2020.116155 (cit. on pp. 6, 53, 77).

[40] A. Gupta, M. S. Ibrahim, and R. Amano. "Effect of jet-to-mainstream momentum flux ratio on mixing process." *Heat and Mass Transfer* 52(3) (2016), pp. 621–634. DOI: 10.1007/s00231-015-1582-7 (cit. on pp. 6, 53).

[41] J. R. Serrano, P. Piqueras, E. Angiolini, C. Meano, and J. De La Morena. "On Cooler and Mixing Condensation Phenomena in the Long-Route Exhaust Gas Recirculation Line." In: *SAE Technical Pa-*

per. 2015. DOI: 10.4271/2015-24-2521 (cit. on pp. 7, 9, 53–55, 57, 58).

[42] A. García, J. Monsalve-Serrano, R. L. Sari, and P. Gaillard. "Assessment of a complete truck operating under dual-mode dual-fuel combustion in real life applications: Performance and emissions analysis." *Applied Energy* 279 (2020), p. 115729. DOI: 10.1016/j.apenergy.2020.115729 (cit. on pp. 7, 54).

[43] P. Olmeda, J. Martín, F. Arnau, and S. Artham. "Analysis of the energy balance during World harmonized Light vehicles Test Cycle in warmed and cold conditions using a Virtual Engine." *International Journal of Engine Research* - (Oct. 3, 2019), pp. 0–18. DOI: 10.1177/1468087419878593 (cit. on pp. 7, 54).

[44] J. Galindo, R. Navarro, D. Tari, and F. Moya. "Development of an experimental test bench and a psychrometric model for assessing condensation on a Low Pressure EGR cooler." *International Journal of Engine Research* 22 (5 2020), pp. 1540–1550. DOI: 10.1177/1468087420909735 (cit. on pp. 7, 54, 111).

[45] J. Galindo, R. Navarro, D. Tari, and F. Moya. "Analysis of condensation and secondary flows at T-junctions using optical visualization techniques and Computational Fluid Dynamics." *International Journal of Multiphase Flow* (2021). DOI: 10.1016/j.ijmultiphaseflow.2021.103674 (cit. on pp. 7, 54, 59, 61–63, 77).

[46] J. Galindo, R. Navarro, D. Tarí, and F. Moya. "Quantitative validation of an in-flow water condensation model for 3D-CFD simulations of three-way junctions using indirect condensation measurements." *International Journal of Thermal Sciences* 172 (2022), pp. 1–17. DOI: 10.1016/j.ijthermalsci.2021.107303 (cit. on pp. 7, 54, 62, 63).

[47] J. M. Luján, H. Climent, B. Pla, M. E. Rivas-Perea, N.-Y. François, J. Borges-Alejo, and Z. Soukeur. "Exhaust gas recirculation dispersion analysis using in-cylinder pressure measurements in automotive diesel engines." *Applied Thermal Engineering* 89 (2015), pp. 459–468. DOI: 10.1016/j.applthermaleng.2015.06.029 (cit. on pp. 7, 10, 99, 102).

[48] V. Macián, J. M. Luján, H. Climent, J. Miguel-García, S. Guilain, and R. Boubennec. "Cylinder-to-cylinder high-pressure exhaust gas recirculation dispersion effect on opacity and NOx emissions in a diesel automotive engine." *International Journal of Engine Research* (2020). DOI: 10.1177/1468087419895401 (cit. on pp. 7, 10, 100, 106, 149).

[49] C. Guardiola, B. Pla, D. Blanco-Rodriguez, and P. O. Calendini. "ECU-oriented models for NOx prediction. Part 1: a mean value engine model for NOx prediction." *Proceedings of the Institution of Mechanical Engineers, Part D: Journal of Automobile Engineering* 229(8) (2015), pp. 992–1015. DOI: 10.1177/0954407014550191 (cit. on pp. 7, 100, 103–105).

[50] X. Tauzia, H. Karaky, and A. Maiboom. "Evaluation of a semi-physical model to predict NOx and soot emissions of a CI automotive engine under warm-up like conditions." *Applied Thermal Engineering* 137 (2018), pp. 521–531. DOI: 10.1016/j.applthermaleng.2018.04.005 (cit. on pp. 7, 100).

[51] A. Sakowitz and L. Fuchs. "Computation of mixing processes related to EGR." In: *TSFP digital library online*. Begel House Inc. 2011. URL: http://www.dl.begellhouse.com/en/references/3ce1b491115b5c16,60d8a9681cb3cfc7,57130c5b30e27450.html (cit. on pp. 7, 100, 109–112, 118, 119, 122, 150).

[52] A. Sakowitz, S. Reifarth, M. Mihaescu, and L. Fuchs. "Modeling of EGR Mixing in an engine intake manifold using LES." *Oil & Gas Science and Technology* 69(1) (2014), pp. 167–176. DOI: 10.2516/ogst/2013118 (cit. on pp. 7, 100, 112, 118, 150, 201, 204).

[53] A. Sakowitz, M. Mihaescu, and L. Fuchs. "Turbulent flow mechanisms in mixing T-junctions by Large Eddy Simulations." *International Journal of Heat and Fluid Flow* 45 (2014), pp. 135–146. DOI: 10.1016/j.ijheatfluidflow.2013.06.014 (cit. on pp. 7, 58, 65, 67, 100, 110).

[54] A. Sakowitz. "Computation and analysis of EGR mixing in internal combustion engine manifolds." PhD thesis. KTH Royal Institute of Technology, 2013. URL: http://www.diva-portal.org/smash/record.jsf?pid=diva2:603864&dswid=6780 (cit. on pp. 7, 100, 105, 110).

[55] S. Ramanathan, A. Hudson, J. Styron, B. Baldwin, D. Ives, and D. Ducu. *EGR and swirl distribution analysis using coupled 1D-3D CFD simulation for a turbocharged heavy duty diesel engine*. Tech. rep. SAE Technical Paper, 2011. DOI: 10.4271/2011-01-2222 (cit. on pp. 8, 107, 108, 112, 117, 200).

[56] S. K. R. Hariganesh, M Sathyanadan, S Krishnan, P Vadivel, and D Vamsidhar. "Computational analysis of EGR mixing inside the intake system & experimental investigation on diesel engine for LCV." *International Journal of Engineering Science & Technology* 3(3) (2011) (cit. on pp. 8, 108, 117, 119).

[57] R. Rahimi, S Jafarmadar, S. Khalilarya, and A Mohebbi. "Numerical and experimental investigations of EGR distribution in a DI turbocharged diesel engine." *Transactions of the Canadian society for mechanical engineering* 37(2) (2013), pp. 247–257. DOI: 10.1139/tcsme-2013-0015 (cit. on pp. 8, 107, 108, 111, 119).

[58] P. Dimitriou, R. Burke, C. D. Copeland, and S. Akehurst. *Study on the effects of EGR supply configuration on cylinder-to-cylinder dispersion and engine performance using 1D-3D co-simulation.* Tech. rep. SAE Technical Paper, 2015. URL: https://saemobilus.sae.org/content/2015-32-0816 (cit. on pp. 8, 100, 107, 110–112, 117, 119, 122, 150, 200, 202).

[59] P. Dimitriou, C. Avola, R. Burke, C. Copeland, and N. Turner. "A Comparison of 1D-3D Co-Simulation and Transient 3D Simulation for EGR Distribution Studies." In: *ASME 2016 Internal Combustion Engine Division Fall Technical Conference*. American Society of Mechanical Engineers. 2016, V001T06A010–V001T06A010. DOI: 10.1115/icef2016-9361 (cit. on pp. 8, 111, 117).

[60] E. Kartaev, V. Emel'kin, M. Ktalkherman, V. Kuz'min, and S. Aul'chenko. "Analysis of mixing of impinging radial jets with crossflow in the regime of counter flow jet formation." *Chemical Engineering Science* 119 (2014), pp. 1–9. DOI: 10.1016/j.ces.2014.07.062 (cit. on pp. 8, 159).

[61] S. Nada, A Fouda, and H. Elattar. "Parametric study of flow field and mixing characteristics of outwardly injected jets into a crossflow in a cylindrical chamber." *International Journal of Thermal Sciences* 102 (2016), pp. 185–201. DOI: 10.1016/j.ijthermalsci.2015.11.017 (cit. on pp. 8, 159).

[62] N. Minocha and J. B. Joshi. "3D CFD simulation of turbulent flow distribution and pressure drop in a dividing manifold system using openfoam." *International Journal of Heat and Mass Transfer* 151 (2020), p. 119420. DOI: 10.1016/j.ijheatmasstransfer.2020.119420 (cit. on pp. 8, 160).

[63] G. R. de Souza, C. de Castro Pellegrini, S. L. Ferreira, F. S. Pau, and O. Armas. "Study of intake manifolds of an internal combustion engine: A new geometry based on experimental results and numerical simulations." *Thermal Science and Engineering Progress* 9 (2019), pp. 248–258. DOI: 10.1016/j.tsep.2018.12.003 (cit. on pp. 8, 159, 205).

[64] *STAR-CCM+*. Release version 12.06.010. CD-adapco. 2018. URL: http://ww.cd-adapco.com (cit. on pp. 9, 26, 30, 34, 42, 59, 61, 100, 107, 112, 114, 119, 170, 190).

[65] *STAR-CCM+*. Release version 14.02.010. Simcenter. 2019. URL: http://www.siemens.com (cit. on pp. 9, 24).

[66] J. Galindo, F. J. Arnau, L. M. García-Cuevas, and P. Soler. "Experimental validation of a quasi-two-dimensional radial turbine model." *International Journal of Engine Research* (2018), p. 1468087418788502 (cit. on pp. 9, 24).

[67] J. Galindo, A. Tiseira, R. Navarro, D. Tarí, H. Tartoussi, and S. Guilain. "Compressor Efficiency Extrapolation for 0D-1D Engine Simulations." In: *SAE Technical Paper*. SAE International, Apr. 2016. DOI: 10.4271/2016-01-0554 (cit. on pp. 9, 32, 33).

[68] J. R. Serrano, P. Olmeda, F. J. Arnau, and V. Samala. "A holistic methodology to correct heat transfer and bearing friction losses from hot turbocharger maps in order to obtain adiabatic efficiency of the turbomachinery." *International Journal of Engine Research* (2019), p. 1468087419834194 (cit. on pp. 9, 32).

[69] J. M. Luján, C. Guardiola, B. Pla, and A. Reig. "Switching strategy between HP (high pressure)-and LPEGR (low pressure exhaust gas recirculation) systems for reduced fuel consumption and emissions." *Energy* 90 (2015), pp. 1790–1798. DOI: 10.1016/j.energy.2015.06.138 (cit. on pp. 10, 22, 54, 102).

Chapter 2

Modeling challenges of inlet hetereogeneity due to LP-EGR and impact on compressor performance

Contents

2.1 Introduction

As was exposed in chapter 1, one of the most extended emissions-reduction technique in diesel engines is the recirculation of the exhaust gases (EGR) and their introduction again in the intake line [12]. Taking into account that fresh air is mixed with exhaust gases, the maximum temperature is lowered during the combustion, so the production of nitrogen oxides (NOx) is drastically reduced [12]. As referered in chapter 1, HP-EGR and LP-EGR can be combined simultaneously in the same engine [12], and control strategies can be applied for taking the best path in every moment of the driving cycle [69]. Focusing on LP-EGR technique, this configuration takes gases that have undergone the exhaust aftertreatment, so the accumulation of pollutants and undesired elements is mainly avoided in the EGR line. Also, the aforementioned issues of uneven distribution of EGR that are exposed in chapter 1 do not appear with this technique due to the longer path. Nevertheless, under certain cold ambients, condensation problems can appear in the mixing of the two streams before the compressor [5, 20] This undesired effect can produce small droplets at the inlet of the compressor and thus, very harmful consequences in the impeller [22].

Nevertheless, if condensation effects are omitted, mixture between air and EGR in LP-EGR configurations was studied in the works of Brune et al. [30, 31]. In these works, different inlet configurations were analyzed experimentally. Brune et al. [31] demonstrated that junctions that provided an improved flow mixing presented greater pressure losses. Nevertheless, the compressor overall parameters were measured in points over a single speed line and the effects of the heterogeneity would need a deeper analysis. In addition, a numerical campaign was developed to analyze some inlet configurations, showing that the direction of the injection and its relative position has significant influence of the mixing behavior [30]. However, this numerical study was carried out with a single operating point, so it is not easy to assess strong conclusions. In the same way, in the works of Vithala et al. [70], several configurations were calculated to analyze the pressure drop in the T-junction for some operating points showing that a simple 90^{o} degrees junction gives a reasonable mixing quality with no significant impact in the pressure drop. However, in this case, the compressor was not included in the geometry, so the effects of this flow homogeneity in the global performance of the compressor were not calculated.

Besides, the influence of mixing and heterogeneity on the global compressor performance was analyzed numerically and with experimental validation in the works of Reihani et al. [32]. The velocity ratio VR coefficient between EGR/air (which have almost the same meaning that J coefficient presented in equation 1.1), and the EGR rate can be described as:

$$VR = \frac{\dot{m}_{EGR} \cdot A_{air}}{\dot{m}_{air} \cdot A_{EGR}} \tag{2.1}$$

$$EGR_{rate} = \frac{\dot{m}_{EGR}}{\dot{m}_{air} + \dot{m}_{EGR}} \tag{2.2}$$

The VR relates the velocity of EGR that enters in the domain in comparison with that of the air flow. In configurations with high VR coefficient (due to high EGR mass flows or smaller EGR areas), the EGR stream is able to penetrate stronger in the air stream due to its greater momentum, so the air-EGR mixing will be higher. In fact, the influence of the VR coefficient in the mixing before the compressor is crucial according to Reihani et al. [32]. They showed that, by considering different insertion angles and high VR factor, can have a positive impact on the overall compressor performance at certain zones of the map due to its influence in the inducer velocity triangle.

The industry standard is to obtain the compressor maps in experimental test cells with a single straight inlet duct, so the impact of including a T-junction with LP-EGR flow more or less mixed with the fresh air should be assessed. Therefore, this work is meant to establish the main effects of mixing changes by different operating points in a T-junction inlet on the compressor performance. In addition, the comparison with the equivalent standard intake will be performed, to check whether the original maps could be still employed when considering turbochargers for LP-EGR applications. The idea of standard inlet will represent the equivalent thermodynamics conditions that the T-junction with air and EGR presents. This equivalent thermodynamic condition will depend on the air and EGR mass flow rates and the inlet temperatures of both streams, considering perfect mixing and enthalpy conservation as will be exposed in section 2.2. Obviously, the inlet temperature and the EGR rate is not constant in all engine operating conditions. However, to limit the degrees of freedom, these variables will be fixed in all the points of this document. Specifically, the EGR rate, that can vary in normal operation between 1 and 40%, will be set to 15%, that would correspond to an engine operating point

with medium load and medium engine speed, being therefore a representative value [71]. This engine working point would be obtained with the compressor working at 130 krpm and 1.8 of compression ratio, so the selected EGR rate corresponds to compressor nominal conditions (see figure 2.3). In addition, if the inlet temperatures and EGR rate are kept constant, it is easy to check than the VR factor will be constant too in all the compressor points. The aforementioned objective will be addressed by conducting a numerical campaign. All the 3D CFD calculations will be carried out in STAR-CCM+ [65] with RANS modelling of the turbulence, which has proved that can achieved suitable results in compressor CFD modelling [5, 30].

2.2 Numerical configuration

2.3 Experimental setup

The experimental installation that has been employed to get the compressor performance maps, is a turbocharger test cell rig that uses a screw compressor to supply power to the turbine. The mass flow that passes through the analyzed compressor is controlled by a backpressure valve at its outlet. The inlet temperature of the compressor is achieved by a water-air heat exchanger and measured by an array of thermocouples. The detailed methodology and process to measure and control the different values of the turbocharger will not be explained in this thesis, but more information of this installation can be found in the works of Galindo et al. [66].

2.4 Geometry and mesh

As mentioned before, the inlet of the compressor is one of the most important regions to be taken into account in the analysis of the LP-EGR configurations. In this document, a T-junction geometry has been selected by its low pressure drop and wide use in experimental essays and its easiness of fabrication [31, 70], because it is only a straight duct into the main flow of air. The standard inlet to represent a typical inlet configuration is developed to impose an equivalent thermodynamic inlet condition without the junction. Both standard and T-junction geometries are presented in figure 2.1, together with the

postprocessing surfaces employed. The length of the intake pipe is extruded 5 diameters, like in the work of Navarro [72]. It has to be noticed that this domain does not present any flaps to control the EGR flow (unlike other studies [5]). In the actual engine, the flap to reduce the EGR rate is indeed placed in the LP-EGR line, but far enough from the T-junction, so it is not modeled in this work. In addition, the flap that can produce additional pressure drop to achieve the desired EGR rate at certain points is located in the exhaust line, acting as a backpressure valve, but is neither modeled.

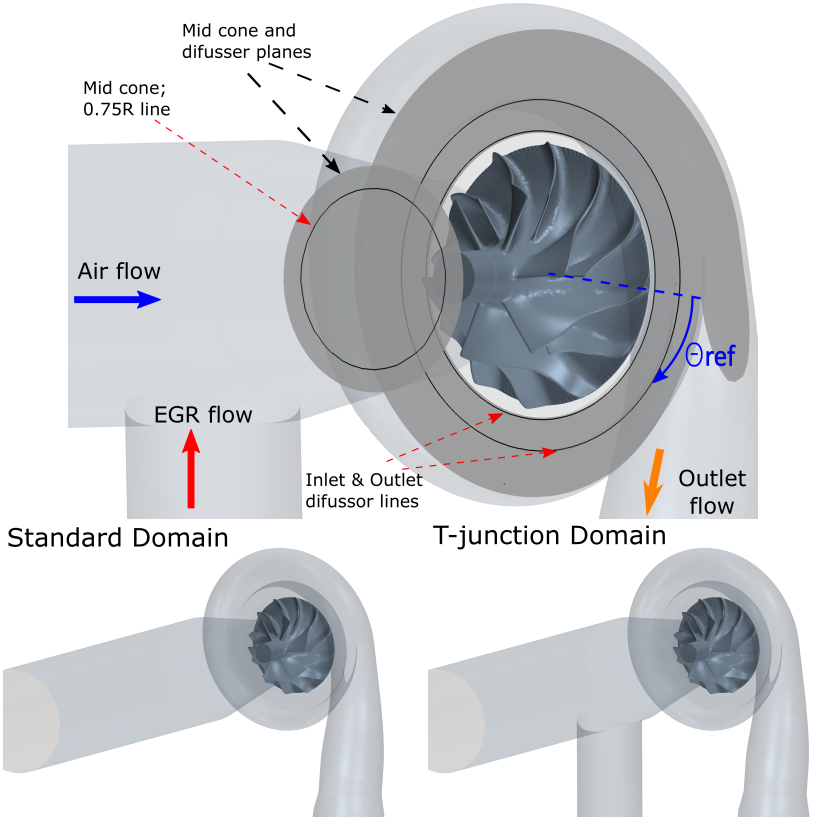

Figure 2.1: Inlet compressor and postprocessing virtual probes and surfaces (top). Numerical configurations analyzed (bottom).

This work presents the same approach in mesh configuration that the one used by Broatch et al. [73]. In this way, a polyhedral mesh is built with a prismatic layer in the walls of the domain, with the aim to solve the boundary

layer in an appropriate way. Since the present work aims to analyze the influence of the inlet geometry in several operating points of the compressor, about 40 simulations have been performed, so a fine mesh is not affordable due to the huge computational resources that would be necessary to carry out the whole numerical campaign. For that reason, a coarser mesh has been employed, i.e., considering an average element size in the impeller region of 2.4mm and 3.4mm in the inlet and outlet regions, which yields an overall cell count of 1.3 million cells. A depiction of this mesh in the rotor region is presented in figure 2.2. Taking into account the wide range of operating conditions, the y+ values in the impeller are placed in the buffer layer at some operating points. In any case, the "all $y+$ wall treatment" [64] has been selected , that will act as a wall function or solve the viscous sublayer, depending on the wall $y+$. Besides, it should provide reasonable results for cells inside the buffer sublayer. The usage of a 4 million cells mesh, with $y+$ values lower than 3 in the impeller, was particularly investigated at best efficiency point, in which the 1.3 million mesh presents $y+$ values between 10-15. Despite the distinct mesh density, the difference when predicting compression ratio was 3%, being 2% when assessing efficiency. In addition, regarding the inlet mixing, the RMSE of the distribution of temperature in a vertical line on mid cone plane of figure 2.1, is around 3K between these meshes. Therefore, the 1.3 million cells mesh can achieve reasonable results with a limited computational effort. Moreover, section 2.5 will show that the considered mesh can predict global variables within a satisfactory range for a global study.

2.5 Setup and operating conditions

The developed methodology by Broatch et al. [73] is again used in this study to define the setup parameters of the numerical simulations. A brief summary of the main features of the configuration is presented:

- The considered cases have been calculated with dry air treated as perfect gas, because the influence of the composition of the EGR flow is not the main objective of this work. In fact, considering that the EGR is cooled, the difference between the specific heats at the considered temperatures is $< 0.5\%$.
- The segregated solver has been used for the resolution of the numerical

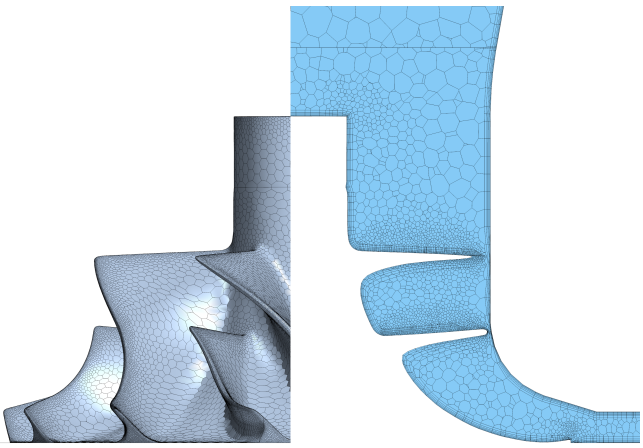

Figure 2.2: Wall mesh (left) and fluid continuum mesh plan on inducer zone

equations. This solver uses 2nd order discretization schemes for the convective terms and Hybrid-Gauss LSQ applied as gradient reconstruction scheme. To deal with the turbulence modelling, a RANS approach with the $SSTk-\omega$ submodel has been selected, which has been widely used and validated in similar works [5, 30, 70, 73].

- For the unsteady cases, a 2nd order implicit scheme has been selected for the transient term, considering a 4°/step as time-step size. Navarro proves that this size of time step is enough to achieve an acceptable accuracy in global variables (with a relative difference less than 1% compared to lower time-step sizes) [72]. With the mesh described in section 2.4, this time-step size provides Courant numbers lower than 10 in the entire domain.

- Concerning the boundary conditions of the numerical domain, the mass flow rate and stagnation temperatures are imposed in the inlet of air and EGR (in the T-junction inlet) and the static pressure is imposed in the outlet of the domain, with radial equilibrium, following the same scheme as the works of Galindo et al. [5].

In section 2.3 a brief description of the experimental facility was presented. The measured conditions will be used as boundary conditions of the simula-

tions, taking as reference the corrected rpm (N^*) and the corrected mass flow rate ($\dot{m}^*$) following the nomenclature of Watson et al. [74]:

$$N^* = N \cdot \sqrt{\frac{T_{ref}}{T_{in,tot}}} \tag{2.3}$$

$$\dot{m}^* = \dot{m}_{tot} \cdot \frac{p_{ref}}{p_{in,tot}} \cdot \sqrt{\frac{T_{in,tot}}{T_{ref}}} \tag{2.4}$$

Being p_{ref} = 101325 Pa and T_{ref} = 288.15 K. Considering a wide range of operation, the ambient temperature can vary between -20°C and 40°C and the EGR temperature between ambient (during engine warm-up) and 120°C (considering 90°C coolant temperature and non-ideal cooler). The inlet total temperatures of the domain will be kept fixed through all the study, being $T_{air,tot}$ = 273 K and $T_{EGR,tot}$ = 333 K, taking into account that these values are referred to an engine in warm-up process in cold ambient, when the cooler has not achieved its nominal temperature yet, and condensation phenomena can appear [5, 20] (although condensation is not calculated in this work). Thus, these temperature values that are imposed are in the same order of the typical values measured in experimental facility. In addition, as was mentioned in previous section, the EGR rate is fixed in 15%, as an average value in all the engine map.

Regarding the standard inlet, taking into account that its objective is to simulate equivalent inlet conditions than the T-junction inlet, the total temperature will be mass averaged in the same way than the works of Brune et al. [30]:

$$T_{in,tot} = \frac{\dot{m}_{air} \cdot T_{air,tot} + \dot{m}_{EGR} \cdot T_{EGR,tot}}{\dot{m}_{air} + \dot{m}_{EGR}} \tag{2.5}$$

Considering that the EGR rate is considered constant, as well as the inlet temperatures of the T-junction cases, temperature of equation 2.5 will be constant and equal to 282 K for all the simulations with standard domain. The difference in this temperature of would have consider multicomponent gas with different specific heats is <0.1%, due to the low differences at the considered temperatures as aforementioned, and also considering that the EGR rate is

15%.

Defining the compression ratio as:

$$\Pi_{t,t} = \frac{p_{out,tot}}{p_{in,tot}} \tag{2.6}$$

the selected operating points are presented in the compressor map of figure 2.3:

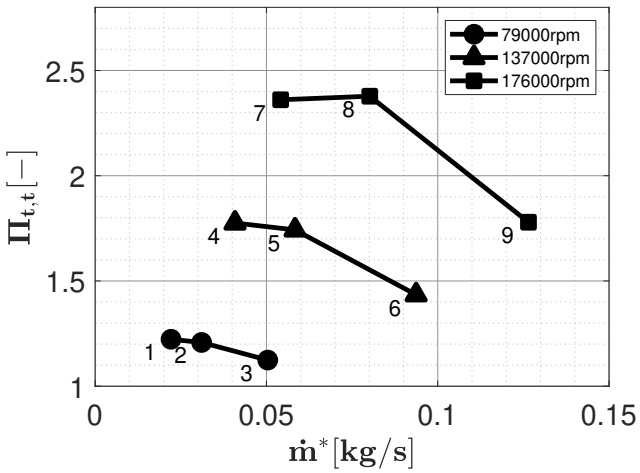

Figure 2.3: Corrected mass-flow / C.R. map of experimental selected points.

This distribution of 9 operating points at 3 different speed lines shown in figure 2.3 is mean to cover all the zones at which the compressor may operate in normal conditions. For that reason, the points are evenly spaced in terms of corrected r.p.m. at each speed line. So, taking into account that the transient schemes will be analyzed too, there will be 9 points in 2 different temporal treatment and 2 domains to calculate. In addition, the influence of interface types in the steady approach is considered too, so a numerical campaign of 40 simulations has been conducted in this chapter.

Regarding the temporal treatment, is necessary a brief description of the differences of steady and unsteady simulations in this type of problems. In a compressor simulation, the impeller region has an inherent motion. The way

in that motion is modelled dictates whether the simulation is steady or unsteady. The unsteady approach is the more realistic approach but has a higher computational cost. In the unsteady approach (URANS) the rotor mesh itself moves at each time step according to prescribed rotations specified by the user [64]. Internal interfaces between the fixed regions and the moving region allow to keep the connectivity between regions even though the rotor mesh is sliding. In the case of a standard compressor the amount of degrees that the mesh rotate is directly related with the time step size of the simulation. Regarding the steady scheme (RANS), is commonly used in turbomachinery, in which a rotating reference frame is applied to the region of the impeller, so that the moving region in the unsteady approach now is static, by converting the absolute velocity into relative velocity and considering inertial forces (centrifugal and Coriolis). As the rotor blades are frozen in space respect the diffuser, the flow field depends of the relative position of the passages. This issue appears if an internal interface as the one used in the unsteady approach is applied, that can be named as point-to-point interface or P2P. However, a mixing plane interface (or MP) can be used instead between the moving region and the static region. With this, the problem of the relative position is overcome because the flow is averaged circumferentially to provide a single radial profile. The differences between these types of simulations and the influence of the described interfaces, P2P and MP in the steady approach will be assessed in next section.

2.6 Results and discussion

2.6.1 RANS-URANS assessing

2.6.1.1 Overall performance comparison

The numerical transient scheme is a very important issue to consider in LP-EGR and turbomachinery simulations. Due to the high unsteadiness that can appear in the impeller region, the behavior and the global parameters of the compressor must be assessed in both temporal approaches to check the differences in the achieved results. Taking into account that the experimental measurements described in section 2.3 were done with a standard inlet, the straight duct intake is considered for the numerical simulation as well. The comparison in terms of compression ratio and corrected mass flow for the

points introduced in figure 2.3 is presented in figure 2.4 as a means to validate the configuration and the mesh of the simulation as well as to notice the differences between transient and steady simulations.

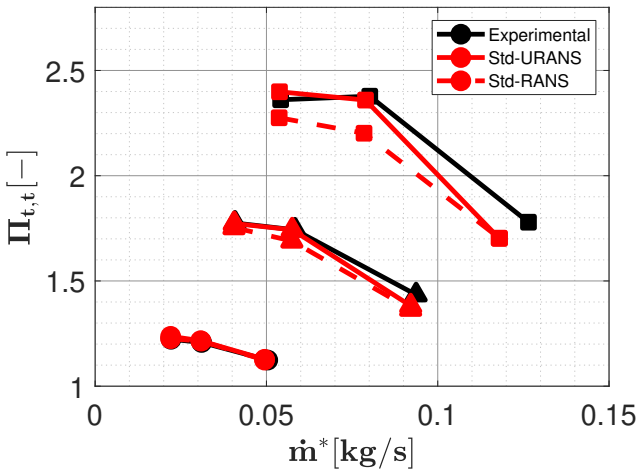

Figure 2.4: Corrected mass-flow / C.R. map of RANS-URANS comparison in standard inlet.

Regarding experimental uncertainties, in the work of Olmeda et al. [75], the measurement errors and its propagation in a turbocharger test bench are properly evaluated. Taking into account that the test bench is the same that the one described in section 2.3, the experimental uncertainties will be similar consieding that the used sensors are the same. In terms of compression ratio, the experimental uncertainties are about 0.2%. With this, the trends depicted in figure 2.4 are not the same in every iso-speed line. When compressor is working at the lowest speed, the temporal treatment seems does not have much influence and provides almost the same results in terms of compression ratio. In medium speeds, the near surge point is captured in an acceptable way by the RANS models but, when the corrected mass flow grows, the accuracy is decreased. Moreover, in high speed points, the steady scheme clearly under-predicts the pressure ratio. In addition, figure 2.4 shows that near choke point 6 and especially point 9 are not well calculated by the URANS model neither. In these points, the slope of the corrected speed line is very pronounced, so, the differences in terms of corrected mass flow are very noticeable. The mesh density and the usage of the segregated solver instead of the coupled one (with enhanced capability to predict transonic flows by requiring a greater compu-

tational effort) are likely the main factors responsible for the lack of accuracy in the choked region.

Regarding the isentropic efficiency, it can be defined as:

$$\eta_s = \frac{T_{in,tot} \cdot \left(\Pi_{t,t}^{(\gamma-1)/\gamma} - 1\right)}{T_{out,tot} - T_{in,tot}} \tag{2.7}$$

The comparison between the RANS and URANS predictions and the adiabatized experimental measurements of isentropic efficiency for the points considered in figure 2.3 are presented in figure 2.5, in which the increasing speed lines correspond to greater mass flow rates. Regarding the isentropic efficiency, the experimental uncertainties are about 2.5%. Comparing figure 2.4 and 2.5, the differences between experiments and the numerical models in terms of efficiency are higher than when assessing compression ratio. Figure 2.5 shows that, at low r.p.m., numerical models have a trend to overpredict the experimental measurement, while at medium and high speeds, the efficiency is lower in the simulations than in the tests. These differences can appear due to several reasons. In the numerical models, the walls are considered as adiabatic, even though the compressor is not perfectly insulated in the experimental measurements, which is a source of discrepancies between numerical results and experimental measurements. The experimental efficiency is underestimated especially at low speed lines when the power is calculated by means of the temperature rise in the compressor, as observed by Galindo et al. [67] since the heat flow from the turbine increases the compressor outlet temperature especially at these operating points, which yields a spurious power increase. Therefore, all the original experimental measurements have been adiabatized following the approach described in the works of Serrano et al. [68], aiming at removing the effect of heat transfer in the measurements to provide adiabatic efficiency values. Serrano et al. [68] developed a method which features an internal and external turbocharger heat transfer model combined with mechanical losses model. These models are calibrated with the diabatic map measurements and the turbocharger geometrical information to obtain the corresponding adiabatic map. In this way, the conducted adiabatic corrections increase the peak experimental efficiency at lowest speed line by 5%. However, this correction should have been even greater, according to the fact that peak efficiency should increase with lower compressor speeds

when adiabatic measurements are conducted [67], as simulations do in figure 2.5.

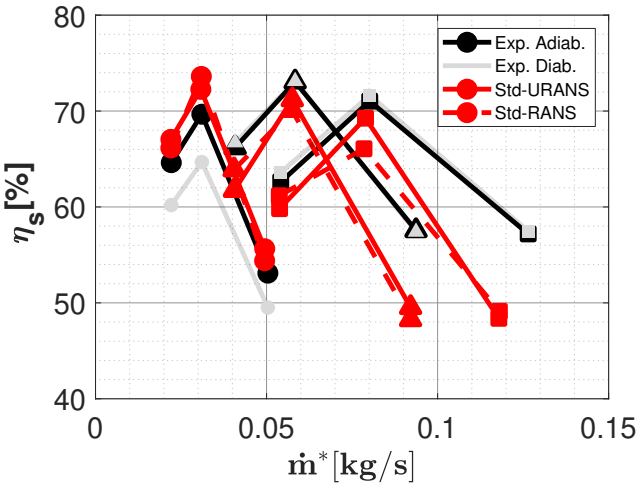

Figure 2.5: Corrected mass-flow / efficiency map of RANS-URANS comparison in standard inlet.

In addition, the error propagation by the measurements must be taken into account too, especially in zones of low speeds [75], so slight errors in temperature measurements, can induce important changes in efficiency. Finally, as mentioned above, the mesh may not be fine enough to achieve the perfect accuracy in all the operating points, so the numerical uncertainty may affect to differences in efficiency depicted in figure 2.5. These differences are clearly showed in the operating points 6 and 9, corresponding to choked conditions. As a summary, the average error in terms of compression ratio in all the considered operating points is about 1.40% and the error in efficiency is about 6.42% comparing the URANS model and the experimental data. For the RANS approach the error grows to 2.8% in compression ratio but is maintained in terms of isentropic efficiency in 6.4%.

2.6.1.2 Heterogeneity in the steady approach

The previous section has shown that the differences between RANS and URANS are limited in terms of global variables for a standard straight inlet. For LP-EGR applications, the steady approach may be hindered though, because the

flow at the inlet of the compressor is heterogeneous, especially when the mixing between streams is very weak [32] In the present work, the temperature is the variable employed to analyze the heterogeneity of the configuration, as figure 2.6 shows. There are 2 zones clearly different; the hotter EGR stream on the bottom side of the inlet of the compressor, aligned with the duct of the T-junction, and the colder air stream on the top side. Figure 2.6 shows only a fine interface between the described zones, where the thermal diffusion takes place. Clearly, the VR factor of equation 2.1 is not very high in this case, due to the low penetration of the EGR stream in the main flow.

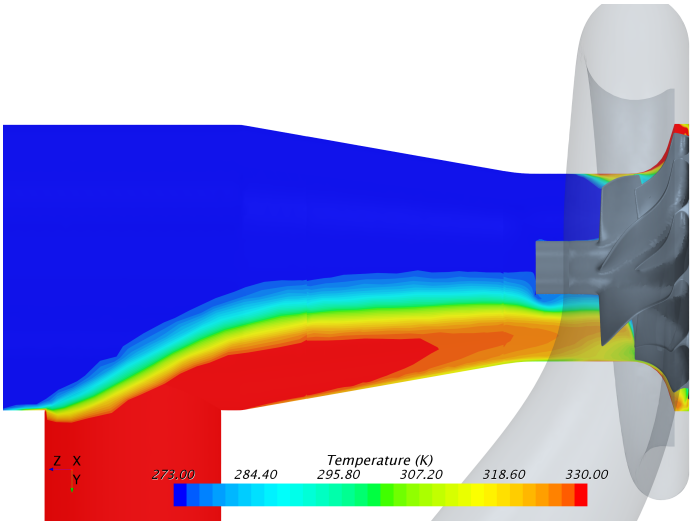

Figure 2.6: Contours of inlet temperature compressor in operating point 5

Regarding the steady simulations, the different types of interfaces that connect the fixed regions with the moving region were described in section 2.5. The mixing plane (MP) interface can be useful to avoid the passage influence on the results, because the flow is circumferentially averaged and transferred in a conservative manner between the regions [64], while the point-to-point (P2P) interface does not use this average. However, using the mixing plane when the domain is working with heterogeneous flow as the one represented in figure 2.6 can lead to non-physical results, as figure 2.7 shows.

In the presented plots, the azimuthal distribution of temperature at the diffuser inlet (circumference included in figure 2.1) is depicted, taking the origin of θ and coordinate direction presented in figure 2.1 (volute tongue and

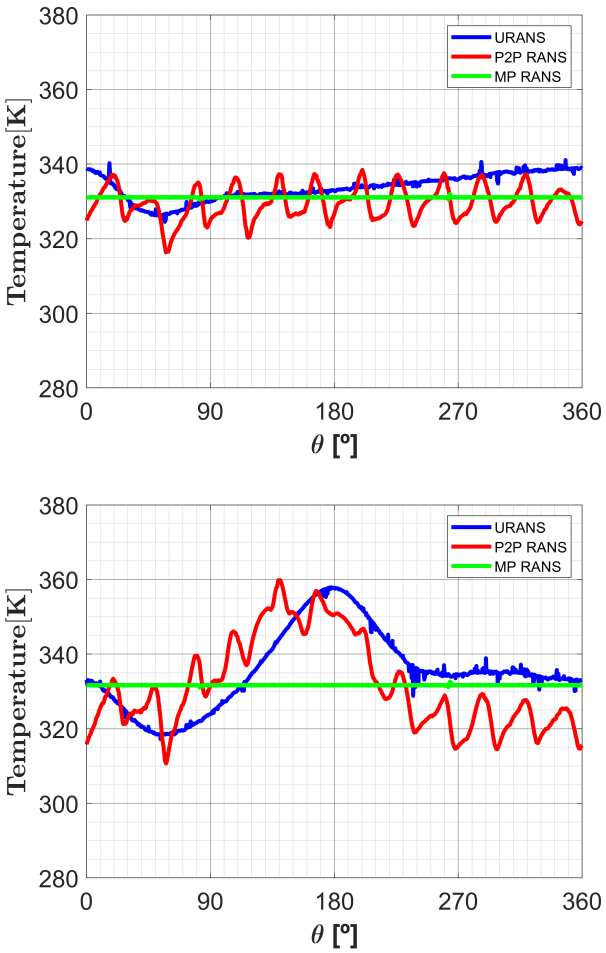

Figure 2.7: Azimuthal temperature distribution at inlet diffuser for RANS (frozen rotor or P2P), RANS with mixing plane (MP) and URANS model in standard inlet (top) and T-Junction inlet (bottom) in operating point 5.

rotating direction). Figure 2.7 includes the predictions obtained with the URANS and the steady RANS approach with the 2 described interfaces for operating point 5 (figure 2.3) with the straight and T-junction inlet geometries. It must be noticed that the temperature of the URANS simulation has been time-averaged, so the rotating jet-wake features are balanced in a fixed reference frame. In the top plot of figure 2.7 it is shown that the usage of

mixing plane is useful for the straight intake as aforementioned, because the temperature is correctly smoothed and therefore, azimuthally constant, alike the URANS case due to the temporal average regarding the fixed reference frame. On the other side, the point-to-point interface keeps an excessive oscillation due to the frozen jet-wake effect of each of the 12 impeller passages. This oscillation is not physical and is mainly produced by the static position of the impeller, and the influence of the passages. However, in the bottom plot of figure 2.7, when T-junction inlet is used, the temperature distribution is not well resolved, because the circumferential average of the MP interface avoids the effect of the heterogeneous flow at the inlet (and outlet) of the moving region. On the contrary, the P2P interface presents a more realistic result in terms of temperature distribution in comparison with the URANS model, despite the non-smoothed jet-wake effect of the impeller passages.

After this assessment, it seems that the mixing plane interface is not suitable to be used in heterogeneous problems due to the circumferential average, at least to predict the temperature fields. However, the steady approach with point-to-point interfaces (also called frozen rotor) could be still applied in the steady state calculations. Although some authors have used the steady schemes to solve this type of problems with and without compressor [30, 70, 32] there are some undesired effects that can appear by using this approach, even though the MP interface is not used. An important problem of the steady approach in heterogeneous incoming flow is clearly visualized in figure 2.8. At first, the EGR flow advances through the bottom side of the inlet duct with no problems (yellow stream) but, when the flow enters in the moving zone (red stream), the steady approach transforms the absolute velocity into relative velocity due to the moving reference frame, causing a spurious deviation ($\Delta\theta$) of the EGR flow in the opposite way of the angular velocity. When the flow arrives to the impeller, the EGR stream is confined to the impeller passage (except for tip leakage), so the relative velocity would now make sense. However, another deviation will appear, because the rotation of the whole passage, when the EGR flow is going through it, is obviously not considered with the steady solver, which entails another circumferential deviation against the URANS case adding more uncertainty in this approach taking into account the first deviation.

Therefore, the amount of deviation that the steady approach can induce to the EGR flow will depend on 2 factors:

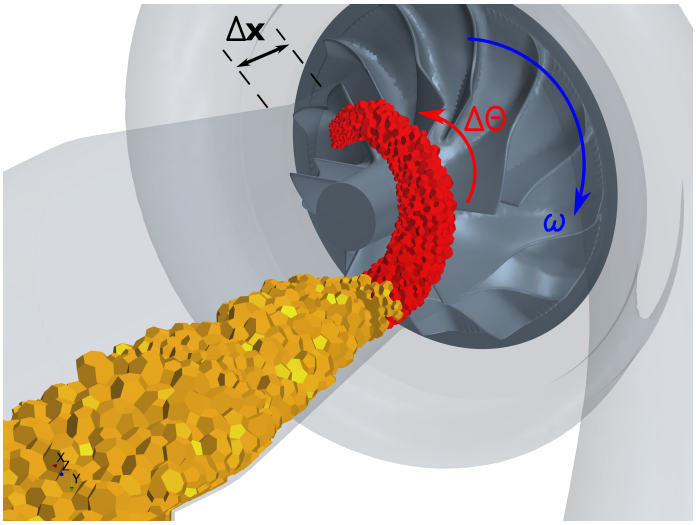

Figure 2.8: Incorrect deviation of inlet EGR flow in steady RANS approach.

- The angular velocity (compressor speed) of the considered operating point. This deviation is produced because the rotor is static in steady simulations.
- The residence times of the flow in these zones (moving region before the inducer and impeller passages), which in turn depend on the meridional velocities (mass flow rate) and the distances travelled by the flow between inlet and outlet rotor interfaces. This deviation is represented in figure 2.8 and is case-dependent.

The main effect of this undesired phenomenon, produced by the steady approach, is the alteration of the discharge zone of the EGR stream in the diffuser, which will not be the same compared to the more realistic URANS approach, this difference depending of the operating point. This fact is assessed in figure 2.9, in which the temperature circumferential profiles at the diffuser inlet for operating points 4 and 6 (see figure 2.1).

The thin red line is the steady RANS solution with P2P interface, in the same way than the red line in figure 2.7. The thick red line corresponding to a moving average applied to the original RANS solution. This moving average is obtained by a sliding window to make an average in every single point of the trace with a 30°size (30°=360°/12 passages). This average reduces the

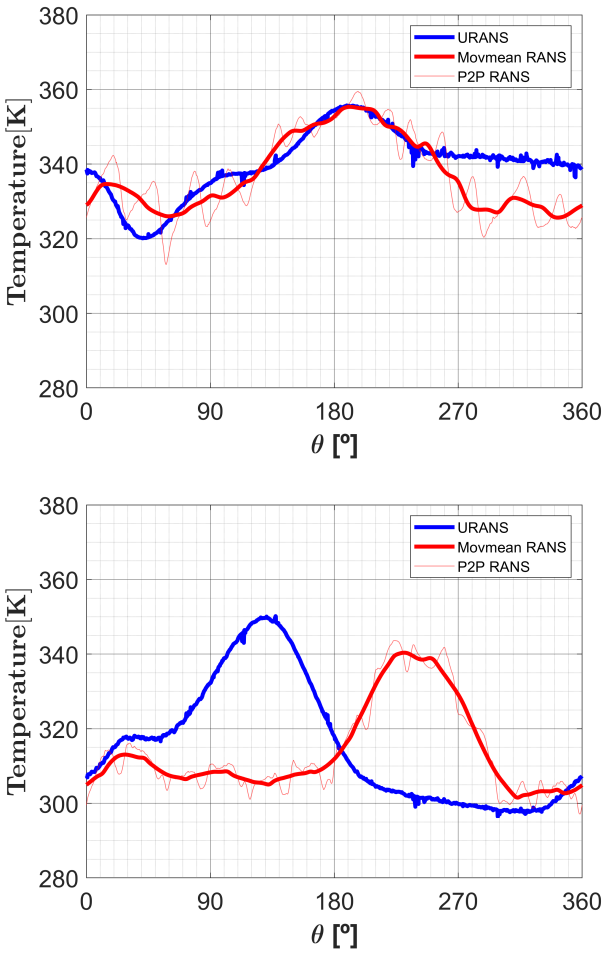

Figure 2.9: Azimuthal temperature distribution at inlet diffuser for RANS (frozen rotor or P2P), RANS averaged (movmean) and URANS model in T-junction inlet for operating point 4 (top) and 6 (bottom).

effect of the 12 sharp oscillations corresponding to the impeller passages and thus gets a smooth signal. The blue line is the unsteady signal. In operating point 4 (top plot of figure 2.9) the discharge angle on the compressor diffuser is almost the same for the steady and unsteady approach (peak temperature is achieved with both approaches close to 200°). It does not mean that the deviation induced of the steady approach is around zero but close to 360°. In

operating point 6 (bottom plot of figure 2.9) the discharge point of the steady case is departed from the temperature peak for the URANS case because the relative velocity through the passage is higher than at point 4 (for the same speed line), so the residence time is lower in the rotor region and thus the deviation angle, which does not reach now the 360°. The comparison between RANS and the more realistic unsteady approach shown in figure 2.9 shows how the deviation in the prediction of the EGR stream discharge in the diffuser region is significant and depends on the working point.

2.6.2 URANS Tjunction-Std inlet comparison

In section 2.6.1 the temporal treatment was assessed. Considering this, the comparison between the results of the T-junction case and the straight inlet case is performed in this section with an unsteady scheme, since it is more realistic than the steady approach. The overall performance of the compressor will be compared in all the operating points, but a brief analysis of the flow field will be performed too.

2.6.2.1 Global parameters assessing

To start this section, the compression ratio presented in equation 2.6 of the calculated operating points with the T-junction and standard straight intakes will be presented in figure 2.10, being the URANS results for the standard inlet the same that were presented in figure 2.4.

In figure 2.4, the trends of the analyzed geometries are very similar in all the range of the compressor map. At low r.p.m. the T-junction inlet gets almost the same compression ratio than the standard inlet configuration that was validated in figure 2.4. In operating point 4, which is relatively closer to surge line, there are more differences between both cases. In fact, the T-junction inlet compression ratio is a little bit higher than the corresponding of the standard case or the experimental. There are some differences too in the near-surge zone in operating point 7 but the trends are not so clear. To get a global point of view of the relative differences in terms of global variables of the compressor between the considered cases, table 2.1 is presented.

In table 2.1 the differences between the standard inlet and the T-joint in

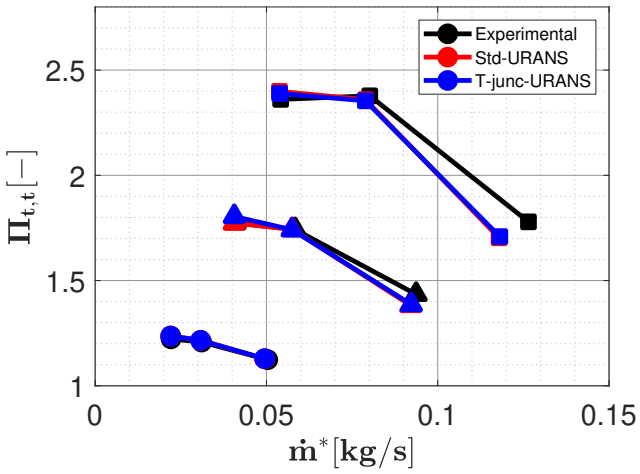

Figure 2.10: Corrected mass-flow / C.R. map of T-junction and standard inlet comparison.

terms of the corrected variables are negligible, all are below 0.5% of relative error so the inlet condition imposed in the standard inlet by equation 2.5 is justified. Regarding compression ratio and isentropic efficiency, the higher differences are mainly in point 4, near of the surge zone. The inherent instabilities of this zone of the compressor map can affect to the achieved results, but even so, the differences are below the 5%. There are some differences too in operating point 6 and 9 in terms of isentropic efficiency, but these points are near of the choke zone and the efficiency will be very low anyway. As a summary, the mean overall error in terms of compression ratio between the cases is 0.37% and in terms of efficiency is 0.89%. After this comparison, for the considered inlet conditions and geometry, the heterogeneity of the incoming flow to the compressor does not affect in a remarkable way to the compressor global parameters when equivalent working points are compared.

2.6.2.2 Mean flow analysis

Although the global performance parameters of the compressor in these operating points are not significantly affected by the type of inlet considered, is necessary to assess the influence of these two cases in the compressor time-averaged flow, to see whether are local flow features that are modified depending on the intake type.

Table 2.1: T-junction and standard cases global variables summary comparison.

Operating Points	ΔN^* [%]	$\Delta \dot{m}^*$ [%]	$\Delta \Pi_{t,t}$ [%]	$\Delta \eta_s$ [%]
1	-0.1	0.1	0.0	0.0
2	0.0	0.0	0.0	0.1
3	0.0	0.0	0.1	1.2
4	-0.1	0.0	1.8	3.9
5	0.0	0.0	-0.1	-0.1
6	0.0	0.2	0.3	1.3
7	0.0	0.1	-0.4	0.1
8	0.0	0.0	-0.2	-0.3
9	0.0	0.2	0.3	1.0

Starting at the inlet, it is clear that the main flow behavior will be different in the considered cases due to the impact of the EGR stream. The difference between the standard and T-junction intakes in the azimuthal distribution of radial velocity on the plane placed in the inlet cone of figure 2.1 (mid-cone at 75% of the corresponding radius) is presented in figure 2.11. Notice that negative radial velocities in figure 2.11 represent flow going from the outer part to the center, mainly due to the tapered angle in the cone that reduces the cross section.

Figure 2.11 shows how the discharge of the EGR flow in the cases with T-junction (presented in figure 2.6) is noticeable with an increment of the negative radial velocity which is stronger in high speed points due to the higher EGR mass flow rate. The negative radial velocity peak is followed by two positive radial velocity increases compared to the straight case due to the two counter-rotating vortices that the T-joint establishes [5]. This effect will be more important for greater VR factor , as investigated in [31, 70]. However, these changes that mainly affect to the radial velocity distribution, are slight in terms of tangential and axial velocities, so that the impact of the T-junction in the velocity triangle at the inducer plane is small, and therefore its influence on the impeller performance (for the considered 15% of EGR rate).

Although the differences in the velocity between the standard inlet and the

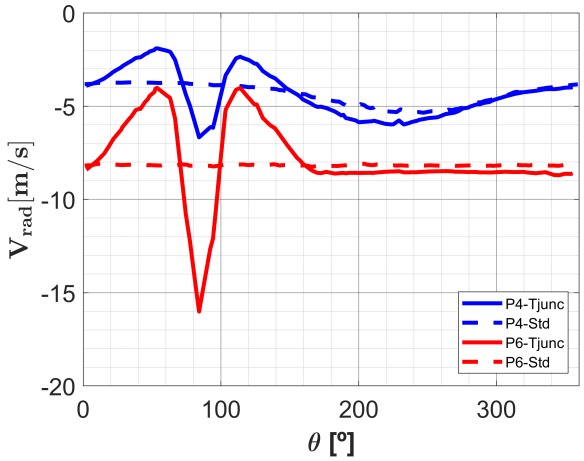

Figure 2.11: Azimuthal distribution of radial velocity in mid inlet cone for T-junction and Std inlet in operating 4 (blue) and 6 (red).

T-junction case are reduced before the impeller, the differences in temperature distribution are more noticeable due to the heterogeneity of the inlet flow after the T-junction. The temperature fields in the diffuser are analyzed to assess whether both configurations still present temperature differences after the impeller. Using STAR-CCM+ [64] data mappers as in previous works [5], the solution of one case is exported and import back in the other configuration. In this way, the temperature fields can be compared by defining a temperature difference:

$$\Delta T = T_{T-junc} - T_{Std} \tag{2.8}$$

Considering this definition, figure 2.12 shows the differences of the temperatures between the cases after mapping the standard intake solution into the diffuser of the T-junction case (see the EGR branch) for operating points at the same iso-speed. The non-zero ΔT contours indicate clear differences in the two cases, and the EGR discharge circumferential position in the diffuser already discussed in section 2.6.1.2 is clearly depicted by a stream of positive ΔT. In operating point 4 (top image in figure 2.12), the EGR discharge zone is about 120-160°regarding the volute tongue, while in operating point 6 (bottom image) is in the range of 90-100°regarding this reference. Taking into account that the represented operating points are at the same speed line,

the differences in the discharge point are due to the mass flow rate. Point 6 presents a greater mass flow rate and thus the velocity along the impeller passages will be higher, and therefore the EGR discharge in the diffuser is located closer to the T-joint (see figure 2.12), due to the lower residence time. In terms of temperature range, figure 2.12 shows that the ΔT is smaller in point 4 than in point 6, since the former is closer to the surge line, so that the residence times are greater and also the secondary and recirculating flows [72], so the air-EGR mixing is improved and the temperature differences are diluted.

After that, it can be concluded that, in terms of temperature, the heterogeneity of the T-junction case is extended to the diffuser, and obviously this feature can not be modeled by a straight inlet case with an equivalent operating condition.

Although the differences in temperature previously described can be remarkables in some operating points, it is necessary to check if this heterogeneity is also seen in the velocity field in the diffuser. The radial velocity comparison between the T-joint and straight intakes is presented in figure 2.13 of the operating points 4 and 6.

This azimuthal distribution in figure 2.13 is plotted in the inlet diffuser line presented in figure 2.1, and the reference for the azimuthal coordinate is the volute tongue, as in figure 2.7 and figure 2.9 . The velocity profiles show strong differences between the operating points. Obviously, the average radial velocity in point 4 is lower than in point 6 due to the lower mass flow. In addition, the radial velocity distribution in operating point 6 is increasing with θ while at point 4 is decreasing, expecting the design point of the diffuser/volute flatter to present a flatter profile than these points in accordance to Navarro [72]. Regarding the comparison between the cases, the velocity traces are very similar but, there are two zones that are slightly different. Around the 90-100°of θ in operating point 6 and around 130-180°in point 4, the radial velocity of the standard intake is higher than the T-junction velocity, being the same zone of the discharge of EGR flow, as can be checked in figure 2.12 On the other side, around 200°of θ, the gap between the cases are in the opposite way, especially in point 6, when the temperature difference is negative, the radial velocity of the T-junction case is higher than the standard, but this effect is not so clear in operating point 4, due to the temperature difference in this point is lower around this zones (see figure 2.12). In any case, figure 2.13 shows

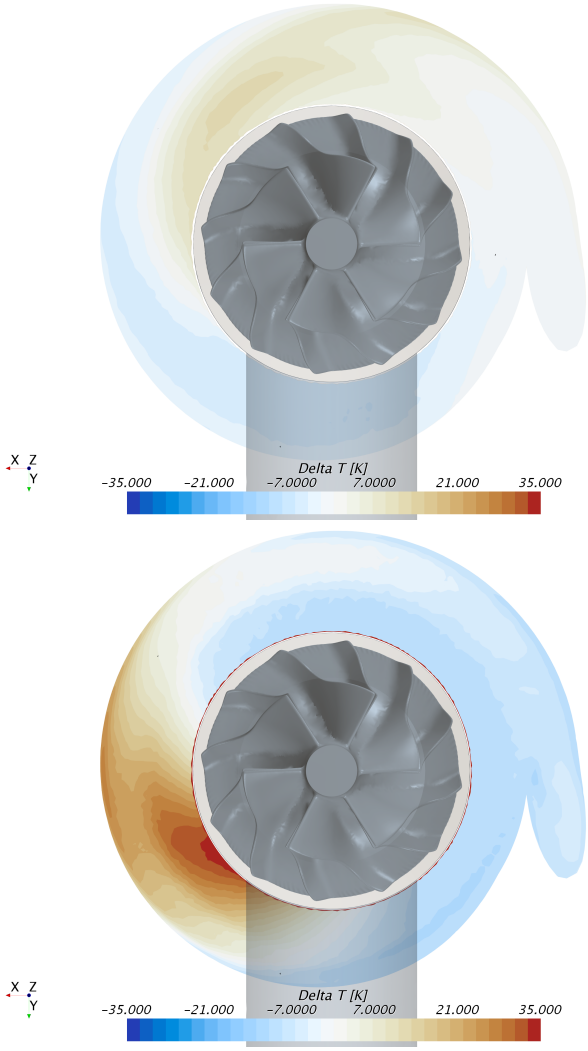

Figure 2.12: Mean temperature differences between T-junction and Std inlet in operating point 4 (top) and 6 (bottom).

that the absolute difference in radial velocity is slight for the studied EGR rate.

To finish this section, it is necessary to check if the described offset in the diffuser temperature is maintained along the rest of the domain, o there is final homogeneization of the air and EGR streams. The temperature at the end of

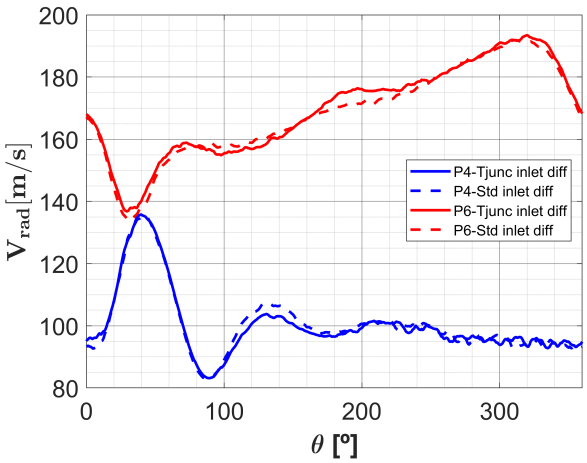

Figure 2.13: Azimuthal distribution of radial velocity in diffuser inlet for T-junction and standard inlet in operating point 6.

both domains is presented in figure 2.14. This section is a transversal plane of the outlet duct, near the end of the domain, and the temperature is again temporally averaged. This figure is a proof that the temperature differences in the diffuser presented in figure 2.12 have been clearly overcome, since in both cases the temperature pattern is quite similar, with an in-plane temperature range of 6 K. Therefore, the mixing effect of the volute and the outlet duct (due to its length) provides these similar contours at the end.

2.7 Conclusions

- A numerical campaign in a wide zone of the compressor map has been developed using experimental measurements to validate the prediction of the global performance. Two intakes have been considered; a single duct to simulate the standard experimental test rig, and a T-junction inlet to simulate the effects of a LP-EGR configuration. The inlet temperature and EGR rate has been fixed throughout the study, so the VR factor is the same to all the compressor points. Table 2.2 shows the computational effort of the simulation campaign conducted in a Intel Xeon E5-2630v3 (2.4GHz) processor for this chapter.
- Regarding the temporal treatment, the steady approach has proved that

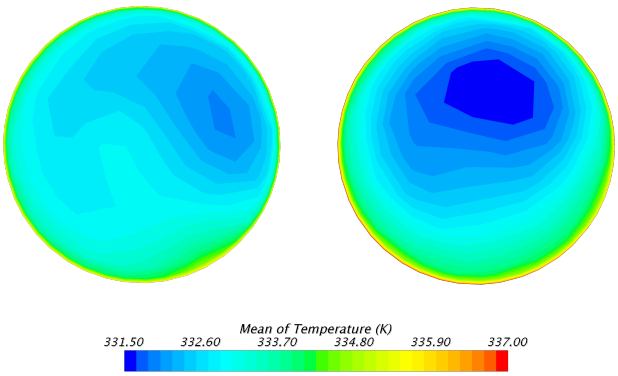

Figure 2.14: Mean of outlet temperature contours of Std case (left) and T-junction case (right) in operating point 6.

Table 2.2: Computational cost of chapter 2

Cases	18
Mesh size (millions)	1.5
Number of cores	16
Hours/case	41.67
Sum of kh*core	12

is not able to represent temperature distributions in a proper way neither the global performance of the compressor at high r.p.m. points. The developed interface assessment has demonstrated that the mixing plane interface must not be used in heterogeneous problems due to the circumferential averaged between the moving regions, especially if local values are mean to be studied. On the other hand, if point-to-point interface is applied, a spurious deviation of the EGR flow appears. To reduce this deviation, a circumferential shift could be implemented in the rotor-diffuser point-to-point interface, if the CFD code allows this possibility. In this way, the spurious deviation would still exist but the injection of EGR in the RANS simulation could be shifted in order to get a similar discharge point than the URANS, regarding the volute tongue. This circumferential shift should consider the distance between rotor inlet and outlet interfaces, the impeller rotating speed and the flow

average streamwise velocity; therefore, being strongly case-dependent. If this correction is not implemented or the mixing plane interface is employed, the steady scheme is not recommended when the compressor works with heterogeneous incoming flow, if one requires an accurate prediction of the temperature field in the rotor and diffuser. However, due to the lower computational effort of RANS against URANS or to get preliminary results, it is still interesting to use the steady approach.

- The differences predicted with the URANS approach between the LP-EGR T-junction and the standard single duct employing an equivalent operating point in the overall compressor parameters is very low, less of 1% of relative error in terms of isentropic efficiency. The temperature distribution in the diffuser has remarkable differences between both cases, especially in points with high r.p.m. However, these differences do not produce important changes in the position of the compressor map what is a different result in comparison with the conclusions of Reihani et al [32]. Nevertheless, as aforementioned, the VR factor is fixed in all the cases to a value near of 0.46. In the works of Reihani et al. [32] the values which this factor is relevant to produce changes in the compressor performance is starting as 0.9. In future works, the same operating points with higher values of VR (higher EGR rates or lower EGR cross section for the same mass flow rates) can be calculated to check the influence in the compressor performance.

- In terms of temperature heterogeneity, the T-junction does present differences (up to 35 K) against the single intake. These differences will increase for greater EGR rates and EGR inlet temperatures, so that the compressor wheel integrity criterion due to overtemperatures should be reviewed. However, the mixing of the streams is almost perfect in the outlet of the discharge duct, so that the benefit of the LP-EGR against HP-EGR in terms of EGR cylinder-to-cylinder dispersion is confirmed.

Chapter 2 Bibliography

[5] J. Galindo, R. Navarro, D. Tarí, and G. García-Olivas. "Centrifugal compressor influence on condensation due to Long Route-Exhaust Gas Recirculation mixing." *Applied Thermal Engineering* 144 (2018), pp. 901 –909. ISSN: 1359-4311. DOI: 10.1016/j.applthermaleng.

2018.09.005 (cit. on pp. x, 4, 22, 24, 25, 27, 28, 41, 42, 53, 54, 58, 61, 73, 124).

[12] J. M. Desantes, J. M. Luján, B. Pla, and J. A. Soler. "On the combination of high-pressure and low-pressure exhaust gas recirculation loops for improved fuel economy and reduced emissions in high-speed direct-injection engines." *International Journal of Engine Research* 14(1) (2013), pp. 3–11. DOI: 10.1177/1468087412437623 (cit. on pp. 3, 4, 22, 54, 99, 102).

[20] J. Galindo, P. Piqueras, R. Navarro, D. Tarí, and C. Meano. "Validation and sensitivity analysis of an in-flow water condensation model for 3D-CFD simulations of humid air streams mixing." *International Journal of Thermal Sciences* 136 (2019), pp. 410 –419. ISSN: 1290-0729. DOI: 10.1016/j.ijthermalsci.2018.10.043 (cit. on pp. 4, 22, 28, 54, 58, 59, 61–63, 73).

[22] S Karstadt, J Werner, S Münz, and R Aymanns. "Effect of water droplets caused by low pressure EGR on spinning compressor wheels." In: *Aufladetechnische Konferenz, Dresden*. 2014 (cit. on pp. 4, 7, 22, 54).

[30] K.-H. Brune, B. Stoffel, B. Matyschok, et al. "CFD-Analysis of the Flow Consisting of Two Mass Flows With Different Temperatures and/or Two Phases in a Turbocompressor." In: *ASME 2006 2nd Joint US-European Fluids Engineering Summer Meeting Collocated With the 14th International Conference on Nuclear Engineering*. American Society of Mechanical Engineers Digital Collection. 2006, pp. 701–711 (cit. on pp. 5, 22, 24, 27, 28, 36, 67, 68).

[31] K.-H. Brune, H.-P. Schiffer, R Christmann, and M Gnewikow. "Experimental investigations of the disturbed inlet-flow structure caused by mixing geometries and its influence on the performance of a turbocharger centrifugal compressor." In: *ASME Turbo Expo 2009: Power for Land, Sea, and Air*. American Society of Mechanical Engineers Digital Collection. 2009, pp. 1295–1304 (cit. on pp. 5, 22, 24, 41).

[32] A. Reihani, J. Hoard, S. Klinkert, C.-K. Kuan, and D. Styles. "Numerical Evaluation of the Effects of Low Pressure EGR Mixer Configuration on Turbocharger Compressor Performance." In: *ASME 2018 Internal Combustion Engine Division Fall Technical Conference*. American Society of Mechanical Engineers Digital Collection. 2018 (cit. on pp. 6, 11, 23, 34, 36, 47, 198).

[64] *STAR-CCM+*. Release version 12.06.010. CD-adapco. 2018. URL: http://ww.cd-adapco.com (cit. on pp. 9, 26, 30, 34, 42, 59, 61, 100, 107, 112, 114, 119, 170, 190).

[65] *STAR-CCM+*. Release version 14.02.010. Simcenter. 2019. URL: http://www.siemens.com (cit. on pp. 9, 24).

[66] J. Galindo, F. J. Arnau, L. M. García-Cuevas, and P. Soler. "Experimental validation of a quasi-two-dimensional radial turbine model." *International Journal of Engine Research* (2018), p. 1468087418788502 (cit. on pp. 9, 24).

[67] J. Galindo, A. Tiseira, R. Navarro, D. Tarí, H. Tartoussi, and S. Guilain. "Compressor Efficiency Extrapolation for 0D-1D Engine Simulations." In: *SAE Technical Paper*. SAE International, Apr. 2016. DOI: 10.4271/2016-01-0554 (cit. on pp. 9, 32, 33).

[68] J. R. Serrano, P. Olmeda, F. J. Arnau, and V. Samala. "A holistic methodology to correct heat transfer and bearing friction losses from hot turbocharger maps in order to obtain adiabatic efficiency of the turbomachinery." *International Journal of Engine Research* (2019), p. 1468087419834194 (cit. on pp. 9, 32).

[69] J. M. Luján, C. Guardiola, B. Pla, and A. Reig. "Switching strategy between HP (high pressure)-and LPEGR (low pressure exhaust gas recirculation) systems for reduced fuel consumption and emissions." *Energy* 90 (2015), pp. 1790–1798. DOI: 10.1016/j.energy.2015.06.138 (cit. on pp. 10, 22, 54, 102).

[70] V. T. Vithala, J. Hoard, D. Assanis, and D. Styles. "3-D Numerical Study of Turbulent Mixing of Intake Air and Exhaust Gas in a Low Pressure EGR System." In: *ASME 2011 Internal Combustion Engine Division Fall Technical Conference*. American Society of Mechanical Engineers Digital Collection. 2011, pp. 893–904 (cit. on pp. 22, 24, 27, 36, 41, 58).

[71] J. Luján, B Pla, S Moroz, and G Bourgoin. "Effect of low pressure EGR on gas exchange processes and turbocharging of a HSDI engine." In: *Proceedings of the conference on thermo-and fluid-dynamic processes in diesel engines (THIESEL 2008), Valencia, Spain, paper E*. Vol. 2. 2008 (cit. on p. 24).

[72] R. Navarro. "A numerical approach for predicting flow-induced acoustics at near-stall conditions in an automotive turbocharger compressor." PhD thesis. Universitat Politècnica de València, 2014. URL: http://hdl.handle.net/10251/44114 (cit. on pp. 25, 27, 43, 203).

[73] A. Broatch, J. Galindo, R. Navarro, and J. García-Tíscar. "Methodology for experimental validation of a CFD model for predicting noise generation in centrifugal compressors." *International Journal of Heat and Fluid Flow* 50 (2014), pp. 134–144. DOI: 10.1016/j.ijheatfluidflow.2014.06.006 (cit. on pp. 25–27).

[74] N. Watson and M. Janota. *Turbocharging the internal combustion engine*. Macmillan International Higher Education, 1982. DOI: 10.1007/978-1-349-04024-7 (cit. on p. 28).

[75] P. Olmeda, A. Tiseira, V. Dolz, and L. García-Cuevas. "Uncertainties in power computations in a turbocharger test bench." *Measurement* 59(Supplement C) (2015), pp. 363 –371. ISSN: 0263-2241. DOI: https://doi.org/10.1016/j.measurement.2014.09.055 (cit. on pp. 31, 33).

Chapter 3

Assessment of air-EGR mixing along LP-EGR junctions and effect on volume condensation

Contents

3.1 Introduction and literature review

As was exposed in chapter 1, there are many engineering fields in which three-way junctions are employed to merge two flows into a single stream, such as nuclear industry [23, 25, 26], internal combustion engines [3, 5] and oil industry [29], to name a few. In all these situations, a main stream meets a secondary flow within the junction, seeking for a quick homogenization or trying to keep the streams separated as much as possible, depending of the considered problem.

Three-way junction flow patterns have been studied by Hosseini et al. [34], Li et al. [76], and Zhou et al. [77], amongst others. Particularly, Hosseini et al. [34] established a classification regarding flow behavior in 4 categories, while Kamide et al. [24] and Kimura et al. [25] considered 3 types of flow patterns: wall-jet, deflecting-jet and impinging-jet.

The mixing process in three-way junctions has being analyzed by different researchers. Large eddy simulations have been conducted by Evrim et al. [38, 39] and Kuczaj et al. [78] in order to study thermal mixing in T-junctions. Gupta et al. [40] employed Reynolds-averaged Navier Stokes (RANS) simulations with $SST\ k-\omega$ turbulence model to find that increasing jet-to-mainstream momentum ratio enhanced mixing. However, none of these works deal with humid air streams and the condensation generated due to their mixing.

It is necessary to mention the difference between the terms "surface condensation" and "volume condensation". The former is driven by the presence of cooled walls (e.g., flow through a heat exchanger [79, 80]), so that related phenomena happening close to the surface (wall heat transfer and thermal boundary layer [81], existence of either dropwise or filmwise condensation [82], etc.) needs to be predicted accurately, but this phenomenom will not be considered in this thesis. On the other hand, volume (or bulk flow) condensation is produced when humid flow achieves dew point conditions without heat release into the surroundings, by means of gas expansion [83] or by mixing with colder flow, being the latter the object of study of this chapter. In this way, volume condensation may even appear when subsaturated wet streams meet. This phenomenon can become an issue in the field of air conditioning [84] and internal combustion engines [41]. In this chapter, the operating conditions considered correspond to junctions employed in internal combustion engines

featuring Low-Pressure Exhaust Gas Recirculation (LP-EGR). As was exposed in chapter 1, this technique consists in reintroducing and mixing the exhaust gases with fresh air, getting a reduction of the maximum temperature in the combustion chamber, and thus, NOx emissions are abated [85, 15, 86]. LP-EGR reintroduces the exhaust gas before the compressor [12, 69], which leads to the possibility of water droplets impacting the compressor wheel if bulk flow condensation arises in the air-EGR three-way junction. LP-EGR layout provides high EGR mass flow rates [42, 87] which is deemed as one of the key factors to increase the thermal efficiency of internal combustion engines [88]. Unfortunately, the related deterioration of compressor performance and integrity [41, 22] limits the applicability of LP-EGR in the scope of cold ambients [43, 44, 89].

Chapter 2 has shown the small impact of the flow heterogeneity of a LP-EGR configuration in the performance of the compressor (less than 1% of difference), for low values of J. However, the role of air-EGR mixing in condensation is beleived to be of paramount importance [5]. As exposed in the approaches of chapter 1, a 3D CFD model was developed by Serrano et al. [21] to analyze junction condensation. This model has been validated in different ways by Galindo et al. [45, 46]. Good accordance between CFD predictions and experimental results has been found in terms of secondary flows (measured by means of laser particle image velocimetry) and condensation patterns (observed with planar laser-induced visualization) [45], as well as condensation mass flow rates (indirectly obtained by temperature measurements with and without condensation) [46]. Junction design should minimize condensation mass flow rate to prevent harm to the LP-EGR compressor, as great impeller erosion was found at experimental impeller durability tests when 3D-CFD simulations predicted the highest condensation rates [20], which can be deemed as another prove of the validity of the 3D CFD model. Galindo et al. [5, 45] have observed that junction geometries that promote strong secondary flows are the ones providing higher condensation mass flow rates, but their research did not go beyond that point. The idea that volume condensation in a three-way junction may be correlated with a quantitative indicator of the mixing of its inlet streams has never been addressed before in the literature, and is the main task of this chapter.

The literature review has established the potential benefits of reducing junction condensation. Despite that flow and mixing phenomena inside a three-way junction have been studied previously, there has not been (to the

authors' knowledge) a work providing a quantitative correlation between mixing and condensation. The present chapter employs a comprehensive numerical campaign (more than 130 simulations) to provide the following original contributions in the framework of mixing and volume condensation. First, a new definition of mixing index is developed, by calculating the unmixed area at a certain section. This index can be computed by considering the transport of a passive scalar or the temperature field. The performance of these versions of the new index is compared against other mixing indexes from the literature. Second, a strong quantitative correlation is derived for the first time between condensation mass flow rate, psychrometric conditions and such mixing indexes. Third, novel junction design guidelines to decrease bulk flow condensation are obtained through the reduction of flow mixing. Particularly, the connection between branch-to-mainstream momentum ratio and mixing is originally exploited to minimize condensation.

The 0D and 3D CFD models employed in this chapter are described in Section 3.2, together with the definitions of mixing indexes and momentum ratio. Section 3.3 provides the correlations between condensation and mixing and the role of momentum ratio in flow patterns and mixing, as well as the design criteria that should be followed to reduce bulk flow condensation. Finally, some concluding remarks are provided in Section 3.4.

3.2 Methods

3.2.1 Junction 0D Model

As aforementioned, the problem studied in this chapter is the mixing between humid air streams in a three-way junction. Serrano et al. [41] developed a 0D model to predict the condensation mass flow rate produced in these situations by considering that both streams end up being perfectly mixed at the outlet. Figure 3.1 depicts the numerical domain that will be described in Section 3.2.2.1, but it can be used as a sketch of such 0D model to present its inputs. Considering the main (or air) leg, the mass flow ($\dot{m}_m$), pressure (P_m), temperature (T_m), and relative humidity (RH_m) must be specified. On the branch (or EGR) duct, the same conditions ($\dot{m}_b$, P_b, T_b) must be declared in exception of the relative humidity, which will be replaced by the specific humidity (w_b). In addition, the model needs the introduction of the outlet

pressure condition (P_{out}) and the 3 main areas of the domain (A_m, A_b, A_{out}). The result of the model is the condensation mass flow rate ($\dot{m}_{cond-0D}$) at the outlet of the three-way junction.

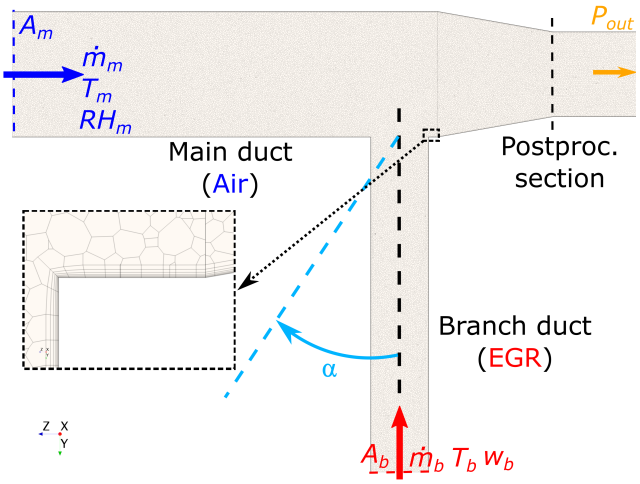

Figure 3.1: Longitudinal plane of T-junction numerical domain showing mesh, boundary conditions and postprocessing plane, with a close-up of the prism layer employed in the branch insertion.

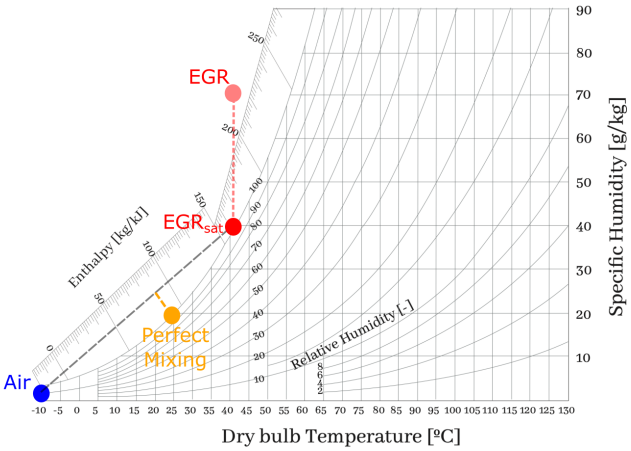

Figure 3.2: Psychrometric diagram at atmospheric pressure, with three-way junction inlet conditions and outlet solution obtained with 0D perfect mixing model.

Figure 3.2 shows a psychrometric diagram. The conditions for the inlet

ducts (depicted in Fig. 3.1) belonging to one of the 128 working points assessed in this chapter are indicated in Fig. 3.2. The particular values of this numerical campaign correspond to the application of three-way junctions to LP-EGR, in which cold air is mixed with warm, humid EGR. Notice how the design of experiments described in Section 3.2.3 delivers a number of supersaturated points (as the one depicted in Fig. 3.2), depending on the combination of values of T_b, w_b and P_{outlet}. In such cases, the first step is to remove the excess of water at the branch duct inlet between the original point and that corresponding to saturated conditions, since both 0D and 3D CFD models (see Section 3.2.2) are devoted to obtain condensation only due to mixing. The equivalent saturated point ("$\mathrm{EGR_{sat}}$" in Fig. 3.2) is obtained by descending vertically from the original point ("EGR") up to the saturation line, since the imposed T_b is a static, dry bulb temperature.

Condensation mass flow rate is then obtained with the 0D model [41] by considering conservation of mass for air and water species, together with the definition of specific humidity w, by virtue of the following equation:

$$\dot{m}_{cond-0D} = \dot{m}_{air} \cdot \frac{w_{air}/1000}{w_{air}/1000 + 1} + \dot{m}_{EGR} \cdot \frac{w_{EGR,sat}/1000}{w_{EGR,sat}/1000 + 1} - \ldots \\ \ldots - (\dot{m}_{air} + \dot{m}_{EGR}) \cdot \frac{w_{PM}/1000}{w_{PM}/1000 + 1} \ . \quad (3.1)$$

In Eq. 3.1, the only unknown is the humidity at the outlet considering a perfect mixing between the inlet streams, i.e., w_{PM}. This solution is obtained graphically at Fig. 3.2 on the basis of conservation equations. First, the gray dashed line connecting the inlet points ("Air" and "$\mathrm{EGR_{sat}}$") and the position at which it crosses the yellow dashed line correspond to a linear weighting of inlet specific humidities and enthalpies regarding the corresponding mass flow rates. Then, the slope of the yellow dashed line of Fig. 3.2 indicates constant enthalpy. This is because heat transfer with the surroundings is neglected, so that the heat released due to condensation is absorbed by the flow itself. Finally, the outlet point is located where the yellow dashed line finds the saturation line, which in turn is calculated by means of Dalton's law and Antoine's equation for humid air. The term "perfect mixing" associated to the 0D model developed by Serrano et al. [41] is here employed because the zero-dimensional consideration of the outlet station inherently assumes it to

be homogeneous, and therefore the inlet streams are considered to be perfectly mixed.

This 0D model will be employed to perform correlations between condensation and mixing predicted by 3D CFD simulations (see section 3.3.1). Besides, section 3.3.2 will show that indeed the condensation predicted by this 0D model is the maximum condensation that could be achieved in the junction, when both streams are perfectly mixed. For more details about the 0D model, please refer to Serrano et al. [41].

3.2.2 Junction 3D CFD model

3.2.2.1 Geometry and mesh

Figure 3.1 shows a longitudinal slice of the numerical domain of the three-way junction, depicting the mesh as well. The modeled geometry represents a 90° three-way junction (T-junction) as could be featured in a LP-EGR system, where fresh air and EGR streams are mixed before the compressor. The short tapered section after the branch duct represents the compressor inlet cone, up until the postprocessing section that would correspond to the compressor inducer plane. Then, the outlet duct is extruded 5 diameters to reduce the impact of the boundary location on the region of interest.

The geometry considered in Fig. 3.1 is similar to those employed by Reihani et al. [33] and Galindo et al. [5, 2], since all of them include the compressor cone. Other authors [70, 53, 20] have modeled T-junctions for LP-EGR applications considering the same cross section for the outlet and main ducts. Besides, the impact of branch diameter and angle regarding the main duct on flow mixing and condensation will be assessed in Section 3.3.5.

The grid depicted in Figure 3.1 is a polyhedral mesh with prism layers to improve near wall resolution, with 3.7 million cells in total. The employed mesh density has been selected by means of an independence mesh study. The main variable that was analyzed in this study is the condensed water $\dot{m}_{cond}$ at the end of the cone (see Fig. 3.1). A 10.4% of difference in condensed water is obtained when replacing a 0.4 million cells mesh by a 3.7 million cells grid. On the other hand, a finer mesh density leading to a 10.8 million cells does not significantly affects condensation compared to the 3.7 million cells grid (3.1% of difference). Having assessed the sensitivity of the mesh

to a global key parameter (condensation mass flow rate), vertical profiles of passive scalar ϕ (see Section 3.2.2.2) at cone outlet diameter are provided in Fig. 3.3 to complete the analysis of discretization error. Figure 3.3 shows a great agreement between the profiles predicted by the grids with 10.8 and 3.7 million cells. Vertical distribution of ϕ simulated using 0.4 million cells presents significant differences with the other two at the bottom part of the cross-section (negative values of y). For the sake of limiting the computational effort, and considering that more than 130 simulations are conducted in this chapter (see section 3.2.3), the 3.7 million mesh is therefore selected for the rest of the study. In addition, this mesh provides a $y^+ < 1.5\%$ in 99% of wall cells even in the more critical conditions (higher mass flows), so this fact assures that the viscous sub-layer is always resolved.

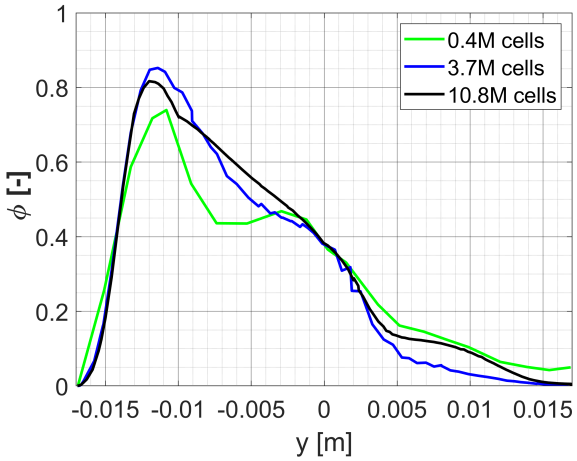

Figure 3.3: Profiles of passive scalar ϕ at the vertical diameter of the cone outlet for different grid resolutions.

3.2.2.2 Numerical setup

The numerical configuration employed in this chapter has been already validated by Galindo et al. [20, 45]. The segregated solver of STAR-CCM+ [64] has been used for the 3D CFD numerical simulations, considering second-order upwind discretization schemes for convective terms. An Eulerian approach is employed to solve the conservation equations. Since a mixture of humid air streams is aimed to be modeled, dry air and water vapor are set as ideal gas

components and their corresponding species equations are included. Continuity, momentum and energy equations are also solved, which can be expressed by means of a general transport equation

$$\frac{\partial(\rho\varphi)}{\partial t} + \nabla\left(\rho\varphi u_i\right) = \nabla\left(\rho\Gamma_\varphi \nabla(\varphi)\right) + S_\varphi \ , \tag{3.2}$$

considering the terms of Table 3.1. RANS turbulence modeling will mainly affect these transport equations by the increment of the *effective* diffusion coefficients of Table 3.1.

Table 3.1: Convective, diffusive and source terms for solved transport equations, excluding turbulence.

Equation	φ	Γ_φ	S_φ
Mass	1	–	S_{vap}
Species	y	D	S_{vap}
Momentum	u_i	ν	$-\partial p/\partial x_i + f_v + S_{\text{mom}}$
Energy	h_0	α	$-Dp/Dt + w_v + S_{\text{ener}}$

The condensation submodel described in Section 3.2.2.3 is employed to transform water vapor into liquid water when appropriate just by the implementation of custom source terms S_φ in Eq. 3.2, thus retaining the Eulerian approach for the sake of computational cost. In this way, features such as droplet nucleation and Lagrangian particle tracking [90, 91, 92] are not included in this model. The employed approach does not consider either any interface tracking methods (such as Volume of Fluid) nor a fluid film model, since surface condensation is not addressed in this Thesis.

Regarding the turbulent approach, the numerical campaign described in Section 3.2.3 is initially calculated using steady RANS with $SST\ k-\omega$ turbulence submodel [93]. Since the flow pattern varies significantly depending on the operating conditions (see Fig. 3.9), there are some working points presenting an oscillating behavior for water condensation. If the oscillation of liquid water mass flow rate at the end of the cone is above 2%, the case is switched to unsteady RANS (URANS), employing a second-order implicit transient solver. In the same way as with the mesh independence, the sensitivity to the time-step size Δt has been evaluated in terms of predicted condensation. In this way, condensation mass flow rate is modified by 0.01 % when replacing $\Delta t = 10^{-5}$ s with a larger $\Delta t = 5 \cdot 10^{-5}$ s. If the time-step size is further

increased from $\Delta t = 5 \cdot 10^{-5}$ to $\Delta t = 10^{-4}$, the variation on condensed water is still slight (0.09 %). Considering again the large numerical campaign and the sensitivity analysis just performed, the unsteady cases are simulated with a time-step size of $\Delta t = 10^{-4}$ s, being in agreement with works of the same scope [20, 45].

Mass flow rate, stagnation temperature, turbulence intensity and component (dry air and water vapor) mass fraction are set at main and branch inlets. Static pressure is determined at the outlet. The particular values of boundary conditions are shown in Section 3.2.3. In addition, a passive scalar is injected with a value of $\phi = 1$ through the branch inlet, whereas the main inlet considers $\phi = 0$. By doing so, the mixing between the air and EGR (branch) streams can be assessed, as will be explained in Section 3.2.5. Walls are considered as adiabatic due to the low conductivity of a typical LP-EGR junction, which explains why volume condensation is the only mechanism in this scope.

3.2.2.3 Condensation submodel

In the present chapter, the condensation submodel was developed and verified by Serrano et al. [21] and validated by Galindo et al. [5, 45]. This model is implemented in STAR-CCM+ [64], allowing to predict the amount of condensed water on a certain operating condition produced by the mixing of the humid streams along the junction.

As a summary, the condensation model compares the psychrometric state of each cell to the corresponding saturated equilibrium state, in order to condense instantaneously the appropriate amount of water when supersaturation exists. To this purpose, the source terms presented in Eqs. 3.3, 3.4 and 3.5:

$$S_{vap} = \frac{\rho \cdot Y_{air} \cdot (w_f - w_i)}{\Delta t} \tag{3.3}$$

$$S_{ener} = -S_{vap} \cdot L \tag{3.4}$$

$$S_{mom} = S_{vap} \cdot \vec{u} \tag{3.5}$$

are included in the corresponding transport equations (see Eq. 3.2 and Table 3.1). The term S_{vap} is subtracted from the water vapor species and injected into a transport equation to represent the generation of condensed liquid water and its motion in the form of fog. In this way, a condensation mass flow rate can be computed at the three-way junction outlet, which will be exploited throughout Section 3.3. Notice also how the release of energy due to condensation (see Eq. 3.4) affects the temperature field, which is a feature that contributes to the inferior performance of mixing indexes defined using temperatures when compared to passive-scalar mixing indexes, as will be shown in Section 3.3.1. For a complete explanation of the hypotheses and characteristics of this condensation submodel, the reader is referred to the work of Serrano et al. [21].

The combination of the 3D CFD setup described in Section 3.2.2.2 and its embedded condensation submodel has been validated against experimental measurements regarding five different aspects. Firstly, the CFD model was able to predict secondary flows in the three-way junction outlet matching those measured with laser particle image velocimetry [45]. Secondly, planar laser-induced visualization provided experimental condensation distributions in agreement with the numerical predictions [45]. Thirdly, temperature numerical and experimental fields at the outlet cross-section were found to be similar [46]. Fourthly, condensation mass flow rates obtained by CFD simulations were in accordance with indirect experimental measurements of condensation mass flow rates [46]. Lastly, CFD predictions of condensation mass flow rate with different junction configurations were found to be strongly correlated with the impeller wear level observed in experimental durability tests [20].

3.2.3 Numerical campaign

An extensive numerical campaign is designed in order to explore mixing flow patterns existing at different operating conditions. Particularly, a 2^{9-2} fractional factorial design is employed, in which the impact of 9 factors on mixing and condensation is assessed through 128 simulations. The identification and assigned numerical values of factors is in accordance with the application of mixing flow in LP-EGR junctions. Nevertheless, Section 3.3.3 will prove that the range of flow patterns of the simulations covers the whole spectrum, so that the findings of this work are not constrained by the field of scope.

The original 2^{9-2} fractional factorial design investigates 2 levels of each factor (low and high) whereas, in this case, working points not producing any condensation were replaced by others that did, taking advantage of an additional intermediate level. Table 3.2 includes the different factors explored with the campaign of 128 simulations, together with the numerical values of the 2 or 3 levels assessed (where appropriate):

Table 3.2: Factors and levels of conducted numerical campaign.

Factor	Definition	Low	Mid	High
$\dot{m}_m$ $[kg/s]$	Mass flow rate of main duct	0.014	-	0.083
EGR_{rate} [%]	EGR rate (see Eq. 3.6)	10	25	40
T_m $[K]$	Static temperature of main duct	263	-	283
T_b $[K]$	Static temperature of branch duct	314	324	334
RH_m [%]	Relative humidity of main duct	50	-	100
w_b $[g/kg]$	Specific humidity of branch duct	30	50	70
I_m [%]	Turbulence intensity of main duct	1	-	10
I_b [%]	Turbulence intensity of branch duct	1	-	10
P_{outlet} $[kPa]$	Outlet static pressure	80	90	100

The factors analyzed in this chapter (see Table 3.2) can be classified into different categories. On the one hand, P, T_m, RH_m are ambient variables which are independent from the engine operating conditions. On the other hand $\dot{m}_m$, EGR_{rate}, T_b and w_b are determined by the working point of the engine. Notice that in this chapter the branch (EGR) mass flow rate is indirectly established by the value of the engine EGR rate (EGR_{rate}), which was defined in chapter 2 in equation 2.2, so, its definition is inmediate:

$$EGR_{rate} = \frac{\dot{m}_{EGR}}{\dot{m}_{EGR} + \dot{m}_{air}} = \frac{\dot{m}_b}{\dot{m}_b + \dot{m}_m} \tag{3.6}$$

Besides, variables w_b and RH_m are directly related with the boundary conditions Y_{air} and Y_{vap} described in section 3.2.2.2, that are required by the simulations. In addition, the impact of turbulence intensity at the air and EGR inlet boundaries is also evaluated through this design of experiments.

The set of works conducted by Galindo et al. [45, 46, 20] to validate the 3D CFD condensation model employed operating conditions in the following range: $\dot{m}_m \in [0.024, 0.067]\, kg/s$, $EGR_{rate} \in [15, 32]\,\%$, $T_m \in [263, 273]\, K$,

$T_b \in [323, 363]\, K$ and $w_b \in [50, 70]\, g/kg$. Therefore, the validation extends over most of the range of the numerical campaign described by Table 3.2.

3.2.4 Definition of momentum ratio (J) and review of literature values

The literature review conducted in the introduction (see chapter 1 and Section 3.1) has shown that some authors [24, 25] claim that the ratio between the momentum of branch and main streams dictates the type of flow pattern, provided that the junction design is kept. Momentum ratio (J) was defined in equation 1.1 and therefore, in this chapter will be defined as:

$$J = \frac{\rho_b \cdot U_b^2}{\rho_m \cdot U_m^2}, \tag{3.7}$$

where ρ_b and U_b are the density and velocity in the branch respectively and ρ_m and U_m the density and the velocity in the main duct.

This parameter J is employed whenever a jet is transversely discharged from a duct into a cross-stream, that can be also confined (three-way junction) or not (jet in crossflow [94, 95]). This chapter deals with the former, so that the existence of an internal flow can be used to evaluate the momentum ratio of Eq. 3.7 in terms of the boundary conditions of the problem. Besides, in the analyzed three-way junctions, the branch duct may not be perpendicular to the main duct (see Fig. 3.1). In order to employ a normal branch-to-main momentum ratio, the following definition will be considered hereinafter:

$$J = \frac{\dot{m}_b^2 \cdot \rho_m \cdot A_m^2}{\dot{m}_m^2 \cdot \rho_b \cdot A_b^2} \cdot cos(\alpha)\ , \tag{3.8}$$

which can be expressed in the following form when combined with Eq. 3.6:

$$J = \frac{{EGR_{rate}}^2 \cdot \rho_m \cdot A_m^2}{(1 - EGR_{rate})^2 \cdot \rho_b \cdot A_b^2} \cdot cos(\alpha)\ . \tag{3.9}$$

In Eqs. 3.8 and 3.9, α is the insertion angle of the branch duct as defined in Fig. 3.1. $\alpha = 0°$ corresponds to a perpendicular branch duct (T-junction)

and positive values of α decrease the normal branch-to-main momentum ratio J, as will be explored in Section 3.3.5.

3.2.5 Reference definitions and new proposals for mixing indexes (MI)

As mentioned in Section 3.1, this chapter studies the mixing process between two humid air streams at a three-way junction (see Fig. 3.1), with the goal of assessing the impact of such mixing in the generated condensation. To do so, it is required to use indicators that allow to quantify how well or bad mixed is the analyzed flow at a certain cross-section of the junction.

3.2.5.1 Mixing indexes on the basis of passive scalar ϕ

Calculating the transport of a passive scalar is a common technique to trace mixing in junctions [53, 96, 97]. It consists in considering a scalar that is advected by the flow without having any impact on the flow field itself, therefore behaving as a postprocessing tool. Section 3.2.2.2 explained that the branch leg considers a value of $\phi = 1$ and the main leg presents $\phi = 0$. In this way, the value of the passive scalar employed in this chapter plays the role of a branch (EGR) mass fraction, which can be understood as a local EGR_{rate} (see Eq. 3.6).

Researchers in the scope of flow mixing [98, 99, 100] often rely on such concentration quantities to define coefficients based on squared concentration deviations, in the spirit of the *intensity of segregation* developed by Danckwerts [101]. A discrete version of Danckwerts' mixing index (MI) is considered in this chapter as a reference for mixing assessed by a passive scalar, with the following definition:

$$MI_{\phi-ref} = 1 - \frac{1/N \cdot \sum \left(\phi_i - \bar{\phi}\right)^2}{\bar{\phi}\left(1 - \bar{\phi}\right)} \tag{3.10}$$

In Eq. 3.10, N is the total amount of elements of the analyzed section, ϕ is the mass fraction of the passive scalar and i is the index of each cell face at the postprocessing cross-section. Application of Eq. 3.10 to both inlet

ducts provides an indeterminate form of type 0/0. On the one hand, the main duct presents pure air, so for each cell $\phi_i = 0$ and therefore $\bar{\phi} = 0$. On the other hand, the branch duct presents pure EGR, so $\phi_i = 1$ and $\bar{\phi} = 1$. Once the streams meet and $\bar{\phi} \neq \{0, 1\}$, Eq. 3.10 requires $\phi_i = \bar{\phi}$ at each and every cell of the cross section to consider that the streams are perfectly mixed ($MI_{\phi-ref} = 1$). If the flow is instead totally segregated, i.e., some cells present $\phi_i = 1$ whereas the rest of elements present $\phi_i = 0$ (there are no cells with an intermediate value of ϕ_i), then $MI_{\phi-ref} = 0$. [1]

In the present chapter, the definition of a new mixing index $MI_{\phi-new}$ employing the passive scalar ϕ has been developed, which will be obtained as:

$$MI_{\phi-new} = 1 - \frac{\sum_i dA_{unmixed-\phi,i}}{\sum_i dA_i} \ . \tag{3.11}$$

The underlying idea of the proposed index $MI_{\phi-new}$ is to quantify the unmixed area in a cross-section. To do so, a piecewise definition is considered for each surface element of the analyzed section:

$$dA_{unmixed-\phi,i} = \begin{cases} \dfrac{\phi_i - \bar{\phi}}{(1-\bar{\phi}) + \delta_{\phi-new}} \cdot A_i & \text{if} \quad \bar{\phi} \leq \phi_i \leq 1 \\ \\ \dfrac{|\phi_i - \bar{\phi}|}{|0-\bar{\phi}| + \delta_{\phi-new}} \cdot A_i & \text{if} \quad 0 \leq \phi_i \leq \bar{\phi} \end{cases} \tag{3.12}$$

where $\bar{\phi}$ is the average of the passive scalar in the section. In this way, Eq. 3.12 classifies the element as rich (top) or lean (bottom) in terms of branch passive scalar ϕ. Then, it weights the element area linearly between a local mixture that coincides with the corresponding section average (which adds zero element area to the unmixed surface) and a fluid parcel coming purely from the main or branch inlet (which keeps its whole element area). Notice that numbers "1" and "0" appearing at the denominators of Eq. 3.12 correspond to the value of passive scalar at branch and main legs, respectively,

[1] Considering Z elements with a value of $\phi_i = 1$ and $N - Z$ elements presenting $\phi_i = 0$, Eq. 3.10 results in $MI_{\phi-ref} = 1 - \frac{1/N\left[Z(1-Z/N)^2 + (N-Z)(0-Z/N)^2\right]}{Z/N(1-Z/N)}$, which yields $MI_{\phi-ref} = 0$.

and $\delta_{\phi-new}$ is a small quantity that has a negligible impact in the results but avoids division by zero. Hence, the developed mixing index $MI_{\phi-new}$ behaves like $MI_{\phi-ref}$ in the asymptotic cases, i.e., it provides $MI_{\phi-new} = 0$ for a completely segregated outlet stream and yields $MI_{\phi-new} = 1$ only for a homogeneous mixture. Besides, the proposed index avoids the indetermination of $MI_{\phi-ref}$ at the inlet legs, as it presents a value of $MI_{\phi-new} = 0$ at the main and branch ducts

Sakowitz et al. [53] also defined a *uniformity index* ranging from 0 to 1 that bears a resemblance to the combination of Eqs. 3.11 and 3.12. However, they employed a reference value corresponding to maximum heterogeneity to normalize their index, instead of the piecewise definition of Eq. 3.12.

3.2.5.2 Mixing indexes on the basis of temperature

An incompressible flow with adiabatic walls presents a temperature flow field that behaves exactly as a passive scalar. This fact can be exploited by experiments to compensate for the impossibility of considering a virtual passive scalar. Temperature is even employed by mildly compressible flows as an indicator of the existence and intensity of compressor stall [102, 103, 104]. In this chapter the ideal gas equation is considered for humid air, but local mach number M at the T-junction does not exceed a value of $M = 0.55$ for the whole numerical campaign described in Section 3.2.3.

A non-dimensional temperature field normalized with the difference between main and branch inlet temperature could be employed for analyzing mixing [78, 105]. However, this method assigns the ends of the [0–1] range to each of the inlet legs, whereas the perfect mixture lays in an intermediate point. For the sake of a fair comparison with the mixing indexes defined in Section 3.2.5, the work of Brune et al. [30] is considered instead. Brune et al. calculate a perfectly-mixed adiabatic temperature T_{ad}, in the same way than equation 2.5 in chapter 2, that is:

$$T_{ad} = \frac{\dot{m}_m \cdot T_m + \dot{m}_b \cdot T_b}{\dot{m}_m + \dot{m}_b} \ . \tag{3.13}$$

After that, they define a local mixing rate ϵ_i, depending on the cell temperature and hot and cold temperatures of the problem, which are T_b and T_m

in this case. The definition of the local mixing rate is presented in equation 3.14:

$$\epsilon_i = \begin{cases} \dfrac{T_i - T_b}{T_{ad} - T_b} & \text{if} \quad T_{ad} < T_i < T_b \\ \\ \dfrac{T_i - T_m}{T_{ad} - T_m} & \text{if} \quad T_m < T_i < T_{ad} \end{cases} \tag{3.14}$$

with T_i being the temperature of each element i of the considered cross-section. Finally, the overall mixing index MI_{T-ref} is computed as:

$$MI_{T-ref} = \epsilon = \frac{1}{N} \sum_{i=1}^{N} \epsilon_i, \tag{3.15}$$

which will be considered in this chapter as the reference mixing index on the basis of temperature (virtual) measurements. The method of Brune et al. [30] as defined by Eqs. 3.13 to 3.15 aims at obtaining values of $MI_{T-ref} = 0$ for unmixed flow and $MI_{T-ref} = 1$ for a perfect mixture, like $MI_{\phi-ref}$ and $MI_{\phi-new}$. Indeed, this is true for a non-reactive and incompressible flow of dry air. However, in this problem the released heat due to condensation (see Eq. 3.4) changes the perfect-mixing temperature from that considered with the inlet temperatures alone (Eq. 3.13). Besides, this adiabatic temperature does not take into account that in an unsteady simulation the mass flow rates of main and branch streams arriving at a section are not necessarily those defined at the boundaries for each and every time step.

To overcome these issues, Eq. 3.12 is adapted to use temperature instead of a passive scalar to provide the following equation:

$$dA_{unmixed-T,i} = \begin{cases} \dfrac{T_i - \bar{T}}{(T_b - \bar{T}) + \delta_{T-new}} \cdot A_i & \text{if} \quad \bar{T} \leq T_i \leq T_b \\ \\ \dfrac{|T_i - \bar{T}|}{|T_m - \bar{T}| + \delta_{T-new}} \cdot A_i & \text{if} \quad T_m \leq T_i \leq \bar{T} \end{cases} \tag{3.16}$$

in which $\bar{T}$ is the average temperature at the considered cross-section and time step. Finally, the proposed mixing index based on temperature (MI_{T-new}) is calculated as:

$$MI_{T-new} = 1 - \frac{\sum_i dA_{unmixed-T,i}}{\sum_i dA_i} \ . \tag{3.17}$$

3.3 Results and discussion

3.3.1 Correlation between condensation and mixing

The main hypothesis of this chapter is the idea that bulk flow condensation can be explained by two independent factors: psychrometry and mixing. The 0D model presented in Section 3.2.1 provides the maximum amount of condensation $\dot{m}_{cond-0D}$ for a certain working point considering that the streams are perfectly mixed, thus carrying the psychrometric information. If the mixing indexes MI defined in Section 3.2.5 are interpreted as the ratio between actual and maximum (perfect) mixture, the real condensation mass flow rate for a three-way junction at certain operating conditions could be predicted by Eq. 3.18:

$$\dot{m}_{cond-pred} = \dot{m}_{cond-0D} \cdot MI \ . \tag{3.18}$$

Equation 3.18 allows a comparison between the predicted condensation $\dot{m}_{cond-pred}$ and the real condensation mass flow rate as obtained from 3D CFD (see Section 3.2.2) at the junction postprocessing section for the whole numerical campaign consisting in 128 simulations. At each working point, $\dot{m}_{cond-0D}$ is calculated from the boundary conditions whereas the different mixing indexes MI defined in Section 3.2.5 are computed at the target section, to assess the potential of each MI in terms of fitting ability.

Figure 3.4 depicts the comparison between condensation mass flow rate observed $\dot{m}_{cond-obs}$ (calculated by means of the 3D CFD model) and $\dot{m}_{cond-pred}$ predicted by Eq. 3.18, using mixing indexes based on passive scalar (Eqs. 3.10 and 3.11). Figure 3.5 is the counterpart of Fig. 3.4 for mixing indexes based on temperature (Eqs. 3.15 and 3.17). As discussed in Section 3.2.2.3, the CFD

model provides mass flow rate $\dot{m}_{cond-obs}$ by simulating volume condensation due to the mixing of humid streams.

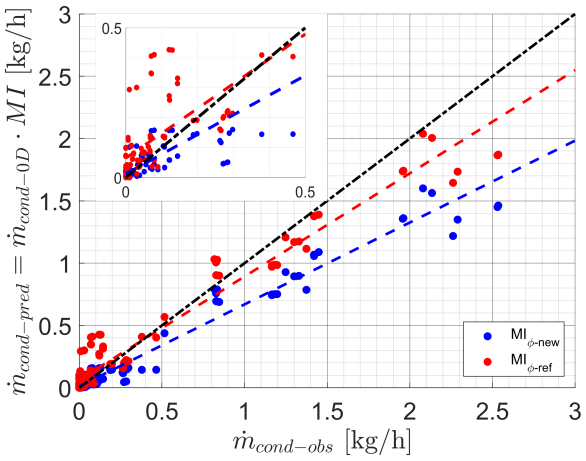

Figure 3.4: Calibration plot of observed versus predicted condensation (obtained using two mixing indexes based on passive scalar), with close-up of the range of $\dot{m}_{cond} = 0 - 0.5\ kg/s$. Bisector and regression lines are also included.

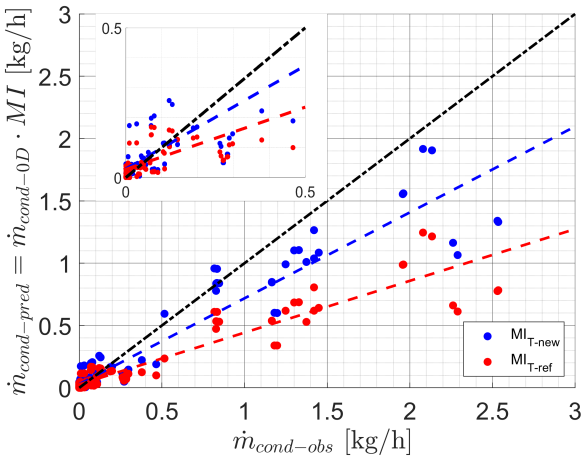

Figure 3.5: Calibration plot of observed versus predicted condensation (obtained using two mixing indexes based on temperature), with close-up of the range of $\dot{m}_{cond} = 0 - 0.5\ kg/s$. Bisector and regression lines are also included.

Bisector of Fig. 3.4 indicates the ideal situation in which $\dot{m}_{cond-pred} =$

$\dot{m}_{cond-obs}$. However, Fig. 3.4 shows how the set of points calculated with Eq. 3.18 by means of $MI_{\phi-new}$ and $MI_{\phi-ref}$ consistently underpredict condensation, which also happens if MI_{T-new} and MI_{T-ref} are employed instead (see Fig. 3.5). Examining Eq. 3.18, several factors can be blamed for the underprediction of condensation using that expression. Firstly, mixing indexes defined in Section 3.2.5 are used in Eq. 3.18 to predict the ratio between the actual condensation and the maximum one, according to global psychrometric considerations. Considering the non-linear behavior of psychrometry (see Section 3.2.1), modifications to the definition of the mixing could enhance their ability to predict $\dot{m}_{cond}$ using Eq. 3.18. For instance, the linear weighting between total segregation and homogeneous flow employed in $MI_{\phi-new}$ (Eq. 3.12) and MI_{T-new} (Eq. 3.16) could be replaced by other weightings that perform better for different junctions and operating conditions. Secondly, Section 3.3.2 will show that maximum condensation is achieved sooner than perfect mixing. Eq. 3.18 attributes all three-dimensional effects to MI, calculating $\dot{m}_{cond-0D}$ with the inlet psychrometric conditions and the junction inlet and oulter cross-sections (see Section 3.2.1). However, local low temperatures due to formation of *vena contracta* and subsequent flow expansion may achieve dew conditions before expected and thus be responsible for a fraction of the observed underprediction of condensation.

Mean absolute error MAE is calculated for the whole numerical campaign as follows:

$$MAE = \frac{1}{K} \cdot \sum_{k=1}^{K=128} \left| \dot{m}_{cond-obs,k} - \dot{m}_{cond-pred,k} \right| \ . \tag{3.19}$$

MAE is employed in table 3.3 to assess the performance of the different mixing indexes studied in this chapter in terms of their *a priori* predicting capability of $\dot{m}_{cond}$ using Eq. 3.18. Table 3.3 shows that $MI_{\phi-ref}$ presents the lowest MAE. Notice that Fig. 3.4 illustrates that the cloud of red points ($MI_{\phi-ref}$) are not so far from the bisector, which would indicate perfect agreement between $\dot{m}_{cond-pred}$ and $\dot{m}_{cond-obs}$. Indeed, the regression line of $MI_{\phi-ref}$ is closer to the bisector than the regression line corresponding to $MI_{\phi-new}$, which is in agreement with the MAE values featured in table 3.3. Likewise, the important difference of slope between the bisector and the regression line of MI_{T-ref} in Fig. 3.5 is related to the largest MAE in table 3.3, which is presented by the same index (MI_{T-ref}).

Even though Eq. 3.18 considering the mixing indexes of Section 3.2.5 is

Table 3.3: Mean absolute error (MAE) of observed vs predicted condensation using different mixing indexes.

Mixing index	$MAE\ [kg/h]$
$MI_{\phi-new}$	0.12
$MI_{\phi-ref}$	0.09
MI_{T-new}	0.11
MI_{T-ref}	0.19

not suitable to predict $\dot{m}_{cond}$ *a priori*, the linear regression lines depicted in Fig. 3.4 show interesting features. The coefficient of determination R^2 can be computed for the corresponding regressions as:

$$R^2 = 1 - \frac{\sum_{k=1}^{K=128}(\dot{m}_{\widehat{cond-pred,k}} - \dot{m}_{cond-pred,k})^2}{\sum_{k=1}^{K=128}(\dot{m}_{cond-pred,k} - \overline{\dot{m}_{cond-pred}})^2} \ . \tag{3.20}$$

Table 3.4 proves that linear regressions provide an excellent fit for the pairs $(\dot{m}_{cond-pred}, \dot{m}_{cond-obs})$, as suggested by Fig. 3.4. Therefore, a calibrated line could be used to predict *a posteriori* $\dot{m}_{cond}$ by calculating the corresponding MI and employing Eq. 3.18. Equation 3.18 also proves that $\dot{m}_{cond-obs}$ is strongly and positively correlated with the mixing indexes. In this way, reducing MI should entail a decrease in condensation, which will be confirmed by sections 3.3.2 and 3.3.5.

Table 3.4: Coefficient of determination (R^2) for linear regressions of condensation predicted using different mixing indexes.

Mixing index	R^2
$MI_{\phi-new}$	0.96
$MI_{\phi-ref}$	0.95
MI_{T-new}	0.90
MI_{T-ref}	0.87

3.3.2 Longitudinal evolution of mixing and condensation and effect of valves

In Section 3.3.1, it has been shown that condensation depends on psychrometric boundary conditions and mixing. In this section, a single working point is considered, seeking for factors that affect mixing (and hence condensation) regardless of the operating conditions. The point selected from the numerical campaign (see section 3.2.3) is the one depicted in the psychrometric diagram of Fig. 3.2.

Two elements are found to produce a significant impact on mixing and condensation: three-way junction geometry and mixing length. Concerning the former, it is important to remind that the objective of this chapter is to find universal design guidelines in a methodical and justified way, so optimization algorithms will not be employed just for the sake of providing the best geometry for this particular case. Section 3.3.5 will explore how to reduce mixing and condensation through the decrease of momentum ratio J, whereas in this section the effect of including junction valves is assessed.

In the scope of LP-EGR, at least one valve is required in the EGR line to obtain the desired EGR rate [106, 107]. If the obtained EGR rate is below the target even with the EGR valve wide open, there are several choices to increase it: a blower can be employed in the EGR line [108], an exhaust flap can be introduced to generate backpressure [109] or a valve can throttle the intake stream before the branch line [110]. The latter is often preferred by automotive manufacturers due to the lower cost [111], creating a compact two-valve junction [21, 20, 5]. An example of such a two-valve three-way junction (bottom part of Figure 3.6) is compared in this section against the standard case without valves (top part of Figure 3.6). The dual-valve geometry presents valves whose diameter agrees with the corresponding duct, which are opened 45° and located 1 corresponding diameter (main duct) and 2 corresponding diameters (branch duct) upstream the intersection of pipes.

In Figure 3.6 the line integral convolution (LIC) of velocity is combined with contours of turbulent viscosity ratio for both cases. In addition, tangential velocity vectors have been added to the representation. All these variables have been time-averaged.

In the standard, valveless case (top part of Fig. 3.6) the branch stream penetrates deeply in the main duct, forcing the inlet stream to surround it and

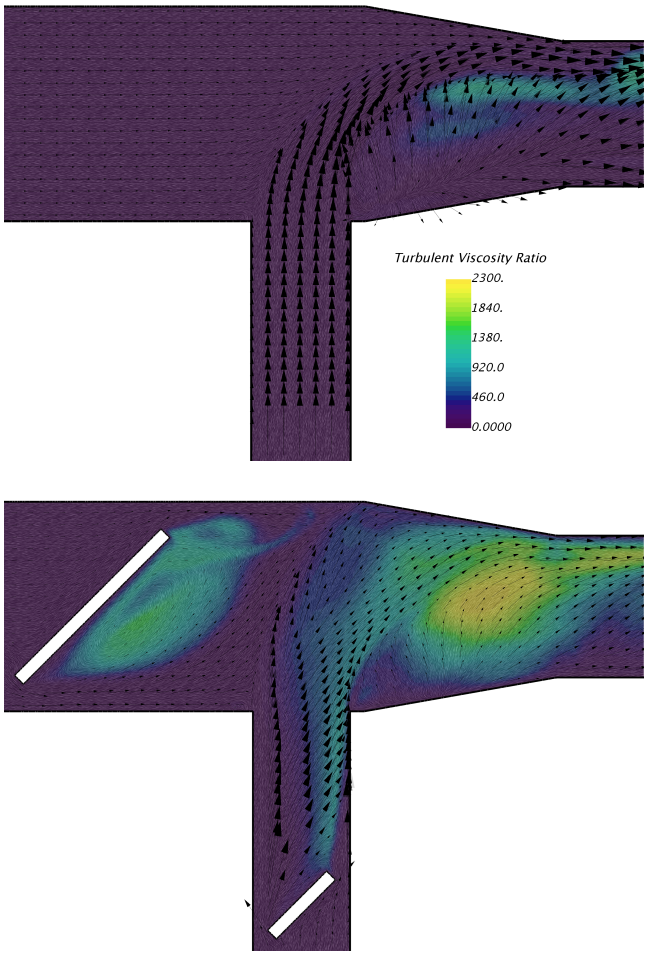

Figure 3.6: Time-averaged results of tangential velocity vectors superimposed over LIC of velocity combined with turbulent viscosity ration contours, for valveless case (top) and dual-valve junction (bottom).

fill the lower side of the cone, creating secondary flows that increase mixing in this region. When valves are implemented in the junction (bottom part of Fig. 3.6), both mechanisms of convective mixing are enhanced. Increase of turbulent viscosity ratio due to the valves as depicted in Fig. 3.6 results in a greater effective diffusion, whereas the secondary flows created due to detachment at the valves promote an increase of vorticity (not shown here)

which boosts the advective mixing.

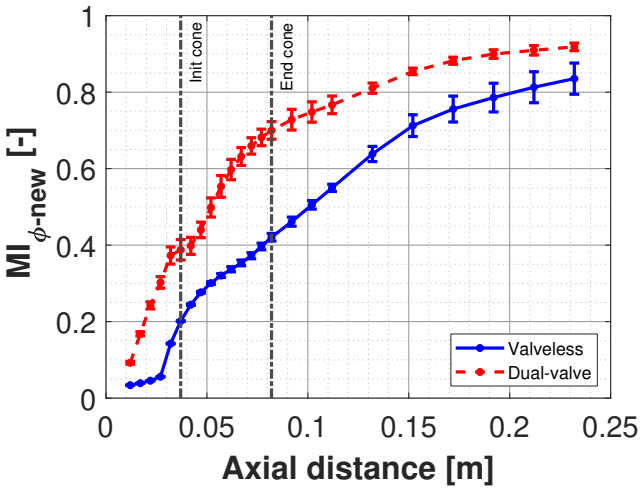

Figure 3.7: Longitudinal evolution of time-averaged $MI_{\phi-new}$ along the main duct for the valveless and dual-valve junctions, with vertical bars representing one standard deviation regarding transient fluctuations.

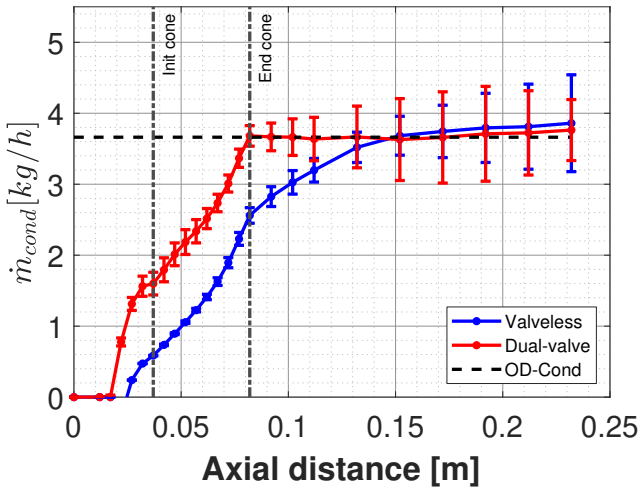

Figure 3.8: Longitudinal evolution of time-averaged condensation mass flow rate along the main duct for the valveless and dual-valve junctions, with vertical bars representing one standard deviation regarding transient fluctuations and $\dot{m}_{cond-0D}$ being indicated by a horizontal dashed line.

Figure 3.7 plots the longitudinal evolution of $MI_{\phi-new}$ (defined in Eq. 3.11) along the main duct for the valveless and dual-valve junctions. The evolution is obtained by sampling the main duct with a set of cross-sections and then conducting the area and time average of $MI_{\phi-new}$ for each surface.

Figure 3.7 starts in the ducts intersection and shows a monotonously increasing mixing index for both cases. As described in Section 3.2.2.1, distance between the end of the cone and the outlet boundary is 5 diameters, so these cases would require a greater length to further develop the mixing and eventually reach homogeneous flow ($MI_{\phi-new} = 1$). In any case, dual-valve junction $MI_{\phi-new}$ is greater than the corresponding value of the valveless case at the same location. Therefore, the change of flow features shown in Fig. 3.6 indeed improve mixing according to Fig. 3.7.

Figure 3.8 compares the axial evolution of generated condensation for the same junction geometry with and without valves. Again, condensation mass flow rate through each cross-section is averaged over time.

Figure 3.8 presents a similar behavior for condensation than the one observed for $MI_{\phi-new}$ (depicted in Fig. 3.7), which proves again the connection between mixing and condensation. In this case, Fig.3.8 shows that condensation grows with increasing distance to the pipe intersection and the dual-valve junction provides more condensation than the valveless geometry. The unsteady oscillations in condensation mass flow rate represented by the vertical bars of Fig. 3.8 start being noticeable before the cone inlet for the dual-valve geometry whereas, for the valveless junction, these fluctuations are not significant until the last section of the tapered duct. The different behavior is in agreement with the features of vorticity and turbulent viscosity ratio already described for Fig. 3.6, with the branch jet creating flow disturbances even at the beginning of the cone region. The interface streams in three-way junctions is known to present transient oscillations and eddies that enhance mixing [112], and this phenomenon requires a different length to develop depending on the flow pattern.

The main difference between mixing and condensation longitudinal evolution is that the asymptotic trend to the theoretical upper bound of condensation ($\dot{m}_{cond-0D}$ as calculated by the 0D perfect mixing model described in Section 3.2.1) is achieved sooner in Fig.3.8 than the value of 1 (perfect mixing) in Fig. 3.7. This can be explained by the underprediction of condensation mass flow rate of Eq. 3.18 discussed in Section 3.3.1.

3.3.3 Mixing flow patterns

Sections 3.3.1 and 3.3.2 have proved that there is a strong correlation between condensation and mixing. This section performs a qualitative analysis of the mixing flow patterns and compares at these situations the scalar fields that can be employed to evaluate mixing (temperature and passive scalar ϕ) and the mass fraction of condensed water Y_{H_2O-liq}.

This chapter follows the classification conducted by Kamide et al. [24] and Kimura et al. [25], which identified 3 types of flow patterns: wall-jet, deflecting-jet and impinging-jet. According to Kamide et al. and Kimura et al., these flow modes are determined by the ratio of branch and main stream momentum, which can be evaluated with the parameter J defined in Eq. 3.8. Table 3.5 shows the values of momentum ratio J in the different studies conducted in this chapter, compared to other works existing in the literature.

Table 3.5: Literature review of assessed range of values for momentum ratio J.

Work (Sections)	Scope	Fluid	A_m/A_b	α [°]	J [-]
Current work (3.3.1, 3.3.4)	EGR	Gas	5	0	0.3–14
Current work (3.3.5)	EGR	Gas	5	0–60	5.7–11.4
Current work (3.3.5)	EGR	Gas	5–1.25	0	0.7–11.4
Galindo et al. [2]	EGR	Gas	2.6	0	3.9
Reihani et al. [33]	EGR	Gas	11.2	0	0.2–7
Galindo et al. [45]	EGR	Gas	5	35	0.1–1.1
Hirota et al. [113]	Cooling	Gas	2	0	0.2–3.4
Kimura et al. [25]	Nuclear	Water	9	0	0.5–19
Bo Su et al. [114]	Nuclear	Water	10.2	0	20.4
Evrim et al. [39]	Nuclear	Water	3.4	0	0.01

Kamide et al. [24] employed main-to-branch momentum ratio M_R to establish the boundaries between flow modes. By virtue of Eq. 3.21

$$J = \frac{4 \cdot D_m}{\pi \cdot D_b} \cdot \frac{1}{M_R} \ , \tag{3.21}$$

the thresholds of Kamide et al. [24] can be translated in terms of J. In

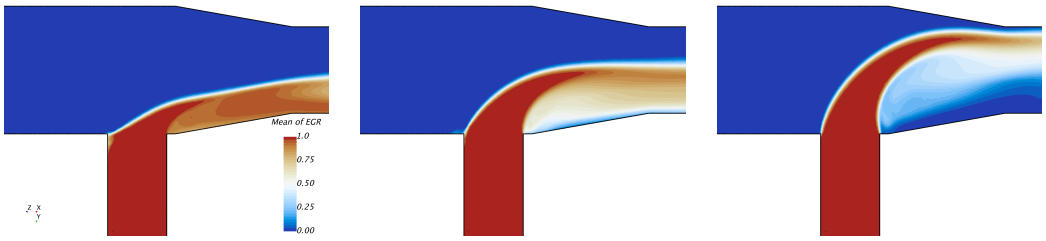

Figure 3.9: Time-averaged contours of passive scalar for wall-jet mode (left), deflecting-jet (middle) and impinging-jet (right).

this way, $J < 2.037$ should present a wall-jet pattern, $J > 7.857$ is expected to feature an impinging jet and intermediate values of $2.037 < J < 7.857$ should behave as a deflected jet. Therefore, the numerical campaign conducted in this chapter spans over a wide range of momentum ratio J that include the flow modes of Kamide et al. [24], as indicated by Table 3.5.

To perform a fair comparison between flow patterns, 3 working points are studied in this section in which all the boundary conditions of Table 3.2 will be constant except for the EGR rate, which will subsequently determine the branch mass flow rate (see Eq. 3.6) as well as momentum ratio J (see Eq. 3.9). The exact values of EGR_{rate} and J for the working points representing the different flow patterns are included in Table 3.6.

Table 3.6: EGR_{rate} and J for the selected representatives of the flow patterns.

Jet pattern	Wall	Deflecting	Impinging
EGR_{rate}	0.1	0.25	0.4
J	1.27	2.86	11.42

Figure 3.9 depicts contours of passive scalar ϕ for the 3 working points aforementioned at the longitudinal plane of Fig. 3.1. Besides, Fig. 3.10 shows contours of mass fraction of condensed water Y_{H_2O-liq} (top row), passive scalar ϕ (middle row) and temperature (bottom row) for the same working points at the postprocessing cross-section displayed in Fig. 3.1. All these scalar fields have been time-averaged.

The analyzed flow patterns present significant differences. First, the wall-jet mode (on the left part of Fig. 3.9) presents a branch stream which does not

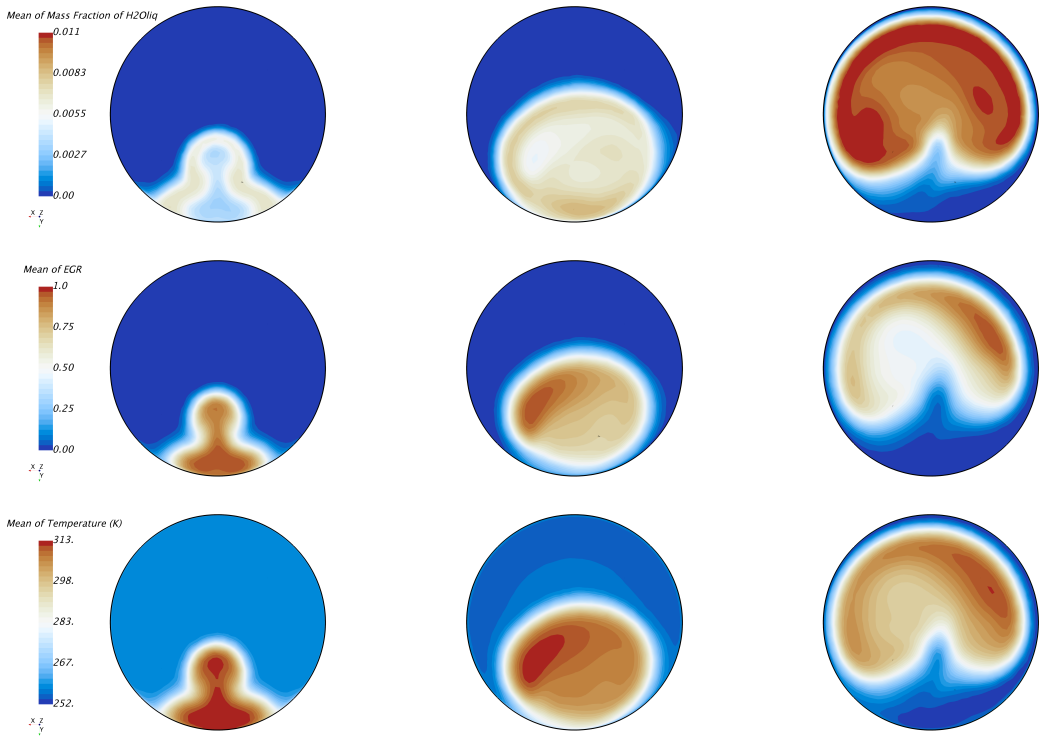

Figure 3.10: Time-averaged results of Y_{H_2O-liq} (top row), passive scalar (middle row) and temperature (bottom row) contours at postprocessing section (Figure 3.1), for wall-jet flow mode (left column), deflecting-jet (middle column) and impinging-jet (right column).

have enough momentum to penetrate in the main stream, so that it is attached to the lower wall (see middle left part of Fig. 3.10). In this case, condensation is produced essentially at the interface between both streams (see top left part of Fig. 3.10), where temperature can get below dew conditions (see bottom left part of Fig. 3.10) and diffusive mixing should take place. To prove the latter, the time-averaged magnitude of the gradient of passive scalar ϕ, $||\nabla\bar{\phi}(t)||$, is compared against the condensed water in Fig. 3.11, showing the qualitative resemblance between these variables.

When the branch stream grows in momentum, it is able to enter into the main duct. For the deflecting-jet mode depicted on the middle of Fig. 3.9, the branch stream is not able to reach the top wall, being deflected by the inlet

stream midway. In this case, the branch stream greater inertia prevents it from turning sharply into the lower wall, thus creating a flow detachment and a subsequent region of lower pressure. A fraction of the inlet stream is then encouraged to take this place by surrounding the branch stream. Now, the core of the branch stream is shifted upwards (see central element of Fig. 3.10) and is more diluted with the inlet stream, extending the locus of temperature below dew conditions (bottom middle part of Fig. 3.10) and thus expanding the region at which condensation appears (see top middle part of Fig. 3.10).

Finally, the branch stream may be fast enough to get close or hit the upper wall, which is known as impinging-jet pattern (right part of Fig. 3.9). The inlet stream is more prone to encircle the branch jet, so the regions for the inlet and branch streams are switched (see right middle part of Fig. 3.10). The enhanced mixing mechanisms promoted by the secondary flows due to impinging-jet pattern increases not only the extension of the condensing region but also its intensity (see top right part of Fig. 3.10), therefore boosting condensation.

3.3.4 Impact of momentum ratio (J) on mixing

Section 3.3.1 proposed a regression for condensation on the basis of psychrometry and mixing, through Eq. 3.18. Indeed, the comprehensive numerical campaign designed in Section 3.2.3 shifts all the factors considered in table 3.2 when moving across the different working points, which entails changes in both psychrometric conditions and mixing mechanisms. To provide a mean-

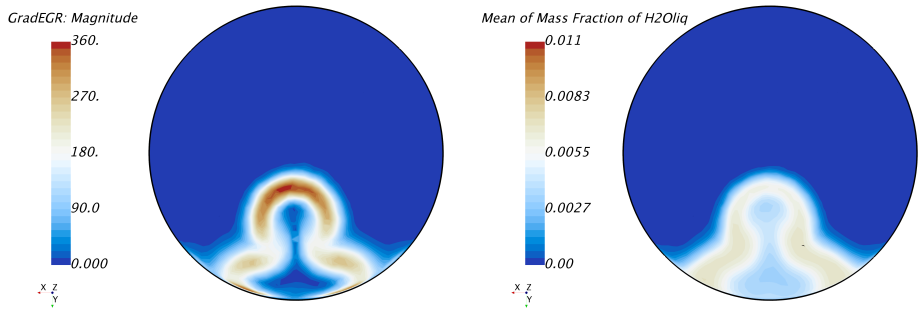

Figure 3.11: Time-averaged contours of $||\nabla\bar{\phi}(t)||$ (left) and Y_{H_2O-liq} (right) at postprocessing section (Figure 3.1), for wall-jet flow mode.

ingful analysis useful for junction designers, it makes sense to consider that the psychrometric conditions cannot be modified. In the spirit of Eq. 3.18, this would imply that $\dot{m}_{cond-0D}$ is a given value, and a minimization of $\dot{m}_{cond}$ can only be obtained by means of decreasing the mixing index MI. In accordance with Section 3.2.1, it can be estimated how modifying the factors involved in $\dot{m}_{cond-0D}$ ($\dot{m}_m$, EGR_{rate}, T_m, T_b, RH_m, w_b and P_{outlet}) result in a change in condensation, through psychrometry. However, the absence of an analytical model for mixing (which should be based on the information of table 3.2 and the junction geometry) makes it more challenging to determine the impact of these features on mixing, although Section 3.3.2 has already provided some guidelines to reduce mixing and condensation by considering a single operating condition. To understand the influence of the change in working point on mixing, condensation is omitted in this section and the analysis is focused only on MI, seeking the key parameter related to the boundary conditions that determines how well mixed are both streams at the target cross-section. In light of the mixing flow patterns described in Section 3.3.3, this section is devoted to the quantification of the correlation between mixing indexes MI and momentum ratio J.

The same 128 simulations considered in Section 3.3.1 are now employed to perform a linear regression between the mixing indexes defined in Section 3.2.5 and the branch-to-main momentum ratio J (Eq. 3.8). The R^2 coefficients (see Eq. 3.20) for these regressions are presented in Table 3.7:

Table 3.7: Coefficient of determination (R^2) for linear regressions of mixing indexes vs momentum ratio J

Mixing index	R^2
$MI_{\phi-new}$	0.97
$MI_{\phi-ref}$	0.67
MI_{T-new}	0.89
MI_{T-ref}	0.67

Table 3.7 shows that mixing can be quantified to a high degree just by considering momentum ratio J for the new mixing indexes proposed in this chapter. However, the linear regression for the reference indexes is much weaker. To gain more insight into the impact of momentum ratio on mixing, Fig. 3.12 presents a scatter plot considering $MI_{\phi-new}$ (Eq. 3.11) and $MI_{\phi-ref}$ (Eq. 3.10) against J for the 128 simulations.

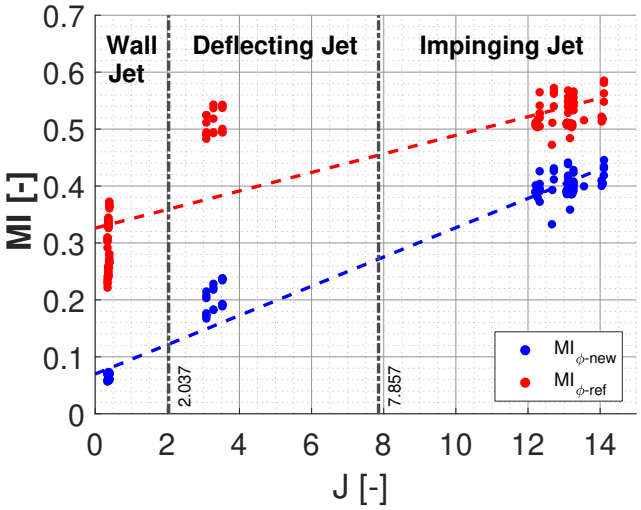

Figure 3.12: Scatter plot of mixing indexes at postprocessing section (Fig. 3.1) versus momentum ratio J for the 128 simulations of the numerical campaign, with linear regressions and regions of different flow patterns.

Figure 3.12 shows that the numerical campaign presents J values grouped around 0.35, 3.5 and 13; which are determined essentially by the EGR rates of Table 3.2. Figure 3.12 also includes the thresholds calculated with Eq. 3.21, confirming that all 3 flow patterns are represented within the numerical campaign. Figure 3.12 displays greater values of $MI_{\phi-ref}$ compared to $MI_{\phi-new}$ for all momentum ratios J. Considering Eq. 3.18, a greater value of MI provides a higher value of $\dot{m}_{cond-pred}$, which will improve the agreement with $\dot{m}_{cond-obs}$ considering the underprediction found for all types of MI in Figs. 3.4 and 3.5. Therefore, the greater values of $MI_{\phi-ref}$ against $MI_{\phi-new}$ result in the lower MAE of the former technique (see Table 3.3). In any case, both trend lines depicted in Fig. 3.12 show an increase of mixing with J as suggested by Section 3.3.3, but there is an important difference of performance between mixing indexes.

Table 3.7 presented a much better goodness of fit between J and $MI_{\phi-new}$ ($R^2 = 0.97$) than the one existing between J and $MI_{\phi-ref}$ ($R^2 = 0.67$). This is confirmed by Fig. 3.12, in which the values of $MI_{\phi-new}$ do not depart significantly from their regression line. $MI_{\phi-ref}$ instead provides similar values for deflecting and impinging jet situations, whereas cases with wall jet pattern present lower $MI_{\phi-ref}$ values but with a great dispersion. This may

seem contradictory to the high $R^2 = 0.95$ (see Table 3.4) found for the linear regression of $MI_{\phi-ref} \cdot \dot{m}_{cond-0D}$. However, the close up of Fig. 3.4 reveals points with huge dispersion at $\dot{m}_{cond}$ close to zero and overpredicted points at $\dot{m}_{cond} \simeq 0.1 kg/s$. The poor performance of $MI_{\phi-ref}$ displayed in Fig. 3.12 does not affect though the impinging jet working points, which present highest J. These cases are obtained with greatest EGR_{rate} (see Eq. 3.9) and $\dot{m}_b$ (see Eq. 3.6), so provide more condensation, as the branch stream is the one with high humidity.

3.3.5 Reducing mixing and condensation by decreasing momentum ratio

Section 3.3.4 has shown that there is a positive correlation between mixing and J, whereas section 3.3.1 proved that greater condensation occurs for higher values of MI. Therefore, this section is devoted to the reduction of mixing and condensation by lowering momentum ratio J.

Assuming perfect gas behavior and neglecting the difference in pressure drop between junction legs[2] and the impact of humidity on density, Eq. 3.9 is simplified as

$$J = \frac{EGR_{rate}{}^2 \cdot T_b \cdot A_m^2}{(1 - EGR_{rate})^2 \cdot T_m \cdot A_b^2} \cdot cos(\alpha) \ , \tag{3.22}$$

which depends on boundary conditions of Table 3.2 and junction design parameters (A_m, A_b, α). Therefore, for a given working point, Eq. 3.22 implies that J can be reduced by lowering A_m or increasing A_b and α (see Fig. 3.1). In this section, the main duct area (A_m) is not modified, as reducing it may contravene other design constraints in terms of pressure drop.

A baseline case with the same A_b and $\alpha = 0°$ as the original junction depicted in Fig. 3.1 is considered. The selected operating conditions correspond to the impinging-jet mode of section 3.3.3, so that there is room to obtain lower values of J. This is the same point shown in the psychrometric chart of Fig. 3.2 and also employed in section 3.3.2. The axis of the branch duct is moved upstream 0.5 diameters, to allow the possibility of implementing

[2] $\frac{p_m}{p_b}$ is comprised between 1 and 1.02 for the whole numerical campaign.

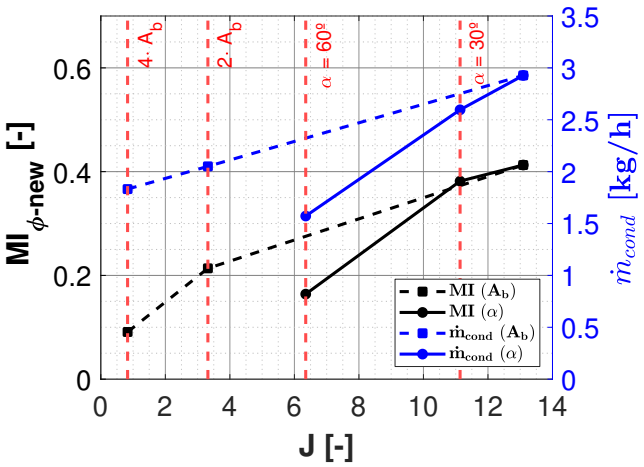

Figure 3.13: Time-averaged results of $MI_{\phi-new}$ and $\dot{m}_{cond}$ at postprocessing section (Fig. 3.1) versus momentum ratio J, when modifying branch duct area A_b and angle α.

the upcoming geometrical modifications. The impact of varying either the area of the branch (A_b) or the branch insertion angle (α) on J, $MI_{\phi-new}$ and condensation is assessed with the following 4 additional cases:

- 2 cases with $2 \cdot A_b$ and $4 \cdot A_b$.
- 2 cases with $\alpha = 30°$ and $\alpha = 60°$

Figure 3.13 presents the results at the postprocessing section (see Fig. 3.1) for the aforementioned cases in terms of $MI_{\phi-new}$ (left vertical axis) and generated condensation $\dot{m}_{cond}$ (right vertical axis). In these parametric analyses the variable not assessed is kept at its default value (A_b or $\alpha = 60°$), so the red labels of Fig. 3.13 indicate only the modified parameter. Figure 3.13 confirms that increasing branch duct area A_b and angle α reduces J and, in turn, condensation and mixing. The considered working point presents an impinging jet mode with the baseline geometry. With the proposed modifications in A_b and α, the same working point could exhibit a deflected jet or even a wall jet pattern, correspondingly.

Figure 3.13 shows that the sensitivity of $\dot{m}_{cond}$ and $MI_{\phi-new}$ to J is greater when increasing than α when enlarging A_b. To provide some insight into this

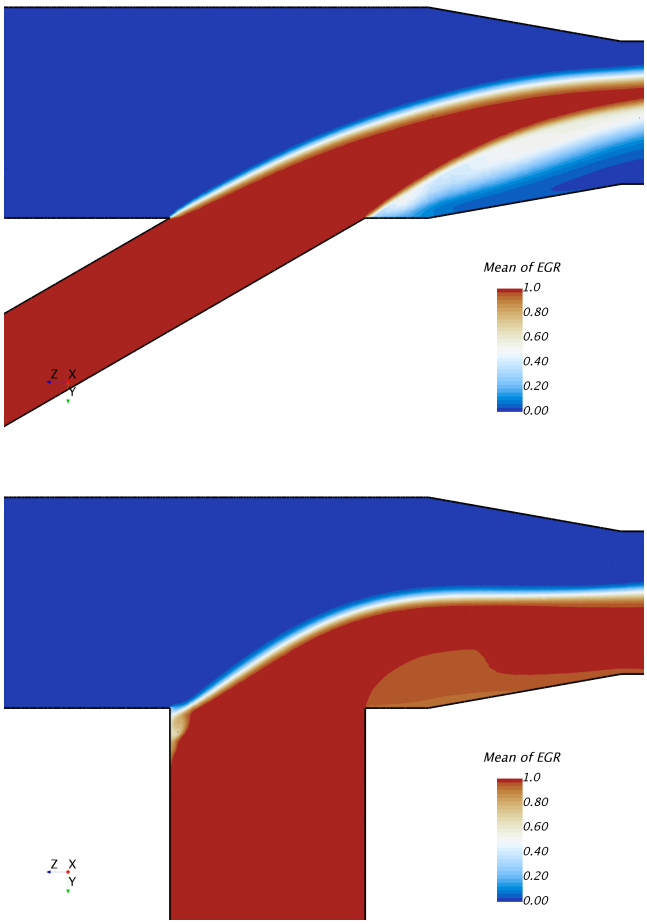

Figure 3.14: Time-averaged contours of passive scalar at longitudinal postprocessing section (Figure 3.1), for cases with $\alpha = 60°$ (top) and $4 \cdot A_b$ (bottom).

characteristic, contours of ϕ are depicted in Fig. 3.14 for junction simulations featuring $\alpha = 60°$ and $4 \cdot A_b$. These two cases present similar values for condensation and mixing according to Fig. 3.13, despite their great difference in terms of J. Indeed, top part of Fig. 3.14 shows that the junction with $\alpha = 60°$ behaves as a deflecting jet, whereas bottom part of Fig. 3.14 displays a wall jet pattern for the case with $4 \cdot A_b$. However, the flow field of the junction with $\alpha = 60°$ differs from the deflecting jet shown in middle part of Fig. 3.9. In

the latter, the branch leg is perpendicular to the inlet and outlet ducts. The stream injected by the branch at middle of Fig. 3.9 is therefore dragged by the inlet flow, creating a wake downstream the jet that enhances mixing. Instead, the junction with $\alpha = 60°$ discharges the branch stream with momentum in direction of the outlet duct, so the wake region and the subsequent boost in mixing is greatly reduced (see top part of Fig. 3.14). Besides, the lower branch cross section compared to the case $4 \cdot A_b$ provides a higher velocity for the jet, which entails a lower residence time for the branch stream to mix with the inlet one.

3.4 Concluding remarks

In this chapter, a fractional factorial design of a numerical campaign consisting of 128 RANS/URANS simulation of two humid streams merging in a T-junction has been conducted. These simulations have been employed to analyze the correlation between flow mixing and volume condensation. To do so, a method to define new mixing indexes through the calculation of the unmixed area has been developed. In this chapter, the mixing indexes have been computed on the basis of a passive scalar and temperature, considering a linear weighting to determine the fraction of unmixed area provided by each grid element. Table 3.8 shows the computational effort of the simulation campaign conducted in a Intel Xeon E5-2630v3 (2.4GHz) processor for this chapter.

Table 3.8: Computational cost of chapter 3

Cases	134
Mesh size (millions)	3
Number of cores	16
Hours/case	33.33
Sum of kh*core	71.46

Condensation mass flow rate has been found to correlate linearly with high coefficients of determination for all mixing indexes, when psychrometric conditions are taken into account throughout a 0D perfect mixing model. For a given working point, the psychrometric conditions are fixed, so the junction designers should focus on reducing mixing if a decrease of bulk condensation is sought. The usage of a passive scalar will allow simulation engineers to optimize junction geometries in terms of mixing and condensation without

requiring to consider an in-flow condensation submodel, such as the one employed in this chapter. Likewise, a humid flow test bench is not needed to assess the behavior of a junction in terms of potential condensation generation, as temperature measurements will suffice. However, both numerical and experimental researchers cannot circumvent these elements (condensation submodel or humid test bench, respectively) if the quantification of the condensation mass flow rate is required. The correlation proposed consistently underpredicts condensation and can be used as a surrogate model only after being calibrated. Conducting similar numerical campaigns with additional junction geometries could be useful to determine whether other weightings for the new mixing indexes provide better *a priori* agreement to predict condensation mass flow rate than the linear weighting employed in this chapter.

This chapter also provides a set of universal guidelines to design junctions with reduced volume condensation, as they have shown to achieve this through the decrease of flow mixing. In this way, valves employed to adjust operating conditions should be placed in other elements or as far as possible from the intersection of ducts. This intersection in turn should be located as close as possible from the target location at which condensation should be minimized. Besides, the branch-to-main momentum ratio J has been found to be a key factor governing the flow patterns and therefore the mixing of inlet streams. Designing a branch leg aligned towards the outlet duct with a diameter as large as possible is likely to provide a wall-jet mode that greatly reduces mixing and condensation. If junction geometry is optimized and impinging-jet flow patterns are avoided in favor of wall-jet and deflecting-jet modes, the new mixing indexes have been found to perform better than the ones considered as references by the literature.

Chapter 3 Bibliography

[2] Galindo, J. and Serrano, J.R. and Navarro, R. and García Olivas, G. "Numerical modeling of centrifugal compressors with heterogeneous incoming flow due to low pressure exhaust gas recirculation." In: *Proceedings of ASME Turbo Expo 2020: Turbomachinery Technical Conference and Exposition*. GT2020-16030. American Society of Mechanical Engineers. 2020. DOI: 10.1115/gt2020-16030 (cit. on pp. ix, 58, 77).

[3] J. Galindo, H. Climent, R. Navarro, and G. García-Olivas. "Assessment of the numerical and experimental methodology to predict EGR

cylinder-to-cylinder dispersion and pollutant emissions." *International Journal of Engine Research* 22(10) (2021), pp. 3128–3146. DOI: 10.1177/1468087420972544 (cit. on pp. ix, 53).

[5] J. Galindo, R. Navarro, D. Tarí, and G. García-Olivas. "Centrifugal compressor influence on condensation due to Long Route-Exhaust Gas Recirculation mixing." *Applied Thermal Engineering* 144 (2018), pp. 901 –909. ISSN: 1359-4311. DOI: 10.1016/j.applthermaleng.2018.09.005 (cit. on pp. x, 4, 22, 24, 25, 27, 28, 41, 42, 53, 54, 58, 61, 73, 124).

[12] J. M. Desantes, J. M. Luján, B. Pla, and J. A. Soler. "On the combination of high-pressure and low-pressure exhaust gas recirculation loops for improved fuel economy and reduced emissions in high-speed direct-injection engines." *International Journal of Engine Research* 14(1) (2013), pp. 3–11. DOI: 10.1177/1468087412437623 (cit. on pp. 3, 4, 22, 54, 99, 102).

[15] Y. Park and C. Bae. "Experimental study on the effects of high/low pressure EGR proportion in a passenger car diesel engine." *Applied energy* 133 (2014), pp. 308–316. DOI: 10.1016/j.apenergy.2014.08.003 (cit. on pp. 4, 54).

[20] J. Galindo, P. Piqueras, R. Navarro, D. Tarí, and C. Meano. "Validation and sensitivity analysis of an in-flow water condensation model for 3D-CFD simulations of humid air streams mixing." *International Journal of Thermal Sciences* 136 (2019), pp. 410 –419. ISSN: 1290-0729. DOI: 10.1016/j.ijthermalsci.2018.10.043 (cit. on pp. 4, 22, 28, 54, 58, 59, 61–63, 73).

[21] J. Serrano, P. Piqueras, R. Navarro, D. Tarí, and C. Meano. "Development and verification of an in-flow water condensation model for 3D-CFD simulations of humid air streams mixing." *Computers & Fluids* 167 (2018), pp. 158 –165. ISSN: 0045-7930. DOI: 10.1016/j.compfluid.2018.02.032 (cit. on pp. 4, 7, 54, 61, 62, 73).

[22] S Karstadt, J Werner, S Münz, and R Aymanns. "Effect of water droplets caused by low pressure EGR on spinning compressor wheels." In: *Aufladetechnische Konferenz, Dresden*. 2014 (cit. on pp. 4, 7, 22, 54).

[23] J. Kickhofel, V. Valori, and H.-M. Prasser. "Turbulent penetration in T-junction branch lines with leakage flow." *Nuclear Engineering and Design* 276 (2014), pp. 43–53. DOI: 10.1016/j.nucengdes.2014.05.002 (cit. on pp. 5, 53).

[24] H Kamide, M Igarashi, S Kawashima, N Kimura, and K Hayashi. "Study on mixing behavior in a tee piping and numerical analyses for evaluation of thermal striping." *Nuclear Engineering and Design* 239(1) (2009), pp. 58–67. DOI: 10.1016/j.nucengdes.2008.09.005 (cit. on pp. 5, 6, 53, 64, 77, 78).

[25] N. Kimura, H. Ogawa, and H. Kamide. "Experimental study on fluid mixing phenomena in T-pipe junction with upstream elbow." *Nuclear Engineering and Design* 240(10) (2010), pp. 3055–3066. DOI: 10.1016/j.nucengdes.2010.05.019 (cit. on pp. 5, 6, 53, 64, 77, 159).

[26] T. Lu, D. Attinger, and S. M. Liu. "Large-eddy simulations of velocity and temperature fluctuations in hot and cold fluids mixing in a tee junction with an upstream straicht or elbow main pipe." *Nuclear Engineering and Design* 263 (Apr. 2, 2013), pp. 32–41. DOI: 10.1016/j.nucengdes.2013.04.002 (cit. on pp. 5, 53).

[29] L. Yang, J. Wang, Y. Jiang, and L. Zou. "Oil-water flow splitting in eccentric annular T-junction tubes. Experimental and CFD analysis." *Chemical Engineering Science* 228 (2020), p. 116000. DOI: 10.1016/j.ces.2020.116000 (cit. on pp. 5, 53).

[30] K.-H. Brune, B. Stoffel, B. Matyschok, et al. "CFD-Analysis of the Flow Consisting of Two Mass Flows With Different Temperatures and/or Two Phases in a Turbocompressor." In: *ASME 2006 2nd Joint US-European Fluids Engineering Summer Meeting Collocated With the 14th International Conference on Nuclear Engineering*. American Society of Mechanical Engineers Digital Collection. 2006, pp. 701–711 (cit. on pp. 5, 22, 24, 27, 28, 36, 67, 68).

[33] A. Reihani, J. Hoard, S. Klinkert, C.-K. Kuan, D. Styles, and G. McConville. "Experimental response surface study of the effects of low-pressure exhaust gas recirculation mixing on turbocharger compressor performance." *Applied Energy* 261 (2020), p. 114349. DOI: 10.1016/j.apenergy.2019.114349 (cit. on pp. 6, 58, 77).

[34] S. M. Hosseini, K. Yuki, and H. Hashizume. "Classification of turbulent jets in a T-junction area with a 90-deg bend upstream." *International Journal of heat and mass transfer* 51(9-10) (2008), pp. 2444–2454. DOI: 10.1016/j.ijheatmasstransfer.2007.08.024 (cit. on pp. 6, 53).

[38] C. Evrim, X. Chu, and E. Laurien. "Analysis of thermal mixing characteristics in different t-junction configurations." *International Journal of Heat and Mass Transfer* 158 (2020), p. 120019. DOI: 10.1016/j.ijheatmasstransfer.2020.120019 (cit. on pp. 6, 53).

[39] C. Evrim and E. Laurien. "Numerical study of thermal mixing mechanisms in t-junctions." *Applied Thermal Engineering* 183 (2021), p. 116155. DOI: 10.1016/j.applthermaleng.2020.116155 (cit. on pp. 6, 53, 77).

[40] A. Gupta, M. S. Ibrahim, and R. Amano. "Effect of jet-to-mainstream momentum flux ratio on mixing process." *Heat and Mass Transfer* 52(3) (2016), pp. 621–634. DOI: 10.1007/s00231-015-1582-7 (cit. on pp. 6, 53).

[41] J. R. Serrano, P. Piqueras, E. Angiolini, C. Meano, and J. De La Morena. "On Cooler and Mixing Condensation Phenomena in the Long-Route Exhaust Gas Recirculation Line." In: *SAE Technical Paper*. 2015. DOI: 10.4271/2015-24-2521 (cit. on pp. 7, 9, 53–55, 57, 58).

[42] A. García, J. Monsalve-Serrano, R. L. Sari, and P. Gaillard. "Assessment of a complete truck operating under dual-mode dual-fuel combustion in real life applications: Performance and emissions analysis." *Applied Energy* 279 (2020), p. 115729. DOI: 10.1016/j.apenergy.2020.115729 (cit. on pp. 7, 54).

[43] P. Olmeda, J. Martín, F. Arnau, and S. Artham. "Analysis of the energy balance during World harmonized Light vehicles Test Cycle in warmed and cold conditions using a Virtual Engine." *International Journal of Engine Research* - (Oct. 3, 2019), pp. 0–18. DOI: 10.1177/1468087419878593 (cit. on pp. 7, 54).

[44] J. Galindo, R. Navarro, D. Tari, and F. Moya. "Development of an experimental test bench and a psychrometric model for assessing condensation on a Low Pressure EGR cooler." *International Journal of Engine Research* 22 (5 2020), pp. 1540–1550. DOI: 10.1177/1468087420909735 (cit. on pp. 7, 54, 111).

[45] J. Galindo, R. Navarro, D. Tari, and F. Moya. "Analysis of condensation and secondary flows at T-junctions using optical visualization techniques and Computational Fluid Dynamics." *International Journal of Multiphase Flow* (2021). DOI: 10.1016/j.ijmultiphaseflow.2021.103674 (cit. on pp. 7, 54, 59, 61–63, 77).

[46] J. Galindo, R. Navarro, D. Tarí, and F. Moya. "Quantitative validation of an in-flow water condensation model for 3D-CFD simulations of three-way junctions using indirect condensation measurements." *International Journal of Thermal Sciences* 172 (2022), pp. 1–17. DOI: 10.1016/j.ijthermalsci.2021.107303 (cit. on pp. 7, 54, 62, 63).

[53] A. Sakowitz, M. Mihaescu, and L. Fuchs. "Turbulent flow mechanisms in mixing T-junctions by Large Eddy Simulations." *International Journal of Heat and Fluid Flow* 45 (2014), pp. 135–146. DOI: 10.1016/j.ijheatfluidflow.2013.06.014 (cit. on pp. 7, 58, 65, 67, 100, 110).

[64] *STAR-CCM+*. Release version 12.06.010. CD-adapco. 2018. URL: http://ww.cd-adapco.com (cit. on pp. 9, 26, 30, 34, 42, 59, 61, 100, 107, 112, 114, 119, 170, 190).

[69] J. M. Luján, C. Guardiola, B. Pla, and A. Reig. "Switching strategy between HP (high pressure)-and LPEGR (low pressure exhaust gas recirculation) systems for reduced fuel consumption and emissions." *Energy* 90 (2015), pp. 1790–1798. DOI: 10.1016/j.energy.2015.06.138 (cit. on pp. 10, 22, 54, 102).

[70] V. T. Vithala, J. Hoard, D. Assanis, and D. Styles. "3-D Numerical Study of Turbulent Mixing of Intake Air and Exhaust Gas in a Low Pressure EGR System." In: *ASME 2011 Internal Combustion Engine Division Fall Technical Conference*. American Society of Mechanical Engineers Digital Collection. 2011, pp. 893–904 (cit. on pp. 22, 24, 27, 36, 41, 58).

[76] X. Li and S. Wang. "Flow field and pressure loss analysis of junction and its structure optimization of aircraft hydraulic pipe system." *Chinese Journal of Aeronautics* 26(4) (2013), pp. 1080–1092. DOI: 10.1016/j.cja.2013.04.004 (cit. on p. 53).

[77] M. Zhou, R. Kulenovic, and E. Laurien. "T-junction experiments to investigate thermal-mixing pipe flow with combined measurement techniques." *Applied Thermal Engineering* 150 (Mar. 5, 2019), pp. 237–249. DOI: 10.1016/j.applthermaleng.2018.12.161 (cit. on p. 53).

[78] A. Kuczaj, E. Komen, and M. Loginov. "Large-Eddy Simulation study of turbulent mixing in a T-junction." *Nuclear Engineering and Design* 240(9) (2010). Experiments and CFD Code Applications to Nuclear Reactor Safety (XCFD4NRS), pp. 2116 –2122. ISSN: 0029-5493. DOI: 10.1016/j.nucengdes.2009.11.027 (cit. on pp. 53, 67).

[79] I. Basler, H. Reister, R. Rossmann, and B. Weigand. "A Simulation Method for the Calculation of Water Condensation inside Charge Air Coolers" (2021). DOI: 10.4271/2021-01-0226 (cit. on p. 53).

[80] R. Cash, A. Talekar, and B. AbdulNour. "A CFD Study of Water Condensation Inside the Tubes of an Automotive Compact Charge Air Cooler Using Large Eddy Simulation Approach." In: *ASME International Mechanical Engineering Congress and Exposition*. Vol. 50626. American Society of Mechanical Engineers. 2016, V008T10A068. DOI: 10.1115/imece2016-66999 (cit. on p. 53).

[81] K. R. Jensen, P. Fojan, R. L. Jensen, and L. Gurevich. "Water condensation: A multiscale phenomenon." *Journal of nanoscience and nanotechnology* 14(2) (2014), pp. 1859–1871. DOI: 10.1166/jnn.2014.9108 (cit. on p. 53).

[82] Q. Sheng, J. Sun, Q. Wang, W. Wang, and H. S. Wang. "On the onset of surface condensation: formation and transition mechanisms of condensation mode." *Scientific reports* 6(1) (2016), pp. 1–9. DOI: 10.1038/srep30764 (cit. on p. 53).

[83] N. Kortsenshtein, E. Samuilov, and A. Yastrebov. "New method of simulation of volume condensation of supersaturated vapor." *High Temperature* 47(1) (2009), pp. 83–94. DOI: 10.1134/s0018151x09010118 (cit. on p. 53).

[84] P. Vojkuvkova, O. Sikula, and J. Weyr. "Assessment of condensation of water vapor in the mixing chamber by CFD method." In: *EPJ Web of Conferences*. Vol. 92. 2015. DOI: 10.1051/epjconf/20159202112 (cit. on p. 53).

[85] M. Zheng, G. T. Reader, and J. G. Hawley. "Diesel engine exhaust gas recirculation—-a review on advanced and novel concepts." *Energy conversion and management* 45(6) (2004), pp. 883–900 (cit. on p. 54).

[86] M. Choi, K. Mohiuddin, N. Kim, and S. Park. "Investigation of the effects of EGR rate, injection strategy and nozzle specification on engine performances and emissions of a single cylinder heavy duty diesel engine using the two color method." *Applied Thermal Engineering* (2021), p. 117036. DOI: 10.1016/j.applthermaleng.2021.117036 (cit. on p. 54).

[87] N. Dimitrakopoulos, G. Belgiorno, M. Tunér, P. Tunestål, and G. Di Blasio. "Effect of EGR routing on efficiency and emissions of a PPC engine." *Applied Thermal Engineering* 152 (2019), pp. 742–750. DOI: 10.1016/j.applthermaleng.2019.02.108 (cit. on p. 54).

[88] X. Yu, N. S. Sandhu, Z. Yang, and M. Zheng. "Suitability of energy sources for automotive application–A review." *Applied Energy* 271 (2020), p. 115169. DOI: 10.1016/j.apenergy.2020.115169 (cit. on p. 54).

[89] H. Song and S. Song. "Numerical investigation on a dual loop EGR optimization of a light duty diesel engine based on water condensation analysis." *Applied Thermal Engineering* 182 (2021), pp. 1–12. DOI: 10.1016/j.applthermaleng.2020.116064 (cit. on p. 54).

[90] S. Schuster, D. Brillert, and F. Benra. "Condensation in Radial Turbines-Part I: Mathematical Modeling." *Journal of Turbomachinery* 140 (2018), pp. 1–9. DOI: 10.1115/1.4040934 (cit. on p. 60).

[91] S. Schuster, D. Brillert, and F. Benra. "Condensation in Radial Turbines-Part II: Application of the Mathematical Model to a Radial Turbine Series." *Journal of Turbomachinary* 140 (2018), pp. 1–7. DOI: 10.1115/1.4040935 (cit. on p. 60).

[92] T. Wittmann, C. Bode, and J. Friedrichs. "The Feasibility of an Euler-Lagrange Approach for the Modeling of Wet Steam." *Journal of Engineering for gas turbines and power* 143 (2021), pp. 1–8. DOI: 10.1115/1.4049859 (cit. on p. 60).

[93] F. R. Menter. "Two-equation eddy-viscosity turbulence models for engineering applications." *AIAA journal* 32(8) (1994), pp. 1598–1605. DOI: 10.2514/3.12149 (cit. on pp. 60, 111).

[94] S. Smith and M. Mungal. "Mixing, structure and scaling of the jet in crossflow." *Journal of fluid mechanics* 357 (1998), pp. 83–122. DOI: 10.1017/s0022112097007891 (cit. on p. 64).

[95] A. R. Karagozian. "The jet in crossflow." *Physics of Fluids* 26(10) (2014), pp. 1–47. DOI: 10.1063/1.4895900 (cit. on p. 64).

[96] W Vicente, M Salinas-Vazquez, C Chavez, and E Carrizosa. "Different numerical methods in the study of passive scalar transport in a pipeline x-junction." *Applied mathematical modelling* 33(3) (2009), pp. 1248–1258. DOI: 10.1016/j.apm.2008.01.022 (cit. on p. 65).

[97] L. Grbčić, L. Kranjčević, I. Lučin, and Z. Čarija. "Experimental and numerical investigation of mixing phenomena in double-Tee junctions." *Water* 11(6) (2019), p. 1198. DOI: 10.3390/w11061198 (cit. on p. 65).

[98] A Schlegel, M Streichsbier, R Mongia, and R Dibble. *A Comparison of the Influence of Fuel/Air Unmixedness on NOx Emissions in Lean Premixed, Non-Catalytic and Catalytically Stabilized Combustion.* Vol. 78699. American Society of Mechanical Engineers, 1997. DOI: 10.1115/97-gt-306 (cit. on p. 65).

[99] D Mira, O Lehmkuhl, P Stathopoulos, T Tanneberger, T. Reichel, C. Paschereit, M Vázquez, and G Houzeaux. "Numerical Investigation of a Lean Premixed Swirl-Stabilized Hydrogen Combustor and Operational Conditions Close to Flashback." In: *Turbo Expo: Power for Land, Sea, and Air*. Vol. 51067. American Society of Mechanical Engineers. 2018, V04BT04A009. DOI: 10.1115/gt2018-76229 (cit. on p. 65).

[100] S. Hossain, M. Ansari, and K.-Y. Kim. "Evaluation of the mixing performance of three passive micromixers." *Chemical Engineering Journal* 150(2-3) (2009), pp. 492–501. DOI: 10.1016/j.cej.2009.02.033 (cit. on p. 65).

[101] P. Danckwerts. "The definition and measurement of some characteristics of mixtures." *Applied Scientific Research, Section A* 3(4) (1952), pp. 279–296. DOI: 10.1016/b978-0-08-026250-5.50050-2 (cit. on p. 65).

[102] J. Andersen, F. Lindström, and F. Westin. "Surge definitions for radial compressors in automotive turbochargers." *SAE International Journal of Engines* 1(1) (2008), pp. 218–231. DOI: 10.4271/2008-01-0296 (cit. on p. 67).

[103] R. Dehner, N. Figurella, A. Selamet, P. Keller, M. Becker, K. Tallio, K. Miazgowicz, and R. Wade. "Instabilities at the Low-Flow Range of a Turbocharger Compressor." *SAE International Journal of Engines*

6(2) (2013), pp. 1356–1367. DOI: 10.4271/2013-01-1886 (cit. on p. 67).

[104] A. Torregrosa, A. Broatch, X. Margot, J. García-Tíscar, Y. Narvekar, and R. Cheung. "Local flow measurements in a turbocharger compressor inlet." *Experimental Thermal and Fluid Science* 88 (2017), pp. 542 – 553. ISSN: 0894-1777. DOI: 10.1016/j.expthermflusci.2017.07.007 (cit. on p. 67).

[105] B. Smith, J. Mahaffy, and K. Angele. "A CFD benchmarking exercise based on flow mixing in a T-junction." *Nuclear Engineering and Design* 264 (2013). SI:NURETH-14, pp. 80 –88. ISSN: 0029-5493. DOI: 10.1016/j.nucengdes.2013.02.030 (cit. on p. 67).

[106] P. Slavík, B. Skočilasová, J. Soukup, and F. Klimenda. "Low pressure EGR valve testing." In: *AIP Conference Proceedings*. Vol. 2118. 1. AIP Publishing LLC. 2019, p. 030040. DOI: 10.1063/1.5114768 (cit. on p. 73).

[107] F. Castillo, E. Witrant, V. Talon, and L. Dugard. "Simultaneous air fraction and low-pressure EGR mass flow rate estimation for diesel engines." *IFAC Proceedings Volumes* 46(2) (2013), pp. 731–736. DOI: 10.3182/20130204-3-fr-2033.00070 (cit. on p. 73).

[108] D. Wang, L. Shi, S. Zhu, B. Liu, Y. Qian, and K. Deng. "Numerical and thermodynamic study on effects of high and low pressure exhaust gas recirculation on turbocharged marine low-speed engine." *Applied Energy* 261 (2020), p. 114346. DOI: 10.1016/j.apenergy.2019.114346 (cit. on p. 73).

[109] G. Boccardo, F. Millo, A. Piano, L. Arnone, S. Manelli, and C. Capiluppi. *A Fully Physical Correlation for Low Pressure EGR Control Linearization*. Tech. rep. SAE Technical Paper, 2017. DOI: 10.4271/2017-24-0011 (cit. on p. 73).

[110] W. Wenzel, U Hanig, J Song, B Bareis, and M Miclea-Bleiziffer. "Inlet swirl throttle for passenger car engines." In: *16. Internationales Stuttgarter Symposium*. Springer. 2016, pp. 951–968. DOI: 10.1007/978-3-658-13255-2_71 (cit. on p. 73).

[111] U. Hanig and M. Becker. "Intake Throttle and Pre-swirl Device for Low-Pressure EGR Systems." *MTZ worldwide* 76(1) (2015), pp. 10–13. DOI: 10.1007/s38313-014-1004-0 (cit. on p. 73).

[112] M. Hirota, E. Mohri, H. Asano, and H. Goto. "Experimental study on turbulent mixing process in cross-flow type T-junction." In: *ICHMT DIGITAL LIBRARY ONLINE*. Begel House Inc. 2009 (cit. on p. 76).

[113] M. Hirota, H. Asano, H. Nakayama, T. Asano, and S. Hirayama. "Three-dimensional structure of turbulent flow in mixing T-junction." *JSME International Journal Series B Fluids and Thermal Engineering* 49(4) (2006), pp. 1070–1077. DOI: 10.1299/jsmeb.49.1070 (cit. on p. 77).

[114] B. Su, Z. Zhu, X. Wang, H. Ke, M. Lin, and Q. Wang. "Effect of temperature difference on the thermal mixing phenomenon in a T-junction under inflow pulsation." *Nuclear Engineering and Design* 363 (2020), p. 110611. DOI: 10.1016/j.nucengdes.2020.110611 (cit. on p. 77).

Chapter 4

Sensitivity of prediction of HP-EGR distribution and corresponding emissions to numerical configuration

Contents

4.1 Introduction

As was exposed in chapter 1, the Exhaust Gas Recirculation (EGR) has become one of the most developed strategies to abate emissions [11, 12]. With the reduction of maximum temperature in the combustion chamber, the formation of Nitrogen Oxides (NOx) are consequently decreased with little penalty in thermal efficiency [115] and particulate emissions, as long as the EGR rates are below a certain threshold [11]. The main characteristics of these techniques have been exposed in chapter 1.

Focusing on HP-EGR configuration, is still the most employed in ICEs due to its simplicity, the faster engine response [16] and the reduction in the pumping losses [12]. As exposed in chapter 1, the challenge of this approach is achieving a homogeneous distribution of the exhaust gases in all the cylinders of the engine [17]. If the EGR distribution between the cylinders is very different, the amount of NOx and particulate matter (PM) will increase, as was demonstrated by Maiboom et al. [19]. Considering that HP-EGR is reintroduced directly in the intake manifold, a good air-EGR mixing across this element is essential to avoid the subsequent increase in cylinder emissions.

The behavior of the mixing between the air and the EGR streams can be studied by experimental techniques as well as numerical simulations. In the experimental measurements, the real behavior of the flow can be assessed through average and instantaneous values [17, 47]. The experimental approach main drawbacks include the necessity (and) of manufacturing the real parts involved and installing them in an engine test cell, the difficulty of instrumenting and performing non-invasive measurements in some engine locations and even the impossibility of providing a time-resolved measure of some relevant variables. In fact, this chapter will provide researchers with a calculation of the error incurred when estimating the EGR rate swallowed by the cylinders with an average CO_2 probe. To overcome these issues, a convenient choice is to conduct numerical simulations combining 0D/1D engine models and 3D Computational Fluid Dynamics (CFD). Obviously, these models need to be validated with the corresponding experimental measurements to guarantee the required accuracy.

In this work, EGR cylinder-to-cylinder dispersion will be predicted in two different manifolds, corresponding to a 4-cyl and 6-cyl engines, at different operating conditions. A calibrated 0D-1D engine model will provide boundary conditions for 3D CFD simulations of the intake manifold. The commercial CFD code STARCCM+ v.12.06 [64] will be used throughout all the study. The numerical predictions will be compared with equivalent experimental simulations. The impact of including the 3D CFD model on the results will be assessed. The influence and interrelation between CFD mesh and time-step size on EGR distribution will be analyzed as well.

In fact, one of the most important features to define when considering a CFD simulation is the turbulence modeling. The mixing of two flows (not only air and EGR) is a large subject of study, starting on the T-junction geometry, i.e. the works developed by Garner et al. [116] and specially, the works of Sakowitz et al. [53, 54, 51, 52]. Regarding turbulence modeling, LES (Large Eddy Simulation) is known to provide results which are correlated with experimental data in mixing geometries as the aforementioned T-Junctions [53, 117] and even intake manifolds [118, 54]. However, the high computational effort of the LES calculations has to be taken into account, especially by the high mesh density that they require. Therefore, RANS (Reynolds Averaged Navier Stokes) simulations are also widely used in EGR dispersion analysis, achieving good results [17, 58]. In addition, in this chapter, turbulence modeling will be evaluated in terms of EGR dispersion as well as CO_2 transient traces and flow field prediction. As will be discussed in section 4.2, it is not common for other works to assess the impact of different RANS closure models on EGR dispersion, let alone to include in the comparison the prediction of the 0D/1D model.

Besides, the influence of the obtained EGR dispersion on pollutant emissions will be assessed by means of NOx and PM models [49, 50]. Usually these models are applied to experimental measurements [48] or embedded into 0D-1D engine models. In this chapter, they will be applied to CFD results in order to quantify the impact of the numerical configuration in the predictions of contaminant, which is a novelty to the author's knowledge. With this, the sensitivity and trade-off of the CFD setup in terms of accuracy will be properly assessed. These regressions are also used to assess the importance of EGR dispersion on emissions for future frameworks with increased EGR rates [14].

In section 4.2, the experimental methods, the 0D/1D model basics and the manifolds 3D CFD model will be described. The sensitivity of 3D CFD simulations to the mesh refinement, time-step size and choice of turbulence model will be discussed in section 4.3, in both manifolds. With the selected final setup, the average and instantaneous validation of different turbulence modeling approaches will be performed in different operating points in section 4.4. Finally, the main conclusions of this chapter will be exposed in section 4.5.

4.2 Methodology

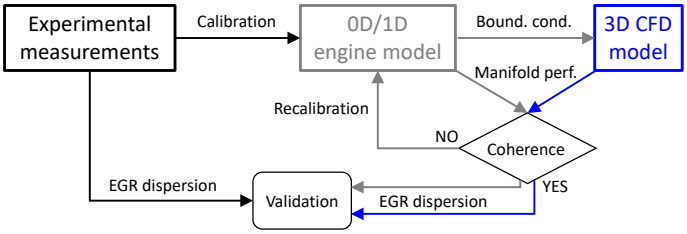

Figure 4.1: Flow chart of methodology employed to predict EGR dispersion. The arrows depicting the usage of experimental, 0D/1D and 3D CFD results are colored black, gray and blue, respectively.

The methodology followed in this chapter in order to predict EGR cylinder-to-cylinder distribution is depicted in Figure 4.1. The experimental measurements described in section 4.2.1 will be useful to calibrate the engine simulation software as well as to conduct a regression analysis between the EGR rate of the 6 cylinder engine and its NOx and PM emissions. This correlation has not been performed in the 4-cyl engine because the operating points that were essayed are fewer, and the amount of experimental data to perform this correlations is not enough. The 3D CFD model of the considered intake manifold is set with the baseline configuration commented in section 4.2.3. The calibrated 0D/1D engine model (section 4.2.2) will provide instantaneous mass flow rates and temperatures that will be applied as boundary condition for the 3D-CFD simulation. The calibration coefficients of the 0D/1D model at the intake manifold will be tuned until its predicted performance is in agreement with the 3D modeling of the same intake manifold (see end of section 4.2.2). When this process is finished, the results provided by the 3D CFD simulations will

be validated against the experimental measurements in terms of average and instantaneous results, including also in the comparison the results from the 0D/1D model. Of course, all of this process will be applied for both considered manifolds.

4.2.1 Experimental apparatus

This section is devoted to expose the main elements of the experimental facility and the conducted measurements used to calibrate the 0D/1D engine model and for the validation of the 3D models. Depending of the considered engine, the main characteristics of the essays are described:

- **4 cylinder engine.** The employed turbo-diesel engine to carried out the experimental measurements is 1.6 liters with 4 cylinders and 16 valves with an EGR system. This engine can provide 320 Nm of maximum torque at 1750 rpm and 96 kW of maximum power at 4000 rpm. The main features of the experimental apparatus are very similar that used in previous works [12, 69, 47] and will be the same in the next engine. At the end of every runner in the intake manifold, and upstream the after-treatment devices (Horiba Mexa 7100DEGR measurement probes of mean percentage of CO2) have been placed. With these probe, CO2 and temperature are obtained when the signal is stable. Taking into account that the CO2 exhaust percentage is known, the EGR rate in every runner can be calculated. Instantaneous pressure probes have been placed at the inlet of air and EGR and inside of the intake manifold, in order to adjust the GT-Power model [119], presented in section 4.2.2 Finally, fast measurements probes of CO2 (*Cambustion*©), provide instantaneous percentage of CO2 along an engine cycle. These probes are located in holes previously prepared, near the runners and in the middle of the manifold, (the probes location is showed in Figure 4.4) with the objective of obtaining the transient evolution of the EGR pulses. Through the measurement of these variables, a better calibration of the 1D model will be achieved.
- **6 cylinder engine.** The turbodiesel engine analyzed in these experiments presents a displacement of 8 liters with 6 cylinders and 24 valves, with a HP-EGR system coupled to reduce pollutant emissions and approved by the *Euro VI Heavy-Duty* standard. To achieve a good cali-

bration of the engine simulation software that will be employed in this document, more than 10 operating points have been measured in different regions of the engine map. In addition, in every operating point, different EGR rates have been applied to obtain the impact on pollutant emissions getting useful data to adjust the HP-EGR configuration. From these essays, both average and instantaneous values have been measured. In several zones of the intake manifold that will be indicated in section 4.2.3, and upstream the after-treatment devices, mean CO_2 has been measured with the same probes than the 4 cylinder engine. The NOx level in parts per millions (ppm) and the particulate matter in FSN (filter smoke number) are measured upstream the aftertreatment devices, in order to obtain the main emission indicators in every operating point. The 0D/1D model needs pressure traces to be calibrated in a proper way, so instantaneous pressure probes have been placed at the inlet of air and EGR ducts, upstream of the numerical domain. In addition, the instantaneous percentage of CO_2 is obtained with the same probes than the previous engine.

4.2.1.1 NOx-PM statistical regression of 6-cylinder engine

As commented in section 4.1, high EGR dispersion between cylinders can produce a huge increment in the PM or NOx emission depending of the excess or lack of EGR rate, respectively. A statistical regression fed with experimental measurements has been employed in this work to translate the EGR distributions of the 3D-CFD models into emission indicators. With this, the sensitivity and trade-off between 3D model accuracy and computational effort can be properly addressed in section 4.3.

Different models have been proposed to predict pollutant emissions in accordance with the EGR rate imposed to the engine in every operating point. In the present work, the model developed by Guardiola et al. [49] has been applied. In this model, NOx emissions are normalized with the emission in 0% EGR rate case ($NO_x/NO_{x,EGR=0}$). Regarding the particulate matter (PM), the emissions with 0% EGR rate are near 0, so the correlation will be directly developed with the absolute value of the filter smoke number indicator (FSN). Guardiola et al. [49] demonstrated that the factor $EGR \cdot 1/\lambda$, being λ the excess of air and EGR the EGR rate as calculated by equation 4.7, is the

most appropriated to make a coherent statistical regression and will be the independent variable for this fitting. The regression regarding NOx is adjusted with an exponential function, in the same way than the works of Guardiola et al. [49]. On the other hand, particulate model is adjusted with a 3^{rd} degree polynomial function. In this way, both regressions are applied to the experimental measurements described in section 4.2.1, getting the graphs presented in Figure 4.2

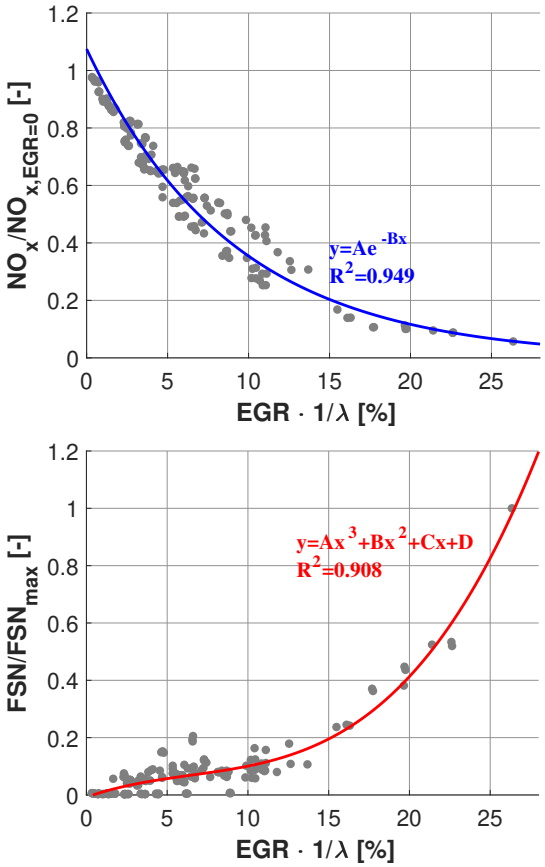

Figure 4.2: Correlation with experimental data using exponential function in the NOx emissions (top) and polynomial function in the PM emission (bottom).

In Figure 4.2, both regressions for NOx emissions and PM are depicted. It must be noticed that the PM model is also normalized with the maximum value for the sake of representing a range bounded between 0 and 1, but the

correlation was performed with the absolute value of FSN. It is clear in this case that the particulate matter grows up in a huge way starting at a certain threshold, while the NOx emissions are reduced in a asymptotic way when the EGR rate are increased. Taking into account that the correlation coefficients (R^2) are beyond the 90%, in the same order than the agreement coefficient of Guardiola et al. [49], both fittings can be applied to each and every cylinder of the 3D-CFD models, to predict the impact of the EGR dispersion in emissions.

The concave shape of the NOx and FSN (PM) curves (see Figure 4.2) illustrate the issue with EGR dispersion. When 2 cylinders depart from the nominal EGR (one swallowing more EGR than it should and the other one less, to keep the EGR balance), the increase of emissions in one cylinder (lack of EGR for NOx and EGR excess for PM) is greater than the decrease of contaminants existing in the other cylinder, so the overall emissions are higher than with a uniform EGR distribution. This non-linear behavior is more noticeable depending on the value of $EGR \cdot 1/\lambda$ of the working point.

4.2.2 1D model

As mentioned in section 4.2.1, the experimental data allows to obtain the main variables used to calibrate and modify the 0D/1D model of the engine. At the same time, this engine model will be the method to obtain the main boundary conditions of the 3D CFD model (see Figure 4.1), in the fashion of other works [119, 54].

The 0D/1D model has been developed in *GT-Power* software, which allows to get a prediction of relevant variables at all engine locations, as long as the model is properly calibrated. The main objective in the calibration is to tune the model coefficients (pressure loss and heat transfer coefficients) in order to match the engine measurements at the corresponding operating point. In this way, the accuracy of the prediction of the required variables to be used as boundary conditions for the 3D CFD model is guaranteed. When an engine simulation is performed, the model has to reach a steady state, in the way that the main variables are periodic. Figure 4.3 shows an example of the agreement obtained by the calibrated model in the prediction of pressure transient evolutions.

In the present chapter, the 1D model has been calibrated by a specific

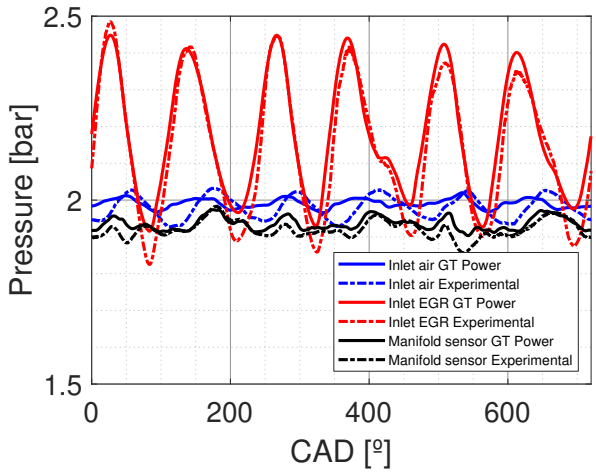

Figure 4.3: 1D model and experimental instantaneous traces of 6 cylinder engine.

methodology in order to achieve a good agreement in all operating point. It must be taken into account, that the calibration of the 1D model in this chapter is developed in the work of Macián et al. [48]. In the model, some variables are predefined in every operating point, i.e. break mean effective pressure (BMEP), engine speed, boost pressure. On the other hand, the model has some variables that will be the degrees of freedom. First, a proportional-integral-derivative (PID) controller has been placed on the EGR valve to assure that the objective EGR rate is achieved in the considered operating point (Galindo et al. [1].). The pressure loss coefficients are properly adjusted thanks to the experimental measurements of instantaneous pressure. In addition, the heat transfer coefficients are adjusted to achieve similar temperatures in comparison with the experimental data in the EGR line. The calibration process, performed for each operating condition, ends when a good agreement against experimental measurements is obtained in terms of pressure, temperature, mass flows and EGR rate. Specifically, the differences between 1D model and experiments on time-averaged mass-flow rate is within 3% for all working points in the 4 cylinder engine. With this, the 1D model provides the 3D model boundary conditions that should be close to the actual experimental transient traces [119].

In EGR dispersion problems, Galindo et al. [120] discuss the possibility of performing 1D-3D co-simulations by coupling the engine model with the 3D

CFD model of the intake manifold, to get a perfect agreement in the boundary conditions of the domain [55, 58]. However, this type of "strong coupling" entails an increase of computational effort, together with other constraints [120]. In this work, the calibrated engine simulation results have been imposed to the 3D models as boundary conditions only in a 1-way direction [119]. Since this approach may produce inconsistencies between the 1D and 3D modeling of the intake manifold, a feedback loop is conducted as a sort of "weak coupling" [120] to guarantee the coherence between both representation of the manifold (see Figure 4.1). In this way, in some operating points (such as point 2 in Table 4.2), the 0D/1D model has been calibrated again at the manifold to match the 3D CFD prediction of pressure drop at the different manifold elements (valves, mixer), where experimental results are not available. Then, the mass flow rate traces obtained by the 0D/1D model are updated to provide new boundary conditions for the 3D CFD model, which in turn may change the prediction of pressure drops. This feedback loop is repeated until the differences in such variables are lower than 5% in average values and 10% in peak-to-peak amplitude in the 6 cylinder engine case. Once the weak coupling is finished, the mass flow rate traces predicted by the 0D/1D model are updated to provide new boundary conditions for the 3D CFD model. In other working points, the manifold pressure loss predictions by 3D CFD and 0D/1D engine model are coherent from the beginning, so the feedback loop is not required.

4.2.3 3D-CFD Baseline Setup

4.2.3.1 Geometry

The software used for the CFD simulations, and the postprocessing of several results has been SIEMENS StarCCM+ [64]. In the 4 cylinder engine, the geometry of the considered domain is presented in Figure 4.4. This geometry has a similar configuration than the manifolds analyzed previously in other studies [55, 57].

As it can be seen in 4.4, the runners point directly to the intake valves, therefore, the domain has 8 outlets. The mixer is introduced directly inside of the manifold, by the central region. This mixer has been designed to introduce the EGR flow in radial way. To achieve that objective, three windows has been placed at the end of the duct. In addition, this duct is closed at the end to promote the mixing in the direction of the windows. It must be pointed out in

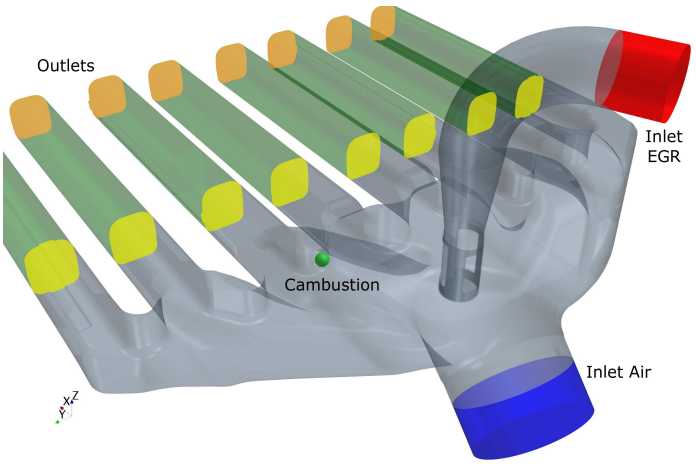

Figure 4.4: 3D computational domain of 4-cylinder manifold, with inlet air extrusion (blue), inlet EGR extrusion (red), outlets extrusions (green) and virtual probe (Cambustion ©)

Figure 4.4 that in air (blue) and EGR (red) inlets as much as in the outlets of the domain (green) straight extrusions have been developed. These extrusions are used to impose the boundary conditions in the domain slightly away of the region of interest to avoid their influence on the solution in the flow field. Additionally, different virtual probes have been added to the domain, as the Cambustion probes, which is highlighted in Figure 4.4, and whose results will be addressed in the validation section in comparison with experimental data.

On the other hand, the 3D CFD numerical domain, corresponding to the 6 cylinder intake manifold of the engine described in section 4.2.1, is presented in Figure 4.5.

Figure 4.5 shows on one side the global perspective of the manifold, and a detailed view of the valves in the intake and EGR lines. The EGR inlet boundary is placed several diameters upstream the EGR valve, while the fresh air inlet is placed upstream the throttle valve. The geometry of this 6 cylinder manifold is different to the ones described in other works, in which the air and EGR streams are directly mixed in the manifold [55, 1] or the cylinders are not equally spaced [57]. The mixer studied in this work (see bottom side of Figure 4.5) can be included in the geometries that mix the air and EGR streams in a T-Junction upstream the manifold, like the manifolds that appear in [17, 56],

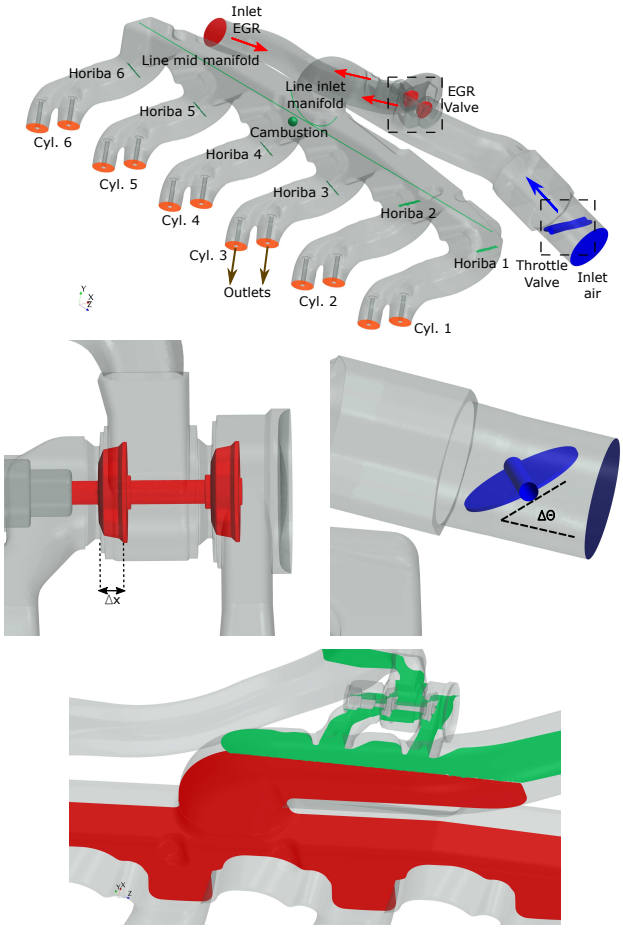

Figure 4.5: Top figure: 3D computational domain of the 6-cylinder manifold with air inlet boundary (blue), EGR inlet boundary (red) and outlets boundaries (orange) (top figure). Detailed view of EGR valve (middle left) and throttle valve (middle right), indicating their corresponding degree of freedom. Bottom figure: close-up at EGR-air mixer and connection between main duct and intake manifold, with two postprocessing planes.

but these engines have 4 cylinders. All things considered, the manifold most similar to the one analyzed in this work is the geometry studied by Sakowitz et al. [51]. Nevertheless, the impact of different mixer geometries in the EGR distribution is out of the scope of this chapter.

Middle left side of Figure 4.5 provides a close-up of the EGR double-seat valve, which connects the EGR line with 2 ducts that will meet the fresh air pipe so as to produce the EGR-air mixing. Notice that the EGR valve has an axial displacement to regulate the EGR rate, so this displacement depends on the operating point of the engine. In the same way, the throttle valve opening (middle right side of Figure 4.5) can be regulated. Both valves are adjusted with the same displacement or angle than in the experimental measurements, in accordance with Table 4.2. In Figure 4.5, the postprocessing probes are highlighted in green color. The *Horiba Mexa 7100DEGR* probes are modeled as a tiny surface, representing the area aspirated by the real probes. Section 4.2.4 shows the method to estimate the EGR rate on the basis of the EGR mass fraction gathered by the $Horiba_{CFD}$ virtual probes. Notice that, due to the heterogeneity of the flow, the EGR rate obtained with this probes may not be the same than the EGR that the cylinders will swallow, which is the relevant EGR rate but cannot be measured. Therefore, an estimation of these deviations is obtained in 4.2.4.2. The Cambustion© probe is modeled as a point in the same place than the real one (close to the entrance of the runner leading to cylinder 4), to provide the instantaneous EGR rate that will be used in the validation of the 3D models.

4.2.3.2 Turbulence model

Turbulence modeling is one of the most important issues to be taken into account in an EGR dispersion problem as mentioned in section 4.1, due to the relevance of the mixing process between air and EGR streams in some geometries or operating points of the engine. Regarding the LES approach, its ability to solve a significant fraction of the turbulent scales should allow an accurate prediction of mixing problems, ranging from simple geometries as T-junction [53, 117] to EGR dispersion in intake manifolds ([51, 53, 54, 118]). RANS approach has been used as well in this type of problems [58, 116]. Therefore, the decision of modeling turbulence in a more detailed way as LES or a more simplified as RANS needs to be addressed. Sakowitz et al. [53] demonstrate that the turbulence structures in a T-junction have not been captured properly with the RANS approach, being too diffusive and with little mixing capacity. In spite of these commented discrepancies of RANS, a different work by Sakowitz et al. [51] shows how the air-EGR mixing in the intake manifold at low frequencies ($\sim$ 60 Hz) the RANS approach and LES approach produce similar results, likely because the EGR dispersion in these conditions

is more governed by the EGR pulses rather than the turbulence mixing. More information regarding this distinctions will be exposed in chapter 5.

In the numerical domain presented in Figures 4.4 and 4.5 the influence of the pulsating effects can be remarkable due to the low frequencies in the considered operating points. Therefore, the URANS approach (*unsteady RANS*) can be a suitable option to get a trade-off between accuracy of the results and computational effort. Particularly, the literature shows a variety of works providing a good agreement between CFD 3D predictions with URANS approach, employing a $k-\varepsilon$ closure model [57, 58, 116, 59]. Thereby, the URANS approach with the $k-\varepsilon$ turbulence submodel has been selected to be the baseline setup of this work. In most of these cited works, the turbulence model is fixed throughout the study. On the contrary, in this work, the influence of the turbulence submodels in EGR dispersion will be assessed, including simulations with $SST\ k-\omega$ turbulence submodel in section 4.4. $SST\ k-\omega$ model was developed to improve the prediction of separated flows compared to $k-\varepsilon$ model [93], which is often confirmed by the better agreement with experimental results of the former [121]. In addition, the possibility of neglecting the impact of turbulence is considered by employing the inviscid model as well.

4.2.3.3 Rest of CFD configuration

The remaining features of the baseline CFD setup are summarized as follows:

- A polyhedral mesh has been employed, improving the resolution of the flow close to the walls by means of a prism layer. The baseline mesh in the 4 cylinder manifold features 1M cells, and the mesh in the 6 cylinder manifold presents 6M cells. Nevertheless, a grid independence analysis is conducted in section 4.3, in which more details about these meshes are provided.
- The air and EGR have been modeled as different non-reactive gas component, instead of EGR being modeled as passive scalar like other works [51]. The main thermodynamical properties of EGR and air are variable with temperature but have been considered as alike, since the error of considering the actual exhaust gas composition is below 2% [122]. Indeed, replacing EGR by air is usual even for experimental facilities [44].

The gas thermodynamic properties $\kappa(T)$ and $\mu(T)$ have been modelled through a Sutherland's law, varying with temperature that is typically used for air and commonly obtains accurate results with an acceptable error over a wide range of temperatures [123]. On the other hand, $C_p(T)$ has been modelled by a polynomial law [124].

- The segregated solver has been used for the resolution of the numerical equations with 2^{nd} order schemes of resolution. A coupled solver would be more adequate to solve cases with high Mach numbers. For the considered operating points, the highest values of Mach are far from transonic values (maximum instantaneous local Mach number below 0.5), so the selected segregated solver is a suitable approach.

- The convective terms of the 3D CFD model are discretized with 2^{nd} order upwind schemes, gradients are reconstructed using a hybrid Gauss-Least Squares method [64] and the temporal scheme of the simulations is 2^{nd} order implicit. Initial time step of the setup is 2°/step in terms of engine crankshaft revolutions, in the same order that the steps in the work of Dimitriou et al. [58]. Subsequently, in section 4.3, a sensitivity study of time-step size will be carried out.

- Different studies in the under-relaxation factors (URFS) have been completed in order to obtain more aggressive values than the default ones. By doing this optimization of the URFS, a reduction of the number of inner iterations is achieved, arriving to converged solution in every time step. Although in other works 10 inner iterations are required for each time step (Dimitriou et al. [58]) in the 4 cylinder manifold, after this URF optimization, the final inner iterations have been fixed in 8. On the other hand, in the 6 cylinder manifold, the inner iterations have been fixed in 10.

- Another important issue to consider is the convergence criteria of the analyzed cases. Since all the cases are unsteady and pulsating, the variables should be cycle-averaged after reaching periodicity. The number of engine cycles to average the results are variable depending of the works and the considered operating points. For example, in the works of Sakowitz et al. [51, 118, 52], the number of cycles vary between 4-10-20 cycles in LES calculations. On the other hand, in 3D RANS coupled with engine simulation software, the number of cycles calculated previously to the coupling are about 10-15 cycles [55, 58]. Taking into account the

achieved results, the number of cycles to make a proper average in this work are about 7-11, depending of the considered operating point. It must be highlighted that while calculations with $k-\varepsilon$ submodel have a very small oscillation when cycle-to-cycle convergence is reached, analysis with SST $k-\omega$ submodel are much more fluctuating.

- Walls are considered as adiabatic, whereas the influence of the type of remaining boundary conditions was assessed by Galindo et al. [1]. According to such studies, imposing $\dot{m}_{inlet} - \dot{m}_{outlet}$ as boundary conditions shown better numerical behavior and provided superior agreement with experimental measurements than other types, so the same approach is employed in this work. A 0D/1D engine model is developed in section 4.2.2 so as to provide the transient traces of these mass flow rates, to be used as boundary conditions by the 3D CFD model.

4.2.4 Virtual probes postprocessing

Taking into account the virtual probes presented in Figures 4.4 and 4.5 it is necessary a brief description of how the EGR rate is obtained depending of the considered probe or analysis. In section 4.2.3.3, it was exposed that the EGR is modeled itself as one species of the simulation (the other is the air species). Therefore, the EGR rate in both manifolds for each cylinder can be calculated as:

$$EGR_i = y_i = \frac{m_{EGR,i}\ [kg]}{m_{tot,i}\ [kg]} \approx \frac{\sum\limits_{cycles} (\dot{m}_{EGR-j} \cdot \Delta t)}{\sum\limits_{cycles} (\dot{m}_{tot-j} \cdot \Delta t)}, \tag{4.1}$$

where $i = 1-6$ in the 6 cylinder engine or $i = 1-8$ (by runner) in the 4 cylinder engine indicates each cylinder (or runner) of the manifold, $\dot{m}_j$ is the EGR or total mass flow rate through each of the outlets of the domain leading to the corresponding cylinder, and the summation is performed over the required number of engine cycles to obtain representative values. To get non-dimensional values, these EGR rates y_i can be presented as deviations against the mean EGR of the case as presented in equation 4.10.

In addition, as explained in section 4.2.2, the *Horiba* probes have been used to measure the mean EGR rate of a certain cylinder. While in the 4 cylinder engine, the *Horiba* probes are placed just in the beginning of the outlets extrusions (see figure 4.4 providing the real amount of EGR that the engine swallow, in the 6 cylinder engine these probes are placed in the manifold in the most representative zones of the cylinders (see Figure 4.5), taking into account the restrictions of space in the experimental facility. Thus, the rate in their virtual counterparts are useful to estimate the deviations between the experimental EGR rate at each cylinder and the corresponding *Horiba* measurement (presented as the vertical bars in Figures 4.23, 4.21 and 4.25), as explained in section 4.2.4.2.

4.2.4.1 6 cylinder engine mean EGR postprocessing

In the 6 cylinder engine manifold, considering the $Horiba_{CFD}$ probes, the EGR rate can be defined as:

$$EGR \approx \frac{m_{EGR} \ [kg]}{m_{tot} - m_{HORIBA_{CFD}} \ [kg]} \tag{4.2}$$

If the *Horiba* probes are used to get the EGR rate, and considering the mass flow rate extracted by the *Horiba* as constant:

$$EGR_{HORIBA_{CFD}}(t) \approx \frac{\cancel{\dot{m}_{HORIBA_{CFD}}} \cdot Y_{EGR}(t) \cdot \cancel{\Delta t}}{(\cancel{\dot{m}_{HORIBA_{CFD}}} \cdot Y_{air}(t) + \cancel{\dot{m}_{HORIBA_{CFD}}} \cdot Y_{EGR}(t)) \cdot \cancel{\Delta t}} \tag{4.3}$$

Therefore, the EGR rate in the numerical $Horiba_{CFD}$ probes can be approximated using only the mass fraction of EGR ($Y_{EGR}(t)$), due to the EGR is modeled as an species of the simulation. This mass fraction can be obtained by a mass flow average [64]:

$$Y_{EGR}(t) = \frac{\sum_f \rho_f Y_{EGR-f} |\mathbf{v}_f \cdot \mathbf{a}_f|}{\sum_f \rho_f |\mathbf{v}_f \cdot \mathbf{a}_f|} \tag{4.4}$$

In equation 4.4, ρ_f is the density of a certain face of the surface, and $\mathbf{v}_f$ and $\mathbf{a}_f$ are the velocity and area vectors respectively. Hence, the final EGR rate in a certain $Horiba_{CFD}$ probe can be obtained as:

$$Y_{EGR-i} = \frac{\sum_{1}^{n} \sum_{CAD} Y_{EGR}(t)/CAD}{n}, \quad n = 1, 2...cycles \tag{4.5}$$

4.2.4.2 6 cylinder engine experimental deviations

It must be noticed that the measured EGR rate by the *Horiba* probes (in a experimental and numerical way, obtained in equation 4.5) may not be the same than the real EGR that the cylinder swallows (the EGR in the outlets, see Figure 4.5 and equation 4.1). Thus, the impact of performing the experimental measurements in the *Horiba* probes instead of in the intake ports must be assessed. The experimental data in these ports is not available, but an approximation of these deviations can be obtained by means of the CFD calculations. First, the numerical deviation between $Horiba_{CFD}$ (local surface) and outlets (whole cross-section) can be calculated:

$$\varepsilon_{outlet-i} = Y_{Horiba_{CFD}-i} - Y_{outlet-i} \tag{4.6}$$

Therefore, for every outlet of the domain the corresponding $\varepsilon_{outlet-i}$ can be obtained. To perform a reliable statistical analysis, it is convenient to consider a large number of cases for every operating point. In this way, additional cases that are not directly analyzed in this work have been used for this particular study to increase the population of the statistical analysis. Consequently, for every $\varepsilon_{outlet-i}$ (normalized with the average EGR rate) and operating point, an average (μ) and standard deviation (σ) are extracted after adjusting the population to a normal distribution. An average p-value of 0.04 is obtained considering all the fittings conducted for the different cylinders and operating points. The distributions of $\varepsilon_{outlet-i}$ for operating point 2 are presented in Figure 4.6.

The deviation between taking the measurement in the $Horiba_{CFD}$ probe instead of in the outlet is small and does not present bias for cylinder 5, in accordance with Figure 4.6. However, in other cylinders the mean of the devia-

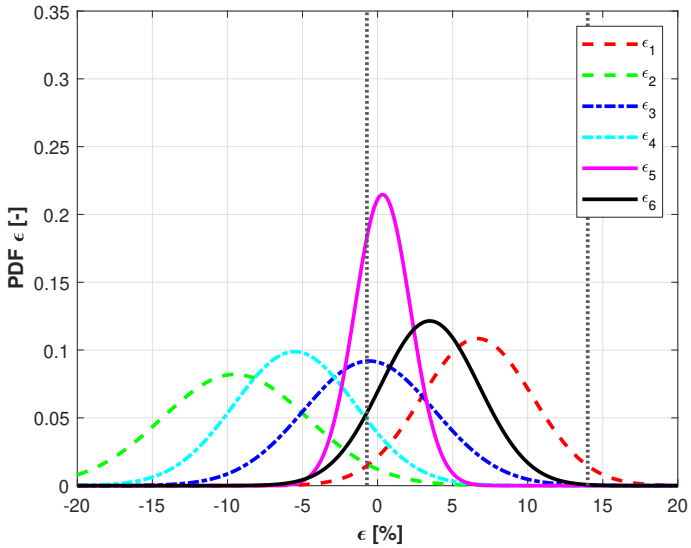

Figure 4.6: Adjusted normal probability distribution functions for $\varepsilon_{outlet-i}$ (calculated using CFD results) in operating point 2. The dotted vertical lines correspond to the 95% criterion ($\mu \pm 2\sigma$) for $\varepsilon_{outlet-1}$.

tions is noticeable (up to 10%) with important standard deviations. Therefore, the error of taking the measurement in the *Horiba* probes will depend of the considered cylinder and operating point and it is notable in some cases. With this statistical fitting of the deviations calculated with CFD, an assessment of the uncertainty of the experimental measurements due to this fact is shown in Figures 4.23, 4.21 and 4.25 as vertical bars.

4.2.4.3 Instantaneous posptrocessing

Regarding the instantaneous results, it is necessary to develop a specific method to make proper comparisons between numerical results and experimental data. The *Cambustion* sensors of the CFD domain have been presented in Figures 4.4 and 4.5. In terms of CO_2 percentage, the EGR rate can be defined according to Luján et al. [17] as:

$$EGR\,[\%] = \frac{[CO_2]_{intake} - [CO_2]_{atm}}{[CO_2]_{exhaust} - [CO_2]_{atm}} \cdot 100 \tag{4.7}$$

Taking into account that $[CO_2]_{atm} \sim 0$, the CO_2 percentage of the CFD calculations can be obtained as:

$$[CO_2]_{intake-CFD}\,[-] = EGR_{Camb}[\%] \cdot \frac{\rho}{\rho_{EGR}} \cdot [CO_2]_{exhaust}, \tag{4.8}$$

being EGR_{Camb} the mass fraction of EGR of the virtual probe and $[CO_2]_{exhaust}$ the percentage of CO_2 in the exhaust for the considered operating point (as measured in essays). Finally, the experimental instantaneous results will present an inherent averaging or *smoothing* effect due to the huge amount of measured cycles and the finite time that the probe needs to analyze the flow composition at each sample. In order to apply this effect to the CFD traces, a moving average is employed using *Matlab* ©. This function performs an average on a certain element of an array considering a number of adjacent elements. The size of the window k_{avg} in which the average is performed, will depend of the sensor sampling period T_{sensor}, and the time step of the numerical simulation Δt_{CFD}, as presented in equation 4.9. This *smoothing* correction is applied to all the instantaneous numerical traces of section 4.4.

$$k_{avg}\,[-] = \frac{T_{sensor}}{\Delta t_{CFD}} \tag{4.9}$$

4.2.5 Operating points

In this work, EGR dispersion is predicted at 4 and 3 different engine working points respectively, depending on the considered engine.

- **4 cylinder engine.** The considered operating points are summarized in Table 4.1 and will be analyzed later in next sections. **For the mesh sensitivity and time step study, the operating point used will be B**, which is very similar to the points used in related works [58, 55, 56, 59], having a medium load and EGR rate. Besides, points A and C have been tested to obtain the dispersion in the engine when operates in low load with high EGR rates (point A) or with low EGR rates (point C). Point D has been tested to obtain the dispersion when the engine works in full load with a little EGR rate that slightly affects to power but achieve a huge reduction of the pollutants [125].

- **6 cylinder engine.** The operating points in this engine cover low, medium and high power range of the engine, being summarized in Table 4.2. In section 4.3.2, **the sensitivity studies will be calculated with operating point 2**, because it is a representative working condition located in the middle of the engine map, with similar speed and load conditions as the points used by Sakowitz et al. [51, 52]. On the other hand, point 1 has been tested to check EGR distribution at low load and low rpm, with throttle and EGR valve regulated to provide the greatest EGR rate studied in this work. Operating point 3 is tested at high loads and lower EGR rate with the throttle valve fully open.

Table 4.1: Operating Points of 4 cylinder engine

Operating point	A	B	C	D
Engine speed	Low	Medium	Low	Medium
BMEP	Very Low	Medium	Low	High
EGR rate (%)	50	20	5	5

Table 4.2: Operating Points of 6 cylinder engine

Operating point	1	2	3
Engine speed	Low	Medium	High
BMEP	Low	Medium	High
EGR rate (%)	20	15	10
$EGR \cdot 1/\lambda$	7	8	5
EGR valve (% more open)	50	100	35
Throttle valve (% more open)	30	60	100

4.3 Sensitivity studies

4.3.1 4 cylinder engine

The initial case (or baseline case) analyzed in this section, starts from a mesh as the presented in Figure 4.7. On the left side of the figure, the wall mesh of the domain is presented; on the right side, two internal planes of the manifold, with the aim of showing the important zones in this case.

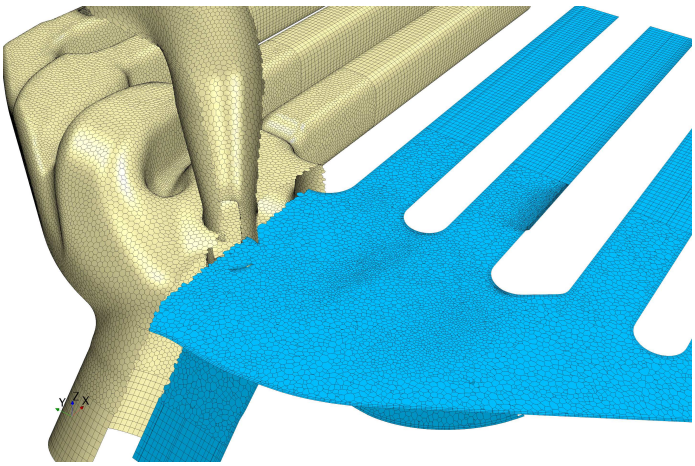

Figure 4.7: Sections of baseline mesh (1M cells) and cylinder runners with surface mesh of 4-cylinder manifold.

The polyhedral mesh used in the baseline case, has an element base size of 2 mm, getting a mesh around 900 thousand cells ($\sim 1M$). This baseline mesh has a similar size than the mesh in the works of Sakowitz et al. [51] and Dimitriou et al. [58] and a little bit finer than the mesh in the works of Rahimi et al. [57] and Karthikeyan et al. [56], which have around 600-700K elements. In spite of these differences, all the meshes are in the same order of magnitude.

For a better understanding of the influence of the mesh in the final results, it has been decided to carry out the mesh independence study with 2 additional meshes for both manifolds. For this 4 cylinder engine manifold, a mesh with lower cell density than the baseline and a mesh with smaller cell base size, especially around the mixer have been included in this study. Therefore, 3 meshes are included in this comparison: 0.2M (coarse), 1M (baseline) and 5M (fine) of elements. Regarding the mesh density, wall $y+$ represents the non-dimensional wall distance to the wall, and is defined as $y+ = u^* \cdot y/\nu$ where u^* is the friction velocity and depends of the wall shear stress, y is the normal distance of the first cell near the wall and ν is the kinematic viscosity [64]. In this work, the fine mesh has an average value of $y+$ in the mixing zone of ~ 2, the baseline mesh has an $y+ \sim 25$, and in the coarser mesh $y+ \sim 40$.

The mesh independence study will be performed focusing in the deviation

of every runner regarding the average level of EGR, as is presented in equation 4.10:

$$\Delta y_{avg} = \frac{y_i - \bar{y}}{\bar{y}} \tag{4.10}$$

In equation 4.10, y_i is the EGR rate in a certain runner and $\bar{y}$ the mean level of EGR. Therefore, the results of this mesh independence study in terms of Δy_{avg} are presented in Figure 4.8:

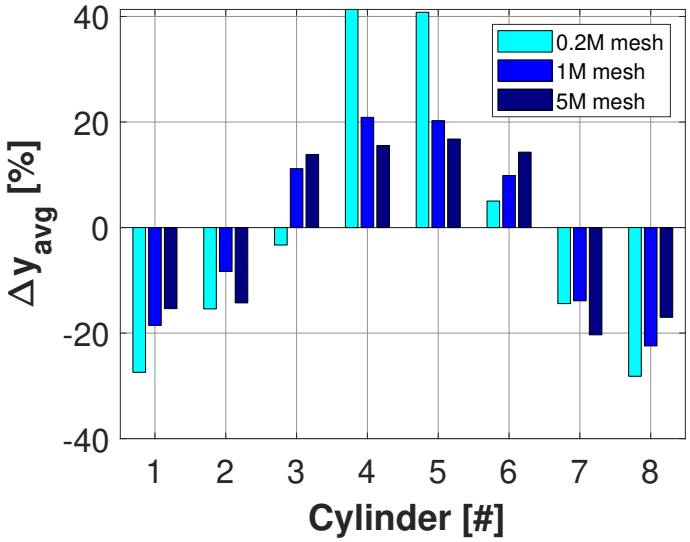

Figure 4.8: EGR rate (Y-axis) of every manifold runner (X-axis) for 3 meshes of the independence mesh study in the 4-cylinder manifold.

Figure 4.8 shows that EGR rate, in mostly of the runners, particularly at the central ones (4-5) appear important differences between the 0.2M element mesh and the others, while the differences between the finer meshes are less noticeables. Nevertheless, can be interesting to analyze these differences not only in a qualitative way but in a quantitative way too. For this purpose, some numerical coefficients will be defined next.

A root mean square error ($RMSE$) index can be developed, to capture the differences in comparison with the reference case in terms of accuracy. For instance, for this mesh sensitivity study, the reference case is 5M mesh. After

a normalization with the averaged EGR rate (equation 4.11), a global value for the considered cases is obtained (Z is the number of runners/cylinders). In addition, a coefficient of variance (COV) is defined in equation 4.12 to quantify the dispersion of a certain distribution of EGR rates. The higher the differences on EGR rate between each cylinder and the average, the greater will be the COV coefficient.

$$RMSE = \sqrt{\frac{\sum_{i=1}^{Z}(y_i - y_{i,ref})^2}{Z}}/\bar{y} \tag{4.11}$$

$$COV = \sqrt{\frac{\sum_{i=1}^{Z}(y_i - \bar{y})^2}{Z}}/\bar{y} \tag{4.12}$$

It can be noticed that this coefficient is simply a normalized standard deviation. Starting from the reference case, a COV error can be defined to analyze the evolution of the dispersion between cases as equation 4.13 shows:

$$\epsilon_{COV} = \frac{COV_{ref} - COV_i}{COV_{ref}} \tag{4.13}$$

Some factors to obtain a quantitative estimation of the differences that can appear in the EGR distribution, can be defined to make easier the comparisons between different configurations. A symmetry factor SF can be defined taking into account that, every runner from 1 to 4 (i) or 1 to 3 in the 6 cylinder engine, will be have an opposed runner ($-i$), i.e. for the runner 1 the opposite will be runner 8, for runner 2 the opposite will be runner 7...and so on. So, this factor is defined as:

$$SF = \sum_{i=1}^{Z/2} \frac{(y_i - y_{-i})^2}{\bar{y}^2} \tag{4.14}$$

In this factor, the difference in EGR rates is squared to avoid the suppression between positive and negative differences. A SF near 0 indicates a very symmetric EGR distribution. Another factor that can be defined deals with the concavity or convexity of the distribution. With the convexity factor

(CF), another aspect of the shape of the distribution is addressed. This factor is defined in equation 4.15:

$$CF = \sum_{i=1}^{Z-2} \left(y_{i+1} - \frac{y_{i+2} + y_i}{2} \right) \cdot \frac{1}{\bar{y}} \tag{4.15}$$

It must be noticed that CF collects the differences between the rates of the considered runner and the average of the adjoints (the previous and the rear). A positive CF will indicate a convex distribution, while if CF is negative, the distribution will be concave.

Taking into account all the summarized equations, the coefficients can be applied into the mesh independence study, getting the numerical values of Table 4.3:

Table 4.3: Summary of coefficients of mesh independence study of 4-cylinder manifold.

Coeff.	$RMSE$	COV	ϵ_{COV}[%]	SF	CF
Units.	[%]	[%]	[%]	[−]	[−]
0.2M	15.53	25.93	-61.88	7.1E-3	0.13
1M	4.80	16.50	-2.89	4.8E-3	0.09
5M	-	16.05	-	4.1E-3	-0.01

The Table 4.3 shows the same conclusions that were presented at first sight in Figure 4.8. The differences in terms of $RMSE$, COV and SF are huge passing from a mesh of 0.2M elements to a 1M mesh, while the next refinement does not show significant improvements. In terms of CF, the tendencies are not so clear. It is true that 1M mesh is more concave than 0.2M, but not in the way that the 5M is. Taking into account that the differences in almost all the coefficients are important between the 1M mesh and the 0.2M, the baseline mesh of 1M elements, seems the more adequate to obtain the setup validation, and is the same order mesh that appears in other works [58, 51]. It is worth mentioning that mesh refinement increases cell density and wall resolution ($y+$). While the coarse mesh (0.2M) was not able to predict the advection term properly, compared to the finer meshes, the significant wall $y+$ reduction from the baseline mesh (1M, $y+ = 25$) to the fine grid (5M,

$y+ = 2$) presents a low impact on the EGR distribution. Therefore, boundary layer resolution seems to play a secondary role in air-EGR mixing.

Another variable to be taken into account to understand the setup influence is the time step size. As was pointed out in section 4.2.3.3 the baseline step is 2 CAD/step, so every engine cycle needs 360 steps to be completed. This sensitivity study will be carried out with 4/2/1 CAD/step, so there will be 3 cases to compare the influence of the time step in the EGR dispersion and the shape coefficients developed in equations 4.11 to 4.14. Figure 4.9 presents the achieved results in this time step size independence study:

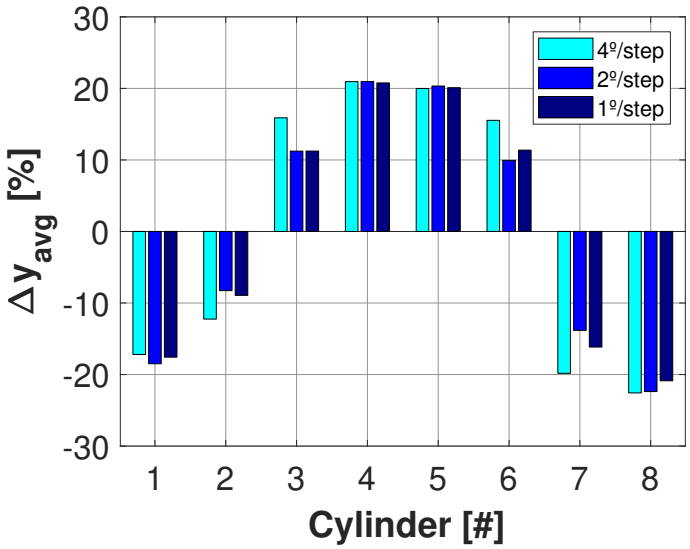

Figure 4.9: EGR rate (Y-axis) of every manifold runner (X-axis) for 3 steps of the time step size study in the 4-cylinder manifold.

The obtained results in terms of EGR rate in every runner for all the time step size are presented in Figure 4.9. The behavior in every runner shows an asymptotic trend, in exception of case 4 CAD/step which have more differences in some runners in comparison with the reminder of time steps studies. Nevertheless, the differences in terms of EGR rate in the runners between the analyzed cases seem smaller in comparison with more accurate step (1 CAD/step). Therefore, take an optimal time step is not easy to choose at first sight. The quantitative differences can be calculated with the exposed coefficients in mesh independence section. These results are presented in Table

4.4:

Table 4.4: Summary of coefficients of time step study of 4-cylinder manifold.

Coeff.	$RMSE$	COV	ϵ_{COV}[%]	SF	CF
Units.	[%]	[%]	[%]	[−]	[−]
4°/step	2.88	18.30	-10.99	8.7E-3	0.038
2°/step	1.18	16.51	-0.09	4.8E-3	0.094
1°/step	-	16.49	-	6.4E-3	0.067

The summarized results in Table 4.4, show very similar trends than the results in Figure 4.9. Although in terms of $RMSE$ there are not very important improvement, in terms of dispersion and shape of EGR distribution, the step of 2 CAD is closer to the most accurate case (1 CAD/step). Therefore, keeping the initial value of time step seems the more reasonable decision, getting a good trade-off between computational effort and accuracy.

4.3.2 6 cylinder engine

The typical methodology followed to conduct mesh and time step sensitivity studies, consists in first refining the mesh with a fixed time-step size until getting grid independence and then, with the final mesh, perform the time-step sensitivity as was developed in the 4 cylinder engine section and other numerical works [126, 5, 127]. However, both parameters are strongly related by the advective Courant number, presented in equation 4.16.

$$C = u\frac{\Delta t}{\Delta x} \tag{4.16}$$

In equation 4.16, u is the flow velocity, Δt is the time-step size and Δx is the size of the considered cell. This number quantifies how many cells the advective information advances in every time step. When an explicit time-advancing scheme is employed, the so-called CFL condition requires $C \leq 1$ to assure the stability of the simulation [128]. For a compressible flow explicit solver, the wave speeds $|u \pm a|$ would play the role of the flow speed u in equation 4.16 [128], which further tightens the constraint. For transient implicit schemes relying on pressure corrections (such as the segregated solver used in

this work), the theoretical limit is removed (the scheme is said to be unconditionally stable). However, in practical applications of implicit schemes with non-linear effects, the maximum Courant number allowed to avoid accuracy and stability issues may be about 1 for scale-resolving simulations [129] and close to 10 for URANS [130, 131].

Considering equation 4.16, reducing the time-step size decreases the Courant number, so lower time-step sizes pose no problem. However, refining the mesh increases C, which could lead to the paradox of simulations with finer meshes but worse accuracy [132, 133]. Therefore, considering the 6 cylinder engine manifold, the time-step size independence is addressed first. Apart from analyzing the sensitivity of time step on EGR distribution and subsequent pollutant emissions (using the developed regression in section 4.2.1.1), the threshold of Courant number that creates issues will be assessed by studying the mass imbalance of the EGR species:

$$Imb[\%] = \frac{\int_{t_0}^{T} \sum \dot{m}_{EGR-outlet,i}(t)dt - \int_{t_0}^{T} \dot{m}_{EGR-inlet}(t)dt}{\int_{t_0}^{T} \dot{m}_{EGR-inlet}(t)dt} \cdot 100 \qquad (4.17)$$

Starting from the baseline time-step size presented in section 4.2.3.3, a higher and two smaller time-step sizes have been calculated at working point 2, i.e., $\Delta t = 4°, 2°, 1°$ and $0.5°/step$. In this way, the presented cases will get significantly different Courant numbers (see equation 4.16), because the mesh is kept (6M cells) and flow velocities will be similar. The results of this study are presented in Figure 4.10 in terms of non-dimensional EGR deviations (Δy_{avg}, as defined in equation 4.10).

Looking at Figure 4.10, most of the runners follow an asymptotic trend regarding the variable Δy_{avg} as time-step size is reduced, e.g., the closest case to the 0.5°/step is the 1°/step case. However, quantitative values are required to determine the point at which it is not worth it a further refinement of the time-step size.

Apart from the developed coefficients in equations 4.11 to 4.14 regarding the pollutant emissions, the developed models in section 4.2.1.1 will be useful to get an estimation of the differences between the analyzed cases. The λ

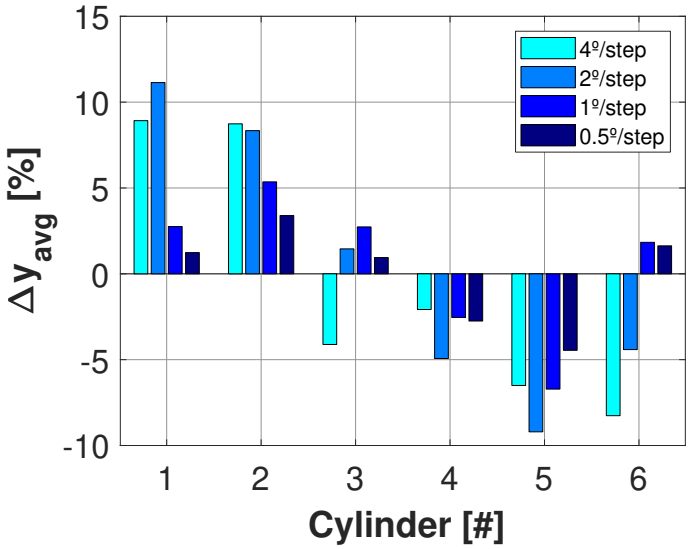

Figure 4.10: EGR rate deviation regarding Δy_{avg} for considered time-step sizes at working point 2 on 6 cylinder engine manifold.

parameter will be considered constant for every cylinder, taking the value of the experimental essays corresponding to the working point assessed (in this section, operating point 2). Therefore, applying the regressions appearing in Figure 4.2, the pollutant emissions produced by each cylinder can be obtained as equations 4.18 and 4.19.

$$NOx_i/NOx_{EGR=0} = \frac{A \cdot e^{-B\cdot(y_i\cdot\lambda^{-1})}}{Z} \tag{4.18}$$

$$FSN_i = \frac{A\cdot(y_i\cdot\lambda^{-1})^3 + B\cdot(y_i\cdot\lambda^{-1})^2 + C\cdot(y_i\cdot\lambda^{-1}) + D}{Z} \tag{4.19}$$

Equations 4.18 and 4.19 assume that all cylinders present the same injection conditions and pressure in chamber. Hence, the impact of EGR dispersion predicted by a CFD simulation on emissions can be calculated using equations 4.18 and 4.19:

$$NOx\ [ppm] = \sum(NOx_i/NOx_{EGR=0})\cdot NOx_{EGR=0} \tag{4.20}$$

$$PM\ [g/h] = \frac{5.32 \cdot \sum(FSN_i) \cdot e^{0.3062 \cdot \sum(FSN_i)}}{0.405} \tag{4.21}$$

The transformation from the filter smoke number (FSN) to the PM mass flow presented in equation 4.21 has been used previously in the work of Maiboom et al. [125]. The presented coefficients have been applied to the time step independence study as exposed in Table 4.5. In addition, an average of the Courant number (equation 4.16) in a section after the mixer and the mass flow rate imbalance (equation 4.17) are shown for all the cases.

Table 4.5: Coefficients of time-step size independence study at working point 2 (6M cells baseline mesh). $RMSE$, ΔNOx, ΔPM coefficients are normalized and compared regarding the 0.5°/step case.

Coeff.	$RMSE$	COV	ΔNOx	ΔPM	$\overline{Cour}$	Imb.
Units.	[%]	[%]	[%]	[%]	[−]	[%]
4°/step	5.20	6.94	0.18	0.23	38.29	10.78
2°/step	4.79	7.31	0.20	0.26	18.28	5.17
1°/step	1.24	3.99	0.04	0.04	8.98	0.39
0.5°/step	-	2.71	-	-	5.10	0.35

Table 4.5 shows a significant improvement in terms of $RMSE$ when the time-step size is reduced from 2°/step to 1°/step, but seems not worth it to change the time-step size again to 0.5°/step due to the low changes. Regarding the pollutant emissions the changes are not so big, and all the cases gets very similar results, so according to this criterion, the coarsest time-step size could be used. However, the changes in Courant are quasi-linear and the values in 4°/step and 2°/step are noticeable high, producing non negligible values of mass flow rate imbalance (above 5%). Discarding therefore the latter cases, the time-step size is fixed in 1°/step to the rest of the document to get a good trade-off between accuracy and computational effort.

When the time-step size is fixed, the mesh independence study can be addressed taking into account the aforementioned limitations of the Courant number. The baseline mesh of this work is presented in Figure 4.11. The highest density of elements is located in the mixer zone, to resolve the mixing between air and EGR streams in a proper way. Thereby, this zone will be

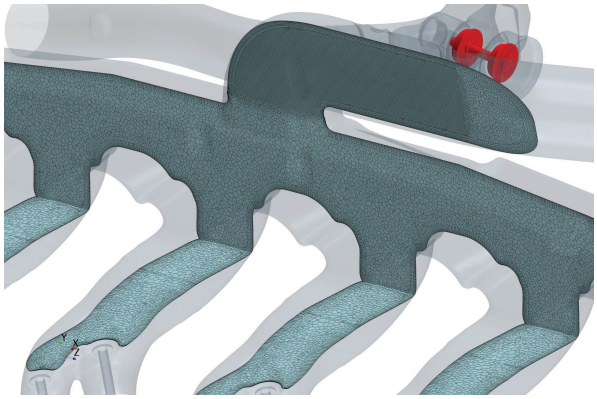

Figure 4.11: Sections of baseline mesh (6M cells) at manifold and cylinder runners.

critical in terms of Courant number, due to the high velocities coming from the air inlet and EGR valve, and the low cell size of the mesh. The relationship between the average cell size and the refinement size of the mesh is fixed for all the meshes. The baseline mesh presented in Figure 4.11 has 6M cells. 2 additional mesh have been developed to conduct the mesh independence study: a coarser mesh of 1.5M of cells and finer mesh of 15M elements. The results of the developed meshes in terms of Δy_{avg} (see equation 4.10) are presented in Figure 4.12.

As it can be noticed in Figure 4.12, some differences appear between the 1.5M mesh and the higher refinement meshes of 6M and 15M. The coarsest mesh provides the greatest dispersion and, apparently, a higher error compared to the most accurate mesh of 15M cells. This is confirmed in a quantitative way by considering the developed coefficients in equations 4.11, 4.12, 4.20, 4.21; which are obtained for this mesh independence study and presented in Table 4.6 with the corresponding values of mean Courant number and mass flow rate imbalance.

In terms of the $RMSE$ coefficient, the improvement by refining the mesh is significant when passing from a coarser mesh of 1.5M to a finer mesh of 6M, but this change is not so remarkable between the baseline mesh and the 15M mesh. Regarding the emissions indicators, the improvement in NOx and PM prediction as the mesh is refined is slight but consistent to the reduction of $RMSE$, with differences below 0.6%. The Courant number is obviously higher in the 15M mesh, but the impact in terms of accuracy (imbalance) is

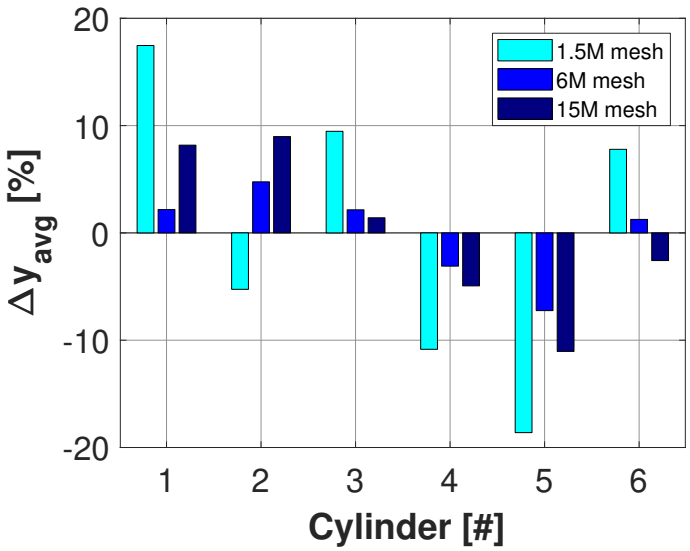

Figure 4.12: EGR rate deviation regarding Δy_{avg} for different mesh refinements at working point 2.

negligible. Taking into account these coefficients, it seems a reasonable decision to maintain the 6M mesh as the final mesh for further validations. In any case, the coarser mesh of 1.5M could have been used with little penalty on emission predictions if computational resources were scarce.

Table 4.6: Coefficients of mesh independence study at working point 2. $RMSE$, ΔNOx, ΔPM coefficients are normalized and compared regarding the 15M case.

Coeff.	$RMSE$	COV	ΔNOx	ΔPM	$\overline{Cour}$	Imb.
Units.	[%]	[%]	[%]	[%]	[-]	[%]
1.5M	8.32	12.56	0.46	0.55	2.45	0.11
6M	3.30	3.99	-0.14	-0.18	8.98	0.39
15M	-	7.10	-	-	12.50	0.59

4.4 Validation

Once the mesh and the time step size have been fixed, the numerical models must be validated against the experimental measurements. The structure of this section will be the same for every manifold and operating point: first, the average cylinder-to-cylinder EGR distribution is displayed, including a quantification of the differences between the predictions and the experimental measurements. Then, cycle-resolved traces of CO_2 are depicted and discussed.

4.4.1 4 cylinder engine

This section starts with the validation of operating point B, taking into account that is the point used in the sensitivity studies of the previous section. The average results of this calculations are depicted on Figure 4.13:

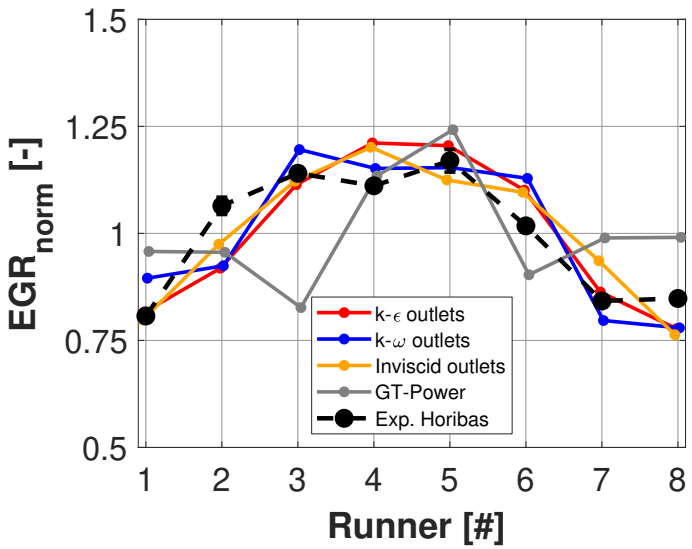

Figure 4.13: EGR rate (Y-axis) of every manifold runner (X-axis) for different turbulent submodels and experimental data (black-dashed) with vertical bars of measurement dispersion of operating point B of 4-cylinder manifold.

Figure 4.13 shows the EGR rate of every runner for all the 3D turbulence submodels and 1D model, in comparison with the experimental data. Taking into account that the experimentally measured EGR rates oscillate during the

acquisition period, a vertical bar is added to the average experimental results, calculated as the standard deviation of these fluctuation over the sampling window. Regarding the EGR distribution, in this operating point, seems that EGR is more swallowed in the experiments by the runners 1 to 4 than the final ones. However, the EGR rate in runner 2 is higher than its symmetric runner (runner 7). For that reason, the EGR distribution is not very symmetrical but do not have much curvature. In addition, it is necessary to notice that the distributions are depicted runner-by-runner instead cylinder-to-cylinder to avoid the errors that the mean of the runners can introduce, diluting the differences between runners, and making the distributions too much equals. Regarding the comparisons between turbulence submodels, at first sight, in Figure 4.13, all of them have captured in an acceptable way the tendencies of experimental EGR rate results.

Table 4.7: Statistical coefficients of operating point B validation of 4-cylinder manifold.

Coeff.	$RMSE$	COV	ϵ_{COV}[%]	SF	CF
Units.	[%]	[%]	[%]	[−]	[−]
$k-\varepsilon$	7.55	16.51	-20.49	0.0048	0.0939
$SST\ k-\omega$	8.02	16.11	-17.61	0.0343	0.0230
Inviscid	7.13	15.05	15.05	0.0092	0.1747
1D model	15.55	12.23	12.23	0.0197	-0.0017
Experimental	-	13.70	-	0.0694	0.1257

Paying attention to the presented coefficients in Table 4.7 while the $RMSE$ is almost the same in all the 3D models, the SF of the $SST\ k-\omega$ submodel is closer to the experimental results than the others submodels. However, the trends are not so clear in the other coefficients, because in the CF the inviscid model is closer to the experimental data as well as in the ϵ_{COV} coefficient. In addition, the 1D model clearly presents a low accuracy when trying to capture the main trends of the EGR dispersion. However, it is better than not considering EGR cylinder-to-cylinder at all (constant EGR rate), since at least it predicts a greater EGR rate in the inner cylinders. Therefore, the temporal shift between the intake and EGR pulses, which is predicted by the 1D model, is one of the main factors that drives the EGR dispersion. Considering that all 3D models (including the inviscid) improve the prediction over the 1D model, a proper resolution of the advection term is important to simulate the air-EGR mixing and thus predict EGR distribution. Finally, the negligible difference

between inviscid and turbulent models suggest a minor role of the diffusion mechanism in the air and EGR mixing of this manifold in working point B.

The instantaneous results of operating point B, have been modified by the smoothing process explained in section 4.2.4.3. The comparison of these numerical results against the non-dimensional CO_2 of the experimental data is depcted in figure 4.14:

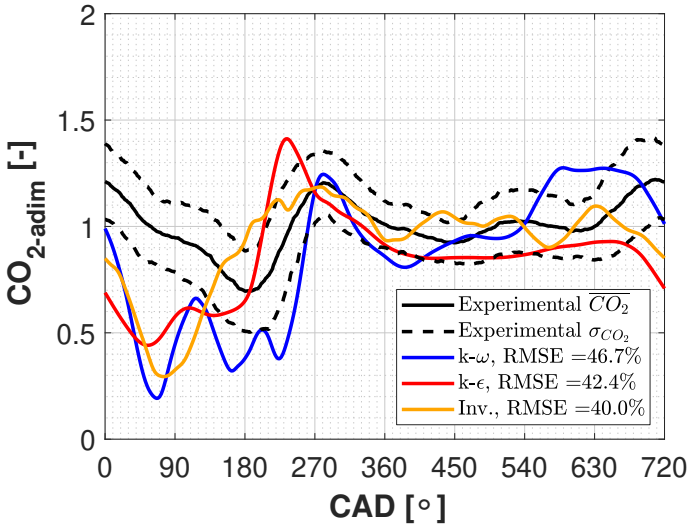

Figure 4.14: Filtered of instantaneous traces of CO_2 in comparison with experimental data in operating point B of 4-cylnder manifold.

First of all, the behavior of the 3D models is much more oscillating than the experimental measurements, and the influence of the different events that can be produced into the manifold is very clear, in spite of the smoothing process that was aforementioned. In this operating point, the similarity of the traces of inviscid model in comparison with the other turbulent submodels is noticeable. Although the low frequencies oscillations seems to be well-captured by the numerical models, lots of high frequencies oscillations are avoided in the experimental results. In fact, the σ of the experimental traces in this operating point is remarkable.

Regarding the other operating points, the results obtained by imposing the boundary conditions coming from point A are presented in Figure 4.15:

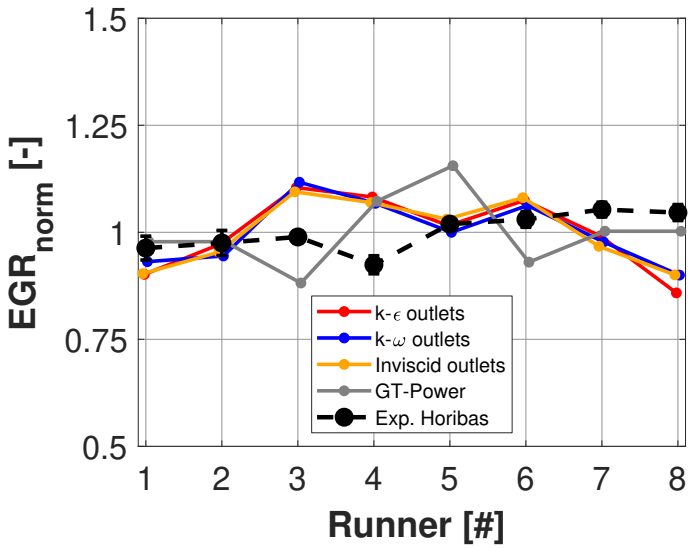

Figure 4.15: EGR rate (Y-axis) of every manifold runner (X-axis) for different turbulent submodels and experimental data (black-dashed) with vertical bars of measurement dispersion of operating point A of 4-cylinder manifold.

This operating point has a very low BMEP and r.p.m. and very high EGR rate as was mentioned in Table 4.1, so these conditions are representing a nearly idle point of the engine. In this operating point, experimental results have a very flat distribution of EGR, because all the runners have very similar EGR rates, with a little growing trend to the final runners (5 to 8). This behavior is common on these operating points with high EGR rate and lower loads, obtaining more flat distributions as was proved in the works of William et al. [134]. On the other hand, turbulence submodels predict almost identical behaviors, qualitatively but quantitatively too, even the inviscid model, so diffusion seems to play a secondary role again. In fact, in table Table 4.8 all the $RMSE$ coefficients of the 3D models are almost the same. The shape of the CFD distribution is more symmetric than the experimental results and the maximum rates are higher. Moreover, although the one-dimensional model has a very different distribution in comparison with the 3D-models, the differences in terms of $RMSE$ or ϵ_{COV} are in the same order in comparison with experiments and the CF is ~ 0. At the end, this operating point is the less reliable to obtain conclusions in terms of numerical models, due to the low r.p.m. and the high EGR rate closer to idle conditions.

Table 4.8: Statistical coefficients of operating point A validation of 4-cylinder manifold.

Coeff.	$RMSE$	COV	$\epsilon_{COV}[\%]$	SF	CF
Units.	[%]	[%]	[%]	[−]	[−]
$k-\varepsilon$	10.20	8.22	-95.95	0.0076	0.1018
$SST\ k-\omega$	9.18	7.11	-69.46	0.0096	0.0454
Inviscid	9.20	7.39	-76.20	0.0019	0.0095
1D model	9.14	7.85	-87.16	0.0585	0.0585
Experimental	-	4.19	-	0.0237	0.0001

The instantaneous validation of operating point A is presented in Figure 4.16 which shows an instantaneous behavior more flatter than the previous operating point. In fact, the experimental results shows a nearly flat trace along the complete engine cycle, while the numerical models present some oscillations at the same part of the cycle. The inviscid approach gets even better results regarding the experimental data in comparison with the others turbulence submodels. Due to the low load of this operating point, the oscillation of the traces are very small.

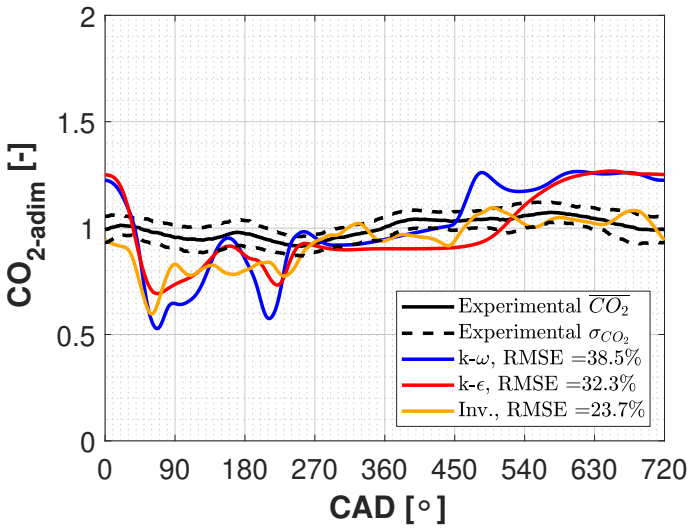

Figure 4.16: Filtered of instantaneous traces of CO_2 in comparison with experimental data in operating point A of 4-cylnder manifold.

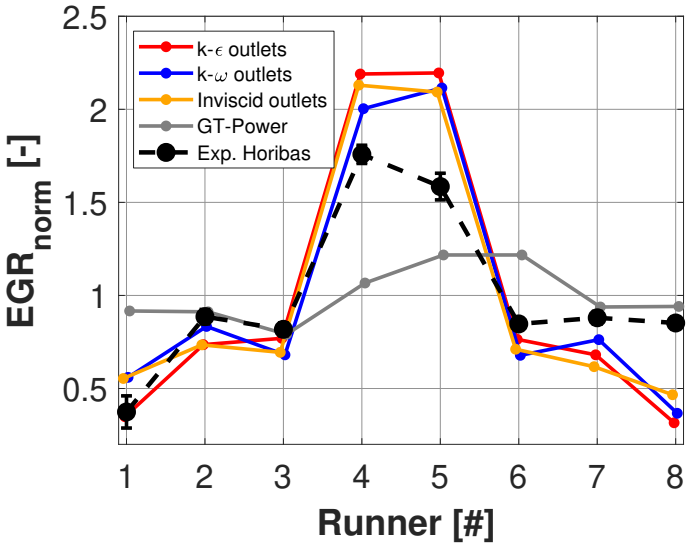

Figure 4.17: EGR rate (Y-axis) of every manifold runner (X-axis) for different turbulent submodels and experimental data (black-dashed) with vertical bars of measurement dispersion of operating point C of 4-cylinder manifold.

Results of operating point C are represented in Figure 4.17. This operating point has the same r.p.m. than point A, but BMEP is slightly higher, and the EGR rate has been reduced nearly 10 times. In Figure 8 the EGR rate differences between central runners and side runners are pronounced, giving to the distribution a "mountain" shape. Runners 4 and 5 (which corresponding to cylinders 2 and 3 respectively) have almost double EGR rate than the contiguous runners. From the point of view of the pollutant emissions, this type of distribution is the worst that can be appear, because the high rates in the central runners can produce an excessive amount of PM and the cylinders 1 and 4 may not reduce NOx in a proper way. However, these differences between runners can be diluted, because the average of the runners of low and high rates maybe the same than the nominal rate of the considered operating point, so probably the impact in terms of emissions would not be so strong. Regarding the 3D models, all turbulence submodels have captured these differences in EGR distribution too. Since neglecting diffusion (inviscid model) has little impact on the EGR dispersion, the advection mechanism again is much more relevant to the air and EGR mixing than diffusion also for working point C. It must be noticed that in these cases a higher EGR rate than the

experiments is obtained in central runners. Even the 1D model predicts a greater EGR rate in the inner runners but with not so great accuracy, so the temporal phasing between EGR and air pulses is somehow important.

The differences of the curves depicted in Figure 4.17 are analyzed in detail in Table 4.9. The COV coefficient is higher in every turbulence submodels than in experimental data because the 'mountain shape' is more pronounced in these cases. On the other hand, in terms of shape of the distribution, the CF factor of the $k-\varepsilon$, and SST $k-\omega$ are not so far of the experimental, due to that the distribution is well predicted in an acceptable way. Paying attention to this coefficient, is noticeable the differences between this operating point and the others in terms of convexity of the distribution. So, this coefficient can be a useful indicator to detect excessive different between contiguous rates. In this point, the one-dimensional model is not able to capture the main trends of the EGR dispersion, but the differences in terms of SF are not so big, because the equal rates of the initial and the final runners, hide the differences between the central runners. So, this behavior shows one limitation of this coefficient.

Table 4.9: Statistical coefficients of operating point C validation of 4-cylinder manifold.

Coeff.	$RMSE$	COV	ϵ_{COV}[%]	SF	CF
Units.	[%]	[%]	[%]	[−]	[−]
$k-\varepsilon$	33.88	70.86	-68.52	0.0041	0.3760
SST $k-\omega$	29.03	62.58	-48.83	0.0547	0.3346
Inviscid	29.64	64.69	-53.85	0.0230	0.1657
1D model	36.35	14.35	65.88	0.2057	-0.0038
Experimental	-	42.05	-	0.2593	0.2700

Figure 4.18 presents the instantaneous results of operating point C.

The instantaneous traces of the numerical models in Figure 4.18 present very similar behavior than the experimental data and between itself. It must be noticeable that the CO_{2-adim} range is 2 times higher than the previous operating points (see Figures 4.14 and 4.16), due to the important pulse at the middle of the engine cycle. Due to the amount of collected experimental cycles, the experimental data presents more "round" shape around the main pulses instead of having the high values of the numerical models, but proba-

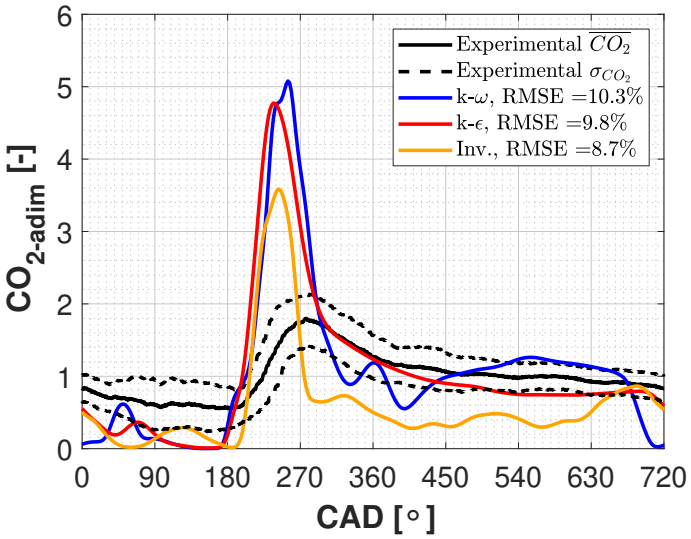

Figure 4.18: Filtered of instantaneous traces of CO_2 in comparison with experimental data in operating point C of 4-cylnder manifold.

bly in some independent engine cycles, the experimental data would present similar shape, taking into account the notable value of σ.

Finally, operating point D results are depicted in Figure 4.19. This operating point has a similar EGR rate than point C, but the load is very high so higher Reynolds number will be achieved.

The experimental EGR distribution in this operating point is almost symmetrical, but slightly displaced to the final runners. Regarding the 3D models, the EGR rate in the central runners is over-predicted, in a similar way than point B (Figure 4.13) in comparison with the experimental data. In addition, a larger difference in terms of EGR rate between $k-\varepsilon$ and SST $k-\omega$ has been obtained. While $k-\varepsilon$ submodel has predicted an almost symmetric dispersion, the SST $k-\omega$ has achieved an asymmetry closer to the obtained in the experimental results. In fact, in Table 4.10 the $RMSE$ of the SST $k-\omega$ is lower than the other submodels, in the same way of the SF. Regarding the CF the 1D model is the only with a $CF < 0$ in the same way than the experiments. This fact is due to the "valleys" of the distribution in the runners 3 and 6 (and the corresponding in the experiments in runners 2 and

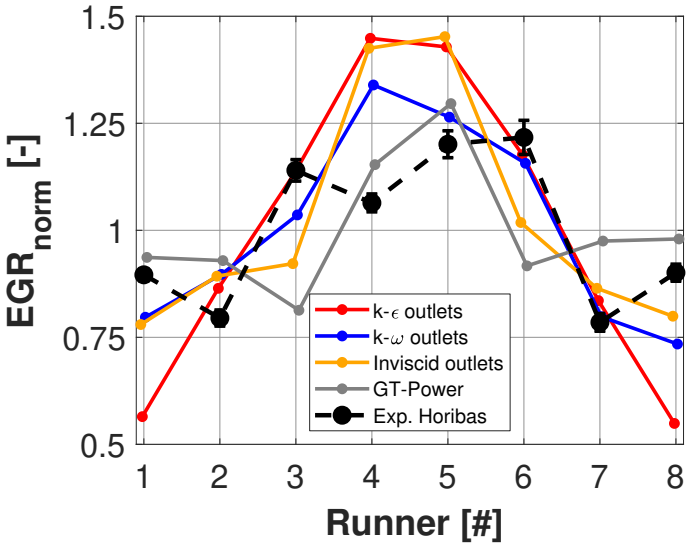

Figure 4.19: EGR rate (Y-axis) of every manifold runner (X-axis) for different turbulent submodels and experimental data (black-dashed) with vertical bars of measurement dispersion of operating point D of 4-cylinder manifold.

7) making the distribution more convex than concave, while the 3D models are predicting distributions with "mountain" shape, especially the $k-\varepsilon$ and inviscid submodels in the same way than point C.

Regarding the instantaneous results of operating point D, are presented in Figure 4.20

From a general point of view of the presented results in Figure 4.20, point D is the worst in the comparison with the experimental data. This mismatching is mainly produced by the average level of CO_2 in the experiments. Regarding this issue, the average level of CO_2 in this operating point (which is non plotted due to confidentiality issues) is two times higher than the average CO_2 level in point C with almost the same EGR rate (see Table 4.1). Considering that the experimental campaign of point D was carried out in different days and lower EGR rates are more difficult to be properly measured, the aforementioned differences could be due to a calibration error of the probe. In addition, although in Table 4.10 was obtained a huge difference with SST $k-\omega$ in comparison with $k-\varepsilon$, in this instantaneous comparison the differences are not so pronounced, but this model is closer to the shape of the experimental

Table 4.10: Statistical coefficients of operating point D validation of 4-cylinder manifold.

Coeff.	$RMSE$	COV	ϵ_{COV}[%]	SF	CF
Units.	[%]	[%]	[%]	[−]	[−]
$k-\varepsilon$	23.50	33.0	-99.04	0.0034	0.2931
$SST\ k-\omega$	13.30	21.6	-30.40	0.0338	0.0818
Inviscid	20.0	25.2	-52.2	0.0111	0.0890
1D model	18.6	14.3	13.9	0.0349	-0.0062
Experimental	-	16.6	-	0.0248	-0.1084

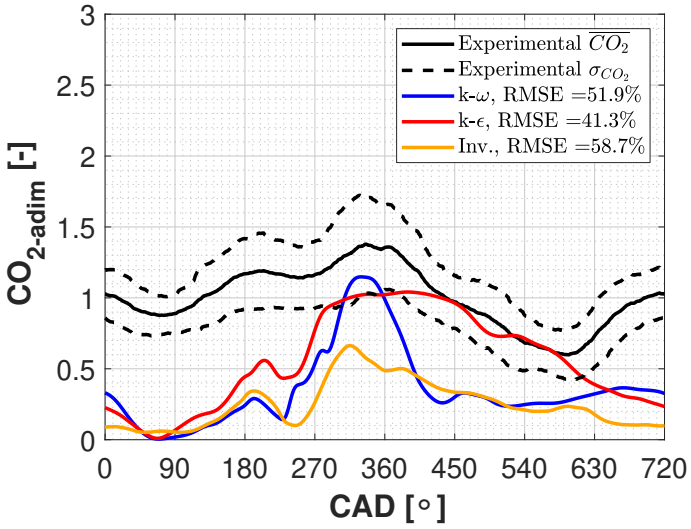

Figure 4.20: Filtered of instantaneous traces of CO_2 in comparison with experimental data in operating point D of 4-cylnder manifold.

traces than the other ones.

4.4.2 6 cylinder engine

It must be noticed that the numerical average results of this section are considered at the outlets of the domain (see Figure 4.5 and equation 4.1) instead of employing the $Horiba_{CFD}$ probes. By considering the real amount of EGR that enters into the cylinders, the comparison does not depend on flow het-

erogeneity inside the runners and is therefore consistent. Nevertheless, the average experimental results used in this section are extracted by the *Horiba* probes, so the deviations between CFD results obtained at $Horiba_{CFD}$ probes and outlet boundaries are displayed in the experimental results, following the developed methodology in section 4.2.4.2 and applying the confindence intervals ($\mu \pm 2\sigma$). On the other hand, the instantaneous results are extracted at the *Cambustion* probes, following the methodology of section 4.2.4.3.

Since operating point 2 has been used in section 4.3.2 to perform the whole sensitivities studies, it will be the first point to assess in this validation process.

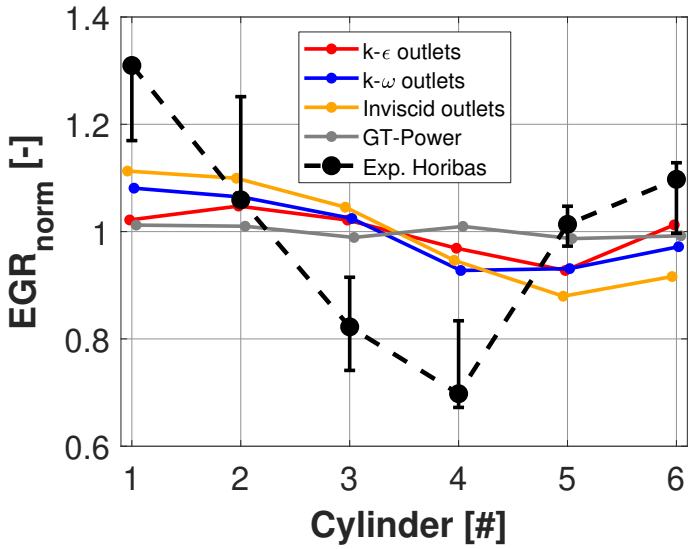

Figure 4.21: Normalized average of EGR rate at the outlets for the 3D-CFD models, 0D/1D model rates and experimental data at *Horiba* probes with experimental deviations of operating point 2.

In Figure 4.21, the X-axis represents the cylinder of the engine while the Y-axis represents the EGR rate normalized with the mean value, being considered at the outlets of the numerical models and at the *Horiba* probes in the experimental data. As aforementioned, the experimental results are presented with vertical bars that indicate the trends of the real amount of EGR that the cylinder would swallow, taking into account the deviations in CFD of the $Horiba_{CFD}$ probes (see section 4.2.4.2).

The comparison displayed in Figure 4.21 shows how the 3D models provide similar patterns in terms of EGR rate dispersion, whereas the GT Power prediction without any 3D model is almost flat. In the experimental data, the EGR distribution has a pronounced "V" shape, with almost twice as much EGR rate in cylinder 1 than in cylinder 4. However, the bias presented by the deviation bars plotted in the experimental data suggest that the *Horiba* probes in this operating point may be overstating the experimental EGR dispersion compared to what actually would be found in the cylinders (please see section 4.2.4.2).

Table 4.11: Coefficients of Point 2 validation. $RMSE$, ΔNOx, ΔPM coefficients are normalized and compared regarding the experimental data.

Coeff.	$RMSE$	COV	ΔNOx	ΔPM
Units.	[%]	[%]	[%]	[%]
$k-\varepsilon$	16.23	3.99	-1.57	-1.83
$k-\omega$	14.51	6.06	-1.48	-1.72
Invis.	15.92	9.05	-1.29	-1.5
0D/1D	16.87	1.07	-1.63	-1.90
Uniform	17.02	0	-1.63	-1.91
Exp.	-	19.66	-	-

To get a quantitative comparison, the coefficients used in section 4.3.2 have been applied in this validation section as well. The corresponding values of working point 2 are presented in Table 4.11. It must be noticed that the pollutants of the experiments used as reference in Table 4.11 (and in the remaining part of this section) are calculated with the regression developed in section 4.2.1.1 instead of directly employing the actual emissions measured at the corresponding operating point, with the aim of applying the same methodology in all considered EGR distributions. Apart from the experimental measurements, the 3D CFD results and the engine model values, a uniform distribution is considered to see the impact of having a certain EGR dispersion in terms of emissions. In Table 4.11 the $RMSE$ of the EGR distributions are almost the same for every numerical model (even the 0D/1D model). The EGR dispersion (COV) is noticeable for the experimental measurements due to the "V" shape presented in Figure 4.21, lower for the 3D CFD simulations, and almost null for the 0D/1D model alone. These differences are translated into a $1.3\% - 2\%$ of error in prediction of NOx and PM emissions. As a summary, the numerical models fail to predict the V-shaped EGR distribution, even though the

experimental sampling at Horiba probes magnifying this difference, because is not taken at cylinder ports.

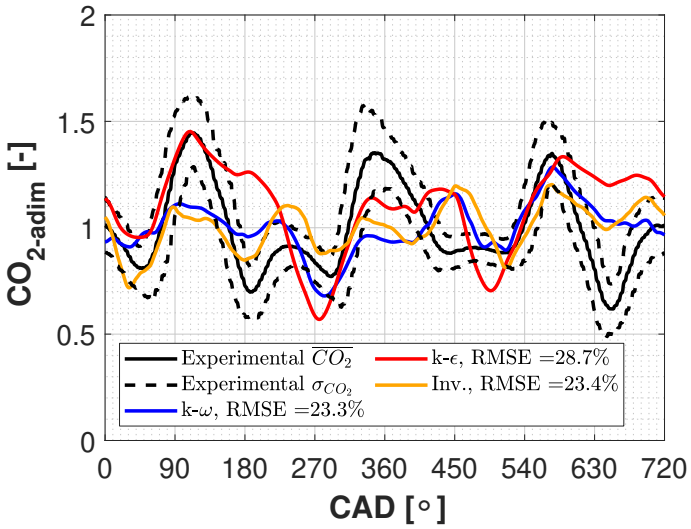

Figure 4.22: Normalized instantaneous traces of CO_2 for the 3D-CFD numerical models, and experimental data of operating point 2.

The cycle-resolved results are presented in Figure 4.22, in which the X axis represents the crank angle degree of the engine while the Y axis represents the normalized (regarding the mean experimental percentage) instantaneous CO_2 percentage. In this plot, the cyclic dispersion of the experimental data is represented by a solid line (average values) and two dashed lines (upper and lower confidence intervales, considering one standard deviation σ).

Considering the instantaneous results plotted in Figure 4.22, the qualitative phasing of the experimental is captured in a reasonable way, but the amplitude of each event is not properly predicted. Quantitatively, the value of $RMSE$ is presented in Figure 4.22, being calculated regarding the mean line of the experimental trace.

Operating point 1 was presented in Table 4.2 as a low load point with a medium-high EGR rate. This point is close to idle conditions. The comparison between time-averages EGR distributions is presented in Figure 4.23.

The results depicted in Figure 4.23 shows that both experimental and nu-

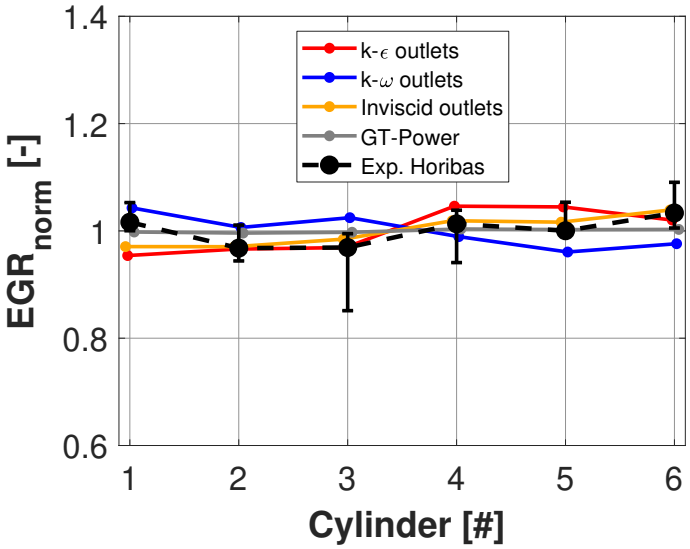

Figure 4.23: Normalized average of EGR rate at the outlets for the 3D-CFD models, 0D/1D model rates and experimental data at *Horiba* probes with experimental deviations of operating point 1.

merical distributions are quite flat (EGR evenly distributed). Also, the vertical bars of the experimental deviations are much lower compared to the previous operating point (see Figure 4.21). This flat behavior in EGR distribution is common in operating points with low loads and medium-high EGR rate as was demonstrated by William et al. [134].

Observing the numerical coefficients presented in Table 4.12 for this operating point, the $RMSE$ of the 3D models is almost the same, while the 0D/1D is even closer to the experimental results. Due to the flat behavior presented in Figure 4.23, the differences in terms of pollutant emissions are negligible.

Regarding the instantaneous comparisons presented in Figure 4.24, the $SST\ k-\omega$ submodel is closer to the experimental trace than the other numerical models, presenting a good qualitative and quantitative prediction of the experimental small fluctuations of CO_2. The oscillations of $k-\varepsilon$ submodel are much more aggressive, despite the smoothing effect due to the running average process explained in 4.2.4.3.

Table 4.12: Coefficients of Point 1 validation. $RMSE$, ΔNOx, ΔPM coefficients are normalized and compared regarding the experimental data.

Coeff.	$RMSE$	COV	ΔNOx	ΔPM
Units.	[%]	[%]	[%]	[%]
$k-\varepsilon$	2.98	3.82	0.02	0.01
$k-\omega$	3.66	2.80	0.01	0.00
Invis.	1.82	2.61	0.00	0.00
0D/1D	1.93	0.29	-0.02	0.00
Uniform	2.10	0	-0.02	0.00
Exp.	-	2.43	-	-

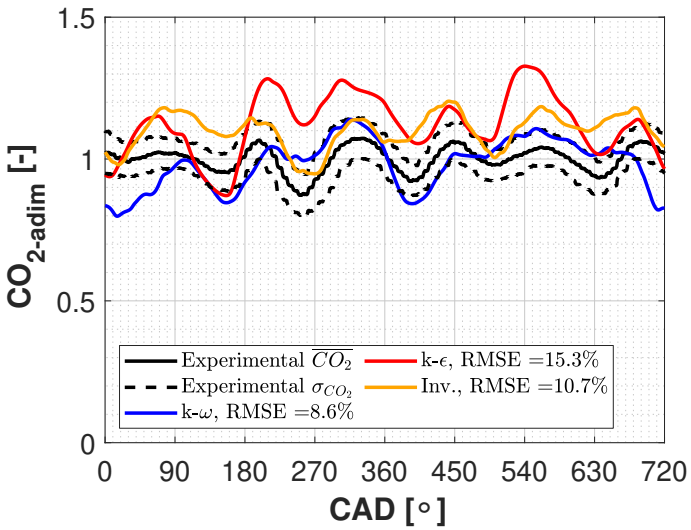

Figure 4.24: Normalized instantaneous traces of CO_2 for the 3D-CFD numerical models, and experimental data of operating point 1.

Operating point 3 was presented before in Table 4.2 as the point with greatest power, employing a low EGR rate. The average results of this operating point in terms of EGR cylinder-to-cylinder distribution are presented in Figure 4.25.

The patterns of the EGR dispersion shown in Figure 4.25 for operating point 3 are the only ones that strongly depend on the considered numerical model. The 0D/1D model is clearly not able to reproduce the experimental

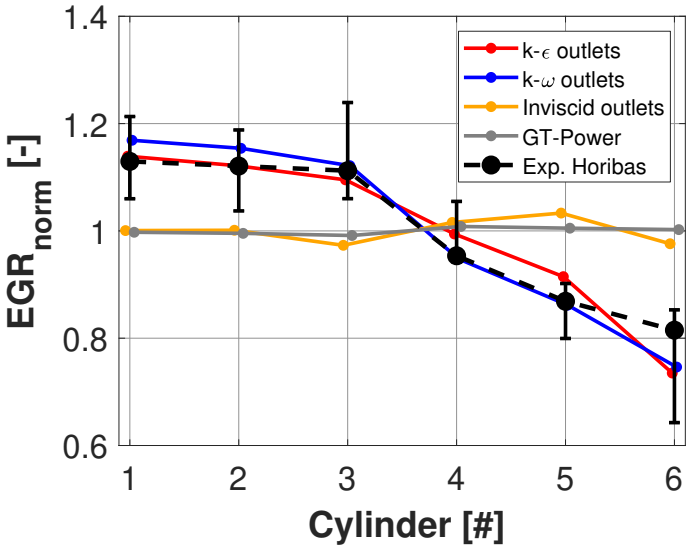

Figure 4.25: Normalized average of EGR rate at the outlets for the 3D-CFD models, 0D/1D model rates and experimental data at *Horiba* probes with experimental deviations of operating point 3.

results, providing a flat distribution in the same way than the other operating points (Figure 4.21 and Figure 4.23). The inviscid approach presents poor average results too, with a very flat distribution, almost the same than the 0D/1D model. On the contrary, both $k-\varepsilon$ and $SST\ k-\omega$ are clearly able to reproduce the behavior of the experimental results, in which there is a monotonous decrease in EGR rate when increasing the cylinder number. In fact, both submodels are within the intervals defined by the *Horiba* deviation bars.

As expected, the coefficients in Table 4.13 show the clear agreement between $k-\varepsilon$ and $SST\ k-\omega$ submodels and the experimental results, in terms of low $RMSE$ and similar COV. Nevertheless, in terms of pollutant emissions the differences between approaches (even uniform distribution) are very low, showing little sensitivity of emissions to EGR dispersion at this operating point.

The instantaneous comparison presented in Figure 4.26 is in accordance with the average results because both $k-\varepsilon$ and $SST\ k-\omega$ present a good agreement with the experimental trace of CO_2. All these three curves present

Table 4.13: Coefficients of Point 3 validation. $RMSE$, ΔNOx, ΔPM coefficients are normalized and compared regarding the experimental data.

Coeff.	$RMSE$	COV	ΔNOx	ΔPM
Units.	[%]	[%]	[%]	[%]
$k-\varepsilon$	3.63	14.19	0.02	-0.03
$k-\omega$	3.07	15.98	0.21	-0.20
Invis.	11.57	2.10	-0.27	0.30
0D/1D	11.42	0.58	-0.28	0.31
Uniform	11.04	0	-0.28	0.31
Exp.	-	12.75	-	-

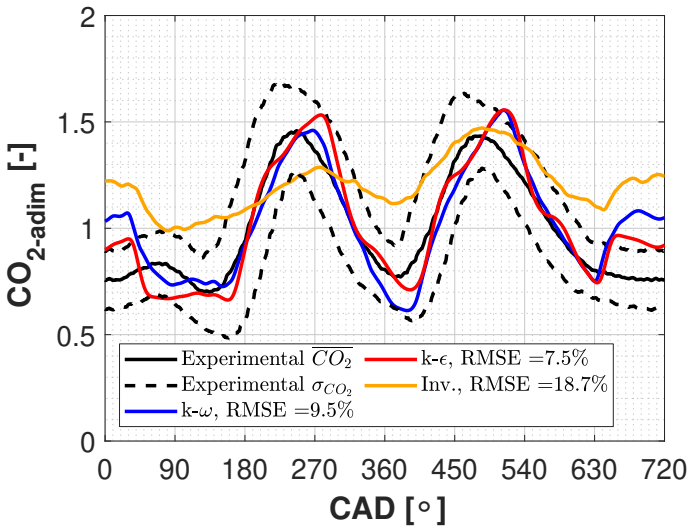

Figure 4.26: Normalized instantaneous traces of CO_2 for the 3D-CFD numerical models, and experimental data of operating point 3.

two major oscillations and a third one of minor entity, whereas 6 peaks are expected for a 6 cylinder engine. This is explained by the Cambustion probe location, which is near the entrance of the 4^{th} runner, as indicated in section 4.2.3. Therefore, depending of the flow pattern at the corresponding operating condition, some EGR pulses may not go through the probe at all. On the other hand, the inviscid model is not able to predict the phasing and intensity of the oscillations in a proper way.

4.4.3 Sensitivity of emissions to EGR dispersion in 6 cylinder engine

For all the cases analyzed in section 4.4.2 so far, the error in terms of pollutant emissions (NOx and PM) against the experimental results are below 2%. Since even uniform distributions have been considering, with $RMSE$ reaching values of 17% (see Table 4.11), the impact of EGR distribution on emissions is low for the studied working points. In the remaining part of this section, the experimental results are employed to assess the sensitivity of emissions to EGR dispersion at different operating conditions, considering a EGR flat distribution as a baseline (EGR rate evenly distributed). To do so, two degrees of freedom are considered. On the one hand, $EGR \cdot 1/\lambda$ factor presented in Figure 4.2, which carries the information of the engine working point. On the other hand, the dispersion itself, which takes into account the mixer and manifold design. To be able to change the latter, the original difference between the EGR rate on a certain cylinder and the average EGR rate is modified by a factor k, thus keeping the same mean EGR. Therefore, the modified EGR rate in the cylinder will be calculated as:

$$EGR_{i-mod} = y_{i-mod} = (y_i - \overline{y}) \cdot k + \overline{y}, \qquad k \geq 0. \tag{4.22}$$

Notice that $k = 0$ in equation 4.22 provides a flat distribution whereas $k = 1$ is the original EGR cylinder-to-cylinder dispersion of the experimental results. In this way, the regressions shown in equations 4.18 and 4.19 allow to interpolate the NOx and PM pollutant emissions of the 6 cylinders by means of modifying the average EGR (and thus $EGR \cdot 1/\lambda$) or dispersion proportionality factor k in equation 4.22.

These emissions are normalized considering the contaminants that a flat distribution with the same mean level of $EGR \cdot 1/\lambda$ factor, would produce, i.e.,

$$\varepsilon_{NOx}(k)\ [\%] = \frac{NOx(k) - NOx(k=0)}{NOx(k=0)} \cdot 100 \tag{4.23}$$

$$\varepsilon_{PM}(k)\ [\%] = \frac{PM(k) - PM(k=0)}{PM(k=0)} \cdot 100 \tag{4.24}$$

This analysis is only conducted for working point 2, due to its high dispersion as was presented in Figure 4.21. The evolution of ε_{NOx} and ε_{PM} in terms of $EGR \cdot 1/\lambda$ and k is presented in Figure 4.27:

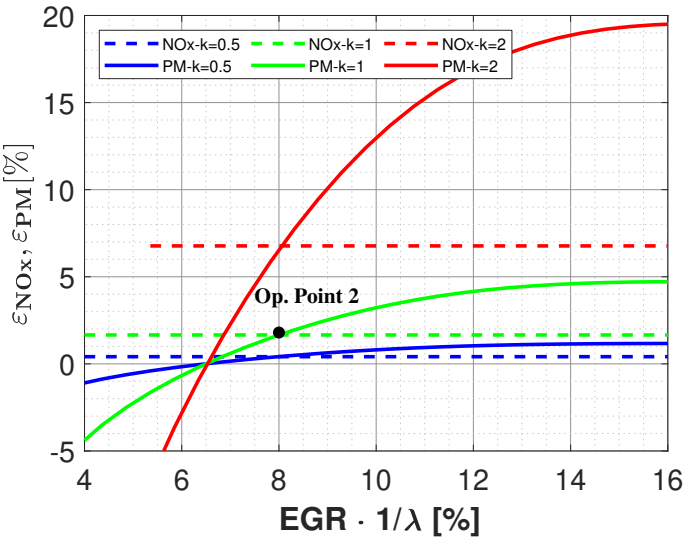

Figure 4.27: Relative differences of NOx and PM emissions between dispersed and flat EGR distributions for Operating Point 2, considering experimental results.

The situation studied in this work for working point 2 ($EGR \cdot 1/\lambda = 8$, as shown in Table 4.2, and $k = 1$) is represented as a dot in Figure 4.27, with a difference in emissions between the actual case and a flat distribution below 2% (see Table 4.11). Considering the same dispersion proportionality factor $k = 1$, an increase in EGR rates to fulfil future emission standards does not affect to the importance of EGR distribution in NOx (green dashed line), due to its exponential regression law (Figure 4.2). On the contrary, the PM fitting suggests an increasing importance of EGR dispersion as the EGR rate is higher, reaching an asymptotic behavior of 5% when doubling the EGR rate ($EGR \cdot 1/\lambda = 16$) with the current dispersion ($k = 1$).

If the dispersion was reduced (blue lines in Figure 4.27 correspond to $k = 0.5$), the impact of EGR dispersion in emissions would be 1% at worst-case scenario. In this way, the effort of predicting the cylinder-to-cylinder EGR distribution is likely not justified. However, if the manifold or mixer design provide a strong EGR dispersion (red lines in Figure 4.27 correspond to $k = 2$), an accurate prediction of the EGR distribution is mandatory. For operating

point 2 with current EGR rate, NOx emissions would be miscalculated by 7% if EGR dispersion is neglected. This error would reach 13% for PM (red solid line) with a future situation in which EGR rate is increase by 25% ($EGR{\cdot}1/\lambda = 10$). Macián et al. [48] also noticed a sudden rise in PM emissions at highest $EGR \cdot 1/\lambda$ when EGR dispersion is increased.

4.5 Conclusions

To summary up this chapter, the following conclusions can be extracted:

- The methodology to predict EGR cylinder-to-cylinder distribution based on experiments, engine modeling and 3D CFD simulations of two different manifolds and operating points has been analyzed. Table 4.14 shows the computational effort of the simulation campaign conducted in a Intel Xeon E5-2630v3 (2.4GHz) processor for this chapter.

Table 4.14: Computational cost of chapter 4

Cases	12	9
Mesh size (millions)	1	6
Number of cores	16	16
Hours/case	38.17	330
Sum of kh*core	7.33	47.52

- Experimental probes for measuring average CO_2 can present significant deviations (up to 20%) in 6-cylinder manifold, when assessing the EGR swallowed by each cylinder, regardless of being located close to the corresponding runner as in the 4-cylinder manifold.

- A statistical regression for NOx and PM emissions is obtained, allowing to quantify the impact of EGR dispersion on emissions in the 6-cylinder manifold.

- When conducting mesh and time-step independence analysis, the Courant number must be considered, despite using transient implicit schemes. In this work, average advective Courant numbers above 15 result in lack of EGR mass conservation (imbalances greater than 5%). However, in the

4-cylinder manifold, considering that mesh is not so dense, a time step of 2° it is enough, which is in the same order than other works [58].

- In 6-cylinder manifold, at low power conditions, EGR distribution is flat, which is properly predicted even by the 0D/1D engine code alone (without CFD 3D). CO_2 transient traces present small oscillations and are qualitatively well captured even by the inviscid model. The homogeneity of the flow is explained by the good mixing between the EGR and air in the main duct, which sends the flow evenly to both sides of the manifold. Such great homogeneity is the reason why the improved geometrical resolution of the flow at the manifold provided by CFD 3D is not relevant in this working point. On the other hand, in the 4-cylinder manifold in points with low power (A and C), EGR distribution is very variable, and while in operating point A, distribution is so flat, in operating point C, EGR presents an inverted "V-shaped" form. The flat distribution in operating points with low load and higher rates was assessed too by William et al. [134].

- In 6-cylinder manifold, the working point at medium power presents a "V-shaped" EGR distribution with significant dispersion, even though its impact on NOx and PM emissions is below 2% compared to a flat distribution. The statistical regression suggests a greater sensitivity of emissions to EGR dispersion (7% for NOx and 13% for PM) if the EGR rate is increased by 25% and the dispersion is doubled. The proposed methodology (engine model+CFD 3D) fails at predicting the EGR distribution in terms of average EGR dispersion ($RMSE \approx 15$) and CO_2 transient traces ($RMSE \approx 15$). The flow behavior is challenging, as the mixer works in an intermediate mode and only a small fraction of the main duct flow is able to turn into the right side of the manifold. The flow presents significant concentration gradients, which cause the greatest deviations between the local CO_2 probes and their corresponding cross-section value (which contributes to the predicting error). Scale-resolving simulations such as LES [51, 52] could therefore present greater accuracy than URANS at these conditions. On the contrary, in operating point B of 4-cylinder manifold, the EGR rate is well-captured by the numerical models. In fact, the instantaneous traces follows the same trends than the local CFD measurement of CO_2 percentage.

- In 6-cylinder manifold, at high power conditions, EGR distribution is monotonously decreasing, which is properly predicted by both $k-\varepsilon$ and

$k-\omega$ turbulent submodels alike. CO_2 transient traces present significant oscillations which are accurately captured by these models, whereas the inviscid configuration provides a much flatter response. In the high power point of 4-cylinder manifold (point D), the average distribution of EGR is captured in an acceptable way by the $k-\omega$ submodel, while the other turbulence submodels present more symmetrical behavior. However, in the instantaneous traces, the experimental percentage seems that present a measurement error, which makes more harder get final conclusions in this operating point.

Chapter 4 Bibliography

[1] J. Galindo, H. Climent, R. Navarro, G. García-Olivas, S. Guilain, and R. Boubennec. "Effect of Numerical Configuration on Predicted EGR Cylinder-to-Cylinder Dispersion." In: *SAE Technical Paper*. 2020. DOI: 10.4271/2020-01-1113 (cit. on pp. ix, 106, 108, 113).

[5] J. Galindo, R. Navarro, D. Tarí, and G. García-Olivas. "Centrifugal compressor influence on condensation due to Long Route-Exhaust Gas Recirculation mixing." *Applied Thermal Engineering* 144 (2018), pp. 901 –909. ISSN: 1359-4311. DOI: 10.1016/j.applthermaleng.2018.09.005 (cit. on pp. x, 4, 22, 24, 25, 27, 28, 41, 42, 53, 54, 58, 61, 73, 124).

[11] N. Ladommatos, S. Abdelhalim, and H. Zhao. "The effects of exhaust gas recirculation on diesel combustion and emissions." *International Journal of Engine Research* 1(1) (2000), pp. 107–126. DOI: 10.1243/1468087001545290 (cit. on pp. 3, 99).

[12] J. M. Desantes, J. M. Luján, B. Pla, and J. A. Soler. "On the combination of high-pressure and low-pressure exhaust gas recirculation loops for improved fuel economy and reduced emissions in high-speed direct-injection engines." *International Journal of Engine Research* 14(1) (2013), pp. 3–11. DOI: 10.1177/1468087412437623 (cit. on pp. 3, 4, 22, 54, 99, 102).

[14] R. D. Reitz, H. Ogawa, R. Payri, T. Fansler, and S. Kokjohn. "IJER editorial: The future of the internal combustion engine." *International Journal of engine Research* 21 (1 2020), pp. 0–8. DOI: 10.1177/1468087419877990 (cit. on pp. 3, 100).

[16] F. Millo, P. F. Giacominetto, and M. G. Bernardi. "Analysis of different exhaust gas recirculation architectures for passenger car diesel engines." *Applied energy* 98 (2012), pp. 79–91. DOI: 10.1016/j.apenergy.2012.02.081 (cit. on pp. 4, 99).

[17] J. M. Luján, J. Galindo, J. R. Serrano, and B. Pla. "A methodology to identify the intake charge cylinder-to-cylinder distribution in turbocharged direct injection Diesel engines." *Measurement Science and Technology* 19(6) (2008), p. 065401. DOI: 10.1088/0957-0233/19/6/065401 (cit. on pp. 4, 7, 8, 99, 100, 108, 116).

[19] A. Maiboom, X. Tauzia, and J.-F. Hétet. "Influence of EGR unequal distribution from cylinder to cylinder on NOx-PM trade-off of a HSDI automotive Diesel engine." *Applied Thermal Engineering* 29(10) (2009), pp. 2043 –2050. ISSN: 1359-4311. DOI: 10.1016/j.applthermaleng.2008.10.017 (cit. on pp. 4, 7, 99).

[44] J. Galindo, R. Navarro, D. Tari, and F. Moya. "Development of an experimental test bench and a psychrometric model for assessing condensation on a Low Pressure EGR cooler." *International Journal of Engine Research* 22 (5 2020), pp. 1540–1550. DOI: 10.1177/1468087420909735 (cit. on pp. 7, 54, 111).

[47] J. M. Luján, H. Climent, B. Pla, M. E. Rivas-Perea, N.-Y. François, J. Borges-Alejo, and Z. Soukeur. "Exhaust gas recirculation dispersion analysis using in-cylinder pressure measurements in automotive diesel engines." *Applied Thermal Engineering* 89 (2015), pp. 459–468. DOI: 10.1016/j.applthermaleng.2015.06.029 (cit. on pp. 7, 10, 99, 102).

[48] V. Macián, J. M. Luján, H. Climent, J. Miguel-García, S. Guilain, and R. Boubennec. "Cylinder-to-cylinder high-pressure exhaust gas recirculation dispersion effect on opacity and NOx emissions in a diesel automotive engine." *International Journal of Engine Research* (2020). DOI: 10.1177/1468087419895401 (cit. on pp. 7, 10, 100, 106, 149).

[49] C. Guardiola, B. Pla, D. Blanco-Rodriguez, and P. O. Calendini. "ECU-oriented models for NOx prediction. Part 1: a mean value engine model for NOx prediction." *Proceedings of the Institution of Mechanical Engineers, Part D: Journal of Automobile Engineering* 229(8) (2015), pp. 992–1015. DOI: 10.1177/0954407014550191 (cit. on pp. 7, 100, 103–105).

[50] X. Tauzia, H. Karaky, and A. Maiboom. "Evaluation of a semi-physical model to predict NOx and soot emissions of a CI automotive engine under warm-up like conditions." *Applied Thermal Engineering* 137 (2018), pp. 521–531. DOI: 10.1016/j.applthermaleng.2018.04.005 (cit. on pp. 7, 100).

[51] A. Sakowitz and L. Fuchs. "Computation of mixing processes related to EGR." In: *TSFP digital library online*. Begel House Inc. 2011. URL: http://www.dl.begellhouse.com/en/references/3ce1b491115b5c16,60d8a9681cb3cfc7,57130c5b30e27450.html (cit. on pp. 7, 100, 109–112, 118, 119, 122, 150).

[52] A. Sakowitz, S. Reifarth, M. Mihaescu, and L. Fuchs. "Modeling of EGR Mixing in an engine intake manifold using LES." *Oil & Gas Science and Technology* 69(1) (2014), pp. 167–176. DOI: 10.2516/ogst/2013118 (cit. on pp. 7, 100, 112, 118, 150, 201, 204).

[53] A. Sakowitz, M. Mihaescu, and L. Fuchs. "Turbulent flow mechanisms in mixing T-junctions by Large Eddy Simulations." *International Journal of Heat and Fluid Flow* 45 (2014), pp. 135–146. DOI: 10.1016/j.ijheatfluidflow.2013.06.014 (cit. on pp. 7, 58, 65, 67, 100, 110).

[54] A. Sakowitz. "Computation and analysis of EGR mixing in internal combustion engine manifolds." PhD thesis. KTH Royal Institute of Technology, 2013. URL: http://www.diva-portal.org/smash/record.jsf?pid=diva2:603864&dswid=6780 (cit. on pp. 7, 100, 105, 110).

[55] S. Ramanathan, A. Hudson, J. Styron, B. Baldwin, D. Ives, and D. Ducu. *EGR and swirl distribution analysis using coupled 1D-3D CFD simulation for a turbocharged heavy duty diesel engine*. Tech. rep. SAE Technical Paper, 2011. DOI: 10.4271/2011-01-2222 (cit. on pp. 8, 107, 108, 112, 117, 200).

[56] S. K. R. Hariganesh, M Sathyanadan, S Krishnan, P Vadivel, and D Vamsidhar. "Computational analysis of EGR mixing inside the intake system & experimental investigation on diesel engine for LCV." *International Journal of Engineering Science & Technology* 3(3) (2011) (cit. on pp. 8, 108, 117, 119).

[57] R. Rahimi, S Jafarmadar, S. Khalilarya, and A Mohebbi. "Numerical and experimental investigations of EGR distribution in a DI turbocharged diesel engine." *Transactions of the Canadian society for me-*

chanical engineering 37(2) (2013), pp. 247–257. DOI: 10.1139/tcsme-2013-0015 (cit. on pp. 8, 107, 108, 111, 119).

[58] P. Dimitriou, R. Burke, C. D. Copeland, and S. Akehurst. *Study on the effects of EGR supply configuration on cylinder-to-cylinder dispersion and engine performance using 1D-3D co-simulation.* Tech. rep. SAE Technical Paper, 2015. URL: https://saemobilus.sae.org/content/2015-32-0816 (cit. on pp. 8, 100, 107, 110–112, 117, 119, 122, 150, 200, 202).

[59] P. Dimitriou, C. Avola, R. Burke, C. Copeland, and N. Turner. "A Comparison of 1D-3D Co-Simulation and Transient 3D Simulation for EGR Distribution Studies." In: *ASME 2016 Internal Combustion Engine Division Fall Technical Conference*. American Society of Mechanical Engineers. 2016, V001T06A010–V001T06A010. DOI: 10.1115/icef2016-9361 (cit. on pp. 8, 111, 117).

[64] *STAR-CCM+*. Release version 12.06.010. CD-adapco. 2018. URL: http://ww.cd-adapco.com (cit. on pp. 9, 26, 30, 34, 42, 59, 61, 100, 107, 112, 114, 119, 170, 190).

[69] J. M. Luján, C. Guardiola, B. Pla, and A. Reig. "Switching strategy between HP (high pressure)-and LPEGR (low pressure exhaust gas recirculation) systems for reduced fuel consumption and emissions." *Energy* 90 (2015), pp. 1790–1798. DOI: 10.1016/j.energy.2015.06.138 (cit. on pp. 10, 22, 54, 102).

[93] F. R. Menter. "Two-equation eddy-viscosity turbulence models for engineering applications." *AIAA journal* 32(8) (1994), pp. 1598–1605. DOI: 10.2514/3.12149 (cit. on pp. 60, 111).

[115] M. Pamminger, B. Wang, C. Hall, R. Vojtech, and T. Wallner. "The impact of water injection and exhaust gas recirculation on combustion and emissions in a heavy-duty compression ignition engine operated on diesel and gasoline." *International Journal of Engine Research* - (Jan. 8, 2019), pp. 0–19. DOI: 10.1177/1468087418815290 (cit. on p. 99).

[116] V. J. Page, C. P. Garner, G. K. Hargrave, and H. K. Versteeg. *Development of a validated CFD process for the analysis of inlet manifold flows with EGR.* Tech. rep. SAE Technical Paper, 2002. DOI: 10.4271/2002-01-0071 (cit. on pp. 100, 110, 111).

[117] M. Georgiou and M. V. Papalexandris. "Turbulent mixing in T-junctions: The role of the temperature as an active scalar." *International Journal of Heat and Mass Transfer* 115 (2017), pp. 793–809. DOI: 10.1016/j.ijheatmasstransfer.2017.08.081 (cit. on pp. 100, 110).

[118] S. Reifarth, E. Kristensson, J. Borggren, A. Sakowitz, and H.-E. Angstrom. *Analysis of EGR/Air Mixing by 1-D Simulation, 3-D Simulation and Experiments.* Tech. rep. SAE Technical Paper, 2014. DOI: 10.4271/2014-01-2647 (cit. on pp. 100, 110, 112).

[119] B Pla. "Análisis del Proceso de la Recirculación de los Gases de Escape de Baja Presión en Motores Diesel Sobrealimentados." PhD thesis. PhD Thesis, Universitat Politècnica de València, Departamento de Máquinas y Motores Térmicos, 2009. DOI: 10.4995/Thesis/10251/4782 (cit. on pp. 102, 105–107).

[120] Galindo, José and Climent, Héctor and Navarro, Roberto. "Modeling of EGR Systems." In: *1D and Multi-D Modeling Techniques for IC Engine Simulation.* Ed. by A. Onorati and G. Montenegro. SAE International, 2020. Chap. 7, pp. 257–278. DOI: 10.4271/9780768099522 (cit. on pp. 106, 107).

[121] P. E. Smirnov, T. Hansen, and F. R. Menter. "Numerical Simulation of Turbulent Flows in Centrifugal Compressor Stages With Different Radial Gaps." In: *Proceedings of GT2007.* GT2007-27376. ASME, 2007. DOI: 10.1115/GT2007-27376 (cit. on p. 111).

[122] Perry, R.H. "Physical and chemical data." *Perry's chemical engineers' handbook* (1984), pp. 7–374 (cit. on p. 111).

[123] F. M. White and I. Corfield. *Viscous fluid flow.* Vol. 3. McGraw-Hill New York, 2006 (cit. on p. 112).

[124] M. J. Moran, H. N. Shapiro, D. D. Boettner, and M. B. Bailey. *Fundamentals of engineering thermodynamics.* John Wiley & Sons, 2010 (cit. on p. 112).

[125] A. Maiboom, X. Tauzia, and J.-F. Hetet. "Influence of high rates of supplemental cooled EGR on NOx and PM emissions of an automotive HSDI diesel engine using an LP EGR loop." *International Journal of Energy Research* 32(15) (2008), pp. 1383–1398. DOI: 10.1002/er.1455 (cit. on pp. 117, 127).

[126] R. Navarro. *Predicting Flow-Induced Acoustics at Near-Stall Conditions in an Automotive Turbocharger Compressor: A Numerical Approach*. Springer, 2018. ISBN: 978-3-319-72248-1. DOI: 10.1007/978-3-319-72248-1 (cit. on p. 124).

[127] Sharma, Sidharath and García-Tíscar, Jorge and Allport, JM and Barrans, Simon and Nickson, AK. "Evaluation of modelling parameters for computing flow-induced noise in a small high-speed centrifugal compressor." *Aerospace Science and Technology* 98 (2020), p. 105697. DOI: 10.1016/j.ast.2020.105697 (cit. on p. 124).

[128] Ferziger, J.H. and Perić, M. *Computational Methods for Fluid Dynamics*. 3rd rev. Berlin: Springer, 2002 (cit. on p. 124).

[129] R. M. Cummings, S. A. Morton, and D. R. McDaniel. "Experiences in accurately predicting time-dependent flows." *Progress in Aerospace Sciences* 44(4) (May 2008), pp. 241–257. ISSN: 0376-0421. DOI: 10.1016/j.paerosci.2008.01.001 (cit. on p. 125).

[130] B. Lakshminarayana. "An Assessment of Computational Fluid Dynamic Techniques in the Analysis and Design of Turbomachinery." *Journal of Fluids Engineering* 113(3) (Sept. 1991), pp. 315–352. ISSN: 0098-2202. DOI: 10.1115/1.2909503. eprint: https://asmedigitalcollection.asme.org/fluidsengineering/article-pdf/113/3/315/5592525/315_1.pdf (cit. on p. 125).

[131] F. Balduzzi, A. Bianchini, R. Maleci, G. Ferrara, and L. Ferrari. "Critical issues in the CFD simulation of Darrieus wind turbines." *Renewable Energy* 85 (2016), pp. 419 –435. ISSN: 0960-1481. DOI: 10.1016/j.renene.2015.06.048 (cit. on p. 125).

[132] S. Družeta, L. Sopta, S. Maćešić, and N. Črnjarić-Žic. "Investigation of the importance of spatial resolution for two-dimensional shallow-water model accuracy." *Journal of Hydraulic Engineering* 135(11) (2009), pp. 917–925. DOI: 10.1061/(asce)0733-9429(2009)135:11(917) (cit. on p. 125).

[133] Z. Boz, F. Erdogdu, and M. Tutar. "Effects of mesh refinement, time step size and numerical scheme on the computational modeling of temperature evolution during natural-convection heating." *Journal of Food Engineering* 123 (2014), pp. 8–16. DOI: 10.1016/j.jfoodeng.2013.09.008 (cit. on p. 125).

[134] J William, A Dupont, R. Bazile, and M. Marchal. "Study of geometrical parameter influence on air/EGR mixing." *SAE transactions* (2003), pp. 1016–1036. DOI: 10.4271/2003-01-1796 (cit. on pp. 133, 143, 150, 201).

Chapter 5

Assessment of air-EGR mixing for different HP-EGR mixers and manifolds

Contents

5.1 Introduction

Considering that in this chapter the focus will be placed in the HP-EGR configuration, in chapter 4 of this document, a NOx model was developed using experimental measurements in the same engine under different conditions. Although the differences that dispersion can introduce in terms of NOx are not so significant once the main EGR rate is fixed, the effect in the PM emission is remarkable especially with higher differences between the EGR values in the cylinder.

In previous chapter, it was shown that the EGR cylinder-to-cylinder dispersion can be important when shifting operating conditions. The main effects that can influence in terms of EGR distribution are the diffusion effects, advective effects and pulsating effects, so it is clear that these effects will have an important role on the mixing in HP-EGR. The underlying idea of this chapter is the possibility of a lower or greater EGR maldistribution for the same working points assessed in chapter 4 when the mixer geometry is modified. For example, in terms of mixing, in chapter 3 the effects of mixing in condensation were deeply analyzed but the geometry was an standard T-junction. In chapter 4 and in this chapter, one of the mixers has radial form. Kartaev et al. [60] found a correlation between the radial penetration of the jet and the counter-flow jet penetration, using other J definition instead of the standard definition from [25] that is applied for T-junctions. In addition, Nada et al. [61] demonstrates that the penetration depth and the momentum ratio J are very important in terms of mixing ratio, even with geometrical modifications. Furthermore, geometrical modifications on the intake manifold, could have a strong impact on other performance characteristics, as was demonstrated by de Souza et al. [63] where they get an improvement in the volumetric efficiency adding a Helmholtz resonator before the intake valves. Thus, all modifications that are planned on a manifold, should check not only an improvement of performance, but also to guarantee that good air-EGR mixing is kept. In this chapter, volumetric efficiency will be considered to remain constant (inlet and outlet boundary conditions will not vary when replacing the mixer geometry), considering that the changes will only be applied to the mixers, not to the lengths or shapes of the manifold itself.

Obviously, EGR dispersion will not be affected only by modifications in

mixer (as studied in this chapter), but also by geometrical modifications in the manifold if any. A greater insight into distribution of turbulence and mixing has been provided by Minocha et al. [62]. In this study, a slightly similar manifold to the 6-cylinder manifold of the previous chapter is analyzed and some geometric modifications are performed. In their study, Minocha et al. demonstrates that the turbulent kinetic energy and the dissipation terms are really high near the initial T-junction but are negligible at the end of the manifold. In addition, Minocha reduces the non-uniformity adding a baffle which reduces the vortex formation after the T-junction [62]. It is clear that some modifications in the domain can be applied in order to improve the EGR dispersion in the manifold, but if the modifications are performed in the mixer, the final result could be very variable. Thus, one of the main issues in this chapter is the study of different mixers in the same manifold and operating conditions in order to achieve 2 important objectives:

- Study the influence of different mixers for each type of manifold (4-cylinders and 6-cylinders), in terms of mixing and EGR distribution in the cylinders, and validate the predictive capacity of the models that have been selected in the previous chapter. The achieved results of this analysis will be compared with experimental distributions of EGR following the same procedure than in chapter 4.
- Considering the achieved results, it could be interesting get some design guidelines in order to improve the mixing between air and EGR, regarding the manifold and operating conditions.

It is necessary to point out that this chapter focuses in 4-cylinder and 6-cylinder manifold geometries, that have been used too in the previous chapter. There are 2 reasons of select these geometries:

- The mixers of 4-cylinder manifold are very different in comparison of 6-cylinder manifold mixer. Mixer in 4-cylinder manifold presents a radial design, and the penetration of the jet follows this direction. On the contrary, the mixer in 6-cylinder manifold present a double T-junction design, with perpendicular penetration of the jet, in the same way than the T-junction of chapter 3.
- The main shape of the manifold is very different, while in 4-cylinder manifold is almost symmetrical and the EGR is injected near the center,

in 6-cylinder manifold EGR is injected very upstream of the cylinders, and not in a symmetrical position.

Thus, having 2 different type of mixers in 2 types of manifold, gives to this chapter a very wide point of view in order to get more universal results and behaviors, and a more strong base to provide design guidelines.

In addition, considering the definition of mixing index that have been developed in chapter 3 and the penetration of the jet in a T-junction J, it is necessary to compute the evolution of the mixing inside the manifold using different geometries and boundary conditions, in order to understand the main contribution to the final EGR dispersion on the cylinders. In addition, the effect of the pulses at the EGR inlet needs to be evaluated, trying to understand its final influence on the results. Thus, in section 5.2 the domains and the main index that it will be taken into account are assessed, including a new index in which the transient rate of EGR is analyzed. After that, with the same numerical configuration of previous chapter, all the results are presented in section 5.5, and the more important conclusions are exposed in section 5.6.

5.2 Numerical domains

5.2.1 Mixers of the 4-cylinder manifold, and corresponding postprocessing entities

The first manifold that is considered in this chapter is the 4-cylinder manifold that appears in chapter 4. For this chapter, two additional mixers have been added to analyze the influence of the geometrical changes. The geometries that will be considered in this manifold are presented in figure 5.1.

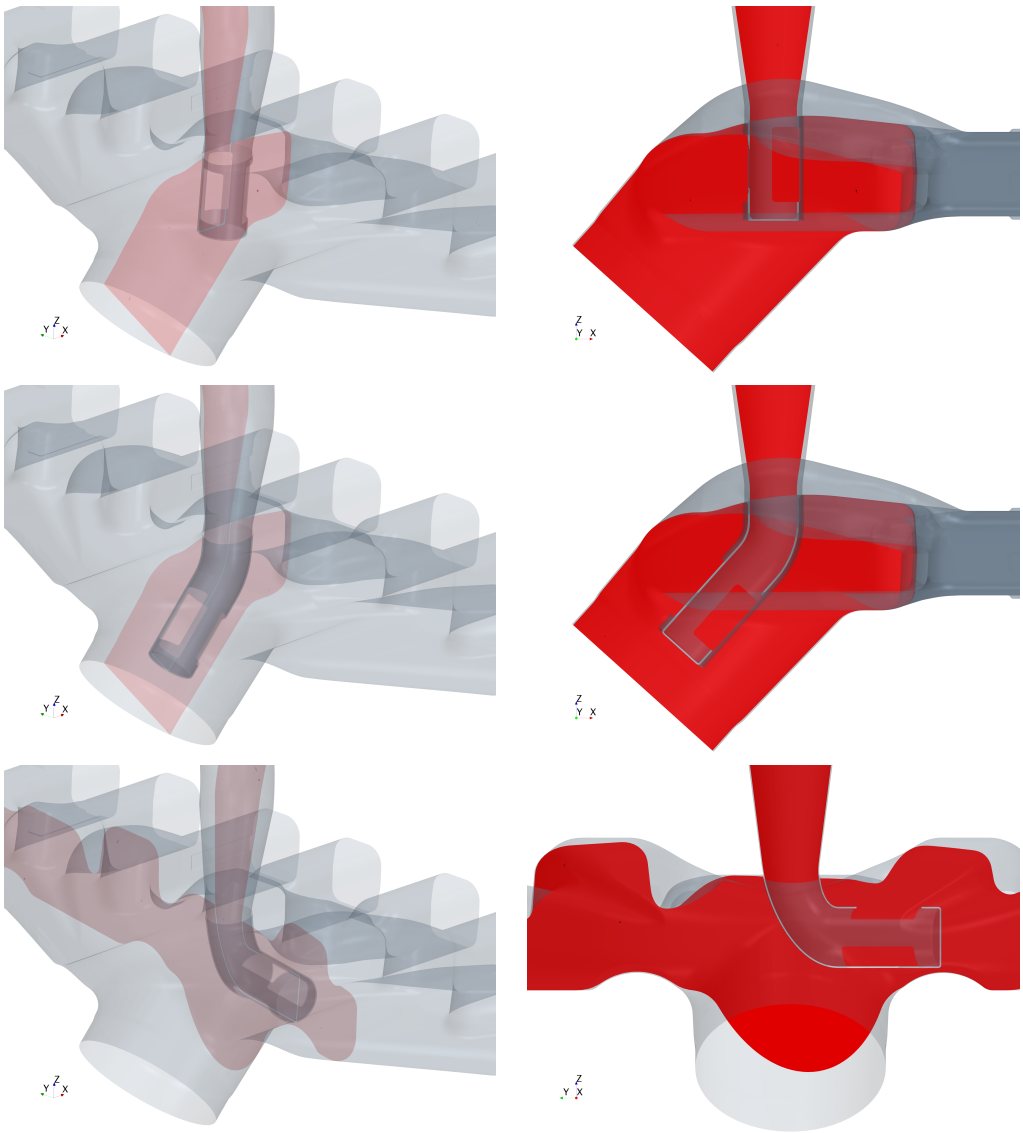

Figure 5.1: Internal geometry of 4-cylinder manifold and transversal mixer plane (left) with zoom in transversal mixer plane (right) for mixer 1 (top), mixer 2 (middle) and mixer 3 (bottom).

As figure 5.1 shows, the new mixers follow different trends of design. Mixer 1 is the same that the used in chapter 4, with a standard shape of a typical

radial mixer. Mixer 2, on the other hand, has been designed to enhance the interaction between the EGR and air streams. On the other hand, the main purpose of mixer 3 is opposed totally to the other mixers. This mixer is totally oriented to the final runners of the manifold. In fact, it has been designed to promote a poor EGR distribution on purpose, in order to assess the ability of the numerical model to predict such EGR dispersion, and compare the results with a well-designed mixer.

The next step, once the geometry is defined, lies in the placement of the different postprocessing in which different analysis will be considered. These planes are presented in figure 5.2.

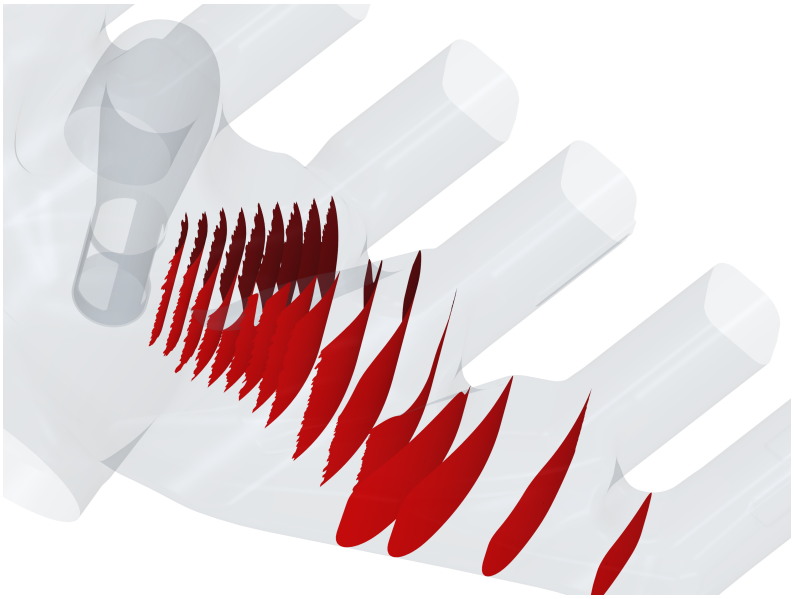

Figure 5.2: Representation of developed cylindrical postprocessing planes in 4-cylinder manifold in the zone of runner 5 to runner 8.

As figure 5.2 shows, different radial planes have been developed. However, compute the interesting variables in the whole radial plane will give false data in terms of dispersion and mixing. Thus, the best way to isolate the interesting data in this geometry, is to split the radial planes in different angle-intervals. In figure 5.2, the postprocessing planes have an opening of 60 degrees, and are oriented to the final cylinders (runners 5 to 8), in order to compute well mixer

3 too (see figure 5.1).

5.2.2 Mixers of the 6-cylinder manifold, and corresponding postprocessing entities

Regarding the 6-cylinder manifold, 2 additional mixers have been modelled too, taking into account that mixer 1 is the one used in chapter 4. To get an overall point of view of all the mixers, they are showed in figure 5.3. Figure 5.3 presents some differences between the considered mixers. Mixer 1 has an ascendent penetration in the main duct, with no very high windows and with a contraction of the main duct. In mixer 2, the window that is placed more upstream, has an important penetration in the below part of the main duct, while the other has an standard shape. Finally, mixer 3 presents a deeper penetration in the left part of the windows, trying to redirect the EGR flow to the main stream with the second window opposed to the air stream. The benefits or disadvantages of every mixer will be assessed in the next sections.

After that, as was performed in the previous manifold, the next step is to define the postprocessing section that will be considered in order to analyze the most important variables. These planes are showed in figure 5.4. As figure 5.4 exhibits, after the mixer, the postprocessing planes are in the main duct in which air and EGR will mix. After the elbow, the big volume of the manifold arrives, and some cylindrical planes are placed in order to analyze the mixing in a radial way since the end of the main duct. After that, only 1 trace have to be considered and for that, the rest of the planes are placed oriented to the final cylinders.

It is necessary to mention that, the $Horiba_{CFD}$ virtual probes that were presented in previous chapter (section 4.2.4), will be used throughout all this chapter in the 6-cylinder manifold, placed exactly in the same location than in the previous chapter (figure 4.5), in order to get proper comparisons with the experimental results that will be presented in next sections of this chapter.

5.3 Setup and operating points

In this chapter, all the analyzed features of the numerical setup will be applied in the analysis of the presented geometries. Thus, as a summary, the main

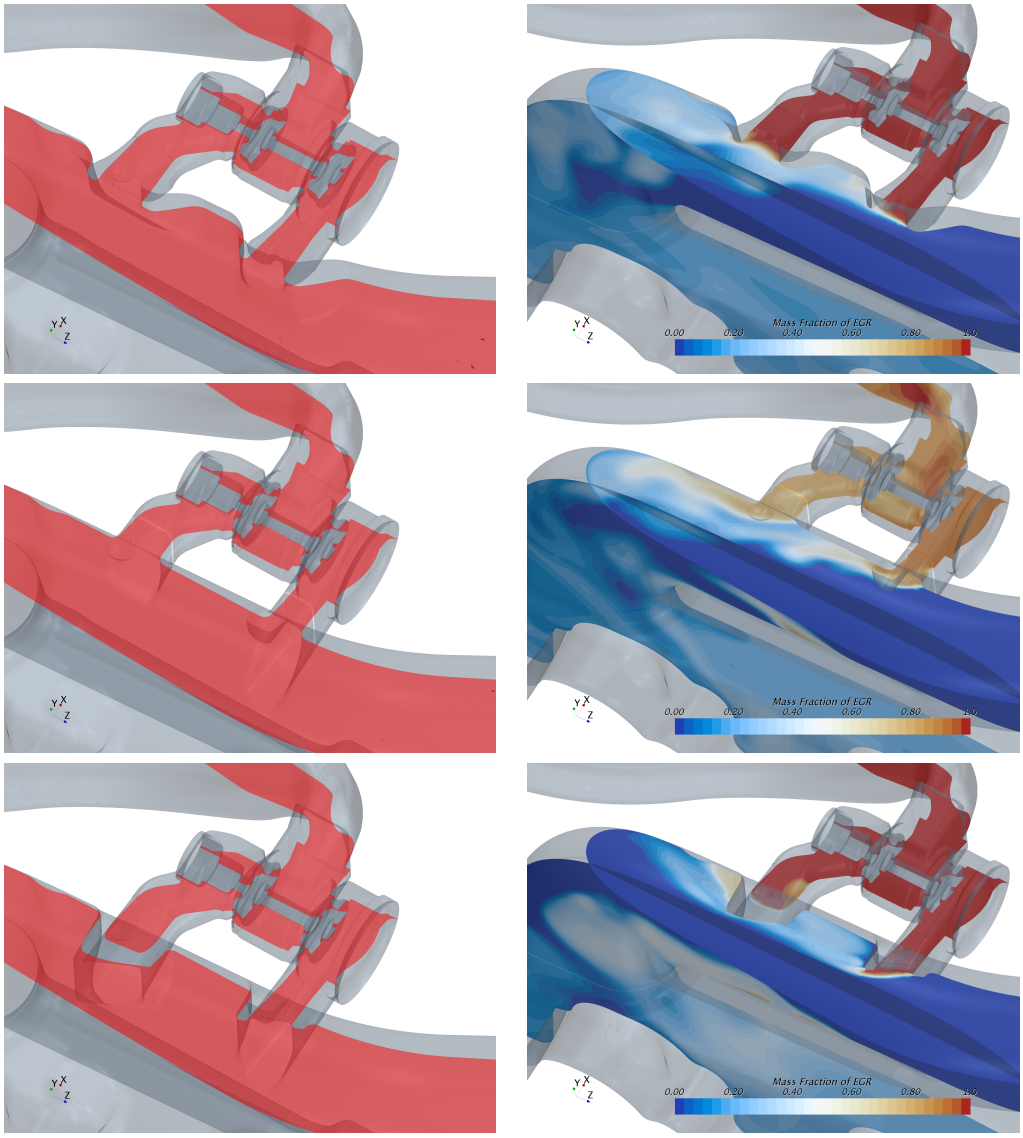

Figure 5.3: Internal geometry for transversal mixing plane (left) with EGR mass fraction contours in mixer zone (right) for mixer 1 (top, contraction of cross section of main duct), mixer 2 (middle, constant cross section of main duct) and mixer 3 (bottom, contraction and 2nd window in opposition of main duct).

Figure 5.4: Representation of developed postprocessing planes in 6-cylinder manifold, on 4-6cylinder zone.

parameters of the numerical setup are presented in table 5.1.

Table 5.1: Numerical Setup Summary

Manifold	4-cyl	6 cyl
Mesh	1M	6M
Time step	2 CAD	1 CAD
Turbulence model	SST $k-\omega$	SST $k-\omega$

In fact, these meshes have been selected after the corresponding independence mesh study for both manifolds, that was developed in sections 4.3.1 and 4.3.2. In these sections the time step independence study was performed too getting the values of table 5.1. Finally, turbulence submodel SST $k-\omega$ demonstrated a good performing in all the operating points of both manifold in section 4.4 of previous chapter. On the other hand, all the operating points that have been considered in the previous chapter, will be calculated too for every presented mixer. More details of these operating points, are presented in tables 4.1 and 4.2.

5.4 Definition of coefficients to assess air-EGR mixing

5.4.1 J definition

One of the most important parameters regarding the mixing is the penetration of the jet in the main stream. As was studied in chapter 3, J has an important influence in terms of mixing in low pressure EGR configurations. This parameter is very useful in order to define the characteristics of the flow inside a T-junction; lower values of J will provide a very attached EGR flow in the insertion, while with higher values of J the penetration of the flow is remarkable, as was presented in figure 3.9 of section 3.3.3. In addition, the influence of J in the mixing between the streams is patent as was presented in figure 3.12 of section 3.3.4. Therefore, it is mandatory to include this factor also in the analysis of HP-EGR mixing.

5.4.1.1 4 cylinder manifold

The 4-cylinder manifold will have some differences in terms of J definition, because the considered mixers are radial unlike the 6 cylinder manifold mixer that are T-junction form. In mixer 1, as figure 5.5 reveals, the orientation of the windows is very important, and must be enumerated in order to distinguish the contribution of every window to the global J index.

In figure 5.5, it is clear that the radial velocity at the outlet of the mixer is the main component that it has to be taken into account in order to compute the penetration of the EGR rate. On the other hand, the main component of the main stream that has to be computed in the J calculation is the tangential velocity. Obviously, the window that is in opposition of the main stream (window 2) the important velocity is the radial in the direction of the mixer.

Thus, the J coefficient in windows 1 and 3 is:

$$J_{w1-w3}(t) = \frac{\rho \cdot U_{rad-EGR}(t)^2}{\rho \cdot U_{tan-air}(t)^2} \cdot Y_{EGR}(t) \tag{5.1}$$

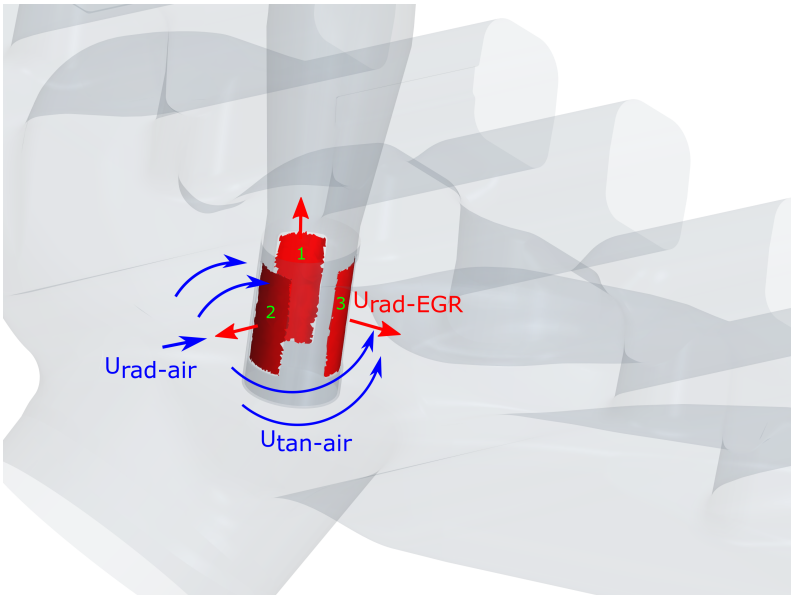

Figure 5.5: Representation of relevant velocities and sections of J coefficient calculation for mixer 1 of 4-cylinder manifold.

while on window 2, the definition of J is:

$$J_{w2}(t) = \frac{\rho \cdot U_{rad-EGR}(t)^2}{\rho \cdot U_{rad-air}(t)^2} \cdot Y_{EGR}(t) \tag{5.2}$$

It is important to mention that, in both equations, the parameter $Y_{EGR}(t)$ is included too. This is because in some intervals of the cycle, the radial velocity of EGR is < 0 and thus, the penetration cannot be computed well. Therefore, with this term, the J is balanced when the penetration is in the correct way. After applying this equation, 3 different J coefficients have been obtained, one for each window of the mixer. The final J coefficient will be obtained as the standard average:

$$J_{avg}(t) = \frac{J_{w1}(t) + J_{w2}(t) + J_{w3}(t)}{3} \tag{5.3}$$

Obviously, in the other 2 mixers, the definition has the same structure, changing between magnitude, radial or tangential velocity of air, depending on

the geometrical situation, while the numerator of the coefficient, will be always obtained using the radial component of the EGR stream in every window.

5.4.1.2 6 cylinder manifold

Regarding the 6-cylinder manifold, the situation in the mixers will be similar as the presented in figure 5.6:

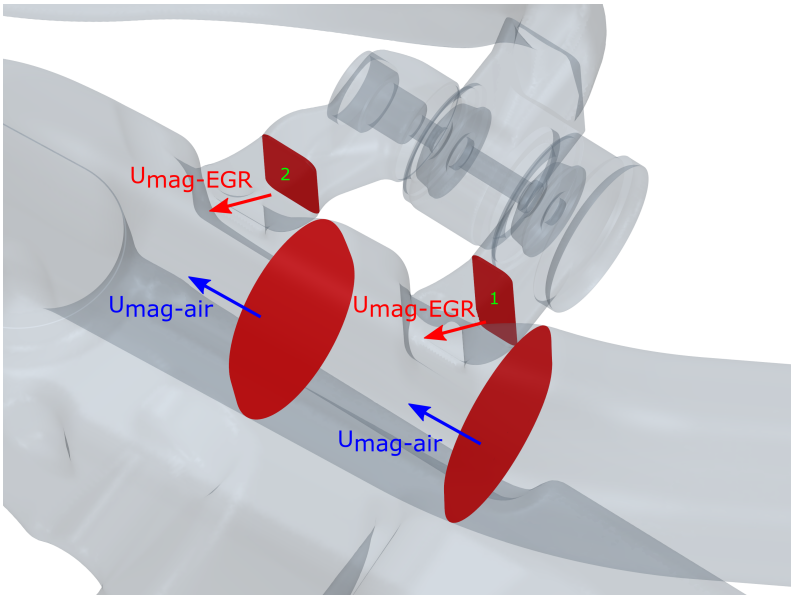

Figure 5.6: Representation of relevant velocities and sections of J coefficient calculation for mixer 1 of 6-cylinder manifold.

Figure 5.6 reveals that in the main duct have been defined 2 transversal planes, which everyone is upstream of the corresponding ducts of the mixer. At the same time, in the EGR line, 2 planes are defined in the division of the mixer. Thus, the definition of J in all the mixers is the same, with the same structure of equation 3.7 of chapter 3. In addition, this equation will be applied in the same way in the 3 considered mixers, since they all follow the same T-junction pattern (see figure 5.3).

5.4.2 Definition of mixing index

Obviously, in order to analyze the main contributions of every mixer in the EGR distribution, it is necessary to compute the mixing index in every post-processing planes that have been presented in figures 5.2 and 5.4. In chapter 3 it has been demonstrated that the mixing indexes that are based on the transport of a passive scalar correlate in a notable way with the mixing and J parameter as figure 3.12 shows. Thus, the selected mixing index will be the $MI_{\phi-new}$ that was defined in section 3.2.5.1 of chapter 3. This mixing index will be computed in the transversal sections provided by the depicted planes of figures 5.2 and 5.4.

5.4.3 TRI definition

It is necessary to mention that all the cases that will be analyzed in this chapter are transient. Thus, although the mixing index in a certain plane is around 1, the amount of EGR that is passing through this plane can be higher or lower than the desired quantity. Therefore, a transient rate index (TRI) is defined as:

$$TRI(t) = Y_{EGR}(t)/EGR_{rate} \tag{5.4}$$

Considering that the velocity is more important in this index, because the amount of EGR that is passing through a cell is more relevant than the surface distribution, the mass fraction of EGR Y_{EGR} is obtained with a mass flow averaged in the corresponding postprocessing plane [64]. With this index, a global point of view can be obtained regarding the transient distribution of EGR inside the manifold.

5.5 Results

5.5.1 EGR distribution results

The first way to understand how the geometrical modifications can have a remarkable impact in the EGR distribution is the comparison of the whole

results in every operating point. In this section, the figures will have the same configuration that the presented in the previous chapter. In fact, some results of figures 4.15, 4.13 4.17, 4.19, will be plotted again in this section. It is necessary to remember that the presented experimental results, have been obtained following the same procedure of chapter 4, as was stated in section 5.1. First of all, the results of 4-cyl engine are showed in figure 5.7.

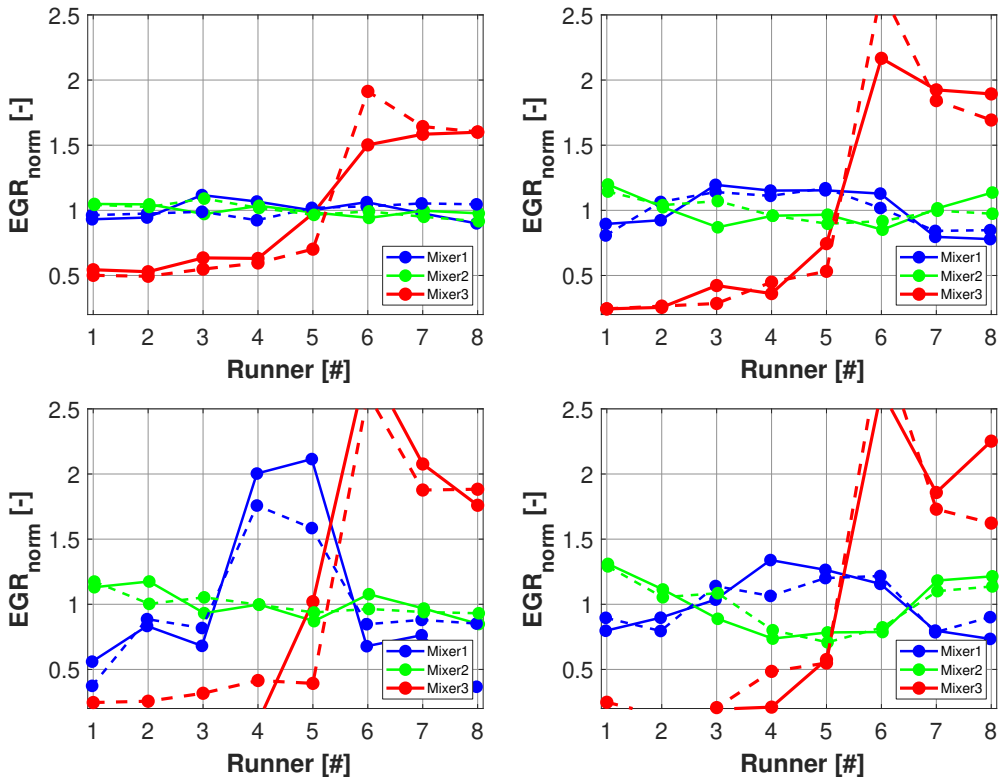

Figure 5.7: EGR distribution plots of operating point A (top left), B (top right), C (bottom left), D (bottom right) on 4-cyl manifold CFD (solid) and experimental measurements (dashed).

The presented results of figure 5.7 reveal very specific trends depending of the considered operating point. In operating point A, the achieved results show that the mixer 2 have no huge benefits in comparison with mixer 1. Both geometries get a very flat distribution of EGR showing that this operating point have enough mixing time due to the low load and the high rate

of the point. On the contrary, both numerical and experimental results show that mixer 3 have, obviously, a bad performance in terms of mixing due to his placement. As expected, the side at which mixer 3 is oriented (runners 5-8) presents higher EGR rate. This trend is validated too in the rest of the operating points.

Operating point B of figure 5.7 reveals that mixer 2 gets a slightly better performance than mixer 1, and the EGR distribution in the experimental and numerical way is flatter in general. Despite of that, the absolute differences are not so important. In the last operating point, the trends are similar to operating point B. In fact, this operating point have the same engine speed than point B, but higher load. Thus, the differences in terms of EGR distribution are not so relevant because although the distribution is more flat in the center, the side-cylinders swallow more EGR, in the opposite way than mixer 1.

On the other hand, in operating point C of figure 5.7 the benefits of mixer 2 are highlighted in comparison with mixer 1. In mixer 1, the EGR distribution is clearly not flat, and the side cylinders will get less EGR than the cylinders of the center. On the other side, mixer 2 gets a very flat distribution and the EGR is well-mixed in the whole domain, which is a more favorable situation.

After analyzing the results in 4-cylinder engine, the next step is to repeat the same procedure in 6-cylinder manifold, in order to capture the main trends of the geometrical modifications. These results are presented in figure 5.8 in the same way than figure 5.8. The results of mixer 1 in figure 5.8 are the same than the $k-\omega$ presented in figures 4.23, 4.21 4.25 of the previous chapter. In operating point 1, the original mixer 1 gets the more favorable EGR distribution in the whole manifold. On the other hand, the EGR has the same behavior with the other analyzed geometries. The EGR of the first cylinders is higher than the last cylinders so there is an indication that the EGR is transported by the main stream and the mixers do not help to the diffusion of the EGR.

In operating point 2, the experimental results of the 3 analyzed mixers are almost the same, and the characteristic V-shape is obtained in the same way. Thus, the geometrical modifications do not seem to produce any improvement

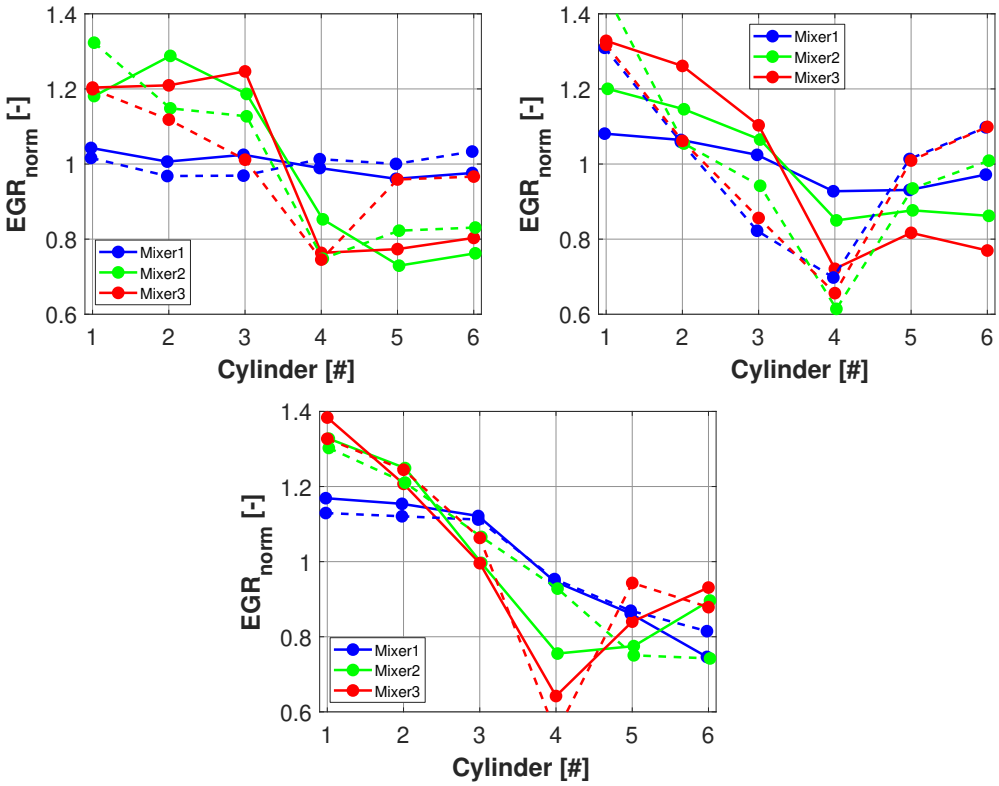

Figure 5.8: EGR distribution plots of operating point 1 (top left), 2 (top right), 3 (bottom) on 6-cyl manifold CFD (solid) and experimental measurements (dashed).

in this operating point. On the contrary, as was presented in previous chapter in figure 4.21, the numerical model is not able to achieve this distribution, getting a more flat mixing of EGR. This trend is maintained in mixer 2 but not in mixer 3. In fact, this mixer gets a V-shape too, but not as aggressive as in the experimental results.

Figure 5.8 shows that point 3 gets a very uneven distribution of EGR. However, in this case, the other mixers get even worst results than the original 1. In fact, mixer 2 and 3 gets a more aggressive results in the experimental but in the numerical way too, so it is clear that the mixing effects are not improved with the other analyzed mixers in comparison with the results of the previous chapter (corresponding to mixer 1).

5.5.2 Analysis of momentum ratio (J)

After the analysis of the EGR distribution, it is necessary to understand better the effects of different mixing mechanisms in these EGR dispersions. As was explained previously, the penetration of the EGR is a key parameter in terms of mixing as was already explained in 3. The main difference regarding J is that, in this chapter, the parameter will be very variable depending on the angle in the engine cycle. Thus, employed an average value of this parameter (as done in chapter 3) can be not very precise. In fact, during some instants of the cycle, the flow in the mixer will experiment backflows, and in such moments the penetration of the jet should not be taken into account. Therefore, a coefficient that provides a numerical value of the amount of time that the mixer is in backflow is defined as:

$$\beta = \frac{\sum t_{U_{mixer}<0}}{t_{cycle}} \tag{5.5}$$

Thus, in this section, the temporal evolution of J will be assessed using the presented equations of section 5.2. The achieved resuls in the 4-cylinder manifold are presented in figure 5.9 using β coefficient in order to indicate the amount of backflows. First of all, it is necessary to mention that the values of J in this manifold will be very high, especially in comparison with the values of 3 and the 6-cylinder manifold values that will be presented later. The main reason of this fact can be explained by equation 5.1. Considering that, in this manifold the mixer is radial, in some moments of the cycle, the radial/tangential velocities can be very low, thus, the penetration of the EGR stream can be very high in small time periods.

Taking this into account, the instantaneous behavior of J in operating point 1 is very similar in terms of pulsations. However, it is clear that mixer 1 gets slightly higher penetration than mixer 2 in the whole engine cycle. The main reason of this fact is that this operating point have low load and higher EGR rate, so the penetration of the stream is higher in a standard mixer while in mixer 2 the main stream still dragging the EGR flow. On the other hand, penetration in mixer 3 is negligible in comparison with the previous mixer. In addition, the β parameter shows that the other mixers get positive penetration during all the cycle, while in mixer 3, the window in front of the main

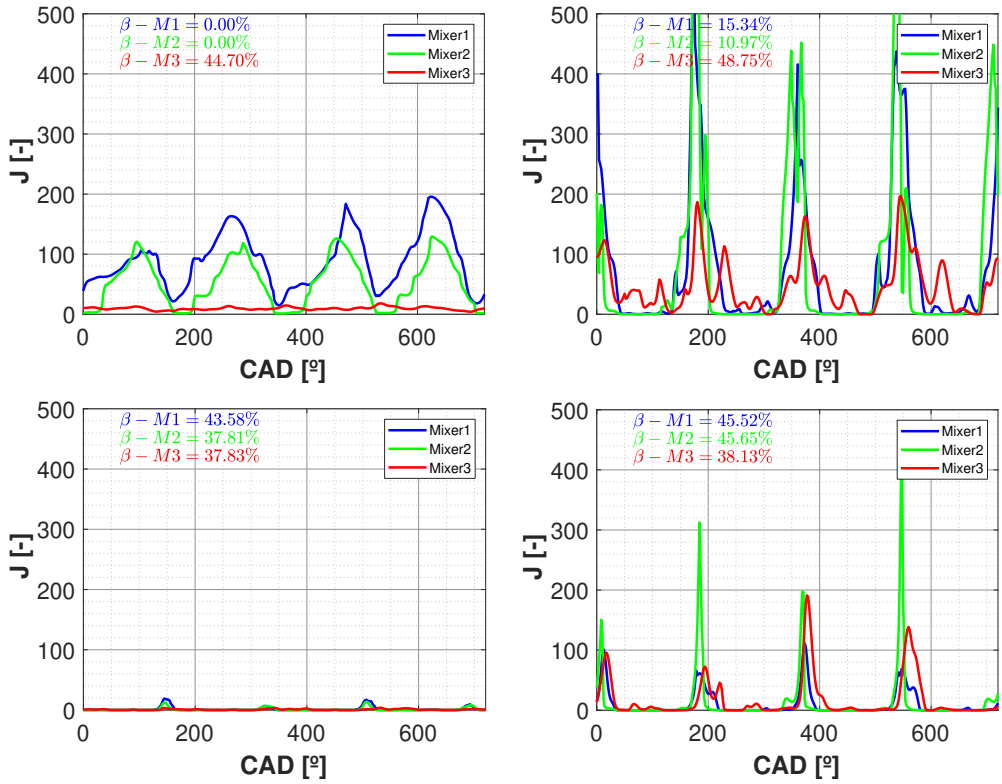

Figure 5.9: Temporal evolution of final J coefficient (equation 5.3) in a single engine cycle, on 4-cyl manifold of operating point A (top left), B (top right), C (bottom left), D (bottom right) with β coefficient values for every mixer.

stream is always in backflow state, and the upper window presents this state half of the cycle (see figure 5.1). Thus, the mean β parameter (mean of the 3 windows) is almost 45% considering that 2 windows are not working properly due to the mixer placement.

Operating point B it is clearly the more pulsating point of the 4-cylinder manifold and the penetration it is notable when the EGR pulses arrive to the mixer. In this case, the penetration is almost the same between mixer 1 and 2, but still being lower in mixer 3. This behavior is not the same in operating point D, because in this case, the load is so high that the penetration of the EGR flow is always mitigated by the main stream (remember that the plotted

traces are the mean of the 3 windows of the mixer). In addition, it is neccesary to mention that the β parameter is higher in these operating points, so the backflows in the mixer appear in a noticeable way in pulsating cases. On one hand, the β parameter of mixer 1 and 2 grows in operating point D due to the higher load of the point, and the main stream enters in the mixer windows, getting negative or zero radial velocity and decreasing the maximum value of J (influence in the mean value). The amount of backflows that every window gets, is not the only indicator of good penetration of the EGR. In fact, mixer 1 gets less penetration than mixer 2 in operating point D, having the same amount of backflows, and this can be one reason of the EGR distribution shape, in which the EGR do not have enough penetration to arrive to the most distant runners (see figure 5.7). On the other hand, β parameter in mixer 3 presents similar values in all the operating points considering that 2 of 3 windows are nearly opposed to the main stream, producing negative radial velocities multiple times during the engine cycle.

Finally, operating point C shows the lowest penetration of all the cases. This operating point combines low r.p.m. and low EGR rate, so the pulses are unable to penetrate in the main stream and all are dragged by the air. Thus, placing a mixer that is oriented to the main stream provides more benefits, as figure 5.7 reveals.

Regarding the 6-cyl manifold, a similar analysis was developed to capture the temporal evolution of J. In this case, the definition of the coefficient J is independent of the considered mixer because all the presented geometries are in the T-junction shape. These results are presented in figure 5.10. Top left plot of figure 5.10 shows very similar behaviors between the considered mixers in terms of jet penetration. In fact, even secondary pulses that do not correspond to the main EGR oscillations, have influence in all of the mixers. In this point, the J values are below 2, so it is clear, as was commented in chapter 3, that this situation is a wall jet configuration. In addition, the β values in this operating point are negligible so this operating point presents a smooth transition of the penetration of the jet. In addition, in bottom part of figure 5.10 the results of operating point 3 are presented. In this case, the 3 mixers get almost the same J evolution in the whole engine cycle, with a very poor penetration of the EGR stream, being a clearly case of wall-jet situation. In these cases the flow arriving to the manifold is not well mixed and this could be lead to EGR maldistribution.

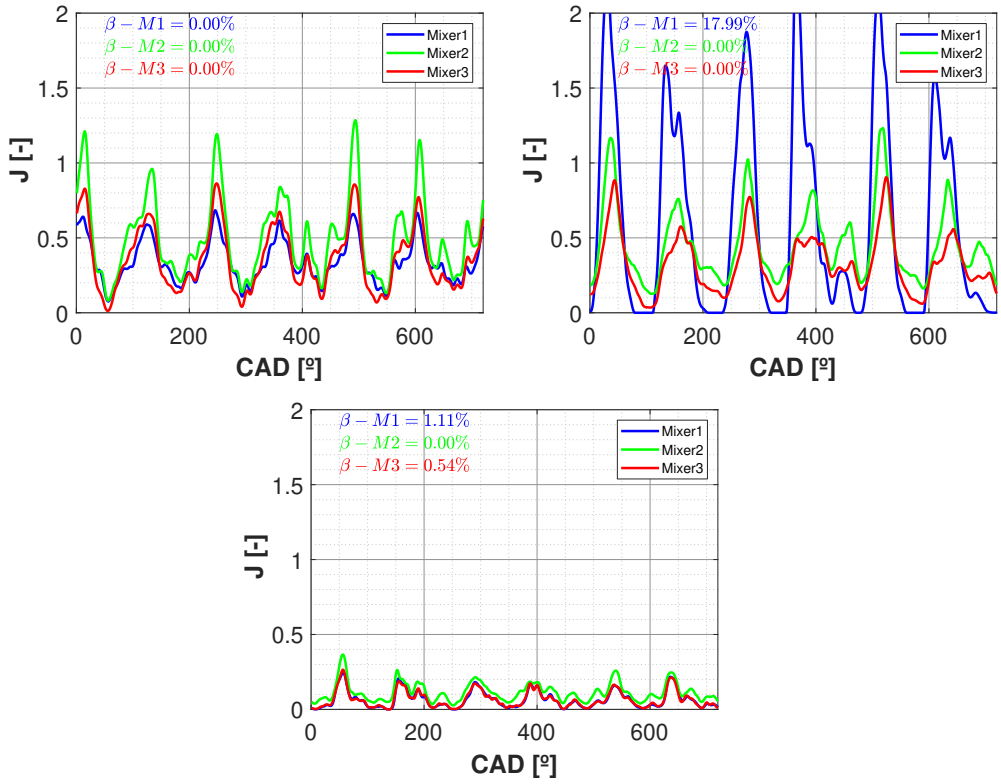

Figure 5.10: Temporal evolution of final J coefficient (average of both windows, see figure 5.6) in a single engine cycle, on 4-cyl manifold of operating point 1 (top left), 2 (top right), 3 (bottom) with β coefficient values for every mixer.

On the other hand, point 2 in top right of figure 5.10 shows that mixer 1 gets clearly the highest EGR penetration of the 3 considered mixers. It is necessary to mention that this mixer presents very high values of β too, so the backflows in this case are important. This β value indicates that the transition of the jet is very unstable, and the oscillations in the mixer are remarkable. On the other hand, mixer 2 and 3 presents lower penetration of the flow in the whole cycle of the engine. Thus, taking into account that the J definition is the same for all the mixers, the differences in terms of jet penetration will be produced by secondary flows in the mixers. In this case, mixer 1 gets deflecting/impinging jet flow configurations in some EGR pulses during the engine cycle.

5.5.3 Analysis of mixing index (MI)

In previous section, the influence of the mixers in the jet penetration has been assessed in all the considered operating points. However, in chapter 3 different mixing indexes that analyze the transversal mixing between 2 considered components were developed and discussed. As was explained in section 5.4, the selected mixing index has been $MI_{\phi-new}$ because this index provided the best overall behavior regarding mixing assessment.

The geometry entities in which the mixing index is considered are presented in figures 5.2 and 5.4 and the final values of the index is obtained with the same procedure than the followed in chapter 3. Regarding the 4-cyl manifold, the evolution of the $MI_{\phi-new}$ in all the considered operating points, is presented in figure 5.11.

In top plot of figure 5.11 the evolution of the mixing index it is the flattest of the whole campaing (combining mixers and operating conditions). In case A, it is clear that mixer 2 provides a higher amount of spatial mixing than the other mixers, specially at the beginning of the domain, because the mixing index is nearly 1 in mixer 2 for all the considered length. On the other hand, mixer 1 and 3 gets more sigmoid/assymptotic trend in the whole length, but mixer 3 it is clearly the worst in terms of mixing in this operating point. In addition, this trend can be showed in terms of EGR contours for the considered mixers in operating point A, as figure 5.12 shows. In the first mixer, the transversal mixing is good but some zones with higher EGR are present, especially in comparison with mixer 2, where the transversal mixing is almost perfect. At the same time, in figure 5.12, mixer 3 reveals that the mixing has very poor quality, considering that the discharge of mixer 3 is very near of the considered plane.

For operating point B and D the evolution of the mixing index gets very similar trends. In both operating points mixer 3 gets the higher level of mixing in the whole domain but the change in the slope is more pronounced in the other mixers. In fact, in the final analyzed length, all the mixers get almost value of perfect mixing, with a little decrease in mixer 1 (that can be produced due to cycle-to-cycle oscillations). These changes in the slope can be produced by the high levels of jet penetration, especially in operating point B, as was

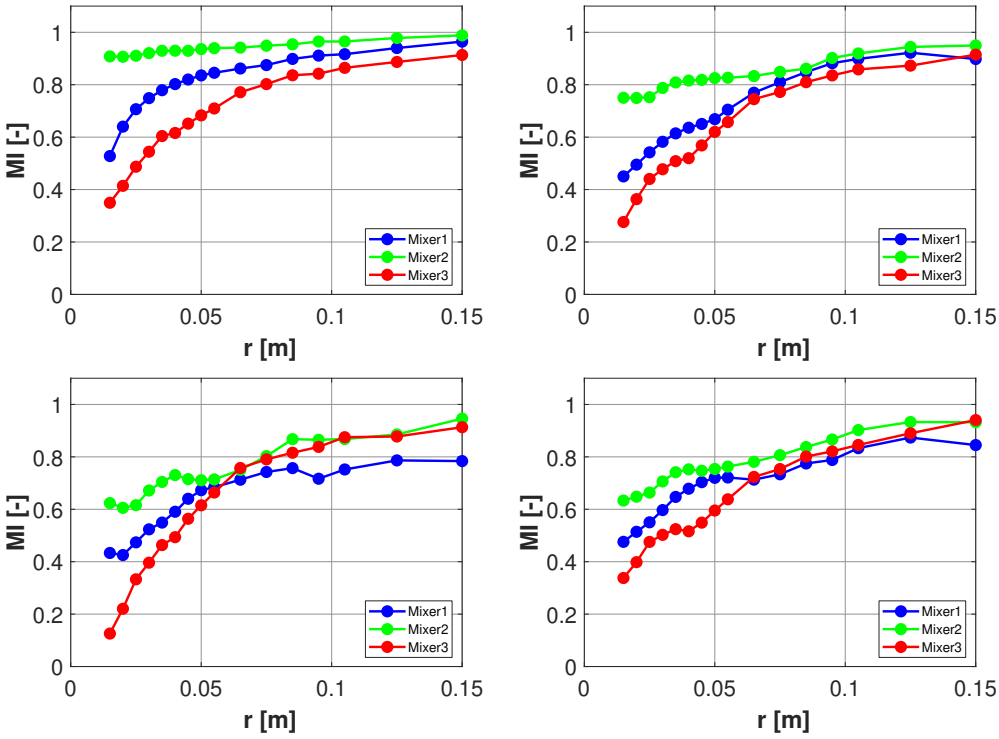

Figure 5.11: Spatial evolution of MI coefficient, on 4-cyl manifold right side (see figure 5.2) of operating point A (top left), B (top right), C (bottom left), D (bottom right).

assessed in figure 5.9.

Finally, in operating point C, the trends are not so clear. In fact, mixer 1 gets clearly the worst mixing index at the end of the considered length, while the other mixers get almost the same results than in other operating points. In this operating point, the EGR rate is very low, and as was assessed in figure 5.9, the jet penetration is almost negligible. Thus, little changes in the cycle can produce variations in terms of mixing, and lower values of EGR rate can be mixed more easily than in other cases, because the load of the point is lower than in points B and D and the time scales are higher. Thus, the EGR has "time" to mix in lower lengths as it can be seeing in mixer 3.

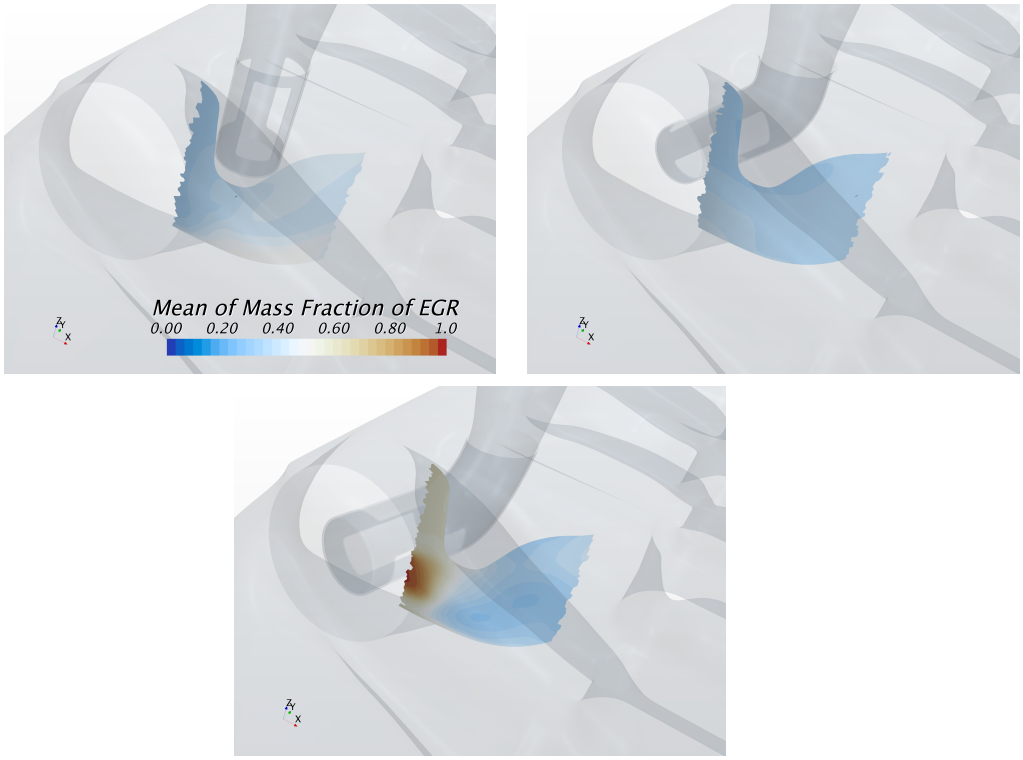

Figure 5.12: Contours of transversal EGR on a cylindrical plane (corresponding to $r = 0.04$ m) of 4-cyl manifold in operating point A for mixer 1 (top-left), mixer 2 (top-right), mixer 3 (bottom).

After the analysis in 4-cylinder manifold, the same assessment can be performed in the 6-cylinder manifold. Obviously, in this case, the postprocessing planes are the presented in figure 5.4, so the shape of the mixer is upstream of the initial analysis in terms of length. Thus, the results of this assessment for every operating point are presented in figure 5.13. Top plot in figure 5.13 shows the results in operating point 1, which has the lower load and the higher EGR rate of the considered operating points. In this case, the presented results follow the same trends than the presented in figure 5.8, in which mixer 1 gets the best EGR distribution of the analyzed mixers. In fact, although the final value of the mixing index is almost 1 for every mixer, the gap at the start of the analysis will have influence in the center-cylinders of the manifold, whereas in the other mixers, the EGR distribution is worse, and this gap can be influential in this fact.

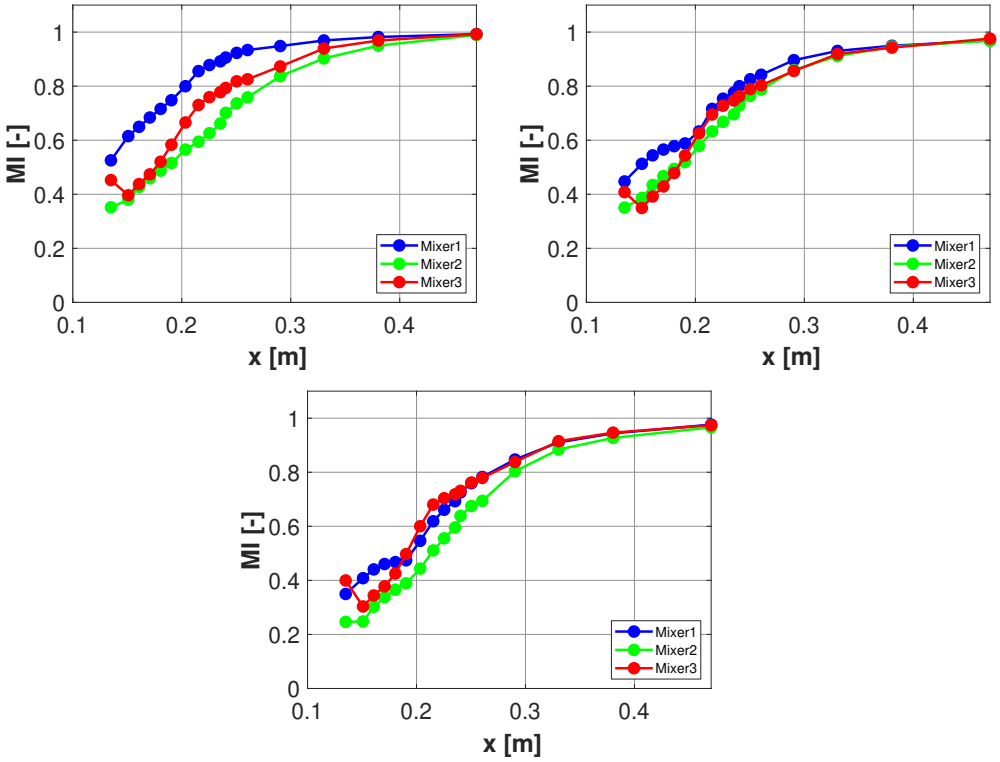

Figure 5.13: Spatial evolution of MI coefficient, on 6-cyl manifold right side (see figure 5.4) of operating point 1 (top left), 2 (top right), 3 (bottom).

In operating point 2 and 3, the differences in terms of transversal mixing between the analyzed mixers is negligible. All of them get the same sigmoid function in terms of length and the main differences only appear at the beginning of the analysis. It is necessary to mention that in mixer 1, when the elbow after the mixer ends (see figure5.4) the change in the slope of the mixing index is important, and the flows gets betters mixing rates in less length.

5.5.4 Analysis of transient rate index (TRI)

As was explained in section 5.2, the transversal mixing computed by the mixing index in previous section, gives an approximation of the quality of the mixing between the considered streams. However, it is clear that not only

the transversal mixing have influence in terms of the final EGR rate of the cylinders, especially after the results that figures 5.11 and 5.13 show. That is the reason for the definition of the TRI.

The planes in which the TRI is calculated are the same than the planes of previous section. The achieved results in the 4-cylinder manifold are presented in figure 5.14. Top plot of figure 5.14 reveals the behavior of the TRI in operating point A. As was commented in other sections, this point has the less load of the considered points with higher EGR rate. Thus, these conditions produce very smooth results in terms of mixing and transient behavior. In fact, the cycle-to-cycle oscillations are very low. In addition, both mixers 1 and 2 present a trend in which the final value of TRI is 1, while the final value of mixer 3 is almost 2, so the transient rate is nearly 2 times higher in this planes than the optimal rate.

Operating point B and D presents almost the same behavior in terms of TRI. The final value in mixer 3 is 2 times higher than the desired one, while in mixer 1 and 2 the trend tries to achieve the 1 value. In addition, mixer 2 presents almost a flat evolution of TRI, and the transient rate is always nearly to 1 value, so the transient evolution of the EGR rate is near to be perfect in all the manifold while the TRI in mixer 1 is really high near to the mixer. It is necessary to mention that the cycle-to-cycle oscillation are noticeable in this 2 operating point. This fact is produced due to the medium-high values of J (see figure 5.9) and due to these oscillations, the average value of TRI it could be less meaningful. Near of the cylinders in these operating points, many differences appear between the mixers in terms of TRI, especially in the plane previous at the final one ($r = 0.125$ m). This phenomenom is very interesting and is showed in figure 5.15. In fact, in figure 5.15, mixer 1 presents almost 1 in a surface very near of the cylinders, while mixer 2 are slightly higher, around 1.5, and mixer 3 is even higher than the other mixers. This discrepancies in the TRI index can produce for example the differences in terms of EGR rate that were presented in figure 5.7 in which mixer 2 are far from the experimental value and the average. Thus, this is a proof of the benefits of consider a transient index too, because while the MI index is almost 1 in mixer 2 in this surface (see figure 5.11), which indicates that the transversal mixing is perfect, the amount of EGR that have be mixed is higher than the average value, thus, the EGR that the cylinder will swallow will be

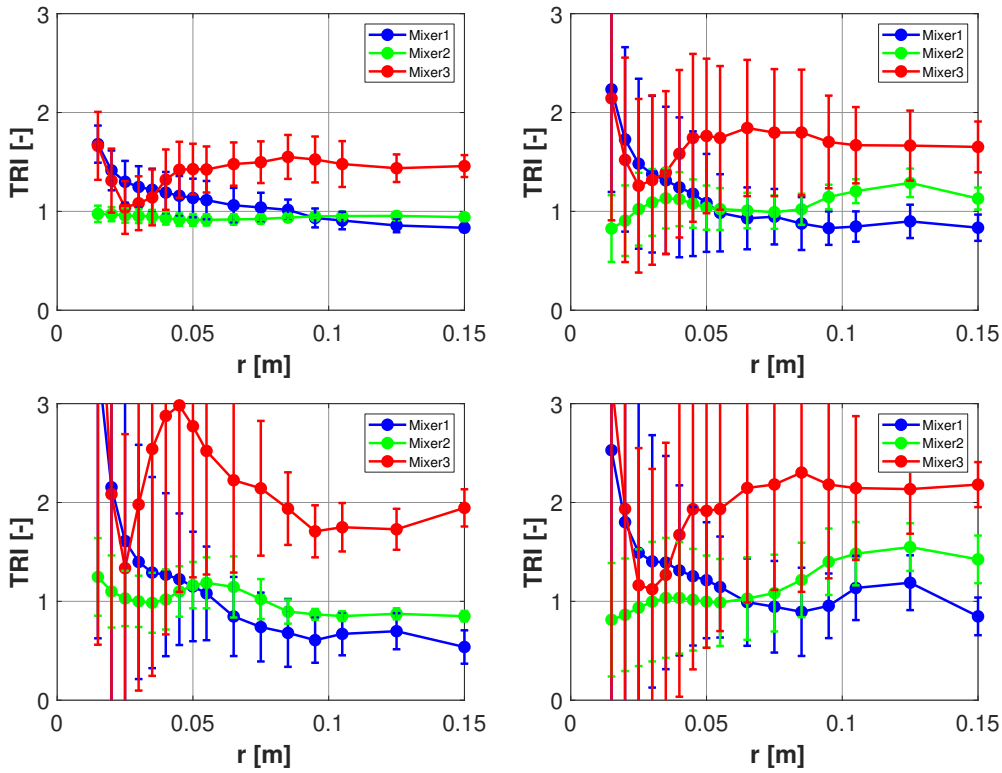

Figure 5.14: Spatial evolution of TRI coefficient, on 4-cyl manifold right side (see figure 5.2) of operating point A (top left), B (top right), C (bottom left), D (bottom right).

higher.

Point C is clearly the more unstable operating point. Although the transient trend of TRI is similar to the other operating points, the oscillations are very high in almost all the manifold, and especially high in the first planes. This fact is produced by the low rate of EGR and medium-low load of the engine. So, little changes in terms of recirculation effects and pressure pulses can change the transient mixing in a noticeable way, especially in comparison with higher EGR rates. In this operating point, mixer 3 has, obviously the higher values of TRI due to its orientation facing one side, while mixer 1 and 2 follows the same behavior than in other operating points.

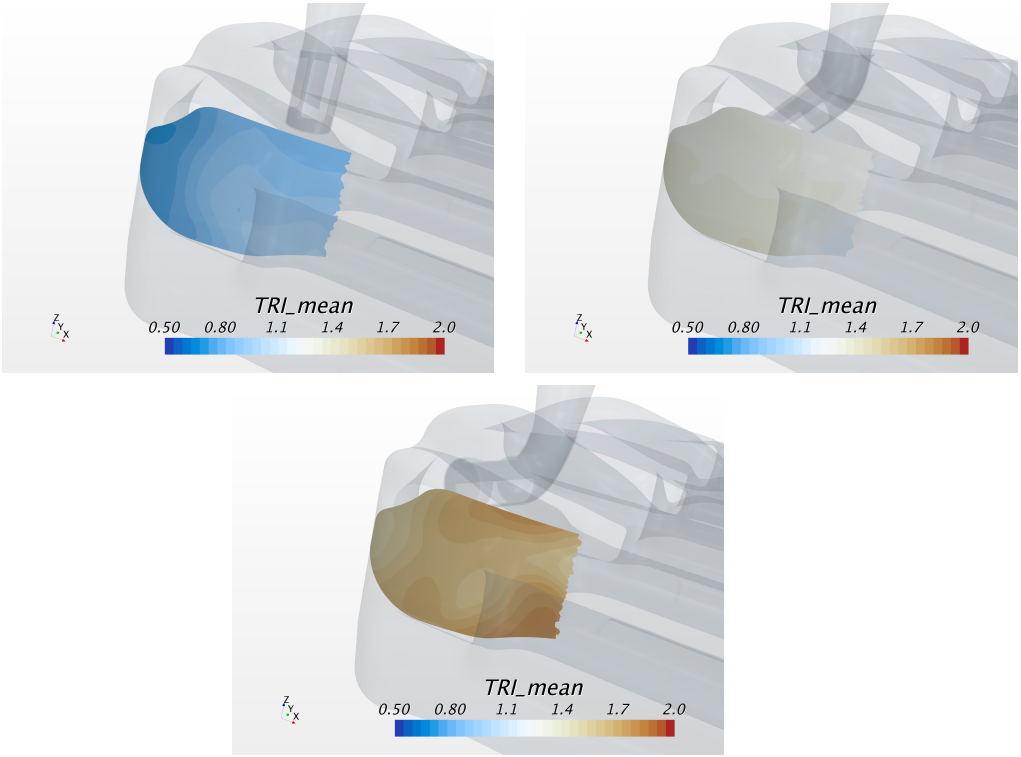

Figure 5.15: Contours of transversal TRI on a cylindrical plane (corresponding to $r = 0.125$ m) of 4-cyl manifold in operating point B for mixer 1 (top-left), mixer 2 (top-right), mixer 3 (bottom).

Regarding the 6-cylinder manifold, the followed procedure is the same than in the previous manifold. Both TRI and its cycle-to-cycle oscillations will be considered in this analysis. The achieved results are presented in figure 5.16. The presented behavior of TRI in figure 5.16 shows some different trends than the MI coefficient in figure 5.13. For example, in operating point 1, the mixer 1 gets a better TRI coefficient near the cylinders, in comparison with the other mixers, because the TRI in the final planes is near the unity, while the MI coefficient is almost the same in the 3 mixers in the corresponding planes. In addition, it is necessary to say that the evolution of TRI in mixer 2 and 3 is very similar for every operating point, while mixer 1 provides smoother transitions, but with higher oscillations (see oscillation values of point 2) which is totally correlated with the J parameter as is represented in figure 5.10. All the oscillations are mitigated after the elbow of the manifold (see figure 5.4)

cause the EGR pulses gets much more volume to be distributed, and the instantaneous concentration decreases.

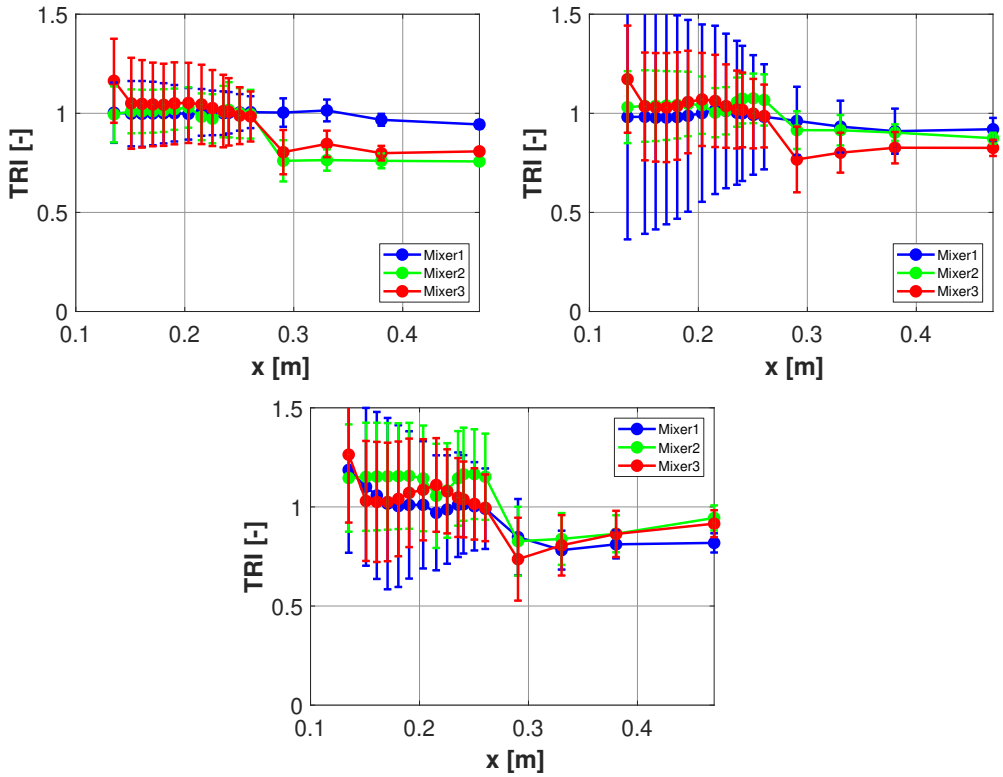

Figure 5.16: Spatial evolution of TRI coefficient, on 6-cyl manifold right side (see figure 5.4) of operating point 1 (top left), 2 (top right), 3 (bottom).

Another interesting phenomenon is the transient differences between operating points with a similar geometry. In previous chapter these differences were presented in section 4.4 where the differences in EGR rate between operating points were highlighted. In figure 5.16 these differences are showed in the values on the final planes of mixer 1 in operating points 2 and 3. To get a wider point of view, the contours of normalized EGR mass fraction (which in fact is the TRI coefficient) are presented in figure 5.17 for operating point 2 and 3 and mixer 1. This comparison of flow fields also explains why point 2 is more challenging to be predicted, as confirmed by the disagreement between numerical and experimental results depicted in figure 5.8. Since the flow is

between two different modes in terms of air and EGR mixing in the main duct as well as ability for the flow of the main duct to turn 180°to the left side of the manifold, the flow field could be more sensitive to small changes. Besides, the local heterogeneity of mean TRI shown in top side of figure 5.8 explain why the $Horiba_{CFD}$ probes (see figure 4.5) depart significantly from the actual EGR rate that gets into the CFD cylinders, which may happen similarly in the experiments, as represented by the large vertical bars of figure 4.21. Obviously, the higher load of operating point 3, makes more difficult to the flow to get a proper distribution in the manifold after the elbow, and most of the fresh air goes to the final cylinders, as were showed too in figure 5.8 for every considered mixer.

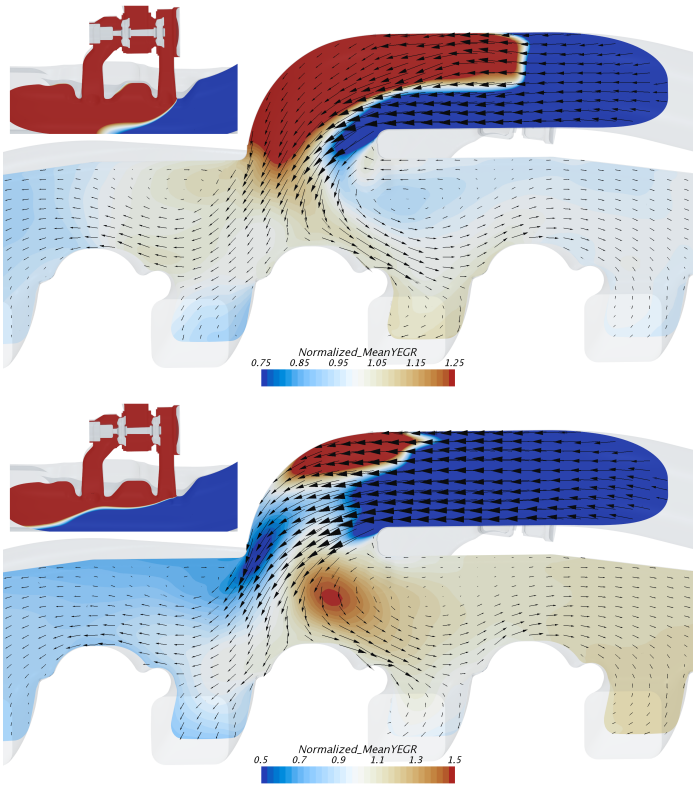

Figure 5.17: Contours of transversal TRI on a transversal plane of 6-cyl manifold for mixer 1 in operating point 2 (top), and 3 (bottom).

5.5.5 EGR pulses and cylinder influence

In previous sections, the spatial evolution of transversal mixing index (MI) and the transient rate index (TRI) have been assessed. After that, it is clear that the diffusion and the advective terms are not the only that have influence in the final EGR that comes to every cylinder. Transient effects produce important changes in terms of EGR distribution, as the differences between MI and TRI index of previous section reveals. Obviously, EGR pulses play an important role in this phenomenom, and produce relevant changes in transient variables as TRI.

The first step to get some quantification regarding the influence of EGR pulses by comparing the obtained results with EGR pulses against other simulation without these pulses. Thus, in this assessment, in the EGR inlet, a constant mass flow will enter to the domain, with the same average value than the previous transient trace of EGR. This analysis has been developed in operating point 2 of 6-cylinder manifold, mounting the first mixer, which have the higher penetration of the EGR pulses (see figure 5.6), and the results are presented in figure 5.18:

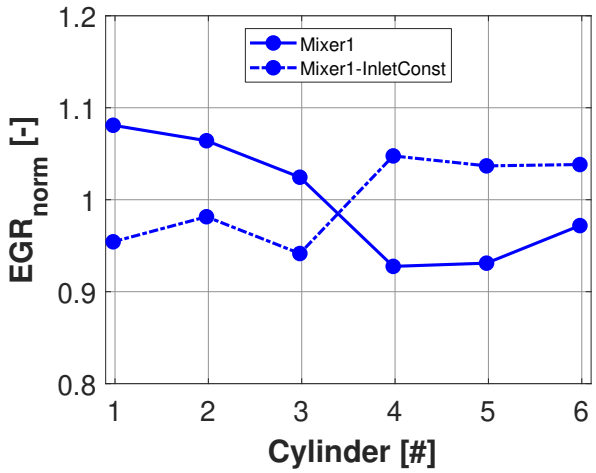

Figure 5.18: EGR distribution with mixer 1 of operating point 2 with standard EGR pulses and constant inlet EGR.

The EGR distributions presented in figure 5.18 shows the changes that produces the suppression of the EGR pulses. The dispersion with a constant

inlet of EGR seems a symmetric version of the original results with EGR pulses. However, if the EGR pulses were the only source of bad distribution of EGR, the results will be a plain distribution in this figure. In figure 5.18 appears the opposite behavior of figure 5.8 and 5.17. With no-pulses, the EGR is distributed in the main stream continuously, instead of being distributed by strokes. Nevertheless, the distribution is not plain at all. Thus, more factors have to be taken into account in the final distribution of EGR to every cylinder.

Another way to study this pulse distribution is using a passive scalar term. If 4 or 6 different scalars are defined (depending of consider 4 or 6-cylinder engine), every EGR pulse can be tracked throughout the manifold, and its distribution in every cylinder can be analyzed. In fact, the final EGR rate (or mass) in every cylinder in an engine cycle can be computed too as:

$$EGR[-] = \frac{\int_{t_0}^{t_{cycle}} \sum_{n}^{N_{puls}} \phi_{pulse-n}(t) \cdot \dot{m}(t) dt}{\int_{t_0}^{t_{cycle}} \dot{m}(t) dt} \tag{5.6}$$

Thus, this pulse-tracking has been applied in operating point B in 4-cylinder manifold and operating point 2 in 6-cylnder manifold, because in both points the EGR pulses are important. The final results are presented in figure 5.19

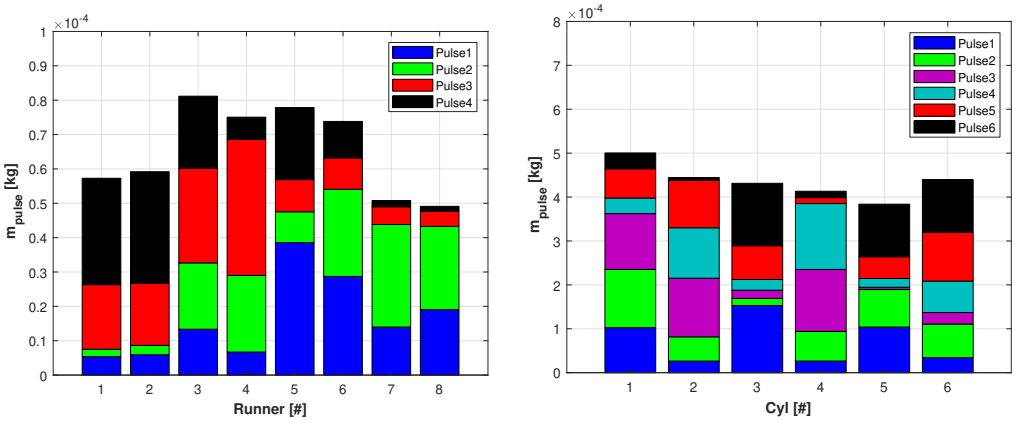

Figure 5.19: EGR pulses distribution of operating point B on 4-cyl manifold (left) and operating point 2 on 6-cyl manifold (right).

In left plot of figure 5.19 the distribution of the different EGR pulses in 4-cylinder manifold are presented. In this operating point and manifold, the EGR pulse distribution is almost symmetrical. For example, the distribution of pulse 1 from runner 1 to runner 8 seems very similar than distribution of pulse 4 from runner 8 to runner 1. In this case, all of the pulses have more or less a well-balanced distribution in every cylinder, so the EGR pulses are not the only reason for a non-flat distribution of EGR.

In right plot of figure 5.19 the pulse distribution in the 6 cylinder manifold do not present very clear trends. As a general point of view, all the pulses seem to have important influence in 3 cylinders of the manifold, and a negligible impact in the other. The only exception to this phenomenom is the pulse 5, which is better distributed in 5 of the 6 cylinders. However, the EGR pulses would be very critical if in some cylinder the total amount of EGR comes from only 1 or 2 pulses. In this case, the distribution is not perfect in terms of EGR pulses, but is better than the referred situation.

Thus, to compute if some EGR pulses are influential in the final EGR rate it is necessary to fulfill 2 different conditions. First condition is related with the amount of mass of pulse that the cylinder swallow, as equation 5.7 presents:

$$\frac{\int_{t_{cycle}} \dot{m}_{EGR-pulse-k} dt}{\int_{t_{cycle}} \dot{m}_{EGR-i} dt} \geq \frac{1}{Z} \tag{5.7}$$

taking into account that $\dot{m}_{EGR-pulse-k}$ is the mass flow of a certain pulse k throughout a certain cylinder i. Therefore, this first condition of equation 5.7 is fulfilled when the amount of mass of a certain pulse is higher than the equivalent part for a perfect mixing $(1/Z)$. The other condition is presented in equation 5.8:

$$\frac{\int_{t_{cycle}} \dot{m}_{EGR-i} dt}{\int_{t_{cycle}} \dot{m}_{i} dt} \geq EGR_{rate} \tag{5.8}$$

This condition lies on the amount of EGR that arrives to a certain cylinder i. This condition is important because although the first condition of equa-

tion 5.7 is accomplished, the relevance is low in the overall performance of the manifold. Thus, when first condition of equation 5.7 and second condition of equation 5.8 are fulfilled, the influence of a certain pulse is relevant, and the cylinder and the pulse are "tuned" in the way that probably the cylinder starts its intake period when the pulse arrives to it.

Another important factor related with the described previous phenomena is the influence in the mean flow of the cylinders itself during his intake period. When the cylinder starts his intake, all the velocity field will change in the influence zone of the cylinder. Thus, it is necessary to approximate this influence zone, and one way to get it is using the streamline in our CFD calculations [64].

First of all, streamlines can be computed considering some seed part in which the streamline starts. So, the flow path can be calculated forward or backward. Therefore, to estimate the influence of the cylinder intake in the rest of the manifold, the streamline must be integrated backwards. In addition, this streamline must be computed inside a velocity field that only is averaged during the intake of the considered cylinder. Thus, the important variables at this point is the length backwards of the streamline L_{strm-n} and the mean velocity field in the considered cylinder $\overrightarrow{\overline{u(t)}}_{intake-n}$.

When this data is obtained, the next step is to get the width of the plane associated to the streamline. Thus, this width is obtained as:

$$W_{strm-n} = \int_{A_{strm-n}} dA / L_{strm-n} \tag{5.9}$$

taking into account that the width of the associated plane is constant. With the width of the associated plane, the time that the flow needs to advance in one cell of the streamline, can be obtained as:

$$t_{cell-strm-n} = \frac{2 \cdot A_{cell-strm-n}}{W_{strm-n} \cdot ||\overrightarrow{\overline{u(t)}}_{intake-n}||} \tag{5.10}$$

taking into account that the cells in the associated plane of the streamline

will be always triangles. Therefore, the time that the velocity field $\overrightarrow{u(t)}_{intake-n}$ needs to go over the streamline with length L_{strm-n} is:

$$t_{strm-n} = \sum_{strm-n} t_{cell-strm-n} \tag{5.11}$$

Thus, the final step of all this process is to adjust the length, in order to achieve a final value of t_{strm-n} that:

$$\epsilon_{strm-n} = |\Delta t_{intake-n} - t_{strm-n}| <= 2\% \tag{5.12}$$

Applying this process to the 6-cylinder manifold, the obtained results are presented in figure 5.20:

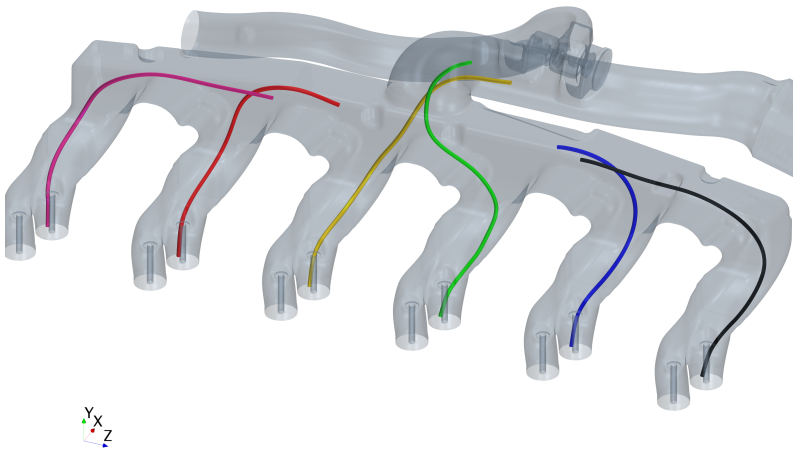

Figure 5.20: Intake length influence of cylinders in 6-cylinder manifold on operating point 2.

As can be observed in figure 5.20, most of the cylinders have shared aspiration zones. Thus, in these zones, the velocity field will change when the cylinders that have influence in their flow field, start their intake period. In

fact, figure 5.20 provides very useful information regarding EGR distribution. For example, it is clear that cylinders 3 and 4 takes the mixing even near of the mixer, and the sides of the manifold, where the EGR has more time to be diffused, are ignored. Thus, this cylinders will swallow a very poor mixed stream, and consequently, the EGR rate will be low, especially in operating points where the EGR pulses are important (see point 2 and J in figure 5.8 and figure 5.6) or operating points where the rate is low and do not have enough penetration (see point 3 and J in figure 5.8 and figure 5.6). This phenomenom is applicable independently of the considered mixer, especially in the experimental cases, because this is a phasing effect, in which the transversal mixing does not have relevance.

5.6 Conclusions

As a summary of this chapter, the following conclusions can be extracted:

- Using the numerical methodology that has been assessed in previous chapter 4, three different mixers in 4-cylinder manifold have been studied in four different operating points. At the same time, three different mixers in 6-cylinder manifold have been assessed in three different operating points. Both manifolds with the corresponding geometrical modifications have been studied regarding the EGR distribution and evolutions of transversal and transient mixing indexes. Table 5.2 shows the computational effort of the simulation campaign conducted in a Intel Xeon E5-2630v3 (2.4GHz) processor for this chapter.

Table 5.2: Computational cost of chapter 5

Cases	12	9
Mesh size (millions)	1	6
Number of cores	16	16
Hours/case	22.9	264
Sum of kh*core	4.40	38.02

- The numerical models get acceptable results in terms of EGR distribution prediction for every mixer in both 4-cylinder and 6-cylinder manifolds. In 4-cylinder manifold, the aligned mixer 2 gets better EGR

distribution for every operating point than the baseline mixer 1, while lateral mixer 3 is obviously the worst mixer due to its bad orientation, but it is a good method to measure the ability of the numerical method to predict these EGR differences. In addition, the benefits of placing mixer 2 oriented to the main stream is clear, and the EGR jet has more time to be mixed before arriving to the cylinders. On the other hand, the differences between mixers in 6-cylinder manifold are not so clear. From a general point of view, the baseline mixer 1 gets the best performance in EGR distribution, in experimental and numerical way too.

- While in 4-cylinder manifold the differences in terms of the momentum ratio coefficient (J) are remarkable depending of the considered mixer, in 6-cylinder manifold are not so high. It has been demonstrated that high values of J can produce important oscillations in terms of transient rate index coefficient TRI (see point B of figure 5.5 and figure 5.14). In addition, the mixing index MI assessment has demonstrated that, with the spatial length between the mixers and the cylinders, it is enough to get very high values of transversal mixing in both manifolds, getting most of them a sigmoid trend regarding the analyzed length. In addition, the differences in terms of MI are low between mixers and operating points (with exception of aligned mixer 2 of 4-cylinder manifold). On the other hand, the differences between mixers and operating points in terms of TRI index are huge for both manifolds. It has been proved that high levels of transversal mixing will not assure a good cylinder-to-cylinder distribution regarding EGR, as is showed in figure 5.11 and figure 5.14 for operating point B.

- The breakdown of how much EGR swallowed by each cylinder comes from a certain EGR pulse has been assessed as well. In fact, the first guidelines to obtain the distribution of the EGR pulses have been developed, getting some conditions to check if some EGR pulse is tuned with a certain cylinder, taking into account too the length of influence of its intake, which has been estimated too in section 5.5.5.

- To summmarize, it is clear that high EGR pulses normally will produce uneven EGR distribution, especially if are tuned with a single cylinder. If the distances between the mixer and every inlet of the domain differs a lot, the probability of a single cylinder taking more EGR than the others of a certain EGR pulse increases. Thus, having centered mixers as mixer 1 and 2 of 4-cylinder manifolds contributes to mitigate that effect, while

in 6-cylinder manifold the distances between the mixer and the cylinders are very different, and this fact can contribute to a more uneven distributions, especially for operating points with important EGR pulses (see experimental traces of operating point 2 of figure 5.8). Thus the interesting phenomenom is that placing a mixer very far for the cylinders will provide very high rates of transversal mixing (see MI contours of figure 5.13) but can lead into a worst transient behavior between the cylinders. In addition, if the mixer is placed in the way that the distances to the cylinders is almost the same (mixer 1 and 2 of 4-cylinder manifold), orienting it to the main stream will improve the mixing and the distribution (see mixer 2 in figure 5.7).

Chapter 5 Bibliography

[25] N. Kimura, H. Ogawa, and H. Kamide. "Experimental study on fluid mixing phenomena in T-pipe junction with upstream elbow." *Nuclear Engineering and Design* 240(10) (2010), pp. 3055–3066. DOI: 10.1016/j.nucengdes.2010.05.019 (cit. on pp. 5, 6, 53, 64, 77, 159).

[60] E. Kartaev, V. Emel'kin, M. Ktalkherman, V. Kuz'min, and S. Aul'chenko. "Analysis of mixing of impinging radial jets with crossflow in the regime of counter flow jet formation." *Chemical Engineering Science* 119 (2014), pp. 1–9. DOI: 10.1016/j.ces.2014.07.062 (cit. on pp. 8, 159).

[61] S. Nada, A Fouda, and H. Elattar. "Parametric study of flow field and mixing characteristics of outwardly injected jets into a crossflow in a cylindrical chamber." *International Journal of Thermal Sciences* 102 (2016), pp. 185–201. DOI: 10.1016/j.ijthermalsci.2015.11.017 (cit. on pp. 8, 159).

[62] N. Minocha and J. B. Joshi. "3D CFD simulation of turbulent flow distribution and pressure drop in a dividing manifold system using openfoam." *International Journal of Heat and Mass Transfer* 151 (2020), p. 119420. DOI: 10.1016/j.ijheatmasstransfer.2020.119420 (cit. on pp. 8, 160).

[63] G. R. de Souza, C. de Castro Pellegrini, S. L. Ferreira, F. S. Pau, and O. Armas. "Study of intake manifolds of an internal combustion engine: A new geometry based on experimental results and numerical simula-

tions." *Thermal Science and Engineering Progress* 9 (2019), pp. 248–258. DOI: 10.1016/j.tsep.2018.12.003 (cit. on pp. 8, 159, 205).

[64] *STAR-CCM+*. Release version 12.06.010. CD-adapco. 2018. URL: http://ww.cd-adapco.com (cit. on pp. 9, 26, 30, 34, 42, 59, 61, 100, 107, 112, 114, 119, 170, 190).

Chapter 6

Concluding remarks

Contents

6.1 Introduction

In this chapter, a summary of the main contributions and achievements of the document will be addressed. Thus, the main findings that have been achieved will be highlighted in section 6.2. In addition, section 6.3 discuss the main limitations of the developed works, which have influence in the accuracy of the results and methodologies that have been applied to get it. At the end of this chapter, in section 6.4 the possible paths of investigations in order to improve the knowledge in the mixing between different streams in internal combustion engines. The total computational cost of this Thesis, which have been addressed in tables 2.2, 3.8, 4.14, 5.2 is about core-hours.

6.2 Summary of findings and contributions

6.2.1 Main original contributions

When a doctoral thesis is developed, it is necessary to analyze what are the original contributions that the author has achieved with its realization. In fact, this section summarizes the main original contributions, which are divided regarding the considered configuration (LP-EGR or HP-EGR):

- Using the steady scheme in LP-EGR calculations, including the compressor, have been demonstrated that this approach cannot represent the temperature distribution properly when an heterogeneous inlet is considered. In fact, the circumferential deviation in the discharge zone of the compressor has been found (see figure 2.9), and the RANS simulation could be shifted in order to get the same discharge point than the URANS approach. Anyway, the correct approach to get reliable results in high-quality simulations, must be the URANS scheme.

- If an heterogeneous inlet in a LP-EGR configuration is considered, the effect in the global compressor performance is not so relevant. This conclusion is different that the achieved by Reihani et al. [32] in which the EGR stream produces remarkable effects in the inlet triangle of the compressor. However, the penetration of the EGR jet in these cases (measured with VR or J) are considerable higher than the used in this

work, in which the geometry and parameter data corresponds to a real operating points of the compressor.

- Considering the suitable mixing indexes, the volume condensation mass flow generated inside a LP-EGR junction correlates linearly with these indexes, even with high coefficients of determination. Thus, if a psychrometric condition is selected, the optimal design of a junction is the one that achieves the lower mixing indexes, in terms of condensation mass flow. In addition, in a humid flow test bench, temperature measurements would be enough to assess the behavior of a junction. However, it must be taken into account that a humid test bench or the condensation submodel are still required if the quantification of the condensation mass flow rate is sought. The main guidelines of junction design are provided with the aim of reduce volume condensation; if the LP-EGR configuration must include any valves, they have to be placed as far as possible of the injection of the EGR stream, trying to decrease the influence of the vortex after the valve, which can be very important in terms of mixing. Furthermore, the injection of the EGR must be placed as close as possible of the inducer plane, in order to avoid increments of mixing along the junction.

- Two different mixing indexes based on a scalar passive fraction and temperature have been developed, in order to compute numerically the amount of non-mixed area on a certain surface. In fact, these mixing indexes have proved that can correlate well regarding J coefficient in LP-EGR configurations and improves the predicted condensation in comparison with other coefficients of the bibliography (see figure 3.5). The developed MI based on scalar values, provides interesting results in HP-EGR configurations for operating points with low load and low and higher EGR rates. In addition, a transient index of mixing (TRI) has been developed in HP-EGR configuration that can provide a lot of information of the amount of EGR that arrives to a certain surface of the manifold.

- In LP-EGR junctions, J has proved that is a key factor to analyze the main flow patterns inside the domain and its correlation with the mixing between the flows is notable. Thus, one optimal design would be a branch or EGR leg aligned towards the outlet duct, in order to reduce J (and therefore, the penetration of the EGR). In addition, if the EGR branch could be designed with higher areas, the penetration of the flow will be

lower, and indeed, the volume condensation produced will be reduced consequently.

- In HP-EGR, the methodology to analyze EGR distribution in conjunction with 1D simulations and experimental measurements has been assessed. The findings regarding this methodology are summarized:
  - The loop between measurements, 1D, and CFD have been applied in most of the analyzed operating points. Despite that some authors have used a 'strong' coupling between 1D and CFD simulations [55, 58], in this document, the calibration was performed using variables like manifold pressure traces and inlet and EGR pressure traces and mass flow values. Operating points with higher oscillation values of EGR have proved that are more difficult to adjust.
  - Regarding the validation of CFD models of HP-EGR using instantaneous measurements of CO_2 percentage, it has been found that experimental probes needs a substantial amount of time to analyze the composition. Thus, higher frequency events are lost in this process. Consequently, some smoothing process of the CFD traces, and some move mean methods process for the experimental traces need to be applied in order to get proper comparisons as was explained in section 4.2.4.
  - The placing of experimental probes must be selected carefully in order to avoid unreal EGR values that comes to the cylinder. These deviations can rise up to 20% in some cases as was assessed in the 6-cylinder manifold engine, while in 4-cylinder manifold the deviations were fewer due to his placement near the final runners of the manifold.
- In HP-EGR, EGR distribution have proved that is a very case-dependent phenomenon, and after the performed studies in chapters 4 and 5, the main global findings of EGR dispersion are summarized:
  - Operating points with high EGR pulses (which are indicated by J parameter) can produce very uneven and non-flat distributions of EGR between cylinders (point B of figure 5.7 and point 2 of figure 5.8). In these cases, transversal mixing (computed by MI) is less important, considering that the transient mixing will be oscillating and variable in the whole length of the manifold (see point B of figure 5.14 and point 2 of figure 5.16). Thus, EGR pulses will be the

cause of bad distribution of EGR, as was referred by Sakowitz et al. [52], and the influence zone of the intake of a certain cylinder will be crucial if the EGR field is not homogeneous (figure 5.20). Therefore, in order to mitigate this effect, it is interesting that the distance between the mixer and every inlet cylinder would be similar. That is the reason which in 6-cylinder manifold all the EGR experimental distributions are non-flat (figure 5.8) and in 4-cylinder manifold mixer 2 provides flatter distribution than mixer 1 in point B. In addition, the discrepancies between CFD and experimental results are influenced too by the non-physical smoothing effect that was explained by Sakowitz et al. [52] and therefore, to get more accurate results, LES modeling of the turbulence would be desirable.

- Operating points with low load and medium/high EGR rates are more susceptible to provide flat distributions of EGR, as proposed by William et al. [134]. In these cases, diffusive effects will have more influence in the EGR trade off, and thus, transversal mixing (MI) will be a good indicator of the final rate. In fact, the best mixer design provides better traces in both transversal and transient mixing index. Considering that, in these operating points, the characteristic times will be higher, consequently, the EGR will be more mixed in the same length, and thus, the differences between mixer 1 and 2 in 4-cylinder manifold are low. (figure 5.8).
- Operating points with high load and low EGR rate are clearly dominated by advective effects, and the diffusive and pulsating effects have less influence in the final EGR rate. Although J can present some higher pulses (see case D figure 5.5) the entire area below the trace is clearly lower than in operating points with higher rates (case B). In addition, point 3 on 6-cylinder manifold presents a negligible penetration (figure 5.6). Therefore, the EGR will be transported by the main stream path and recirculations. In fact, in 6-cylinder manifold, the main stream have more difficult to turn around the elbow to the first cylinders (see figure 5.17). Thus, that is the reason why the 3 mixers present an asymmetrical EGR distribution with more EGR in the first cylinders (see point 3 of figure 5.8) because most of the main stream takes the straight path. At the same time, in point D the slightly differences in terms of J provides more penetration to the EGR and then, is transported to the far cylinders, while with less penetration, the main stream transport the EGR

to the nearest cylinders. In addition, having a symmetrical mixer in a symmetrical manifold as 4-cylnder case, the advective effects provide almost symmetrical distributions of EGR (see experimental data of case D of figure 5.7).

- In operating points that present low load and low EGR rate, diffusion mechanisms are of greater importance than advective or pulsating effects. In fact, mixer 2 provides clearly better mixing rates than mixer 1 (see case C of figure 5.11) and thus, EGR distribution is clearly flatter for this mixer.

- The developed statistical regression of pollutants on 6-cylinder manifold have proved that even with "V-shaped" distributions of EGR as operating point 2 of figure 5.8 its impact on the pollutants is below 2% in comparison with a totally flat EGR distribution. In fact, dispersion and EGR rate has to increase 50% and 25% respectively, the impact on emissions would be around 7% for NOx and 13% for PM (in comparison with a flat distribution case, see figure 4.27).

6.2.2 Other findings

Apart from the described main contributions, some methodological aims and other findings are listed:

- The developed mixing indexes have proved on LP-EGR configurations, that some volume condensation will be produced by psychrometric conditions, and the rest will be produced by the mixing between air and EGR streams. In fact, 0D model will always provide the highest value of condensation that can be generated on a certain geometry and operating conditions (see figures 3.7 and 3.8).

- When several studies of mesh and time-step size are performed, the Courant number must be taken into account in order to avoid deviations in EGR mass conservation. This issue has been overcome in 6-cylinder manifold working with 1 CAD of time step size, while in 4-cylinder manifold, 2 CAD is enough and the same order than the work of Dimitriou et al. [58]. An interesting paradox can appear when a higher density mesh can produce this continuity deviations if Courant number is not considered.

- During the validation process of CFD models in HP-EGR, inviscid approach has proved that can provide similar results that more complex models in both average and instantaneous traces of CO_2 percentage. In symmetrical manifold, inviscid approach is suitable to provide very symmetrical distributions of EGR.

- New methodologies have been developed in HP-EGR assessment regarding the intake and EGR pulses. On one hand, the commented methodology in section 5.5.5 provides an overall point of view of the distribution of every EGR pulse, and some guidelines to analyze if some cylinder are tuned with a certain pulse are exposed. On the other hand, using proper CFD tools, a methodology to get an approach of the influence length of the cylinders is presented, allowing to understand the causes of a certain distribution of EGR in a not well-mixed manifold.

6.3 Limitations

Although the main objectives exposed in chapter 1 have been achieved, it is necessary to mention the main limitations that are in the scope of this document:

- Obviously, the bigger limitation of this thesis is that mainly all the achieved results are obtained in a numerical way. Although most of the numerical models have been validated against experimental measurements and support the reliability of the conclusions, some uncertainties can appear in every simulation, considering that mixing is a very case-dependent phenomenon.

- The analysis of heterogeneous inlet in chapter 2 at different operating points of the compressor, have been carried out with a 1.3 million cells. Although the main variables were compared with a finer mesh of 4 million cells and the overall compressor parameters and temperature traces indicates very similar results, a finer mesh would be desirable to model all the compressor map, especially in points in which the $y+$ factor can grow up in a remarkable way. In fact, Navarro demonstrates that 9 million cells is a reasonable mesh size in operating points near to surge region [72]. Furthermore, in chapter 2 only 1 type of jet penetration was

considered in the whole study, so the influence of this factor was not assessed.

- Although several mesh independence and time step independence studies were performed in chapter 3 and chapter 4, the turbulence approach has been fixed to RANS submodels in the whole thesis. However, in some operating points, it would have been interesting that some bigger scales were resolved, in order to capture better the influence in the mixing of these eddies. In fact, in operating point 2 of 6-cylinder manifold, the LES (or even DES) convenience was stated by Sakowitz et al. in a similar operating point [52].

- In chapter 4 a statistical regression model was developed thanks to the amount of operating points that was measured in the experimental facility. However, to check the influence of the numerical deviations on the pollutants a similar model could have been made in 4-cylinder manifold too and perform a similar analysis of the pollutant emissions.

- As was stated previously, all the developed thesis are very case-dependent. In chapter 2, the heterogeneous inlet assessment was performed in one centrifugal compressor while in chapter 3 the most standard junction between air and EGR is the selected to perform the design of experiments. Thus, the conclusions stated in section 6.2 are limited to these geometries.

6.4 Suggestions for future studies

After the realization of this thesis, some paths of investigations have opened in order to go deep in some aspects of the mixing in EGR configurations.

6.4.1 LP-EGR suggestions

- The influence of an heterogeneous inlet have been assessed in chapter 2, however, although the main performance of the compressor have been analyzed, a deeper analysis of the local effects of this phenomenon could be perform, even exploring the differences between channels of the impeller by different methods to get an average values of local variables. In

addition, as was commented in section 6.3, only 1 type of jet-penetration mode was considered, so it would be desirable that more variety in J were analyzed in this type of studies.

- Using the 0D condensation model, a linear correlation with the developed and bibliography mixing indexes have been performed in chapter 3. However, the behavior of these mixing indexes with non-linear correlations could be studied, in order to obtain their results regarding the final condensation of the junction.
- The new mixing indexes developed in this document have been defined with several piecewise functions. Some alternatives in the mixing indexes definition could be studied in LP-EGR junctions.
- The effect of imposing transient conditions could be studied in order to assess their influence in the condensation generation and in the mixing indexes. In addition, the whole LP-EGR system could be included with transient inlet conditions with the TRI index in order to study the variation of the instantaneous level of EGR rate.

6.4.2 HP-EGR suggestions

- Considering that EGR dispersion is a very case-dependent phenomenon, the optimal numerical setup could be studied in more than 1 operating point to compare the results, regarding the dominant effects of the inlet conditions.
- Although the design guidelines that have been provided by this thesis are focused in the EGR distribution, the influence of these modifications in the volumetric efficiency of the manifold could be assessed. In addition, the effects on EGR dispersion of some geometrical modifications, as the ones presented by De Souza et al. [63], to improve volumetric efficiency could be studied to analyze their influence in EGR distribution.
- The effects of the EGR pulses and the intake opening of the cylinders in the final EGR distribution could be studied, getting a wider point of view of the dominant effects in the whole operation range of the engine.

Chapter 6 Bibliography

[32] A. Reihani, J. Hoard, S. Klinkert, C.-K. Kuan, and D. Styles. "Numerical Evaluation of the Effects of Low Pressure EGR Mixer Configuration on Turbocharger Compressor Performance." In: *ASME 2018 Internal Combustion Engine Division Fall Technical Conference*. American Society of Mechanical Engineers Digital Collection. 2018 (cit. on pp. 6, 11, 23, 34, 36, 47, 198).

[52] A. Sakowitz, S. Reifarth, M. Mihaescu, and L. Fuchs. "Modeling of EGR Mixing in an engine intake manifold using LES." *Oil & Gas Science and Technology* 69(1) (2014), pp. 167–176. DOI: 10.2516/ogst/2013118 (cit. on pp. 7, 100, 112, 118, 150, 201, 204).

[55] S. Ramanathan, A. Hudson, J. Styron, B. Baldwin, D. Ives, and D. Ducu. *EGR and swirl distribution analysis using coupled 1D-3D CFD simulation for a turbocharged heavy duty diesel engine*. Tech. rep. SAE Technical Paper, 2011. DOI: 10.4271/2011-01-2222 (cit. on pp. 8, 107, 108, 112, 117, 200).

[58] P. Dimitriou, R. Burke, C. D. Copeland, and S. Akehurst. *Study on the effects of EGR supply configuration on cylinder-to-cylinder dispersion and engine performance using 1D-3D co-simulation*. Tech. rep. SAE Technical Paper, 2015. URL: https://saemobilus.sae.org/content/2015-32-0816 (cit. on pp. 8, 100, 107, 110–112, 117, 119, 122, 150, 200, 202).

[63] G. R. de Souza, C. de Castro Pellegrini, S. L. Ferreira, F. S. Pau, and O. Armas. "Study of intake manifolds of an internal combustion engine: A new geometry based on experimental results and numerical simulations." *Thermal Science and Engineering Progress* 9 (2019), pp. 248–258. DOI: 10.1016/j.tsep.2018.12.003 (cit. on pp. 8, 159, 205).

[72] R. Navarro. "A numerical approach for predicting flow-induced acoustics at near-stall conditions in an automotive turbocharger compressor." PhD thesis. Universitat Politècnica de València, 2014. URL: http://hdl.handle.net/10251/44114 (cit. on pp. 25, 27, 43, 203).

[134] J William, A Dupont, R. Bazile, and M. Marchal. "Study of geometrical parameter influence on air/EGR mixing." *SAE transactions* (2003), pp. 1016–1036. DOI: 10.4271/2003-01-1796 (cit. on pp. 133, 143, 150, 201).

Global bibliography

[1] J. Galindo, H. Climent, R. Navarro, G. García-Olivas, S. Guilain, and R. Boubennec. "Effect of Numerical Configuration on Predicted EGR Cylinder-to-Cylinder Dispersion." In: *SAE Technical Paper*. 2020. DOI: 10.4271/2020-01-1113 (cit. on pp. ix, 106, 108, 113).

[2] Galindo, J. and Serrano, J.R. and Navarro, R. and García Olivas, G. "Numerical modeling of centrifugal compressors with heterogeneous incoming flow due to low pressure exhaust gas recirculation." In: *Proceedings of ASME Turbo Expo 2020: Turbomachinery Technical Conference and Exposition*. GT2020-16030. American Society of Mechanical Engineers. 2020. DOI: 10.1115/gt2020-16030 (cit. on pp. ix, 58, 77).

[3] J. Galindo, H. Climent, R. Navarro, and G. García-Olivas. "Assessment of the numerical and experimental methodology to predict EGR cylinder-to-cylinder dispersion and pollutant emissions." *International Journal of Engine Research* 22(10) (2021), pp. 3128–3146. DOI: 10.1177/1468087420972544 (cit. on pp. ix, 53).

[4] J Galindo, A Gil, R Navarro, and G García-Olivas. "Numerical assessment of mixing of humid air streams in three-way junctions and impact on volume condensation." *Applied Thermal Engineering* 201 (2022), p. 14. DOI: https://doi.org/10.1016/j.applthermaleng.2021.117676 (cit. on p. ix).

[5] J. Galindo, R. Navarro, D. Tarí, and G. García-Olivas. "Centrifugal compressor influence on condensation due to Long Route-Exhaust Gas Recirculation mixing." *Applied Thermal Engineering* 144 (2018), pp. 901 –909. ISSN: 1359-4311. DOI: 10.1016/j.applthermaleng.2018.09.005 (cit. on pp. x, 4, 22, 24, 25, 27, 28, 41, 42, 53, 54, 58, 61, 73, 124).

[6] J. S. Gaffney and N. A. Marley. "The impacts of combustion emissions on air quality and climate - From coal to biofuels and beyond." *Atmospheric Environment* 43(1) (2009). Atmospheric Environment - Fifty Years of Endeavour, pp. 23 –36. ISSN: 1352-2310. DOI: 10.1016/j.atmosenv.2008.09.016 (cit. on p. 2).

[7] J. Janaun and N. Ellis. "Perspectives on biodiesel as a sustainable fuel." *Renewable and Sustainable Energy Reviews* 14(4) (2010), pp. 1312–1320. DOI: 10.1016/j.rser.2009.12.011 (cit. on p. 2).

[8] M.-B. Ricardo, P. Apostolos, and M. Yang. "Overview of boosting options for future downsized engines." *Science China Technological Sciences* 54(2) (2011), pp. 318–331. DOI: 10.1007/s11431-010-4272-1 (cit. on p. 3).

[9] A. García, J. Monsalve-Serrano, S. Martínez-Boggio, and K. Wittek. "Potential of hybrid powertrains in a variable compression ratio downsized turbocharged VVA Spark Ignition engine." *Energy* 195 (2020), p. 117039. DOI: 10.1016/j.energy.2020.117039 (cit. on p. 3).

[10] A. G. Des Buttes, B. Jeanneret, A. Kéromnès, L. Le Moyne, and S. Pélissier. "Energy management strategy to reduce pollutant emissions during the catalyst light-off of parallel hybrid vehicles." *Applied Energy* 266 (2020), p. 114866. DOI: 10.1016/j.apenergy.2020.114866 (cit. on p. 3).

[11] N. Ladommatos, S. Abdelhalim, and H. Zhao. "The effects of exhaust gas recirculation on diesel combustion and emissions." *International Journal of Engine Research* 1(1) (2000), pp. 107–126. DOI: 10.1243/1468087001545290 (cit. on pp. 3, 99).

[12] J. M. Desantes, J. M. Luján, B. Pla, and J. A. Soler. "On the combination of high-pressure and low-pressure exhaust gas recirculation loops for improved fuel economy and reduced emissions in high-speed direct-injection engines." *International Journal of Engine Research* 14(1) (2013), pp. 3–11. DOI: 10.1177/1468087412437623 (cit. on pp. 3, 4, 22, 54, 99, 102).

[13] M. Lapuerta, A. Ramos, D. Fernandez-Rodriguez, and I. Gonzalez-Garcia. "High-pressure versus low-pressure exhaust gas recirculation in a Euro 6 diesel engine with lean-NOx trap: Effectiveness to reduce NOx emission." *International Journal of Engine Research* - (Nov. 14, 2018), pp. 0–9. DOI: 10.1177/1468087418817447 (cit. on p. 3).

[14] R. D. Reitz, H. Ogawa, R. Payri, T. Fansler, and S. Kokjohn. "IJER editorial: The future of the internal combustion engine." *International Journal of engine Research* 21 (1 2020), pp. 0–8. DOI: 10.1177/1468087419877990 (cit. on pp. 3, 100).

[15] Y. Park and C. Bae. "Experimental study on the effects of high/low pressure EGR proportion in a passenger car diesel engine." *Applied energy* 133 (2014), pp. 308–316. DOI: 10.1016/j.apenergy.2014.08.003 (cit. on pp. 4, 54).

[16] F. Millo, P. F. Giacominetto, and M. G. Bernardi. "Analysis of different exhaust gas recirculation architectures for passenger car diesel engines." *Applied energy* 98 (2012), pp. 79–91. DOI: 10.1016/j.apenergy.2012.02.081 (cit. on pp. 4, 99).

[17] J. M. Luján, J. Galindo, J. R. Serrano, and B. Pla. "A methodology to identify the intake charge cylinder-to-cylinder distribution in turbocharged direct injection Diesel engines." *Measurement Science and Technology* 19(6) (2008), p. 065401. DOI: 10.1088/0957-0233/19/6/065401 (cit. on pp. 4, 7, 8, 99, 100, 108, 116).

[18] C. Guardiola, B. Pla, P. Bares, and A. Stefanopoulou. "Cylinder charge composition observation based on in-cylinder pressure measurement." *Measurement* 131 (2019), pp. 559–568. DOI: 10.1016/j.measurement.2018.08.024 (cit. on p. 4).

[19] A. Maiboom, X. Tauzia, and J.-F. Hétet. "Influence of EGR unequal distribution from cylinder to cylinder on NOx-PM trade-off of a HSDI automotive Diesel engine." *Applied Thermal Engineering* 29(10) (2009), pp. 2043 –2050. ISSN: 1359-4311. DOI: 10.1016/j.applthermaleng.2008.10.017 (cit. on pp. 4, 7, 99).

[20] J. Galindo, P. Piqueras, R. Navarro, D. Tarí, and C. Meano. "Validation and sensitivity analysis of an in-flow water condensation model for 3D-CFD simulations of humid air streams mixing." *International Journal of Thermal Sciences* 136 (2019), pp. 410 –419. ISSN: 1290-0729. DOI: 10.1016/j.ijthermalsci.2018.10.043 (cit. on pp. 4, 22, 28, 54, 58, 59, 61–63, 73).

[21] J. Serrano, P. Piqueras, R. Navarro, D. Tarí, and C. Meano. "Development and verification of an in-flow water condensation model for 3D-CFD simulations of humid air streams mixing." *Computers & Fluids* 167 (2018), pp. 158 –165. ISSN: 0045-7930. DOI: 10.1016/j.compfluid.2018.02.032 (cit. on pp. 4, 7, 54, 61, 62, 73).

[22] S Karstadt, J Werner, S Münz, and R Aymanns. "Effect of water droplets caused by low pressure EGR on spinning compressor wheels." In: *Aufladetechnische Konferenz, Dresden*. 2014 (cit. on pp. 4, 7, 22, 54).

[23] J. Kickhofel, V. Valori, and H.-M. Prasser. "Turbulent penetration in T-junction branch lines with leakage flow." *Nuclear Engineering and Design* 276 (2014), pp. 43–53. DOI: 10.1016/j.nucengdes.2014.05.002 (cit. on pp. 5, 53).

[24] H Kamide, M Igarashi, S Kawashima, N Kimura, and K Hayashi. "Study on mixing behavior in a tee piping and numerical analyses for evaluation of thermal striping." *Nuclear Engineering and Design* 239(1) (2009), pp. 58–67. DOI: 10.1016/j.nucengdes.2008.09.005 (cit. on pp. 5, 6, 53, 64, 77, 78).

[25] N. Kimura, H. Ogawa, and H. Kamide. "Experimental study on fluid mixing phenomena in T-pipe junction with upstream elbow." *Nuclear Engineering and Design* 240(10) (2010), pp. 3055–3066. DOI: 10.1016/j.nucengdes.2010.05.019 (cit. on pp. 5, 6, 53, 64, 77, 159).

[26] T. Lu, D. Attinger, and S. M. Liu. "Large-eddy simulations of velocity and temperature fluctuations in hot and cold fluids mixing in a tee junction with an upstream straicht or elbow main pipe." *Nuclear Engineering and Design* 263 (Apr. 2, 2013), pp. 32–41. DOI: 10.1016/j.nucengdes.2013.04.002 (cit. on pp. 5, 53).

[27] R. Tunstall, D. Laurence, R. Prosser, and A. Skillen. "Large eddy simulation of a T-Junction with upstream elbow: The role of Dean vortices in thermal fatigue." *Applied Thermal Engineering* 107 (Aug. 25, 2017), pp. 672–680. DOI: 10.1016/j.applthermaleng.2016.07.011 (cit. on p. 5).

[28] J.-l. Chen, L.-m. He, X.-m. Luo, H.-t. Bai, and Y.-h. Wei. "Simulation of oil-water two phase flow and separation behaviors in combined T junctions." *Journal of Hydrodynamics* 24(6) (2012), pp. 848–857. DOI: 10.1016/s1001-6058(11)60312-0 (cit. on p. 5).

[29] L. Yang, J. Wang, Y. Jiang, and L. Zou. "Oil-water flow splitting in eccentric annular T-junction tubes. Experimental and CFD analysis." *Chemical Engineering Science* 228 (2020), p. 116000. DOI: 10.1016/j.ces.2020.116000 (cit. on pp. 5, 53).

[30] K.-H. Brune, B. Stoffel, B. Matyschok, et al. "CFD-Analysis of the Flow Consisting of Two Mass Flows With Different Temperatures and/or Two Phases in a Turbocompressor." In: *ASME 2006 2nd Joint US-European Fluids Engineering Summer Meeting Collocated With the 14th International Conference on Nuclear Engineering*. American Society of Mechanical Engineers Digital Collection. 2006, pp. 701–711 (cit. on pp. 5, 22, 24, 27, 28, 36, 67, 68).

[31] K.-H. Brune, H.-P. Schiffer, R Christmann, and M Gnewikow. "Experimental investigations of the disturbed inlet-flow structure caused by mixing geometries and its influence on the performance of a turbocharger centrifugal compressor." In: *ASME Turbo Expo 2009: Power for Land, Sea, and Air*. American Society of Mechanical Engineers Digital Collection. 2009, pp. 1295–1304 (cit. on pp. 5, 22, 24, 41).

[32] A. Reihani, J. Hoard, S. Klinkert, C.-K. Kuan, and D. Styles. "Numerical Evaluation of the Effects of Low Pressure EGR Mixer Configuration on Turbocharger Compressor Performance." In: *ASME 2018 Internal Combustion Engine Division Fall Technical Conference*. American Society of Mechanical Engineers Digital Collection. 2018 (cit. on pp. 6, 11, 23, 34, 36, 47, 198).

[33] A. Reihani, J. Hoard, S. Klinkert, C.-K. Kuan, D. Styles, and G. McConville. "Experimental response surface study of the effects of low-pressure exhaust gas recirculation mixing on turbocharger compressor performance." *Applied Energy* 261 (2020), p. 114349. DOI: 10.1016/j.apenergy.2019.114349 (cit. on pp. 6, 58, 77).

[34] S. M. Hosseini, K. Yuki, and H. Hashizume. "Classification of turbulent jets in a T-junction area with a 90-deg bend upstream." *International Journal of heat and mass transfer* 51(9-10) (2008), pp. 2444–2454. DOI: 10.1016/j.ijheatmasstransfer.2007.08.024 (cit. on pp. 6, 53).

[35] Y. Wang, P. Wang, and T. Lu. "Experimental investigation of the thermal fluctuations in hot and cold fluids mixing in a T-junction filled with spherical particles." *Applied thermal engineering* 71(1) (2014), pp. 310–316. DOI: 10.1016/j.applthermaleng.2014.06.010 (cit. on p. 6).

[36] W.-f. Li, Y. Wei, G.-y. Tu, Z.-h. Shi, H.-f. Liu, and F.-c. Wang. "Experimental study about mixing characteristic and enhancement of T-jet reactor." *Chemical Engineering Science* 144 (2016), pp. 116–125. DOI: 10.1016/j.ces.2016.01.024 (cit. on p. 6).

[37] G. Chuang and Y. Ferng. "Experimentally investigating the thermal mixing and thermal stripping characteristics in a T-junction." *Applied Thermal Engineering* 113 (2017), pp. 1585–1595 (cit. on p. 6).

[38] C. Evrim, X. Chu, and E. Laurien. "Analysis of thermal mixing characteristics in different t-junction configurations." *International Journal of Heat and Mass Transfer* 158 (2020), p. 120019. DOI: 10.1016/j.ijheatmasstransfer.2020.120019 (cit. on pp. 6, 53).

[39] C. Evrim and E. Laurien. "Numerical study of thermal mixing mechanisms in t-junctions." *Applied Thermal Engineering* 183 (2021), p. 116155. DOI: 10.1016/j.applthermaleng.2020.116155 (cit. on pp. 6, 53, 77).

[40] A. Gupta, M. S. Ibrahim, and R. Amano. "Effect of jet-to-mainstream momentum flux ratio on mixing process." *Heat and Mass Transfer* 52(3) (2016), pp. 621–634. DOI: 10.1007/s00231-015-1582-7 (cit. on pp. 6, 53).

[41] J. R. Serrano, P. Piqueras, E. Angiolini, C. Meano, and J. De La Morena. "On Cooler and Mixing Condensation Phenomena in the Long-Route Exhaust Gas Recirculation Line." In: *SAE Technical Paper*. 2015. DOI: 10.4271/2015-24-2521 (cit. on pp. 7, 9, 53–55, 57, 58).

[42] A. García, J. Monsalve-Serrano, R. L. Sari, and P. Gaillard. "Assessment of a complete truck operating under dual-mode dual-fuel combustion in real life applications: Performance and emissions analysis." *Applied Energy* 279 (2020), p. 115729. DOI: 10.1016/j.apenergy.2020.115729 (cit. on pp. 7, 54).

[43] P. Olmeda, J. Martín, F. Arnau, and S. Artham. "Analysis of the energy balance during World harmonized Light vehicles Test Cycle in warmed and cold conditions using a Virtual Engine." *International Journal of Engine Research* - (Oct. 3, 2019), pp. 0–18. DOI: 10.1177/1468087419878593 (cit. on pp. 7, 54).

[44] J. Galindo, R. Navarro, D. Tari, and F. Moya. "Development of an experimental test bench and a psychrometric model for assessing condensation on a Low Pressure EGR cooler." *International Journal of Engine Research* 22 (5 2020), pp. 1540–1550. DOI: 10.1177/1468087420909735 (cit. on pp. 7, 54, 111).

[45] J. Galindo, R. Navarro, D. Tari, and F. Moya. "Analysis of condensation and secondary flows at T-junctions using optical visualization techniques and Computational Fluid Dynamics." *International Journal of Multiphase Flow* (2021). DOI: 10.1016/j.ijmultiphaseflow.2021.103674 (cit. on pp. 7, 54, 59, 61–63, 77).

[46] J. Galindo, R. Navarro, D. Tarí, and F. Moya. "Quantitative validation of an in-flow water condensation model for 3D-CFD simulations of three-way junctions using indirect condensation measurements." *International Journal of Thermal Sciences* 172 (2022), pp. 1–17. DOI: 10.1016/j.ijthermalsci.2021.107303 (cit. on pp. 7, 54, 62, 63).

[47] J. M. Luján, H. Climent, B. Pla, M. E. Rivas-Perea, N.-Y. François, J. Borges-Alejo, and Z. Soukeur. "Exhaust gas recirculation dispersion analysis using in-cylinder pressure measurements in automotive diesel engines." *Applied Thermal Engineering* 89 (2015), pp. 459–468. DOI: 10.1016/j.applthermaleng.2015.06.029 (cit. on pp. 7, 10, 99, 102).

[48] V. Macián, J. M. Luján, H. Climent, J. Miguel-García, S. Guilain, and R. Boubennec. "Cylinder-to-cylinder high-pressure exhaust gas recirculation dispersion effect on opacity and NOx emissions in a diesel automotive engine." *International Journal of Engine Research* (2020). DOI: 10.1177/1468087419895401 (cit. on pp. 7, 10, 100, 106, 149).

[49] C. Guardiola, B. Pla, D. Blanco-Rodriguez, and P. O. Calendini. "ECU-oriented models for NOx prediction. Part 1: a mean value engine model for NOx prediction." *Proceedings of the Institution of Mechanical Engineers, Part D: Journal of Automobile Engineering* 229(8) (2015), pp. 992–1015. DOI: 10.1177/0954407014550191 (cit. on pp. 7, 100, 103–105).

[50] X. Tauzia, H. Karaky, and A. Maiboom. "Evaluation of a semi-physical model to predict NOx and soot emissions of a CI automotive engine under warm-up like conditions." *Applied Thermal Engineering* 137 (2018), pp. 521–531. DOI: 10.1016/j.applthermaleng.2018.04.005 (cit. on pp. 7, 100).

[51] A. Sakowitz and L. Fuchs. "Computation of mixing processes related to EGR." In: *TSFP digital library online*. Begel House Inc. 2011. URL: http://www.dl.begellhouse.com/en/references/3ce1b491115b5c16,60d8a9681cb3cfc7,57130c5b30e27450.html (cit. on pp. 7, 100, 109–112, 118, 119, 122, 150).

[52] A. Sakowitz, S. Reifarth, M. Mihaescu, and L. Fuchs. "Modeling of EGR Mixing in an engine intake manifold using LES." *Oil & Gas Science and Technology* 69(1) (2014), pp. 167–176. DOI: 10.2516/ogst/2013118 (cit. on pp. 7, 100, 112, 118, 150, 201, 204).

[53] A. Sakowitz, M. Mihaescu, and L. Fuchs. "Turbulent flow mechanisms in mixing T-junctions by Large Eddy Simulations." *International Journal of Heat and Fluid Flow* 45 (2014), pp. 135–146. DOI: 10.1016/j.ijheatfluidflow.2013.06.014 (cit. on pp. 7, 58, 65, 67, 100, 110).

[54] A. Sakowitz. "Computation and analysis of EGR mixing in internal combustion engine manifolds." PhD thesis. KTH Royal Institute of Technology, 2013. URL: http://www.diva-portal.org/smash/record.jsf?pid=diva2:603864&dswid=6780 (cit. on pp. 7, 100, 105, 110).

[55] S. Ramanathan, A. Hudson, J. Styron, B. Baldwin, D. Ives, and D. Ducu. *EGR and swirl distribution analysis using coupled 1D-3D CFD simulation for a turbocharged heavy duty diesel engine.* Tech. rep. SAE Technical Paper, 2011. DOI: 10.4271/2011-01-2222 (cit. on pp. 8, 107, 108, 112, 117, 200).

[56] S. K. R. Hariganesh, M Sathyanadan, S Krishnan, P Vadivel, and D Vamsidhar. "Computational analysis of EGR mixing inside the intake system & experimental investigation on diesel engine for LCV." *International Journal of Engineering Science & Technology* 3(3) (2011) (cit. on pp. 8, 108, 117, 119).

[57] R. Rahimi, S Jafarmadar, S. Khalilarya, and A Mohebbi. "Numerical and experimental investigations of EGR distribution in a DI turbocharged diesel engine." *Transactions of the Canadian society for mechanical engineering* 37(2) (2013), pp. 247–257. DOI: 10.1139/tcsme-2013-0015 (cit. on pp. 8, 107, 108, 111, 119).

[58] P. Dimitriou, R. Burke, C. D. Copeland, and S. Akehurst. *Study on the effects of EGR supply configuration on cylinder-to-cylinder dispersion and engine performance using 1D-3D co-simulation.* Tech. rep. SAE Technical Paper, 2015. URL: https://saemobilus.sae.org/content/2015-32-0816 (cit. on pp. 8, 100, 107, 110–112, 117, 119, 122, 150, 200, 202).

[59] P. Dimitriou, C. Avola, R. Burke, C. Copeland, and N. Turner. "A Comparison of 1D-3D Co-Simulation and Transient 3D Simulation for EGR Distribution Studies." In: *ASME 2016 Internal Combustion Engine Division Fall Technical Conference*. American Society of Mechanical Engineers. 2016, V001T06A010–V001T06A010. DOI: 10.1115/icef2016-9361 (cit. on pp. 8, 111, 117).

[60] E. Kartaev, V. Emel'kin, M. Ktalkherman, V. Kuz'min, and S. Aul'chenko. "Analysis of mixing of impinging radial jets with crossflow in the regime of counter flow jet formation." *Chemical Engineering Science* 119 (2014), pp. 1–9. DOI: 10.1016/j.ces.2014.07.062 (cit. on pp. 8, 159).

[61] S. Nada, A Fouda, and H. Elattar. "Parametric study of flow field and mixing characteristics of outwardly injected jets into a crossflow in a cylindrical chamber." *International Journal of Thermal Sciences* 102 (2016), pp. 185–201. DOI: 10.1016/j.ijthermalsci.2015.11.017 (cit. on pp. 8, 159).

[62] N. Minocha and J. B. Joshi. "3D CFD simulation of turbulent flow distribution and pressure drop in a dividing manifold system using openfoam." *International Journal of Heat and Mass Transfer* 151 (2020), p. 119420. DOI: 10.1016/j.ijheatmasstransfer.2020.119420 (cit. on pp. 8, 160).

[63] G. R. de Souza, C. de Castro Pellegrini, S. L. Ferreira, F. S. Pau, and O. Armas. "Study of intake manifolds of an internal combustion engine: A new geometry based on experimental results and numerical simulations." *Thermal Science and Engineering Progress* 9 (2019), pp. 248–258. DOI: 10.1016/j.tsep.2018.12.003 (cit. on pp. 8, 159, 205).

[64] *STAR-CCM+*. Release version 12.06.010. CD-adapco. 2018. URL: http://ww.cd-adapco.com (cit. on pp. 9, 26, 30, 34, 42, 59, 61, 100, 107, 112, 114, 119, 170, 190).

[65] *STAR-CCM+*. Release version 14.02.010. Simcenter. 2019. URL: http://www.siemens.com (cit. on pp. 9, 24).

[66] J. Galindo, F. J. Arnau, L. M. García-Cuevas, and P. Soler. "Experimental validation of a quasi-two-dimensional radial turbine model." *International Journal of Engine Research* (2018), p. 1468087418788502 (cit. on pp. 9, 24).

[67] J. Galindo, A. Tiseira, R. Navarro, D. Tarí, H. Tartoussi, and S. Guilain. "Compressor Efficiency Extrapolation for 0D-1D Engine Simulations." In: *SAE Technical Paper*. SAE International, Apr. 2016. DOI: 10.4271/2016-01-0554 (cit. on pp. 9, 32, 33).

[68] J. R. Serrano, P. Olmeda, F. J. Arnau, and V. Samala. "A holistic methodology to correct heat transfer and bearing friction losses from hot turbocharger maps in order to obtain adiabatic efficiency of the turbomachinery." *International Journal of Engine Research* (2019), p. 1468087419834194 (cit. on pp. 9, 32).

[69] J. M. Luján, C. Guardiola, B. Pla, and A. Reig. "Switching strategy between HP (high pressure)-and LPEGR (low pressure exhaust gas recirculation) systems for reduced fuel consumption and emissions." *Energy* 90 (2015), pp. 1790–1798. DOI: 10.1016/j.energy.2015.06.138 (cit. on pp. 10, 22, 54, 102).

[70] V. T. Vithala, J. Hoard, D. Assanis, and D. Styles. "3-D Numerical Study of Turbulent Mixing of Intake Air and Exhaust Gas in a Low Pressure EGR System." In: *ASME 2011 Internal Combustion Engine Division Fall Technical Conference*. American Society of Mechanical Engineers Digital Collection. 2011, pp. 893–904 (cit. on pp. 22, 24, 27, 36, 41, 58).

[71] J. Luján, B Pla, S Moroz, and G Bourgoin. "Effect of low pressure EGR on gas exchange processes and turbocharging of a HSDI engine." In: *Proceedings of the conference on thermo-and fluid-dynamic processes in diesel engines (THIESEL 2008), Valencia, Spain, paper E*. Vol. 2. 2008 (cit. on p. 24).

[72] R. Navarro. "A numerical approach for predicting flow-induced acoustics at near-stall conditions in an automotive turbocharger compressor." PhD thesis. Universitat Politècnica de València, 2014. URL: http://hdl.handle.net/10251/44114 (cit. on pp. 25, 27, 43, 203).

[73] A. Broatch, J. Galindo, R. Navarro, and J. García-Tíscar. "Methodology for experimental validation of a CFD model for predicting noise generation in centrifugal compressors." *International Journal of Heat and Fluid Flow* 50 (2014), pp. 134–144. DOI: 10.1016/j.ijheatfluidflow.2014.06.006 (cit. on pp. 25–27).

[74] N. Watson and M. Janota. *Turbocharging the internal combustion engine*. Macmillan International Higher Education, 1982. DOI: 10.1007/978-1-349-04024-7 (cit. on p. 28).

[75] P. Olmeda, A. Tiseira, V. Dolz, and L. García-Cuevas. "Uncertainties in power computations in a turbocharger test bench." *Measurement* 59(Supplement C) (2015), pp. 363 –371. ISSN: 0263-2241. DOI: https://doi.org/10.1016/j.measurement.2014.09.055 (cit. on pp. 31, 33).

[76] X. Li and S. Wang. "Flow field and pressure loss analysis of junction and its structure optimization of aircraft hydraulic pipe system." *Chinese Journal of Aeronautics* 26(4) (2013), pp. 1080–1092. DOI: 10.1016/j.cja.2013.04.004 (cit. on p. 53).

[77] M. Zhou, R. Kulenovic, and E. Laurien. "T-junction experiments to investigate thermal-mixing pipe flow with combined measurement techniques." *Applied Thermal Engineering* 150 (Mar. 5, 2019), pp. 237–249. DOI: 10.1016/j.applthermaleng.2018.12.161 (cit. on p. 53).

[78] A. Kuczaj, E. Komen, and M. Loginov. "Large-Eddy Simulation study of turbulent mixing in a T-junction." *Nuclear Engineering and Design* 240(9) (2010). Experiments and CFD Code Applications to Nuclear Reactor Safety (XCFD4NRS), pp. 2116 –2122. ISSN: 0029-5493. DOI: 10.1016/j.nucengdes.2009.11.027 (cit. on pp. 53, 67).

[79] I. Basler, H. Reister, R. Rossmann, and B. Weigand. "A Simulation Method for the Calculation of Water Condensation inside Charge Air Coolers" (2021). DOI: 10.4271/2021-01-0226 (cit. on p. 53).

[80] R. Cash, A. Talekar, and B. AbdulNour. "A CFD Study of Water Condensation Inside the Tubes of an Automotive Compact Charge Air Cooler Using Large Eddy Simulation Approach." In: *ASME International Mechanical Engineering Congress and Exposition*. Vol. 50626. American Society of Mechanical Engineers. 2016, V008T10A068. DOI: 10.1115/imece2016-66999 (cit. on p. 53).

[81] K. R. Jensen, P. Fojan, R. L. Jensen, and L. Gurevich. "Water condensation: A multiscale phenomenon." *Journal of nanoscience and nanotechnology* 14(2) (2014), pp. 1859–1871. DOI: 10.1166/jnn.2014.9108 (cit. on p. 53).

[82] Q. Sheng, J. Sun, Q. Wang, W. Wang, and H. S. Wang. "On the onset of surface condensation: formation and transition mechanisms of condensation mode." *Scientific reports* 6(1) (2016), pp. 1–9. DOI: 10.1038/srep30764 (cit. on p. 53).

[83] N. Kortsenshtein, E. Samuilov, and A. Yastrebov. "New method of simulation of volume condensation of supersaturated vapor." *High Temperature* 47(1) (2009), pp. 83–94. DOI: 10.1134/s0018151x09010118 (cit. on p. 53).

[84] P. Vojkuvkova, O. Sikula, and J. Weyr. "Assessment of condensation of water vapor in the mixing chamber by CFD method." In: *EPJ Web of Conferences*. Vol. 92. 2015. DOI: 10.1051/epjconf/20159202112 (cit. on p. 53).

[85] M. Zheng, G. T. Reader, and J. G. Hawley. "Diesel engine exhaust gas recirculation—-a review on advanced and novel concepts." *Energy conversion and management* 45(6) (2004), pp. 883–900 (cit. on p. 54).

[86] M. Choi, K. Mohiuddin, N. Kim, and S. Park. "Investigation of the effects of EGR rate, injection strategy and nozzle specification on engine performances and emissions of a single cylinder heavy duty diesel engine using the two color method." *Applied Thermal Engineering* (2021), p. 117036. DOI: 10.1016/j.applthermaleng.2021.117036 (cit. on p. 54).

[87] N. Dimitrakopoulos, G. Belgiorno, M. Tunér, P. Tunestål, and G. Di Blasio. "Effect of EGR routing on efficiency and emissions of a PPC engine." *Applied Thermal Engineering* 152 (2019), pp. 742–750. DOI: 10.1016/j.applthermaleng.2019.02.108 (cit. on p. 54).

[88] X. Yu, N. S. Sandhu, Z. Yang, and M. Zheng. "Suitability of energy sources for automotive application–A review." *Applied Energy* 271 (2020), p. 115169. DOI: 10.1016/j.apenergy.2020.115169 (cit. on p. 54).

[89] H. Song and S. Song. "Numerical investigation on a dual loop EGR optimization of a light duty diesel engine based on water condensation analysis." *Applied Thermal Engineering* 182 (2021), pp. 1–12. DOI: 10.1016/j.applthermaleng.2020.116064 (cit. on p. 54).

[90] S. Schuster, D. Brillert, and F. Benra. "Condensation in Radial Turbines-Part I: Mathematical Modeling." *Journal of Turbomachinery* 140 (2018), pp. 1–9. DOI: 10.1115/1.4040934 (cit. on p. 60).

[91] S. Schuster, D. Brillert, and F. Benra. "Condensation in Radial Turbines-Part II: Application of the Mathematical Model to a Radial Turbine Series." *Journal of Turbomachinary* 140 (2018), pp. 1–7. DOI: 10.1115/1.4040935 (cit. on p. 60).

[92] T. Wittmann, C. Bode, and J. Friedrichs. "The Feasibility of an Euler-Lagrange Approach for the Modeling of Wet Steam." *Journal of Engineering for gas turbines and power* 143 (2021), pp. 1–8. DOI: 10.1115/1.4049859 (cit. on p. 60).

[93] F. R. Menter. "Two-equation eddy-viscosity turbulence models for engineering applications." *AIAA journal* 32(8) (1994), pp. 1598–1605. DOI: 10.2514/3.12149 (cit. on pp. 60, 111).

[94] S. Smith and M. Mungal. "Mixing, structure and scaling of the jet in crossflow." *Journal of fluid mechanics* 357 (1998), pp. 83–122. DOI: 10.1017/s0022112097007891 (cit. on p. 64).

[95] A. R. Karagozian. "The jet in crossflow." *Physics of Fluids* 26(10) (2014), pp. 1–47. DOI: 10.1063/1.4895900 (cit. on p. 64).

[96] W Vicente, M Salinas-Vazquez, C Chavez, and E Carrizosa. "Different numerical methods in the study of passive scalar transport in a pipeline x-junction." *Applied mathematical modelling* 33(3) (2009), pp. 1248–1258. DOI: 10.1016/j.apm.2008.01.022 (cit. on p. 65).

[97] L. Grbčić, L. Kranjčević, I. Lučin, and Z. Čarija. "Experimental and numerical investigation of mixing phenomena in double-Tee junctions." *Water* 11(6) (2019), p. 1198. DOI: 10.3390/w11061198 (cit. on p. 65).

[98] A Schlegel, M Streichsbier, R Mongia, and R Dibble. *A Comparison of the Influence of Fuel/Air Unmixedness on NOx Emissions in Lean Premixed, Non-Catalytic and Catalytically Stabilized Combustion.* Vol. 78699. American Society of Mechanical Engineers, 1997. DOI: 10.1115/97-gt-306 (cit. on p. 65).

[99] D Mira, O Lehmkuhl, P Stathopoulos, T Tanneberger, T. Reichel, C. Paschereit, M Vázquez, and G Houzeaux. "Numerical Investigation of a Lean Premixed Swirl-Stabilized Hydrogen Combustor and Operational Conditions Close to Flashback." In: *Turbo Expo: Power for Land, Sea, and Air*. Vol. 51067. American Society of Mechanical Engineers. 2018, V04BT04A009. DOI: 10.1115/gt2018-76229 (cit. on p. 65).

[100] S. Hossain, M. Ansari, and K.-Y. Kim. "Evaluation of the mixing performance of three passive micromixers." *Chemical Engineering Journal* 150(2-3) (2009), pp. 492–501. DOI: 10.1016/j.cej.2009.02.033 (cit. on p. 65).

[101] P. Danckwerts. "The definition and measurement of some characteristics of mixtures." *Applied Scientific Research, Section A* 3(4) (1952), pp. 279–296. DOI: 10.1016/b978-0-08-026250-5.50050-2 (cit. on p. 65).

[102] J. Andersen, F. Lindström, and F. Westin. "Surge definitions for radial compressors in automotive turbochargers." *SAE International Journal of Engines* 1(1) (2008), pp. 218–231. DOI: 10.4271/2008-01-0296 (cit. on p. 67).

[103] R. Dehner, N. Figurella, A. Selamet, P. Keller, M. Becker, K. Tallio, K. Miazgowicz, and R. Wade. "Instabilities at the Low-Flow Range of a Turbocharger Compressor." *SAE International Journal of Engines* 6(2) (2013), pp. 1356–1367. DOI: 10.4271/2013-01-1886 (cit. on p. 67).

[104] A. Torregrosa, A. Broatch, X. Margot, J. García-Tíscar, Y. Narvekar, and R. Cheung. "Local flow measurements in a turbocharger compressor inlet." *Experimental Thermal and Fluid Science* 88 (2017), pp. 542 – 553. ISSN: 0894-1777. DOI: 10.1016/j.expthermflusci.2017.07.007 (cit. on p. 67).

[105] B. Smith, J. Mahaffy, and K. Angele. "A CFD benchmarking exercise based on flow mixing in a T-junction." *Nuclear Engineering and Design* 264 (2013). SI:NURETH-14, pp. 80 –88. ISSN: 0029-5493. DOI: 10.1016/j.nucengdes.2013.02.030 (cit. on p. 67).

[106] P. Slavík, B. Skočilasová, J. Soukup, and F. Klimenda. "Low pressure EGR valve testing." In: *AIP Conference Proceedings*. Vol. 2118. 1. AIP Publishing LLC. 2019, p. 030040. DOI: 10.1063/1.5114768 (cit. on p. 73).

[107] F. Castillo, E. Witrant, V. Talon, and L. Dugard. "Simultaneous air fraction and low-pressure EGR mass flow rate estimation for diesel engines." *IFAC Proceedings Volumes* 46(2) (2013), pp. 731–736. DOI: 10.3182/20130204-3-fr-2033.00070 (cit. on p. 73).

[108] D. Wang, L. Shi, S. Zhu, B. Liu, Y. Qian, and K. Deng. "Numerical and thermodynamic study on effects of high and low pressure exhaust gas recirculation on turbocharged marine low-speed engine." *Applied Energy* 261 (2020), p. 114346. DOI: 10.1016/j.apenergy.2019.114346 (cit. on p. 73).

[109] G. Boccardo, F. Millo, A. Piano, L. Arnone, S. Manelli, and C. Capiluppi. *A Fully Physical Correlation for Low Pressure EGR Control Linearization.* Tech. rep. SAE Technical Paper, 2017. DOI: 10.4271/2017-24-0011 (cit. on p. 73).

[110] W. Wenzel, U Hanig, J Song, B Bareis, and M Miclea-Bleiziffer. "Inlet swirl throttle for passenger car engines." In: *16. Internationales Stuttgarter Symposium.* Springer. 2016, pp. 951–968. DOI: 10.1007/978-3-658-13255-2_71 (cit. on p. 73).

[111] U. Hanig and M. Becker. "Intake Throttle and Pre-swirl Device for Low-Pressure EGR Systems." *MTZ worldwide* 76(1) (2015), pp. 10–13. DOI: 10.1007/s38313-014-1004-0 (cit. on p. 73).

[112] M. Hirota, E. Mohri, H. Asano, and H. Goto. "Experimental study on turbulent mixing process in cross-flow type T-junction." In: *ICHMT DIGITAL LIBRARY ONLINE.* Begel House Inc. 2009 (cit. on p. 76).

[113] M. Hirota, H. Asano, H. Nakayama, T. Asano, and S. Hirayama. "Three-dimensional structure of turbulent flow in mixing T-junction." *JSME International Journal Series B Fluids and Thermal Engineering* 49(4) (2006), pp. 1070–1077. DOI: 10.1299/jsmeb.49.1070 (cit. on p. 77).

[114] B. Su, Z. Zhu, X. Wang, H. Ke, M. Lin, and Q. Wang. "Effect of temperature difference on the thermal mixing phenomenon in a T-junction under inflow pulsation." *Nuclear Engineering and Design* 363 (2020), p. 110611. DOI: 10.1016/j.nucengdes.2020.110611 (cit. on p. 77).

[115] M. Pamminger, B. Wang, C. Hall, R. Vojtech, and T. Wallner. "The impact of water injection and exhaust gas recirculation on combustion and emissions in a heavy-duty compression ignition engine operated on diesel and gasoline." *International Journal of Engine Research* - (Jan. 8, 2019), pp. 0–19. DOI: 10.1177/1468087418815290 (cit. on p. 99).

[116] V. J. Page, C. P. Garner, G. K. Hargrave, and H. K. Versteeg. *Development of a validated CFD process for the analysis of inlet manifold flows with EGR.* Tech. rep. SAE Technical Paper, 2002. DOI: 10.4271/2002-01-0071 (cit. on pp. 100, 110, 111).

[117] M. Georgiou and M. V. Papalexandris. "Turbulent mixing in T-junctions: The role of the temperature as an active scalar." *International Journal of Heat and Mass Transfer* 115 (2017), pp. 793–809. DOI: 10.1016/j.ijheatmasstransfer.2017.08.081 (cit. on pp. 100, 110).

[118] S. Reifarth, E. Kristensson, J. Borggren, A. Sakowitz, and H.-E. Angstrom. *Analysis of EGR/Air Mixing by 1-D Simulation, 3-D Simulation and Experiments*. Tech. rep. SAE Technical Paper, 2014. DOI: 10.4271/2014-01-2647 (cit. on pp. 100, 110, 112).

[119] B Pla. "Análisis del Proceso de la Recirculación de los Gases de Escape de Baja Presión en Motores Diesel Sobrealimentados." PhD thesis. PhD Thesis, Universitat Politècnica de València, Departamento de Máquinas y Motores Térmicos, 2009. DOI: 10.4995/Thesis/10251/4782 (cit. on pp. 102, 105–107).

[120] Galindo, José and Climent, Héctor and Navarro, Roberto. "Modeling of EGR Systems." In: *1D and Multi-D Modeling Techniques for IC Engine Simulation*. Ed. by A. Onorati and G. Montenegro. SAE International, 2020. Chap. 7, pp. 257–278. DOI: 10.4271/9780768099522 (cit. on pp. 106, 107).

[121] P. E. Smirnov, T. Hansen, and F. R. Menter. "Numerical Simulation of Turbulent Flows in Centrifugal Compressor Stages With Different Radial Gaps." In: *Proceedings of GT2007*. GT2007-27376. ASME, 2007. DOI: 10.1115/GT2007-27376 (cit. on p. 111).

[122] Perry, R.H. "Physical and chemical data." *Perry's chemical engineers' handbook* (1984), pp. 7–374 (cit. on p. 111).

[123] F. M. White and I. Corfield. *Viscous fluid flow*. Vol. 3. McGraw-Hill New York, 2006 (cit. on p. 112).

[124] M. J. Moran, H. N. Shapiro, D. D. Boettner, and M. B. Bailey. *Fundamentals of engineering thermodynamics*. John Wiley & Sons, 2010 (cit. on p. 112).

[125] A. Maiboom, X. Tauzia, and J.-F. Hetet. "Influence of high rates of supplemental cooled EGR on NOx and PM emissions of an automotive HSDI diesel engine using an LP EGR loop." *International Journal of Energy Research* 32(15) (2008), pp. 1383–1398. DOI: 10.1002/er.1455 (cit. on pp. 117, 127).

[126] R. Navarro. *Predicting Flow-Induced Acoustics at Near-Stall Conditions in an Automotive Turbocharger Compressor: A Numerical Approach*. Springer, 2018. ISBN: 978-3-319-72248-1. DOI: 10.1007/978-3-319-72248-1 (cit. on p. 124).

[127] Sharma, Sidharath and García-Tíscar, Jorge and Allport, JM and Barrans, Simon and Nickson, AK. "Evaluation of modelling parameters for computing flow-induced noise in a small high-speed centrifugal compressor." *Aerospace Science and Technology* 98 (2020), p. 105697. DOI: 10.1016/j.ast.2020.105697 (cit. on p. 124).

[128] Ferziger, J.H. and Perić, M. *Computational Methods for Fluid Dynamics*. 3rd rev. Berlin: Springer, 2002 (cit. on p. 124).

[129] R. M. Cummings, S. A. Morton, and D. R. McDaniel. "Experiences in accurately predicting time-dependent flows." *Progress in Aerospace Sciences* 44(4) (May 2008), pp. 241–257. ISSN: 0376-0421. DOI: 10.1016/j.paerosci.2008.01.001 (cit. on p. 125).

[130] B. Lakshminarayana. "An Assessment of Computational Fluid Dynamic Techniques in the Analysis and Design of Turbomachinery." *Journal of Fluids Engineering* 113(3) (Sept. 1991), pp. 315–352. ISSN: 0098-2202. DOI: 10.1115/1.2909503. eprint: https://asmedigitalcollection.asme.org/fluidsengineering/article-pdf/113/3/315/5592525/315_1.pdf (cit. on p. 125).

[131] F. Balduzzi, A. Bianchini, R. Maleci, G. Ferrara, and L. Ferrari. "Critical issues in the CFD simulation of Darrieus wind turbines." *Renewable Energy* 85 (2016), pp. 419 –435. ISSN: 0960-1481. DOI: 10.1016/j.renene.2015.06.048 (cit. on p. 125).

[132] S. Družeta, L. Sopta, S. Maćešić, and N. Črnjarić-Žic. "Investigation of the importance of spatial resolution for two-dimensional shallow-water model accuracy." *Journal of Hydraulic Engineering* 135(11) (2009), pp. 917–925. DOI: 10.1061/(asce)0733-9429(2009)135:11(917) (cit. on p. 125).

[133] Z. Boz, F. Erdogdu, and M. Tutar. "Effects of mesh refinement, time step size and numerical scheme on the computational modeling of temperature evolution during natural-convection heating." *Journal of Food Engineering* 123 (2014), pp. 8–16. DOI: 10.1016/j.jfoodeng.2013.09.008 (cit. on p. 125).

[134] J William, A Dupont, R. Bazile, and M. Marchal. "Study of geometrical parameter influence on air/EGR mixing." *SAE transactions* (2003), pp. 1016–1036. DOI: 10.4271/2003-01-1796 (cit. on pp. 133, 143, 150, 201).

"I would rather have questions that can't be answered than answers that can't be questioned."

Richard Feynman.